

DTIC FILE COPY

AFOSK-TR-66-1004

2

AD-A200 936

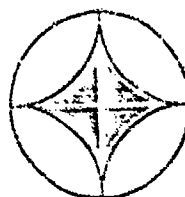
EXPERIMENTAL AND THEORETICAL RESPONSE
OF MULTIPHASE POROUS MEDIA
TO DYNAMIC LOADS

FINAL REPORT

DTIC
ELECTE
OCT 06 1988
S D

DISTRIBUTION STATEMENT A

Approved for public release
Distribution Unlimited



APPLIED
RESEARCH
ASSOCIATES, INC.

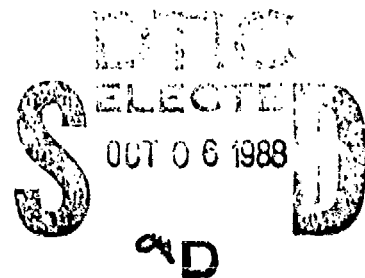
Engineering and Applied Science

(2)

EXPERIMENTAL AND THEORETICAL RESPONSE
OF MULTIPHASE POROUS MEDIA
TO DYNAMIC LOADS

FINAL REPORT

1 September 1988



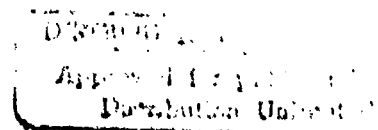
Prepared for

Air Force Office of Scientific Research
Bolling Air Force Base
Washington, DC 20332-6448

Under Contract No. F49620-85-C-0102

Prepared by

Kwang J. Kim
Scott E. Blouin
Daniel E. Chitty
Douglas H. Merkle



Applied Research Associates, Inc.
New England Division
South Royalton, Vermont 05068

UNCLASSIFIED

SECURITY CLASSIFICATION OF THIS PAGE

REPORT DOCUMENTATION PAGE

Form Approved
OMB No. 0704-0188

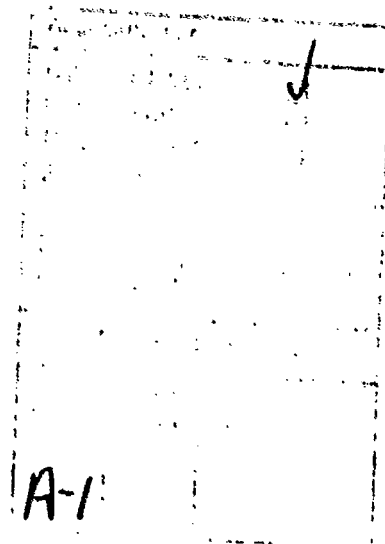
1a. REPORT SECURITY CLASSIFICATION UNCLASSIFIED			1b. RESTRICTIVE MARKINGS NONE		
2a. SECURITY CLASSIFICATION AUTHORITY N/A since UNCLASSIFIED			3. DISTRIBUTION/AVAILABILITY OF REPORT Approved for public release; distribution unlimited		
2b. DECLASSIFICATION/DOWNGRADING SCHEDULE N/A since UNCLASSIFIED					
4. PERFORMING ORGANIZATION REPORT NUMBER(S) ARA-5967-88			5. MONITORING ORGANIZATION REPORT NUMBER(S) AFOSR-TR-88-1004		
6a. NAME OF PERFORMING ORGANIZATION Applied Research Associates, Inc.		6b. OFFICE SYMBOL (if applicable)	7a. NAME OF MONITORING ORGANIZATION AFOSR/NA		
6c. ADDRESS (City, State, and ZIP Code) Box 120A, Waterman Road South Royalton, Vermont 05063			7b. ADDRESS (City, State, and ZIP Code) Bldg 410 Bolling AFB, DC 20332-6448		
8a. NAME OF FUNDING/SPONSORING ORGANIZATION Air Force Office of Scientific Research		8b. OFFICE SYMBOL (if applicable)	9. PROCUREMENT INSTRUMENT IDENTIFICATION NUMBER F49620-85-C-0102		
8c. ADDRESS (City, State, and ZIP Code) Building 410 Bolling AFB Washington, D.C. 20332-6448			10. SOURCE OF FUNDING NUMBERS		
			PROGRAM ELEMENT NO. 6.1102F	PROJECT NO. 2302	TASK NO. C1
11. TITLE (Include Security Classification) EXPERIMENTAL AND THEORETICAL RESPONSE OF MULTIPHASE POROUS MEDIA TO DYNAMIC LOADS: FINAL REPORT					
12. PERSONAL AUTHOR(S) Kim, Kwang J., Blouin, Scott E., Chitty, Daniel E., and Merkle, Douglas H.					
13a. TYPE OF REPORT Final		13b. TIME COVERED FROM 870701 TO 880630		14. DATE OF REPORT (Year, Month, Day) 880901	
15. PAGE COUNT 242					
16. SUPPLEMENTARY NOTATION N/A					
17. COSATI CODES			18. SUBJECT TERMS (Continue on reverse if necessary and identify by block number) Wave Propagation, Two-phase Modeling, Liquefaction, Soil and Rock Properties, Numerical Analysis (geotechnical), Geotechnical Analysis, Explosive Effects (JES)		
FIELD	GROUP	SUB-GROUP			
19. ABSTRACT (Continue on reverse if necessary and identify by block number) This report summarizes results of a combined experimental/theoretical/numerical study of the response of multiphase porous media subjected to high intensity static and dynamic loads. Theoretical models for fully coupled porous skeletons subjected to static and dynamic loads are developed for saturated and partially saturated conditions. These theoretical models are incorporated into numerical codes which are used in a systematic study of multiphase response which includes: - modeling of liquefaction in saturated soils and rocks; - wave propagation in saturated porous media, including modeling of compressional waves of the first and second kind; and - the role of pore fluid in damping, wavespeed and liquefaction as a function of the material properties of the porous skeleton. The theoretical and numerical work is supported by an experimental program which: (continued next page)					
20. DISTRIBUTION/AVAILABILITY OF ABSTRACT <input checked="" type="checkbox"/> UNCLASSIFIED/UNLIMITED <input type="checkbox"/> SAME AS RPT. <input type="checkbox"/> DTIC USERS			21. ABSTRACT SECURITY CLASSIFICATION UNCLASSIFIED		
22a. NAME OF RESPONSIBLE INDIVIDUAL Major Steven C. Boyce			22b. TELEPHONE (Include Area Code) (202)767-6963		22c. OFFICE SYMBOL AFOSR/NA

Block 19 (continued)

- defines a fluid friction relationship for frictional energy dissipation in the laminar, transitional and turbulent flow regimes;
- provides measurements of the compressibility of soil and rock grains, including the influence of occluded porosity;
- documents the liquefaction process in saturated porous soils and rock under compressive loadings similar to those from explosions; and
- measures the influence of grain fracturing on porous skeleton response and relates the degree of fracturing to stress level and the relative magnitudes of the shear and compressional components of the loadings.

TABLE OF CONTENTS

<u>Section</u>	<u>Page</u>
1 Project Overview	1
2 Formulation of Field Equations for the Multiphase Model. . . .	29
3 Dynamic Multiphase Finite Element Formulations for MPDAP . . .	53
4 MPDAP Verification Problems.	69
5 Numerical and Theoretical Treatment of Waves of the First and Second Kind.	105
6 Experimental Evaluation of Fluid Flow in Ducts and Soils . . .	121
7 Two-Phase Response of Saturated Limestone.	141
 <u>Appendix</u>	
A MPDAP: Multiphase Dynamic Analysis Program - User's Manual . .	189
B Steady State Flow Data Through Enewetak Beach Sand	209



SECTION 1

PROJECT OVERVIEW

1.1 SUMMARY OF OBJECTIVES AND METHODOLOGY

The response of saturated soils and rocks to high intensity blast loadings is a subject of intense concern to the United States Air Force. Previous studies (Blouin and Kim, 1983; Blouin and Kim, 1984a; Blouin and Shinn, 1983) clearly defined the role of blast induced liquefaction on the cratering processes from both nuclear and high explosive charges and the subsequent flow and consolidation of liquefied material surrounding and beneath the crater. These studies have been used by the Air Force and the Defense Nuclear Agency (DNA) to help explain the anomalously large, shallow craters which were observed in the saturated geologies of the Pacific Proving Grounds where all U.S. high yield nuclear surface tests were fielded.

In addition, prediction of the ground shock transmitted by a surface or shallow buried explosion to nearby surface or deeply buried hardened structures is a key element in the design and evaluation of such structures. In order to make reliable ground shock predictions in saturated geologic media, use of multiphase material models and numerical codes is needed.

This report summarizes results of a three year combined experimental and theoretical study of the fundamental behavior of multiphase porous materials subjected to high intensity dynamic loadings. The overall and specific objectives of this study were:

1. To design and conduct laboratory experiments which identify key response mechanisms and measure the behavior of saturated porous materials. Specific areas of concentration under this task included:
 - a) design, fabrication and utilization of a device to measure fluid friction and inertial flow resistance through ducts and soil and rock samples at high pore pressure gradients including flow in the laminar, transitional and turbulent flow regimes;

- b) measurements of the compressibility of soil and rock grains, including the influence of occluded porosity on the grain compressibility;
 - c) documentation of the liquefaction process in both soils and porous rocks under uniaxial strain loadings similar to those produced by explosive loadings; measurement of the amount of consolidation of the soil and rock specimens following liquefaction;
 - d) experimentally determine the amount and severity of grain breakage as a function of both strain/stress path and stress magnitudes; relate the microscopic grain crushing response to the degree of shear and compression generated during the various types of loadings; and
 - e) experimentally determine the drained skeleton response and the undrained total stress, pore pressure and effective stress response under various simple and complex loading conditions.
2. The development of advanced fully coupled material models which accurately represent the dynamic multiphase response behavior of saturated and partially saturated soils and rocks. Specific areas of concentration under this task included;
- a) formulation of a pore fluid flow relationship which describes the pore fluid flow resistance under dynamic loading conditions in both the laminar and turbulent regimes; and
 - b) development of a procedure to model the influence of occluded porosity on the response of saturated and partially saturated soils and rocks;
3. Formulate and implement both the theoretical models and experimental results into two-phase and multiphase codes. Specific accomplishments under this task include:

- a) development of the numerical code NKOCF which is used to numerically model the hydrostatic and uniaxial undrained response of saturated porous materials;
 - b) development of the code TWAVE which provides rapid closed form solutions of wave propagation and damping in saturated porous materials having linear elastic skeletons, including definition of compressional waves of the first and second kind;
 - c) development of the numerical finite element code MPDAP which utilizes a single point stress calculational technique and an innovative method of computing pore fluid flow to maximize computational efficiency; features of MPDAP include:
 - nonlinear fluid friction model for both laminar and turbulent flow;
 - a fully coupled compressibility model;
 - a number of drained skeleton material models ranging from simple linear elastic to advanced elasto-plastic models with strain hardening and softening;
 - single, two and three-phase capability;
 - static, dynamic and quasi-static capability with pore fluid flow;
 - d) development of modifications to our existing, but less sophisticated two-phase finite element code TPDAPII. These modifications were developed as a result of the MPDAP theoretical formulations and were used in many of the numerical studies under this project.
4. Utilize numerical and theoretical codes to help analyze experimental results, to predict laboratory and field behavior, and to conduct numerically based experiments and parameter studies which will further advance our understanding of complex multiphase phenomena. Specific accomplishments under this task include:
- a) modeling of undrained laboratory response of saturated soils and rocks to a variety of load-unload conditions, including the

modeling of liquefaction in soils and rocks due to single hydrostatic and uniaxial strain loading cycles;

- b) numerically model wave propagation in saturated soils and rocks due to dynamic loadings, including definition of the liquefaction front and motion of the pore fluid as a function of position behind the wave front;
- c) theoretical calculations of wave propagation, velocity and energy damping as a function of the skeleton permeability and excitation frequency; define the existence of compressional waves of the first and second kinds and determine propagation velocities and damping differences between the two wave types; and
- d) numerically model the theoretical wave propagation results in "c" above at specific values of excitation frequency and permeability to determine the role of pore fluid motion on damping and wavespeed and to isolate the physical phenomena which govern propagation of waves of the second kind.

An integrated experimental/theoretical/calculational approach has been used to satisfy the above objectives. In this approach, each of these three aspects of the program is mutually supported by the other two. For example, in the shock consolidation laboratory tests reported by Kim, Blouin and Timian, 1987, liquefaction of porous limestone and apparent negative hysteresis in the pore pressure-volume strain curve were both observed. Numerical simulations of those experiments utilizing the NKOCF code, developed from our fully coupled two-phase model, allowed us to duplicate the experimental results and identify the governing two-phase phenomena which produced these surprising results. On other occasions, we have identified theoretical uncertainties, such as dynamic pore fluid friction, and designed and analyzed experiments to define the controlling equations and material property parameters used in the theoretical formulation and numerical implementation. When used in these ways, the combined experimental/theoretical/numerical approach has been a powerful technique for solving problems which might prove intractable to solution by any single element of these three.

This report is the third and final report on this study. There have been two annual reports by Kim, Blouin and Timian, 1986 and 1987, summarizing developments at the end of the first and second years, respectively. In some cases, the material presented in those reports is complete and will not be repeated in this report. Rather, a short summary of the significant findings from these two reports is included in Subsection 1.2. In other cases, material presented in these reports has been supplemented or finalized during the last year. In these cases, the final development of these materials is included as a section of this report, with the previous work incorporated into this final presentation.

Key individuals responsible for this project at ARA include the following:

- Dr. Kwang Jin Kim: Co-Principal Investigator, Senior Engineer - theoretical analysis, numerical implementation and analysis, experimental analysis;
- Mr. Scott E. Blouin: Co-Principal Investigator, Principal Engineer - experiment design and analysis, theoretical and numerical analysis;
- Dr. Douglas Merkle: Principal Engineer - theoretical analysis;
- Mr. David Timian: Staff Engineer - experiment design and analysis;
- Mr. Daniel Chitty: Senior Engineer - experiment design and analysis;
- Ms. Elizabeth Smith: Staff Engineer - numerical analysis;
- Mr. Lawrence Merkle: Technician - numerical development and analysis;
- Mr. Kenneth McIntosh: Staff Technician - experiment design, execution and analysis;
- Mr. Steven Quenneville: Technician - experiment design, execution and analysis;

- Mr. Douglas McIntosh: Technician - experiment design, execution and analysis.

A number of formal presentations have been given presenting work accomplishment under this study or presenting results and analysis which were strongly supported by this study. Among these are:

- 1) "Fundamental Analysis of Wave Propagation and Liquefaction in Multiphase Porous Media" by Scott E. Blouin, Kwang J. Kim, David A. Timian; Presented at AFOSR Soil Mechanics Seminar, MIT, 14-15 September 1987.
- 2) "Strength and Deformation Properties of Salem Limestone" by Scott Blouin and Daniel Chitty; Presented at DNA Material Properties Working Group, Weidlinger Associates, New York, NY, 19 July 1988.
- 3) "Some Aspects of Two-Phase Modeling Investigated Under Sponsorship of AFOSR" by Kwang Kim and Scott Blouin; Presented at DNA Range to Effect EPW Meeting, SAIC, Albuquerque, NM, 17-18 May 1988.
- 4) "Comparisons and Calculations of Laboratory Properties of Various Limestones" by Scott Blouin, Kwang Kim and James Drake; Presented at DNA Range to Effect Meeting, Los Alamos National Laboratory, 20 January 1988.
- 5) "Preliminary Comparisons of Salem and DNA Limestone" by Scott Blouin, Kwang Kim and Robert Walker; Presented at DNA Range to Effect Meeting, SAIC, Albuquerque, NM, 17-18 May 1988.

In addition to the above and other formal presentations, research results from this study have been supplied on a continuing basis to universities, research companies, national laboratories and government organizations in the form of copies of briefings and annual reports, and consultations. Government organizations and national laboratories to which we have supplied information include:

Defense Nuclear Agency
Air Force Weapons Laboratory

Air Force Engineering and Services Laboratory
Los Alamos National Laboratory
Sandia National Laboratory
Lawrence Livermore National Laboratory

1.2 SUMMARY OF SIGNIFICANT FINDINGS AND ACCOMPLISHMENTS

In Subsections 1.2.1 and 1.2.2, we briefly summarize the significant findings and accomplishments which are fully described in our previous annual reports and which are not updated and described in Sections 2 through 7 of this report. References to appropriate sections in the previous annual reports are included. In Subsection 1.2.3, we briefly summarize the findings presented in Section 2 through 7 of this report.

1.2.1 Summary of Laboratory Experiments and Analysis from Previous Annual Reports

- a. Grain Compressibility and Influence of Occluded Porosity - Kim, Blouin and Timian, 1986 Section 2.

The compressibility of the solid grains is an integral part of the constitutive formulations for multiphase response (see Section 2). The compressibilities of the mineral constituents such as quartz and calcium carbonate making up most of the soils of interest are generally available in the literature from sources such as Bridgman, 1931 and Simmons and Wang, 1971. During a previous study Blouin et al., 1984, observed that the grains of the carbonate soils and rocks from Enewetak Atoll contained a high degree of microporosity within the grains themselves. The pervasiveness of these micropores explains why in situ densities of many carbonate soils and rocks are so low. A porosity value of 50% is typical of both the uncemented and cemented sediments at Enewetak. In the case of Enewetak beach sand, perhaps a third of the bulk porosity is due to the intragranular microporosity.

If the micropore space in the carbonate sediments is not fully saturated, resultant undrained compressibilities can be much greater than those predicted using the solid grain compressibilities from the literature. In essence, the

bulk moduli of the solid grains could be greatly reduced by the presence of the unsaturated micropores, leading to a substantially more compressible bulk mixture. Under a high stress load-unload cycle, such a mixture would exhibit permanent compaction and high energy absorption, neither of which are characteristic of fully saturated materials. Thus, it is important to characterize the grain compressibility of materials with microporosity to insure that appropriate relationships for grain compressibility are available.

A laboratory high pressure vessel was modified to enable us to measure the compressibility of known volumes of fluid (kerosene) within the vessel. By mixing predetermined amounts of soil or rock grains in the fluid, the compressibility of the grains can be determined by measuring the compressibility of the fluid-grain mixture. There is no effective stress applied to the grains in this test; the only stress acting on them is the fluid pressure.

The grain bulk moduli of the various soils and rocks examined in this suite of tests are summarized in Table 1.1. The grains all exhibited essentially linear elastic response to the peak applied pressure of about 5 kb. Quartz sand, steel ball bearings and solid limestone produced bulk moduli which agree well with published values. Most of the soils and rock grains had bulk moduli of about 6.0×10^6 psi, about 55% of the modulus of the solid limestone. While this is apparently a significant reduction, in reality it will have little influence on the response of the Enewetak materials because the water making up 50% of the sample is more than an order of magnitude more compressible than the grains. Thus, it was concluded that the micropores are probably mostly saturated in these materials and result in a 20% to 45% reduction in grain modulus.

b. Liquefaction of Saturated Soil and Rock Under Undrained Uniaxial Strain Loadings - Kim, Blouin and Timian, 1986 Section 3, 1987 Section 7.

A series of uniaxial strain load-unload consolidation tests was run on porous limestone and soils from Enewetak Atoll. The test specimens were subjected to an undrained load-unload cycle in a high pressure oedometer during

which pore pressure was monitored. Following unloading, the pore pressure was allowed to drain until the samples had consolidated to their original effective vertical stress at the start of each test.

Figure 1.1, parts a, b and c, show a typical data set on a saturated low strength limestone having a porosity of 42%. Part a shows the total stress response, part b the pore pressure response and part c the effective stress response. Point "a" at the start of the undrained loading shows the initial conditions, i.e. effective stress of about 300 psi, pore pressure of about 300 psi and total stress of 600 psi. The sample is loaded undrained to point "c". At point "b", early in the undrained loading, the cementation in the skeleton breaks down. This is clearly shown by the effective stress response of Figure 1.1c. Prior to the breakdown of cementation more than half of the total applied stress is carried by the limestone skeleton; but following the cementation breakdown only 5% of the additional applied stress is carried by the skeleton. The balance of the total applied stress is carried by the pore water.

From point "c", the undrained sample is unloaded to a state of zero stress at "e". As shown in Figure 1.1, the skeleton is strongly hysteretic and unloads very rapidly until at "d" where the effective stress drops to zero and a state of liquefaction is achieved. Note that at point "d" the overall volume strain is still 1.4% and the total stress is still over 11,000 psi. From point "d" to point "e" the sample is liquefied and the total stress equals the pore pressure. Also note that the hysteresis in the total stress curve is positive, i.e. energy is being dissipated, while the apparent hysteresis in the pore pressure load-unload cycle is negative. The negative hysteresis results from the rapid drop in stress on the solid grains as the skeleton unloads. The grains tend to expand rapidly in the pore fluid resulting in additional pore pressure and the apparent negative hysteresis.

At point "e" the pore pressure line is opened and shortly thereafter total stress is again applied and the sample is allowed to drain and consolidate until the effective stress reaches its pretest value at point "f". The strain during consolidation to the original effective stress is nearly 80%

of the strain reached during the undrained loading. The average residual strain, or subsidence, is 85% of the peak strain reached in the undrained loadings. By computing the peak dynamic strain fields from explosive detonations, this average consolidation can then be used to estimate the portions of total crater volumes which can be attributed to post-liquefaction consolidation.

c. Grain Damage as a Function of Stress Path and Magnitude - Kim, Blouin and Timian, 1987 Section 7.

A systematic study of grain crushing over a variety of stress paths to several different peak mean stresses was conducted. Relating the measured grain crushing to the stress-strain data from the various tests provides insight into the similarities and differences between the different types of loadings on the microscopic levels, and particularly into the differences and similarities between the microscopic response of granular materials under shear and compressive loadings. Drained hydrostatic compression, uniaxial strain, and triaxial compression tests were run on sieved carbonate beach sand samples having a uniform grain size between 0.425 and 0.60 mm. The tests were run to several peak mean stresses, thus providing a variation in the shear stress component of the loading between the various test types.

The comparison of grain damage for the 10,000 psi mean stress tests, presented in Figure 1.2, shows a moderate to high degree of damage with 36% to 49% of the grains broken into a smaller size interval. The material loaded in hydrostatic compression sustained the least damage, with 36.4% of the grains reduced in size. Damage from the combined hydrostatic and shear loadings ranged from 42.2% for the TXC test to 49.1% for the K_0 test. The differences between the three tests is in proportion to the shear strain energy imparted to each sample, with the hydrostatic serving as the zero shear baseline.

In order to more clearly define the role of shear strain, an additional triaxial compression test was run at the same confining pressure, but to a much higher shear strain energy. Severe grain damage was sustained by this triaxial sample loaded under the same 8,400 psi confining pressure as the

10,000 psi mean stress sample, but carried to a maximum mean stress of 15,350 psi and a maximum stress difference of 20,900 psi. Nearly 80% of the grains were reduced in size, with over half the total post-test weight having grain sizes of less than .106 mm. Shear strain energy imparted to the 15,350 psi sample was about an order of magnitude greater than that of the 10,000 psi triaxial compression test.

In order to concisely and quantitatively describe the grain damage we developed a technique which uses the pretest and post-test log mean grain sizes to compute a grain damage factor, D_f . The grain damage factor is a measure of both the amount and severity of the grain damage. A sample with most of its grains crushed to a fine powder has a much larger grain damage factor than a sample with the same percentage of its grains broken into only slightly smaller pieces. As shown in Table 1.2, the grain damage factor ranges from 0.011 for the 1,000 psi hydrostatic sample to 0.743 for the 15,350 mean stress triaxial compression sample. The maximum possible grain damage factor is 1.0.

1.2.2 Summary of Theoretical Development, Code Implementation and Numerical Analysis From Previous Annual Reports

Most of the theoretical model development, its implementation into the codes, and verification problems and parametric analysis using the codes are summarized in Sections 2 through 5 of this report, with much of the detailed development covered in Kim, Blouin and Timian, 1986 and 1987. The theoretical formulations for the numerical code NKOCF for the prediction of undrained uniaxial strain and hydrostatic loadings is not covered in these sections. NKOCF code implementation and code verification, were fully described by Kim, Blouin and Timian, 1986 Section 5 and Kim, Blouin and Timian, 1987 Sections 2 and 3 and Appendices A and B, and will be briefly summarized here.

NKOCF models the undrained hydrostatic and uniaxial strain response of saturated porous soils and rocks. It uses the measured drained skeleton properties as input and provides the total stress response, effective stress response and pore pressure response as output. It employs an incremental numerical technique to model the nonlinear fully coupled volumetric response described in Section 2, using a nonlinear compressibility of fresh water or

sea water and a nonlinear compressibility model for the solid grains, both described by Kim, Blouin and Timian, 1987 Section 3.

Comparison of an undrained uniaxial strain load-unload cycle on saturated porous limestone computed using NKOCF with test data is shown in Figure 1.3, parts a through c. The agreement between the numerical calculation and the test data is quite good, especially considering that the calculated response was developed from measured drained skeleton response on a similar, but not identical rock sample and from constitutive models for each of the components which were developed independently of the test data.

During the current year, NKOCF was further modified to incorporate a nonlinear unloading capability which duplicates the actual drained skeleton unloading, rather than the original bilinear approximation used in the 1987 version. This new capability is demonstrated against test data in Section 7 of this report.

1.2.3 Summary of Experimental, Theoretical and Numerical Results From Sections 2 Through 7

a. Section 2 - Formulation of Field Equations for the Multiphase Model

In Section 2 of this report, the theoretical and experimental two and three-phase modeling work reported in the two previous annual reports is combined with work performed during the past year to develop the final formulation of the field equations which are incorporated into MPDAP, the multiphase code described in Sections 3 and 4.

Features and advantages of the new formulations over the previous multiphase formulations in TPDAPII include:

1. generalized nonlinear fluid friction equation which models dynamic pore water flow in both the laminar and turbulent flow regimes; and
2. fully coupled continuity relationships in which volumetric strain compatibility and pressure/stress equilibrium between the pore fluid, solid grains and porous skeleton are maintained.

The six governing field equations used in MPDAP are summarized at the end of Section 2.

b. Section 3 - Dynamic Multiphase Finite Element Formulations for MPDAP

The field equations in Section 2 represent the fundamental governing equations for an infinitesimal element of saturated porous medium. Global equilibrium equations for specified boundary conditions are derived in Section 3 by applying the principles of virtual work to the field equations.

Innovative aspects of these formulations include:

1. formulation of the global equilibrium equations for stresses in the bulk medium and for pore fluid flow based on the principals of virtual work and complimentary virtual work, respectively; and
2. use of pore pressure at the element nodes to represent relative motion of the pore fluid which eliminates one degree of freedom in two-dimensional calculations and two degrees of freedom in three-dimensional calculations, resulting in significant reductions in computational running time and storage requirements.

The MPDAP global equilibrium equations are summarized in Section 3.9.

c. Section 4 - MPDAP Verification Problems

The features and capabilities of the multiphase code, MPDAP, are described in Section 3 and a number of verification problems presented which compare the MPDAP output to established closed form solutions of simple problems or to previous TPDAP solutions for more complex problems. The four verification problems presented in Section 4 include comparison of MPDAP solutions with:

1. the closed form solution for an undrained uniaxial strain loading;
2. the closed form solution for spherical elastic wave propagation in a single phase medium;

3. Terzaghi's closed form solution for quasi-static flow and consolidation under a uniaxial strain loading; and
4. TPDAPII solutions for one-dimensional wave propagation resulting from simulated explosive loadings of both a saturated soil and rock.

d. Section 5 - Numerical and Theoretical Treatment of Waves of the First and Second Kind

In Section 5, theoretical development and coding of a solution for wave propagation in saturated porous elastic media is reviewed. This work, reported in detail by Kim, Blouin and Timian, 1987 Sections 4 and 5, resulted in the code TWAVE which uses the closed form solutions to rapidly compute wavespeeds and damping over a wide range of material properties. Significant findings from TWAVE include the following:

1. Existence of two types of compressional waves in saturated porous media; conventional compressional waves analogous to those in a single phase material, termed waves of the first kind, and much slower highly damped compressional waves termed waves of the second kind.
2. Wavespeeds of both types of waves have a lower and upper bound wavespeed which is dependent on the excitation frequency and/or the material permeability. Wavespeed increases with increasing excitation frequency and with increasing permeability.
3. In waves of the first kind, the rate of wavespeed increase is greatest at frequencies and permeabilities around which damping is a maximum.

In Section 5 of this report, TPDAPII solutions for wave propagation having skeleton properties and permeabilities chosen to highlight the wavespeed and damping differences are compared to the TWAVE solutions and analyzed to determine the factors governing the damping variations and

wavespeed changes and to determine the phenomena behind propagation of waves of the second kind. Conclusions from this comparison include the following:

1. Both the material skeleton and pore water are in compression during passage of waves of the first kind. Pore fluid friction is at a maximum where damping and wavespeed increases are at a maximum. At the lower bound wavespeed, there is no relative motion between the pore water and the porous skeleton.
2. Waves of the second kind appear to be associated with a surge of pore fluid moving through the skeleton. Pressure in the pore water is compressive, while stress in the porous skeleton is tensile during passage of waves of the second kind. The pore water is moving in the direction of wave propagation while the porous skeleton is moving in the opposite direction.

e. Section 6 - Experimental Evaluation of Fluid Flow in Ducts and Soils

A series of fluid flow test data is reported by Kim, Blouin and Timian, 1987 Section 8 and in Section 6 of this report. Flow velocities of up to 3700 in/s, fluid acceleration to nearly 1000 Gs and pressure gradients of up to 350 psi/in were achieved in some of the dynamic flow tests. Results of this study were as follows:

1. Recommendation of a fluid flow equation which models flow in both the laminar and turbulent flow regimes;
2. Development of an apparatus and experimental techniques for the determination of the flow coefficients in the above equations for porous soils and rocks; and
3. Demonstration that pore fluid flow for explosive loadings will be largely in the turbulent flow regime where the pore pressure gradient is proportional to the square of the pore fluid velocity relative to the skeleton. It was also demonstrated that Biot's theoretical formulation for the increase in fluid friction with

increasing excitation frequency can be ignored in the turbulent regime.

f. Section 7 - Two-Phase Response of Saturated Limestone

In Section 7, a series of drained and undrained test data on Indiana limestone are analyzed using NKOCF and two-phase constitutive properties. Drained and undrained hydrostatic, uniaxial strain, triaxial compression under constant confining pressure and specified strain path tests were conducted. Analysis of the four test types showed that:

1. Undrained hydrostatic and uniaxial strain response was in excellent agreement with calculations using the revised version of NKOCF. Total stress, effective stress and pore pressure response closely matched the test data over the entire load-unload cycle.
2. Undrained triaxial strength and deformation prior to failure were in good agreement with predictions based on effective stress theory and two-phase models. However, strengths and pore pressure response during the latter stages of shearing appear to contradict the response predicted by effective stress theory and two-phase models. We believe this apparent contradiction is due to inherent shortcomings of the test itself, caused by lateral constraint from the steel end caps. Use of such test data could lead to gross inaccuracies in modeling in situ response.
3. Drained and undrained strain path tests that imposed a variety of strain paths on the test specimens following uniaxial strain compression will prove to be a real challenge to material modelers. These strain path tests, which are typical of strain paths from explosive loadings, point up the need for an advanced single element two-phase code which can exercise various saturated skeleton models over arbitrary strain and stress

paths. Test results were generally consistent with response that would be predicted with two-phase models, though the effective stress response may be difficult to match with existing skeleton models. The test results highlight the dependence of strength on the strain path (as predicted by effective stress theory and two-phase models) and clearly demonstrate the inadequacy of using equivalent single-phase calculations for predicting response to explosive loadings in saturated porous materials.

Table 1.1 Bulk modulus values obtained from grain compressibility tests.

<u>Material</u>	<u>Bulk Modulus</u>	
	(psi x 10 ⁶)	(MPa x 10 ⁴)
Steel Ball Bearings	22.2	15.31
Quartz Sand	5.2	3.58
Solid Limestone	11.0	7.59
Enewetak Beach Sand	9.1	6.27
Silt-Sand-Gravel from KAM-2	5.6	3.86
Ground Silt-Sand-Gravel from KAM-2	6.1	4.21
Vugular Limestone	5.7	3.93
Cemented Material from XSA-2	6.1	4.21

Table 1.2a. Summary of post-test grain size distribution and grain damage; uniform Enewetak beach sand, $G_s = 2.78 \text{ gm/cm}^3$.

SIEVE NO.	SIZE INTERVAL mm	VIRGIN SAMPLE %	HY to $\sigma_m = 1,000 \text{ psi}$ Y4A7 % Retained	K ₀ to $\sigma_m = 1,000 \text{ psi}$ U22A7 % Retained	TXC to $\sigma_m = 1,000 \text{ psi}$ G5BEC7 % Retained	TXS at $\sigma_m = 1,000 \text{ psi}$ G6A7 % Retained
40	.425 - .60	100.	97.18	94.68	93.3	94.3
50	.30 - .425	-	2.43	4.32	4.2	3.5
70	.212 - .30	-	.16	.62	1.2	1.1
100	.150 - .212	-	.08	.22	.6	.5
140	.106 - .150	-	.07	.13	.3	.2
200	.075 - .106	-	.03	.04	.1	.2
PAN	.0 - .075	-	.05	.09	.3	.2
<u>LOG MEAN GRAIN SIZE</u>						
Initial: D_0 (mm)		.50	.50	.50	.50	.50
Final: G_0 (mm)		.50	.495	.490	.480	.480
Damage Factor: $D_f = \frac{D_0 - G_0}{D_0 - D_m}$		0.0	.011	.023	.046	.046
<u>Initial Dry Density</u>						
lb/ft^3				105.77	105.40	104.97

Table 1.2b. Summary of post-test grain size distribution and grain damage; uniform Enewetak beach sand, $G_s = 2.78 \text{ gm/cm}^3$ (continued).

HY to $\sigma_m = 10,000 \text{ psi}$ V20A7 & Retained	K ₂ to $\sigma_m = 10,000 \text{ psi}$ U11A7 & Retained	TXC to $\sigma_m = 10,000 \text{ psi}$ G5D4E7 & Retained	TXS at $\sigma_m = 10,000 \text{ psi}$ G11C7 & Retained	TXC to $\sigma_m = 15,350 \text{ psi}$ U23A6B7 & Retained
63.59	50.91	57.8	55.6	21.59
14.23	16.63	13.6	14.4	12.17
6.29	8.49	6.5	6.9	6.82
5.00	6.18	5.2	5.7	7.41
4.19	5.25	4.8	4.9	23.04
2.76	3.39	3.2	3.3	5.12
6.94	8.95	8.9	9.2	21.85
.50	.50	.50	.50	.50
.340	.305	.319	.315	.177
.358	.448	.415	.425	.743
105.21	103.09	105.94	105.86	104.64

Shock Consolidation (M3186) KAM-2A Depth = 362.2 ft

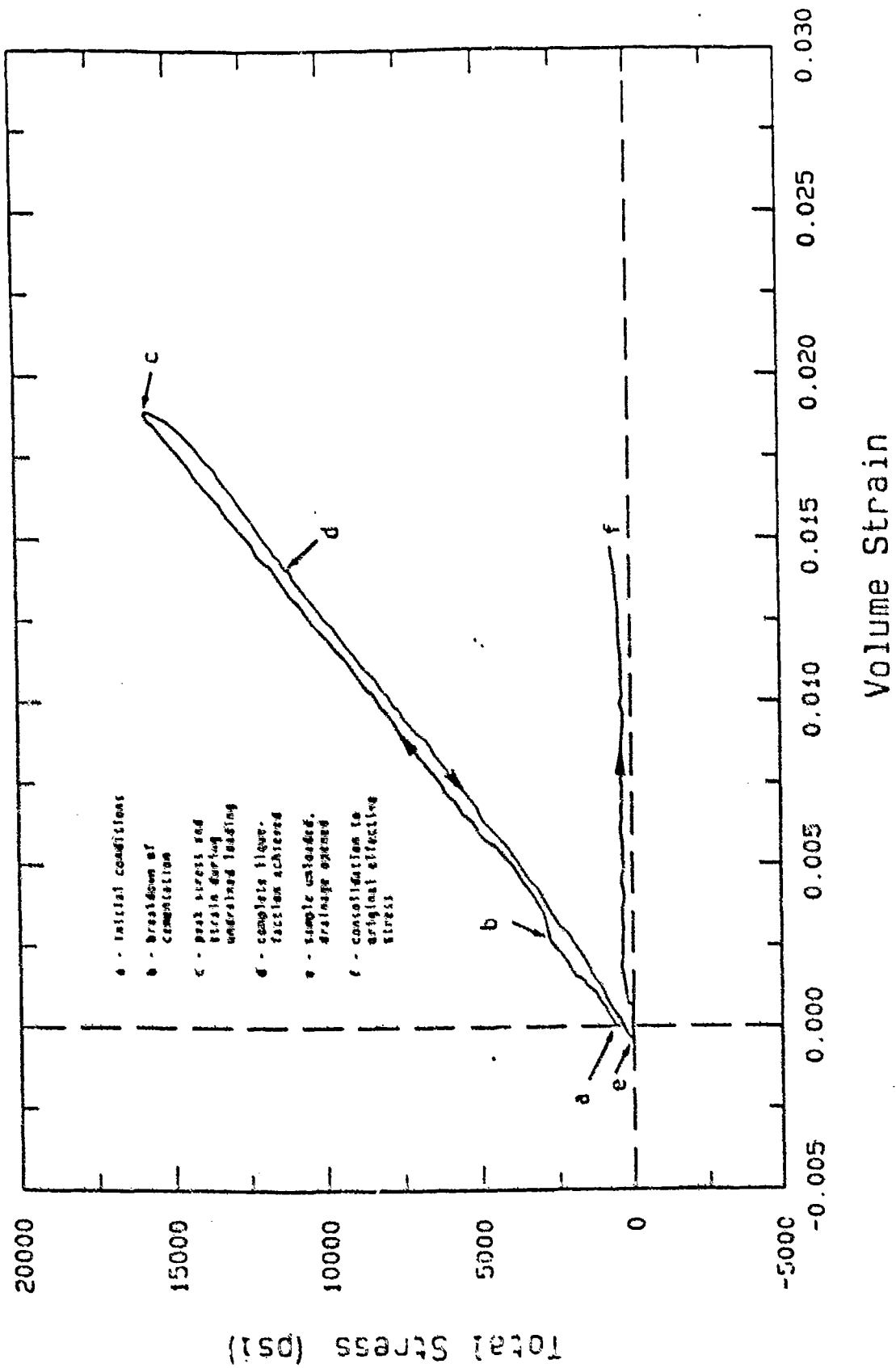


Figure 1.1a. Shock consolidation test M3186 on low strength porous limestone; total stress response.

Shock Consolidation (M31B6) KAM-2A Depth = 362.2 ft

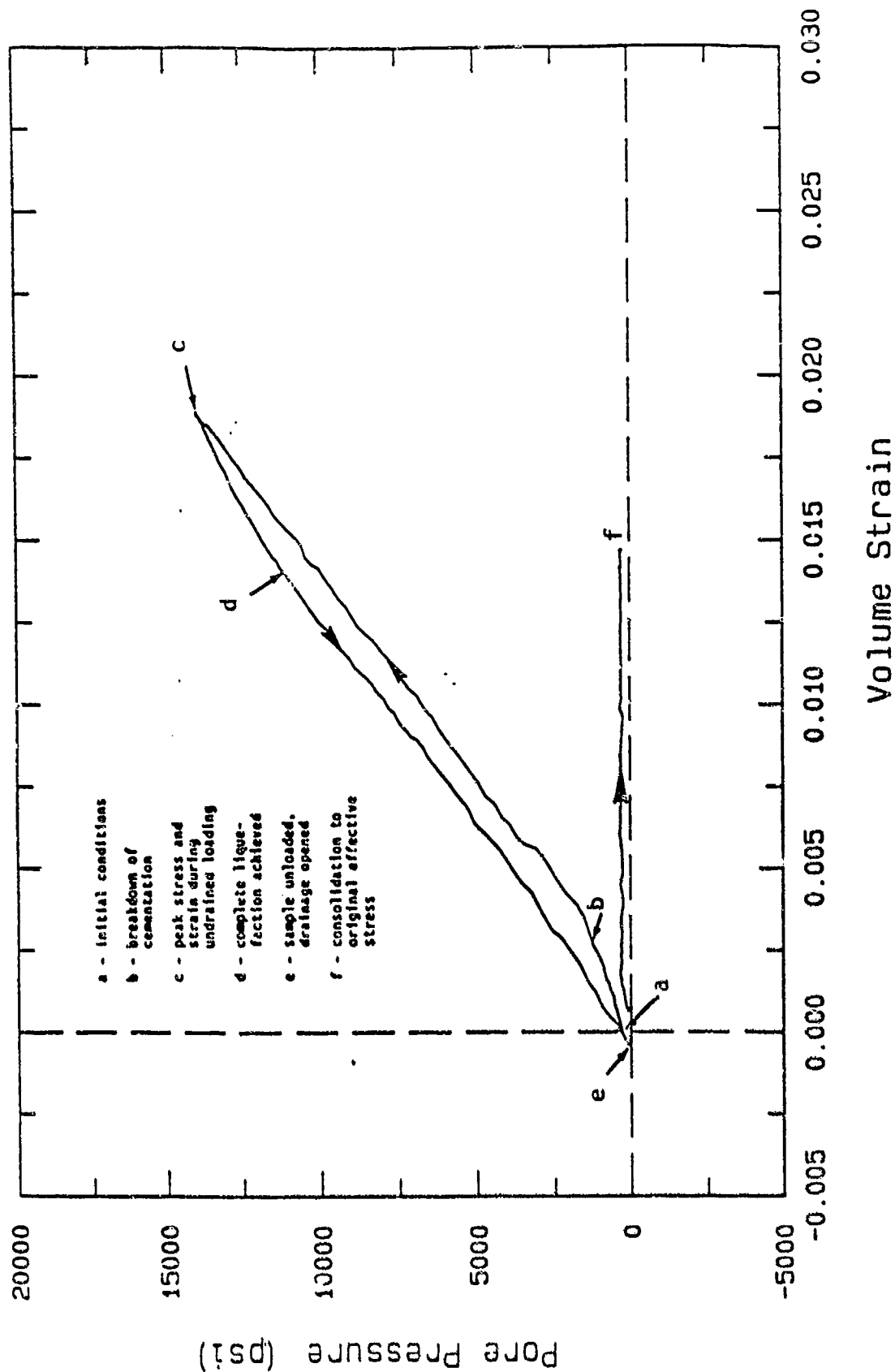


Figure 1.1b. Shock consolidation test M31B6 on low strength porous limestone; pore pressure response.

Shock Consolidation (M31B6) KAM-2A Depth = 362.2 ft

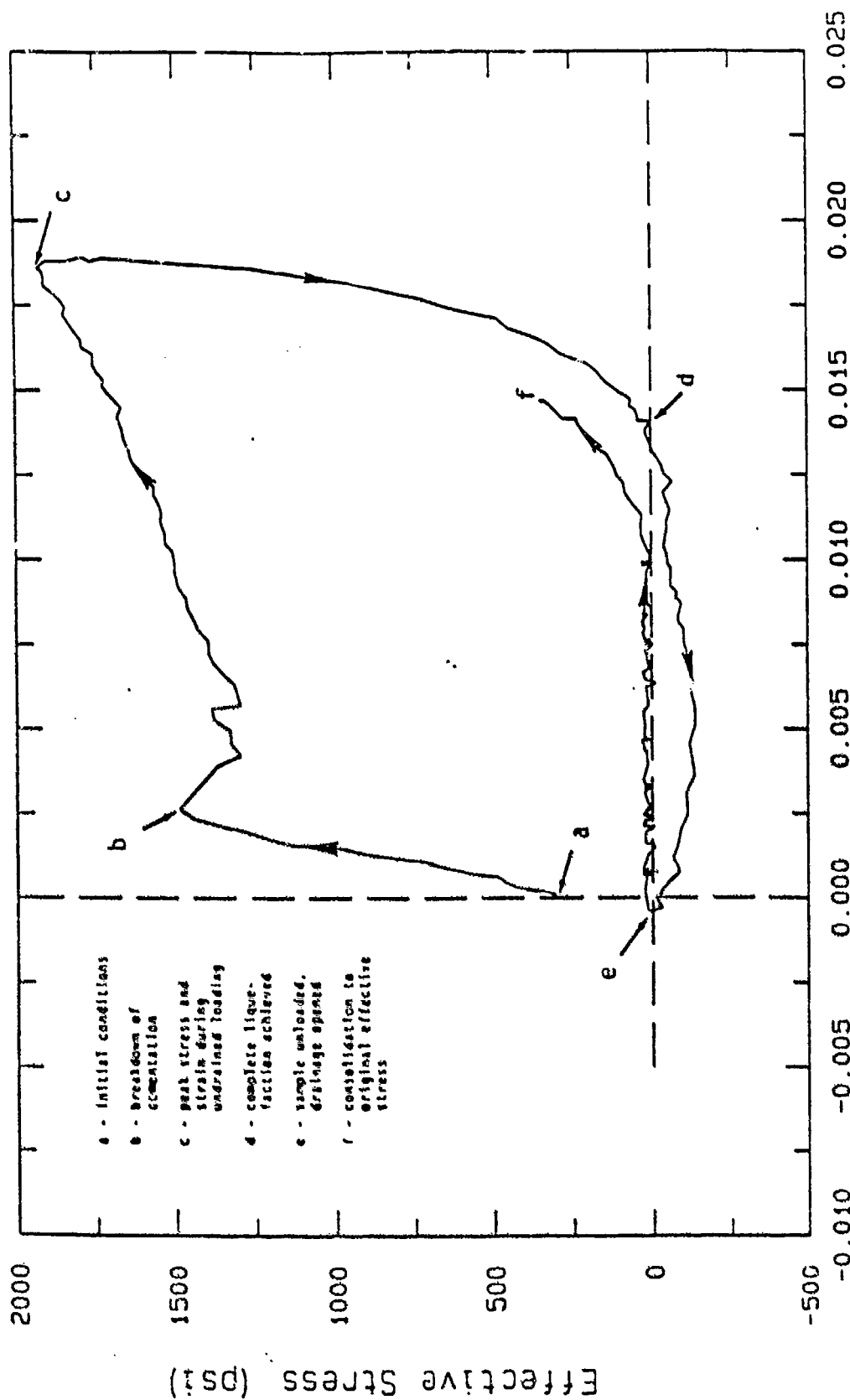
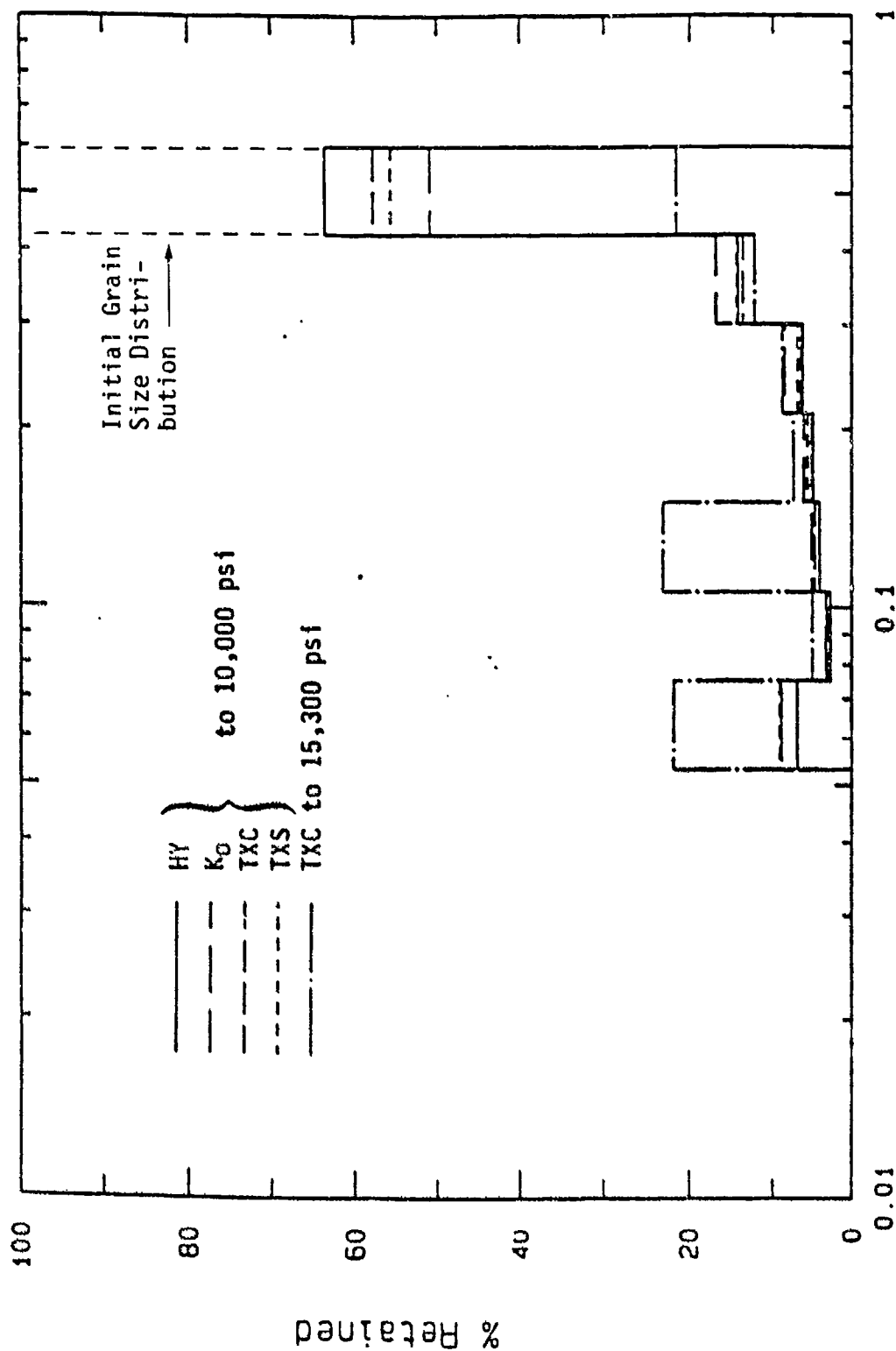


Figure 1.1c. Shock consolidation test M31B6 on low strength porous limestone; effective strength response.

Grain Size Distributions



Grain Size (mm)

Figure 1.2. Comparison of post-test grain size and weight fraction distribution from samples loaded to 10,000 psi and 15,350 psi mean stress.

Shock Consolidation (A2A6) KAM-2A

Depth = 353.8 ft

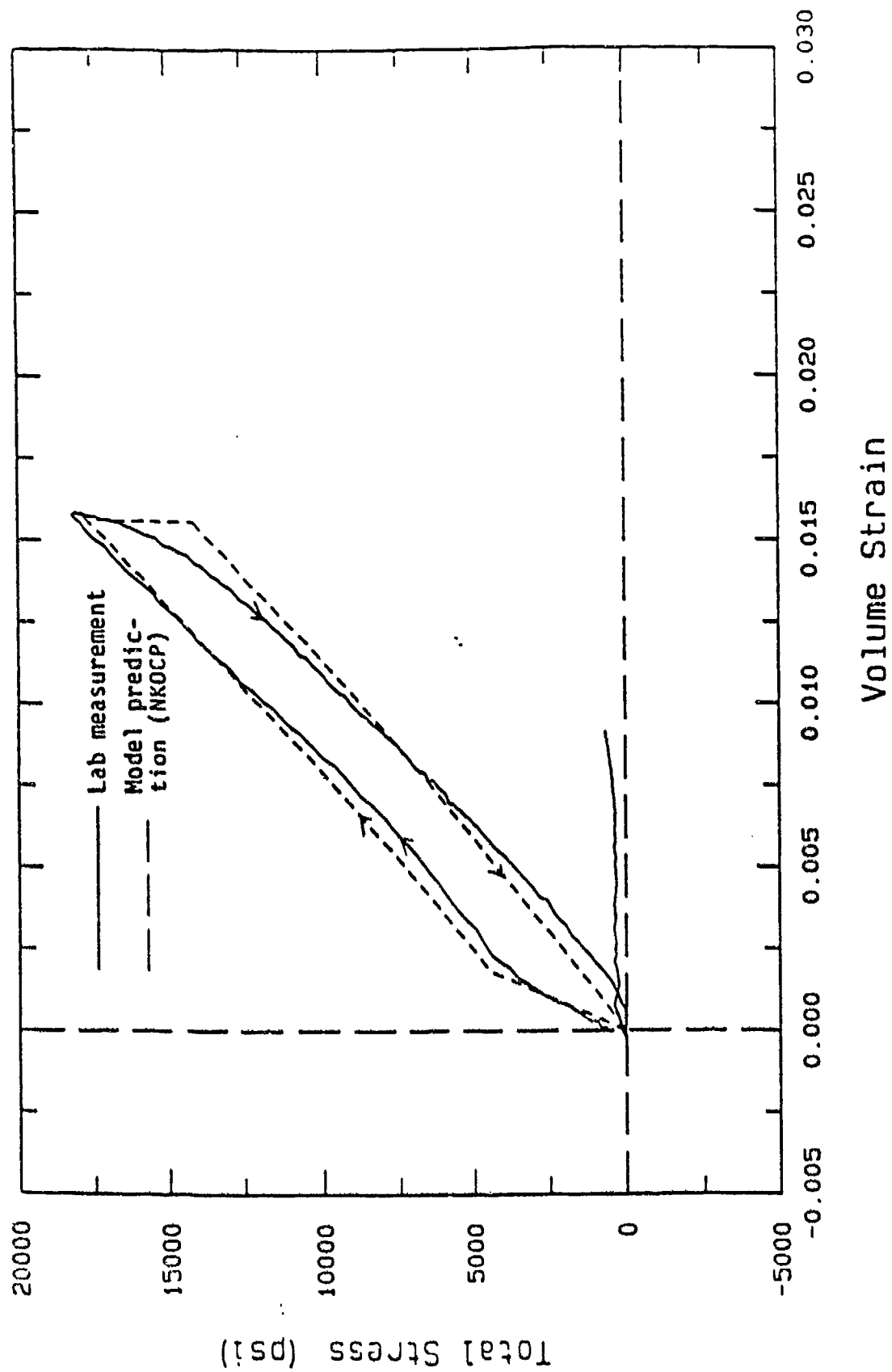


Figure 1.3a. Comparison of total stress response of saturated porous limestone with numerical simulation.

Shock Consolidation (A2A6) KAM-2A

Depth = 353.8 ft

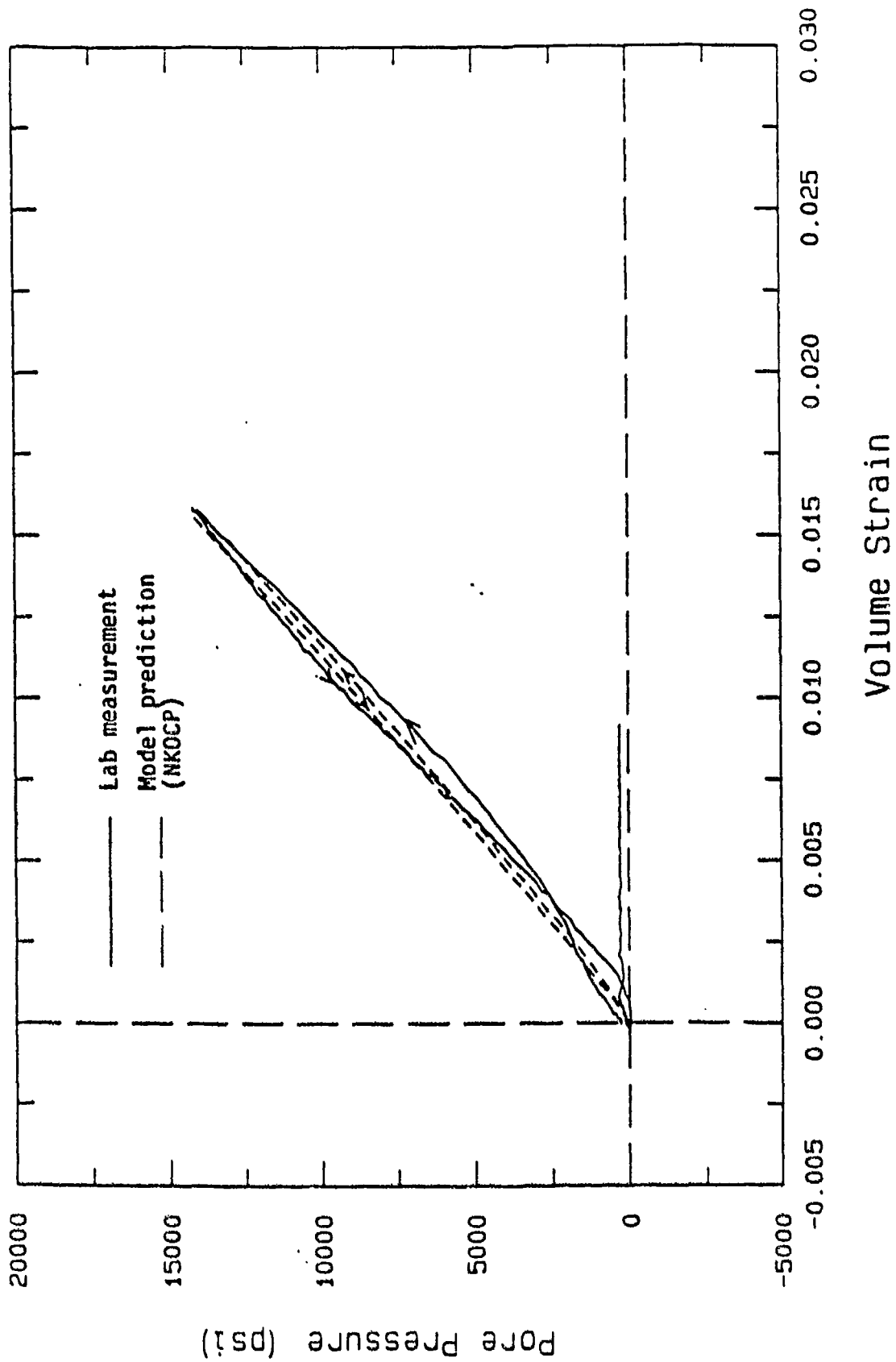


Figure 1.3b. Comparison of pore pressure response of saturated porous limestone with numerical simulation.

Shock Consolidation (A2A6) KAM-2A
Depth = 353.8 ft

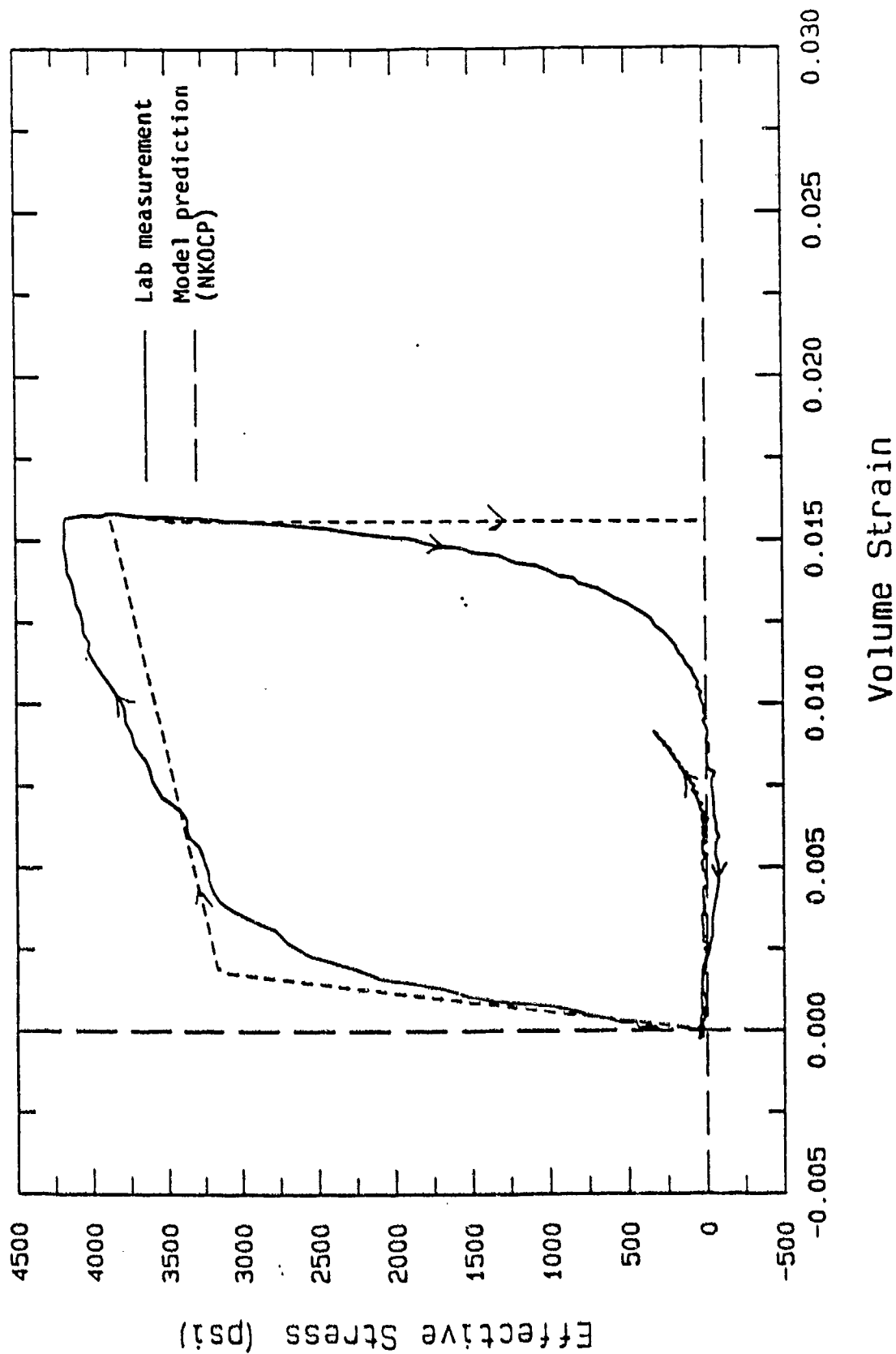


Figure 1.3c. Comparison of effective axial stress response of saturated porous limestone with numerical simulation.

SECTION 2

FORMULATION OF FIELD EQUATIONS FOR THE MULTIPHASE MODEL

2.1 INTRODUCTION

The initial theoretical formulations to be incorporated into the multiphase code MPDAP were originally presented by Kim, Blouin and Timian, 1986 and 1987. During the past year the original formulations have been revised to provide more efficient and accurate computational algorithms including the modification of the dynamic flow equation based on the results of our dynamic flow tests described in Section 6.

The revised theoretical formulations have been incorporated into the MPDAP code during the past year and verification problems have been run. Features and advantages of the new formulations over previous multiphase formulations include the following:

1. Generalized nonlinear fluid friction equation which models dynamic pore water flow in both the laminar and turbulent flow regimes;
2. Fully coupled continuity relationships in which volumetric strain compatibility and pressure/stress equilibrium between the pore fluid, solid grains and porous skeleton are maintained;
3. Formulation of the global equilibrium equations for stresses in the bulk medium and for pore fluid flow based on the principals of virtual work and complimentary virtual work, respectively; and
4. Use of pore pressure at the element nodes to represent relative motion of the pore fluid which eliminates one degree of freedom in two-dimensional calculations and two degrees of freedom in three-dimensional calculations, resulting in significant reductions in computational running time and storage requirements.

2.2 THEORETICAL FORMULATIONS

2.2.1 Notation

Note that positive signs have been used for elongation and tension. A comma denotes differentiation with respect to the subsequent indices and the superposed dot denotes time rate. Prime indicates effective stress or pressure.

$\{u\}$: skeleton displacement
$\{U\}$: absolute fluid displacement
$\{w\}$: apparent fluid displacement relative to the solid skeleton
$\{\sigma\}$: total stress
$\{\sigma'\}$: effective stress
p	: total pressure
p'	: effective pressure
π	: pore fluid pressure
$\{\pi, i\}$: pore fluid pressure gradient vector
$\{e\}$: skeleton strain
ϵ_v	: skeleton volumetric strain
ϵ_f	: pore fluid volumetric strain
ϵ_g	: solid grain volumetric strain
ϵ_F	: volumetric diffusion of pore fluid
$\{u\}_e$: element nodal skeleton displacement vector
$\{\pi\}_e$: element nodal pore fluid pressure
$\{u\}$: global nodal skeleton displacement vector
$\{\pi\}$: global nodal fluid pressure
$\{T\}$: applied boundary traction
\hat{Q}	: specified boundary flow velocity (flux)
$\{b\}$: body force vector (generally equals gravity force)
k	: Darcy's coefficient of permeability
$[D^{ep}]$: elasto-plastic stress-strain matrix for skeleton
$\{1\}$: unit vector $\{1\}^T = \langle 1 \ 1 \ 1 \ 0 \ 0 \ 0 \rangle$
n	: porosity
C_f	: pore fluid compressibility

C_{aw} : compressibility of air-water mixture
 C_g : compressibility of solid grains
 α : compressibility of soil-water mixture with zero effective stress
 K_m : bulk modulus of soil water mixture with zero effective stress
 K_s : bulk modulus of skeleton
 K_f : bulk modulus of pore fluid
 M_s : constrained modulus of skeleton
 ρ : bulk mass density of mixture
 ρ_d : dry density of skeleton
 ρ_f : fluid mass density
 ρ_g : mass density of solid grains
 m_g : mass of solid grains in volume V_t
 V_t : total skeleton volume
 γ_f : unit weight of the pore fluid
 r : mass increment factor (approximation of Biot's fluid viscosity parameter)
 β_f : Ward's fluid friction coefficient for turbulent flow
 β, γ : parameters in Newmark's β numerical time integration method
 θ : parameter in Wilson's θ numerical time integration method
 δ_{ij} : Kronecker's delta
 $[M_t]$: Mass Matrix

 $[K_T]$: tangent skeleton stiffness matrix
 $[C]$: coupling matrix between solid skeleton and pore fluid
 $[E]$: pore fluid compressibility matrix
 $[H]$: fluid friction energy dissipation matrix
 (F) : nodal force vector
 (R) : internal resistance force vector
 (\bar{Q}) : equivalent boundary flow vector

2.2.2 Field Equations

Effective Stress Law

Terzaghi's effective stress equation is fundamental to the development of the fully coupled model. It relates the total applied stress, σ , to the pore

pressure, π , and the effective stress, σ' , according to

$$\sigma_{ij} = \sigma'_{ij} + \delta_{ij}\pi \quad (2-1)$$

where

$$\begin{aligned} \sigma_{ij} &= \text{total stress} \\ \sigma'_{ij} &= \text{effective stress} \\ \delta_{ij} &= \text{Kronecker's delta} \\ \delta_{ij} &= 0 \quad \text{if } i \neq j \\ \delta_{ij} &= 1 \quad \text{if } i = j \end{aligned}$$

Constitutive Equation for Skeleton Deformation

The deformation of the porous skeleton is related to the applied effective stress and the pore pressure acting on the solid grains. The stress-strain relationship is given by

$$\{d\sigma'\} = [D^{ep}] (\{d\epsilon\} - \frac{C_g}{3} \{1\}d\pi) \quad (2-2)$$

The last term in Equation 2-2 is the strain in the skeleton resulting from compression of the solid grains by the pore pressure.

Continuity Equation of Pore Fluid Flow

The continuity equation for pore fluid flow is derived from mass conservation relationships. The volumetric strain of the pore fluid, ϵ_f , is given by

$$d\epsilon_f = - \frac{d\rho_f}{\rho_f} = C_f d\pi \quad (2-3)$$

where

$$\begin{aligned} C_f &= \text{pore fluid compressibility} \\ \pi &= \text{pore fluid pressure} \end{aligned}$$

$$d\epsilon_g = - \frac{d\rho_g}{\rho_g} = C_g d\pi + \frac{C_g}{1-n} dp' \quad (2-4)$$

where C_g = bulk compressibility of solid grains
 p' = effective mean pressure

The dry density, ρ_d , is given by

$$\rho_d = \frac{m_g}{V_t} = (1 - n)\rho_g \quad (2-5)$$

where m_g is the mass of the solid grains in skeleton volume V_t . The change in dry density is given by

$$d\rho_d = -\rho_d d\epsilon_v \quad (2-6)$$

where ϵ_v = is the volumetric strain of the skeleton. Differentiating Equation 2-5 with respect to n and ρ_g gives

$$d\rho_d = (1 - n) d\rho_g - \rho_g dn \quad (2-7)$$

Equating 2-6 and 2-7 yields

$$d\epsilon_v = \frac{dn}{1-n} - \frac{d\rho_g}{\rho_g} \quad (2-8)$$

Conservation of mass for the pore fluid within a specified initial volume of saturated porous material is given by

$$n \rho_f V_t = \bar{n} \bar{\rho}_f \bar{V}_t \quad (2-9)$$

where as illustrated in Figure 2.1, the terms to the left of the equal sign represent the fluid mass under the initial conditions and the terms to the

right represent the same fluid mass under deformed conditions. Equation 2-9 may be expressed in infinitesimal incremental form as

$$n\rho_f V_t = (n + dn)(\rho_f + d\rho_f)(1 + d\epsilon_f) V_t \quad (2-10)$$

where

ϵ_f = volumetric diffusion of pore fluid as depicted in Figure 2.1.

Solving Equation 2-10 for $d\epsilon_f$ and discarding second order terms yields

$$d\epsilon_f = -\frac{dn}{n} - \frac{d\rho_f}{\rho_f} \quad (2-11)$$

Equation 2-11 is combined with Equation 2-8 by elimination of dn to yield

$$(1 - n)d\epsilon_v + nd\epsilon_f + (1 - n)\frac{d\rho_g}{\rho_g} + n\frac{d\rho_f}{\rho_f} = 0 \quad (2-12)$$

Combining Equations 2-3 and 2-4 with 2-12 gives

$$n(d\epsilon_f - d\epsilon_v) + d\epsilon_v - \frac{1}{K_m} d\pi - C_g dp' = 0 \quad (2-13)$$

where K_m is the bulk modulus of the solid/fluid mixture which is expressed by

$$K_m = \frac{1}{nC_f + (1 - n)C_g} \quad (2-14)$$

The change in effective mean pressure is given by

$$dp' = K_S (de_V - C_g d\pi) \quad (2-15)$$

Substituting Equation 2-15 into 2-13 gives

$$n(de_f - de_V) + (1 - C_g K_S) de_V + \left(C_g^2 K_S - \frac{1}{K_m}\right) d\pi = 0 \quad (2-16a)$$

$$\text{or } n(de_f - de_V) = \left(\alpha - \frac{C_g^2}{9} \{1\}^T [Dep] \{1\}\right) d\pi - \left(\{1\}^T - \frac{C_g}{3} \{1\}^T [Dep]\right) \{de\} \quad (2-16b)$$

Equation of Motion for the Bulk Mixture

The differential equation of motion governing the bulk mixture is expressed by equating the stress gradient to the inertial resistance as

$$\sigma_{ij,j} = (1 - n)\rho_S \ddot{u}_i + n\rho_f \ddot{u}_i \quad (2-17)$$

$\sigma_{ij,j}$ is the total stress gradient applied to an infinitesimal element of saturated material at some given time. $\sigma_{ij,j}$ is expressed in tensor notation and represents the stress gradient in each of three mutually perpendicular coordinates (e.g. see Mendleson, 1968). For instance, in the x direction,

$$\sigma_{xj,j} = \frac{\partial \sigma_{xx}}{\partial x} + \frac{\partial \sigma_{xy}}{\partial y} + \frac{\partial \sigma_{xz}}{\partial z} = (1 - n)\rho_S \ddot{u}_x + n\rho_f \ddot{u}_x \quad (2-18)$$

The term $(1 - n)\rho_S$ is the mass of the soil skeleton per unit volume of saturated material, where n is the porosity and ρ_S is the mass density of the solid grains. u_i is the displacement of the skeleton in the i direction and \ddot{u}_i is the acceleration of the skeleton in the i direction. The term $n\rho_f$ is the

mass of pore fluid per unit volume of saturated material where ρ_f is the mass density of the pore fluid. \ddot{U}_i is the absolute displacement of the pore fluid in the i direction.

The bulk mass density of the saturated material, ρ , is given by

$$\rho = (1 - n)\rho_s + n\rho_f \quad (2-19)$$

Substitution of the value for $(1 - n)\rho_s$ from Equation 2-19 into Equation 2-17 gives

$$\sigma_{ij,j} = (\rho - n\rho_f)\ddot{U}_i + n\rho_f\ddot{U}_i \quad (2-20)$$

A term w_i is introduced which is the apparent fluid displacement in the i direction relative to the soil skeleton and is given by

$$w_i = n(U_i - u_i) \quad (2-21)$$

In seepage problems, w_i is referred to as the discharge displacement. It describes the discharge of fluid through a soil mass of unit area. The discharge velocity, or apparent relative velocity, \dot{w}_i , between the soil particles and pore water is the velocity of water in a discharge duct of unit area needed to maintain the actual relative velocity in the porous soil of the same unit area. The actual relative velocity between the skeleton and the pore water is given by \dot{w}_i/n . Finally, \ddot{w}_i is the apparent relative acceleration between the soil skeleton and pore water given by

$$\ddot{w}_i = n(\ddot{U}_i - \ddot{u}_i) \quad (2-22)$$

Equation 2-20 can be expressed in terms of the apparent relative fluid acceleration as simply

$$\sigma_{ij,j} = \rho \ddot{u}_i + \rho_f \ddot{w}_i$$

(2-23)

Equation of Motion for Pore Fluid

Over the past several years our equation describing the motion of the pore fluid relative to the skeleton has undergone several evolutionary revisions. The original version, described by Kim and Blouin, 1984, utilized an approximation to Biot's fluid friction equations given by

$$\pi_{,i} = \underbrace{\rho_f \ddot{u}_i + \frac{\rho_f}{n} \ddot{w}_i}_{\text{Inertial Components}} + \underbrace{\frac{\gamma_f}{K} \dot{w}_i + \frac{\rho_f r}{n} \dot{w}_i}_{\text{Frictional Components}} \quad (2-24)$$

where

π_i = pore pressure gradient

\ddot{u}_i = absolute skeleton acceleration

\dot{w}_i = apparent fluid velocity relative to the skeleton

\ddot{w}_i = apparent fluid acceleration relative to the skeleton

ρ_f = pore fluid mass density

γ_f = unit weight of the pore fluid

n = porosity

k = Darcy's coefficient of permeability

r = mass increment factor

The first two terms to the right of the equal sign, the inertial components, represent the portion of the pressure gradient resulting from acceleration or deceleration of the pore fluid. The last two terms represent the portion of the pore pressure gradient due to fluid friction associated with the relative motion between the pore fluid and solid skeleton. The two fluid friction terms are based on Biot's work and are proportional to the relative

fluid velocity and acceleration, respectively. The first friction term is identical to Darcy's law for steady state flow conditions. The second friction term is a generalization of Biot's frequency dependent friction term.

Biot expressed the pore pressure gradient, $\pi_{,i}$, as

$$\pi_{,i} = \rho_f \ddot{U}_i + D_i \quad (2-25)$$

where $\rho_f \ddot{U}_i$ is the inertial force per unit volume of pore fluid and D_i represents the viscous friction force between the pore fluid and the soil skeleton per unit volume of pore fluid. Solving Equation 2-22 for \ddot{U}_i and substitution into Equation 2-25 gives

$$\pi_{,i} = \frac{\rho_f}{n} \dot{w}_i + \rho_f \ddot{U}_i + D_i \quad (2-26)$$

Biot showed that the viscous friction term, D_i , is a function of the excitation frequency, ω , the pore geometry, the dynamic viscosity, μ , and the apparent relative velocity between the pore fluid and the skeleton, \dot{w}_i . In an actual soil the flow of pore water would follow very complicated paths which are difficult to describe. These flow paths would involve numerous variations in direction and in cross sectional area. Biot employed models of the flow paths which are gross simplifications of the actual paths. He assumed two simple flow geometries; flow through a series of parallel circular ducts and flow through a series of parallel flat ducts. Flow conditions in the flat duct are depicted schematically in Figure 2.2.

For dynamic laminar flow, Biot (1956) derived the exact expression for the viscous friction term, D_i , for both circular and flat ducts which is given by

$$D_i = \gamma_f \frac{F(k)}{k} \dot{w}_i \quad (2-27)$$

where γ_f is the unit weight of pore fluid, $F(k)$ is the viscous friction correction factor, and k is the coefficient of permeability. $F(k)$ is a complex function given by

$$F(\kappa) = f_1(\kappa) + i f_2(\kappa) \quad (2-28)$$

The magnitudes of the real part, $f_1(\kappa)$, and imaginary part, $f_2(\kappa)$, are plotted in Figure 2.3 as a function of nondimensional parameter, κ , which is defined as

$$\kappa = \bar{r} \kappa_0 \quad (2-29)$$

$$\text{where} \quad \kappa_0 = \left(\frac{8}{n g} \right) \omega k^{\frac{1}{2}} \quad (2-30)$$

In Equations 2-29 and 2-30, g is the gravitational acceleration, ω is the excitation frequency, and the factor, \bar{r} , is the constant which is dependent on the shape of the flow path. For Generalized Darcy's Flow (also called Poiseuille Flow), $f_1(\kappa)$ and $f_2(\kappa)$ are independent of κ and $\bar{r} = 0$. For the circular duct, \bar{r} is unity. And for the flat duct, the value of r is approximately equal to $\sqrt{2/3}$.

An approximation of Equation 2-27 was developed by Kim and Blouin (1984) and is given by

$$D_i = \frac{\gamma_f}{K} \dot{w}_i + \frac{\rho_f}{n} r \ddot{w}_i \quad (2-31)$$

where

γ_f = unit weight of pore fluid

r = empirical mass increment factor which treats the dynamic fluid friction as though it was an increase in inertial mass of r

The theoretical value of r is $1/3$ for the circular duct and $1/5$ for the flat duct. Equation 2-31 is a good approximation when the nondimensional parameter, κ , is less than 2.

Substitution of Equation 2-31 into Equation 2-26 gives

$$\pi_i = \frac{\rho f}{n} (1 + r) \ddot{w}_i + \rho_f \ddot{u}_i + \frac{\gamma f}{K} \dot{w}_i \quad (2-32)$$

which has been rewritten as Equation 2-24 to separate the frictional terms from inertial terms.

In order to better understand the influence of Biot's dynamic frictional resistance the normalized relative flow velocity distribution in a flat duct given by Biot (1956) is plotted in Figure 2.4 as a function of the fluid viscosity and excitation frequency. The shape of the velocity profile is a function of the nondimensional parameter β which is defined as

$$\beta = a_1 \sqrt{\frac{\omega}{\nu}} \quad (2-33)$$

where

a_1 = half height of flat duct

ω = excitation frequency

ν = kinematic viscosity

Figure 2.4 illustrates the influence of excitation frequency on the shape of the flow velocity distribution in the flat duct for a constant fluid viscosity. For low excitation frequencies the distribution is parabolic, the same as that for steady state laminar flow. As the excitation frequency increases, the velocity distribution is pinched toward the center of the duct, indicating widening static boundary layers along the duct walls.

The next addition to the equation of motion for the pore fluid was an additional term to account for frictional energy losses during turbulent flow conditions. Figure 2.5 shows theoretical velocity distributions in a flat duct in both the laminar and turbulent flow regimes. Laminar flow occurs at Reynolds numbers of less than 2000. For steady state laminar flow the velocity

distribution is parabolic about the center of the duct (Poiseuille flow). For nonsteady state flow, Biot's theoretical analysis indicates a change in the flow velocity profile such as shown in Figure 2.4 and 2.5. In this flow state fluid friction increases, but flow remains laminar.

When the Reynolds number is greater than approximately 2000, the flow becomes turbulent with a velocity distribution in the direction of flow similar to that shown in Figure 2.5, where there is a very sharp velocity gradient adjacent to the duct walls. The flow lines in the turbulent regime are no longer parallel and there are random particle motions transverse to the direction of flow.

As described in Section 6, we have experimentally verified a generalized turbulent flow relationship of the form

$$\pi_{,i} = a\dot{w}_i + b\dot{w}_i^2 + c\dot{w}_i + \rho_f \ddot{u}_i \quad (2-34)$$

where

$\pi_{,i}$ = pore pressure gradient

w_i = apparent flow velocity relative to the
solid skeleton

\dot{w}_i = apparent relative pore fluid acceleration

a, b & c = flow parameters which are a function of microscale
parameters including pore sizes and geometries,
overall porosity, viscosity, etc.

ρ_f = fluid mass density

\ddot{u}_i = skeleton acceleration

In the laminar flow regime the parameters in Equation 2-34 are given by

$$\left. \begin{aligned} a &= \frac{\gamma_f}{K} \\ b &\approx 0 \\ c &= (1+r) \frac{\rho_f}{\eta} \end{aligned} \right\} \quad (2-35)$$

where

γ_f = fluid unit weight

ρ_f = fluid mass density

K = coefficient of permeability

r = mass increment factor which approximates
the influence of excitation frequency

($r = 1/5$ for flat ducts and

$r = 1/3$ for circular ducts)

In the turbulent flow regime the flow parameters of Equation 2-34 are given by

$$\left. \begin{aligned} a &= \frac{\gamma_f}{K} \\ b &= \frac{\beta_f}{K^{1/2}} \\ c &= \frac{\rho_f}{\eta} \end{aligned} \right\} \quad (2-36)$$

where

β_f = Ward's turbulent flow constant which is

a function of the pore geometry and pore fluid
viscosity and which is determined experiment-

ally from steady state turbulent flow tests

(see Kim, Blouin and Timian, 1987).

Note that in the turbulent regime the random transverse particle motions result in elimination of the mass increment factor r from the flow parameter

c. Section 6 presents validation of Equation 2-36 for flow in a flat duct with velocities up to 4000 in/s and fluid accelerations to nearly 1000 g's. Flow parameters a and b have also been validated for steady state turbulent flow in porous soils.

The experimental results in Section 6, along with the previous experimental work (Kim, Blouin and Timian, 1986 and 1987), demonstrate that the turbulent pore water flow regime will dominate the fluid friction response in explosive loadings of saturated soils and rocks at stress levels of interest to civil engineering problems. Turbulent flow develops nearly simultaneously with arrival of the dynamic stress wave from an adjacent explosion. Laminar (or Darcy) flow is relevant only at late times after passage of the dynamic stress waves. The experimental and theoretical results demonstrate that Biot's theoretical work (1956, 1962A, 1962B), which is used by some investigators to describe transient flow, is not applicable in the turbulent flow regime.

Partial Saturation

In numerous geologic settings the soil or rock is not fully saturated. Rischbieter et al. (1977) demonstrated that even a minute amount of entrapped air drastically alters the pore pressure response in multiphase porous materials. Thus, a complete treatment of multiphase media should include the capability of calculating stress wave propagation and pore fluid response in three-phase porous materials.

Kim (1982) developed a unique formulation for the compressibility of the air-water mixture in partially saturated porous media. This formulation has been extensively applied in quasi-static problems and verified against experimental data.

The compressibility, C_{aw} , of the air-water mixture in partially saturated media is given by

$$C_{aw} = (1 - S_o + H_c S_o) \frac{\pi_{ao}}{(\pi + T)^2} \quad (2-37)$$

where

S_o = initial degree of saturation

H_c = coefficient of solubility (Henry's constant)

π_{ao} = initial pore air pressure (absolute)

π = current pore water pressure (absolute)

T = pressure difference between the air and pore water due to surface tension

As indicated by Equation 2-37, the compressibility of the air-water mixture is nonlinear with respect to the current pore water pressure. This relationship has been shown to be applicable when the degree of pore water saturation is above approximately 85%, and the air water mixture is thought to exist in an occluded state with the air contained as small bubbles within the pore fluid.

The pressure difference, T , in Equation 2-37 is determined experimentally from undrained hydrostatic tests on partially saturated samples with a known degree of saturation (Kim, 1982).

The treatment of partially saturated materials utilizes the same flow field equations as described in the preceding discussion. However, the compressibility of the pore fluid, C_f , is given by Equation 2-37. In other words, the porous skeleton is assumed to be filled with an equivalent fluid which has the same compressibility as the air-water mixture.

At some value of pore fluid pressure the air bubbles undergo a complete collapse and the compressibility of the air-water mixture becomes approximately equal to the compressibility of the pore water.

Summary of Field Equations

A summary of all the field equations implemented in MPDAP includes:

1. Effective Stress Law,

$$\sigma_{ij} = \sigma'_{ij} + \delta_{ij} \pi \quad (2-1)$$

2. Skeleton Deformation Relationship,

$$\{d\sigma'\} = [D^{ep}] \left(\{d\epsilon\} - \frac{C_g}{3} \{1\} d\pi \right) \quad (2-2)$$

3. Pore Fluid Continuity Equation,

$$n(d\epsilon_F - d\epsilon_V) + (1 - C_g K_S) d\epsilon_V + \left(C_g^2 K_S - \frac{1}{K_m} \right) d\pi = 0 \quad (2-16)$$

4. Bulk Mixture Motion,

$$\sigma_{ij,j} = (\rho - n\rho_f)\ddot{u}_i + n\rho_f\ddot{u}_i \quad (2-20)$$

5. Pore Fluid Relative Motion,

$$\pi_{,i} = a\dot{w}_i + b\dot{w}_i^2 + c\dot{w}_i + \rho_f\ddot{u}_i \quad (2-34)$$

where $a = \frac{\gamma_f}{K}$

and $b \approx 0$

$$c = (1+r) \frac{\rho_f}{n}$$

for laminar flow conditions, and

$$b = \frac{\beta_f}{K^{3/2}}$$

$$c = \frac{\rho_f}{n}$$

for turbulent flow conditions

6. Partial Saturation

$$C_f = C_{aw}$$

(2-38)

Conservation of Fluid Mass

$$n \rho_f V_t = n' \rho_f' V_t'$$

V_t = apparent fluid volume before compression

$V_t' = (1 + \epsilon_f) V_t$: apparent fluid volume after compression

ϵ_v = volumetric strain of porous skeleton

ϵ_f = volumetric diffusion of pore fluid

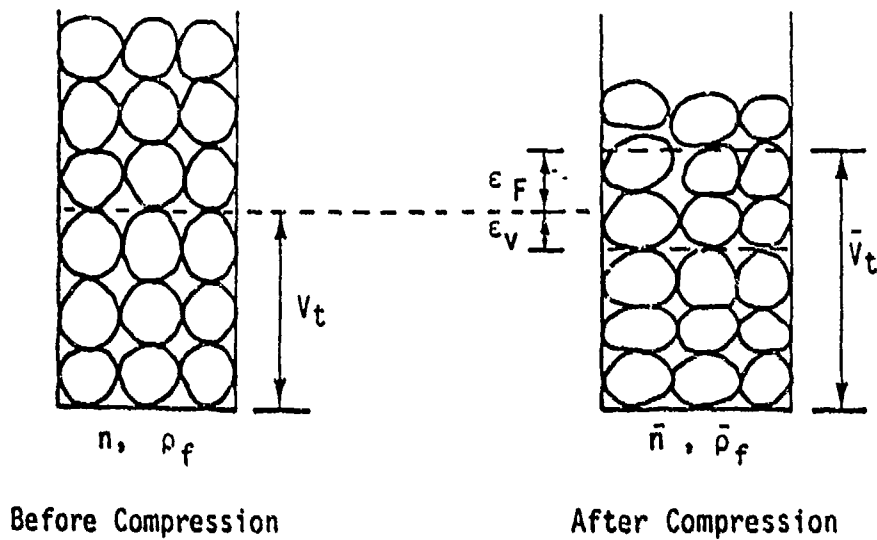


Figure 2.1. Schematic illustration of conservation of pore fluid mass in saturated porous materials.

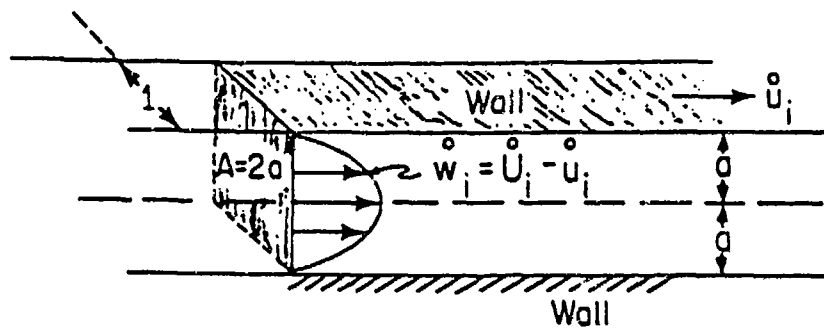


Figure 2.2 Schematic view of fluid flow in a flat duct.

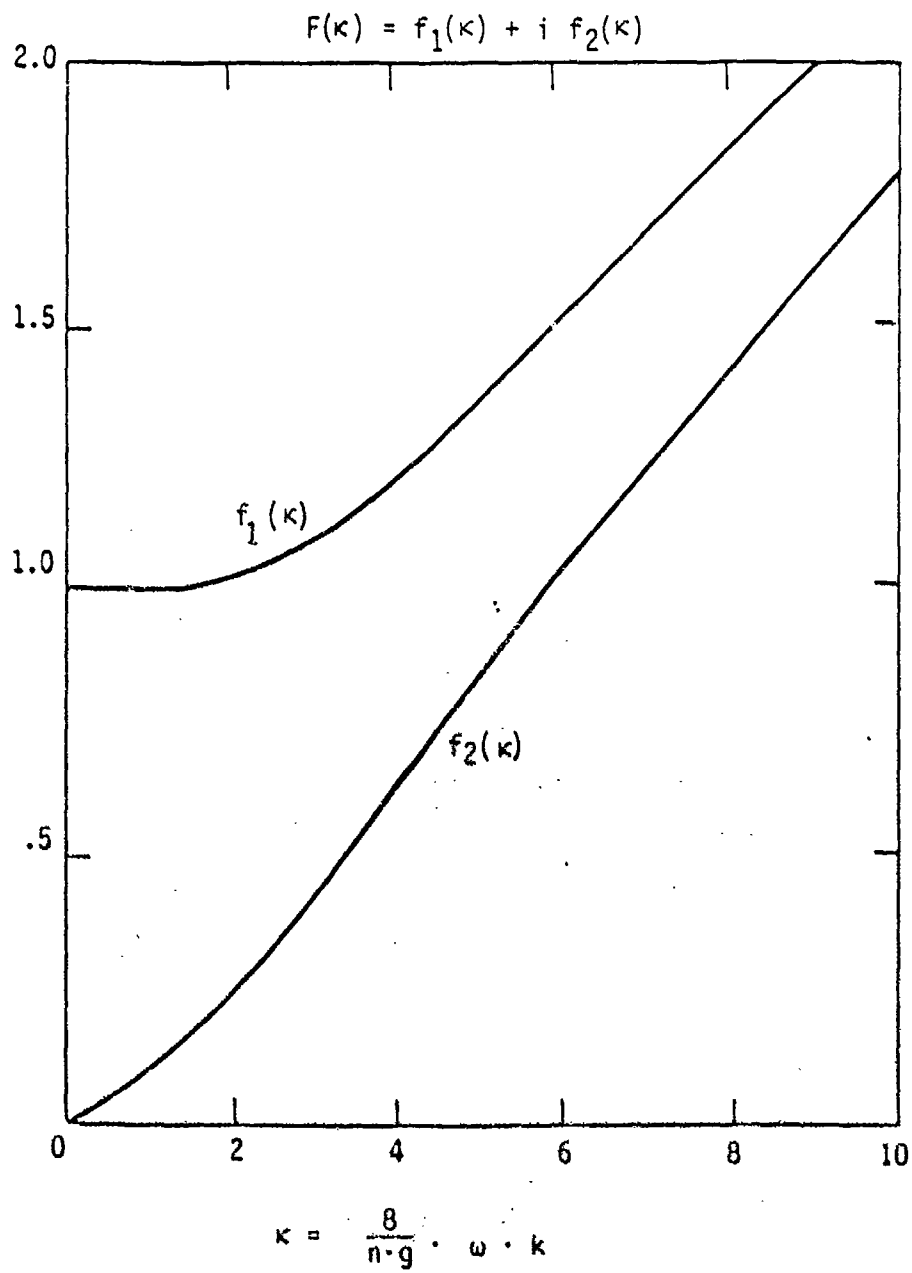


Figure 2.3. Viscous friction correction factor, $f(\kappa)$, as a function of κ .

VELOCITY DISTRIBUTION

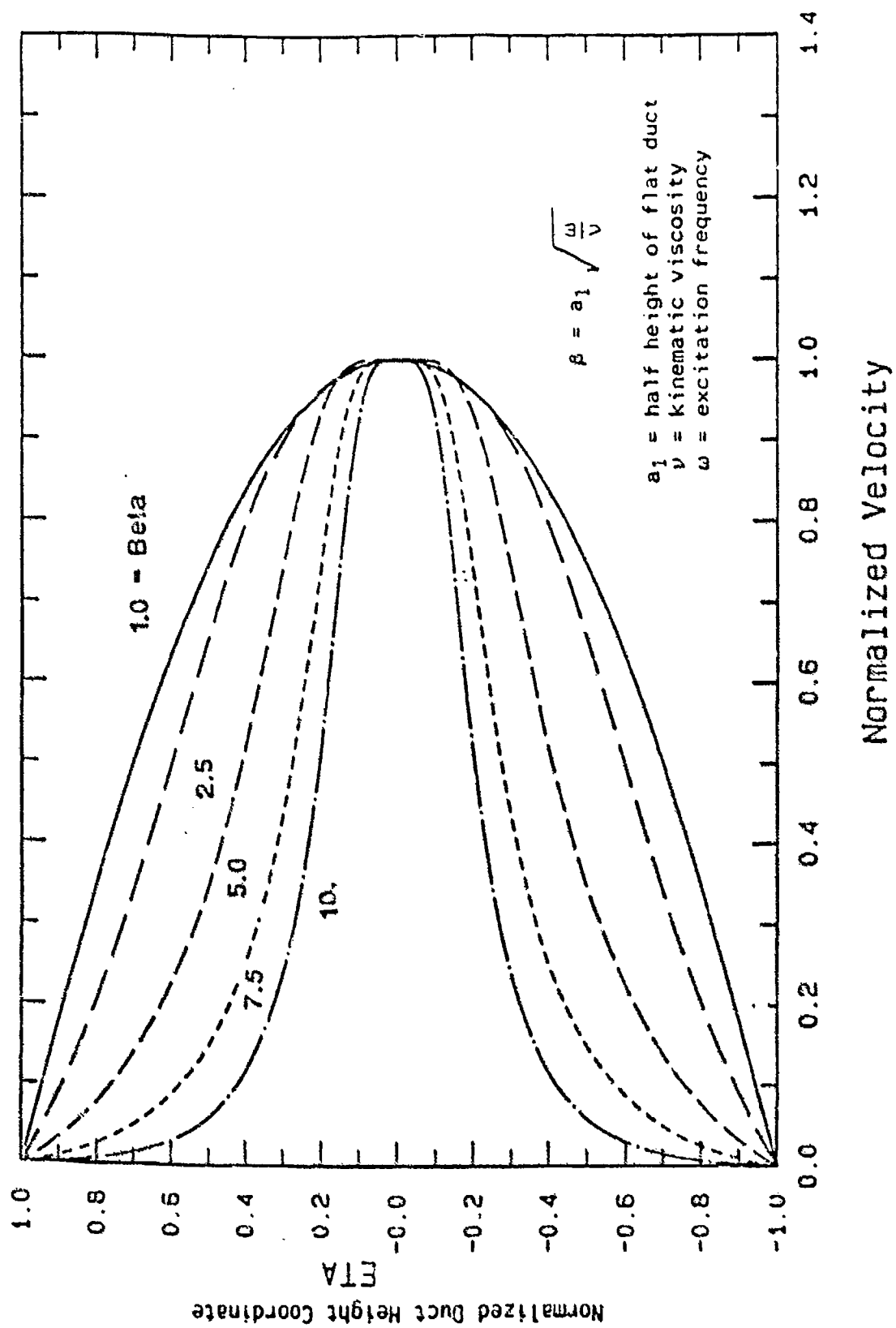


Figure 2.4. Influence of excitation frequency on velocity distribution in a flat duct.

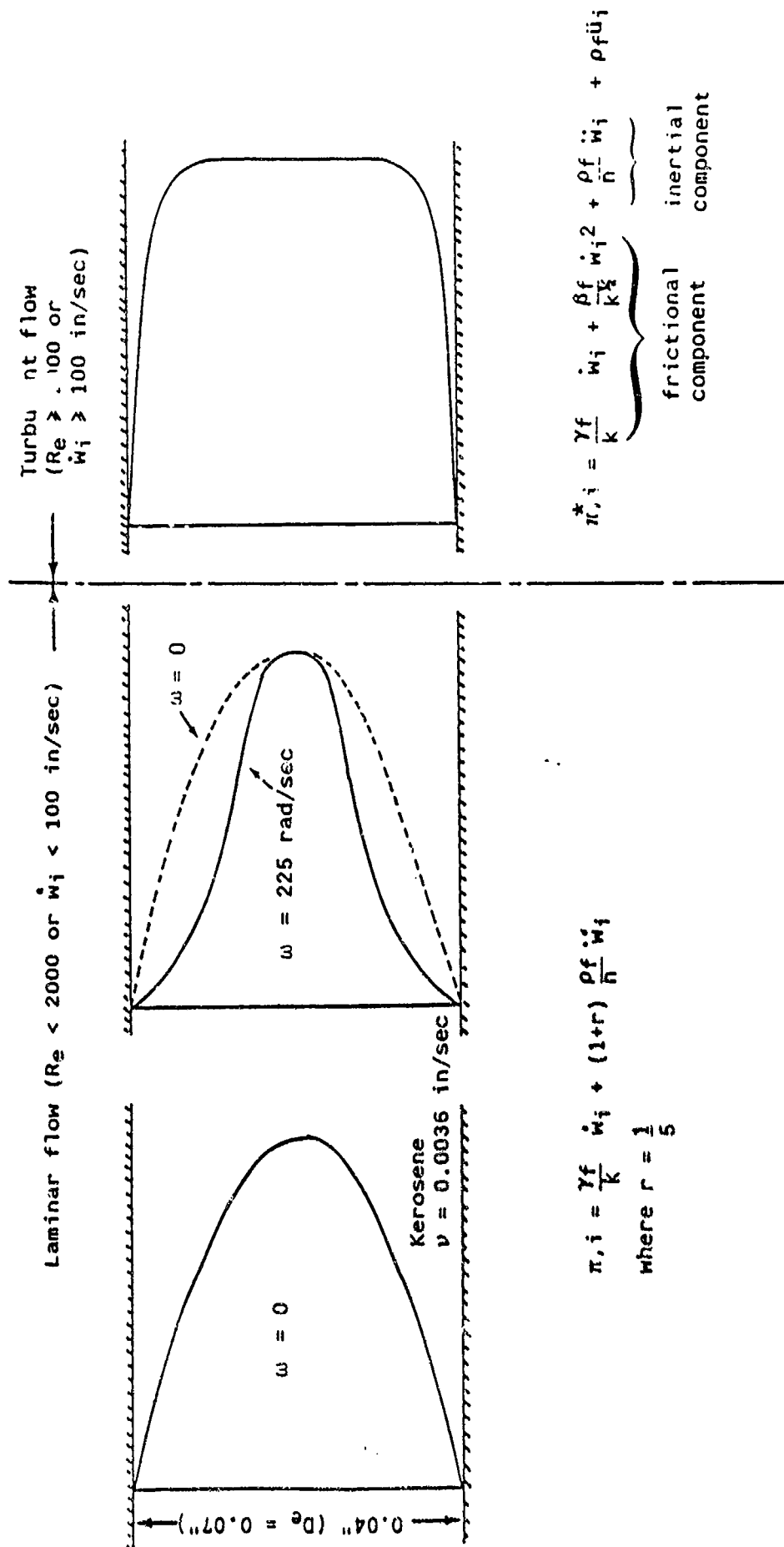


Figure 2.5. Velocity distributions in a flat duct.

SECTION 3

DYNAMIC MULTIPHASE FINITE ELEMENT FORMULATIONS FOR MPDAP

3.1 INTRODUCTION

The field equations in Section 2 represent the fundamental governing equations for an infinitesimal element of saturated porous medium. Using the finite element method, the values of the field variables at any point within the element can be computed from the element nodal values. Global equilibrium equations for specified boundary conditions can then be derived by applying the principles of virtual work. These global equations are incorporated into MPDAP as described in this section.

As noted in the previous section, pore pressure at the element nodes is used to compute pore pressure gradients, which are in turn used to compute the relative flow of the pore fluid. This approach is used in place of the more conventional technique whereby relative fluid displacement vectors are defined at each element node. This eliminates one degree of freedom per node in two-dimensional calculations and two degrees of freedom per node in three-dimensional calculations, resulting in large reductions in running time and storage requirements.

3.2 SPATIAL DISCRETIZATION

Within each element, field variables can be expressed in terms of the element nodal values using the assumed shape functions.

$$\begin{aligned} \{u\} &= [N] \{U\}_e \\ \{\epsilon\} &= [B] \{U\}_e \\ \pi &= \langle G \rangle \{\pi\}_e \\ \{\pi, i\} &= [A] \{\pi\}_e \end{aligned} \tag{3-1}$$

where the above notation is described in Section 2.2.1.

3.3 INCREMENTAL FORM OF TOTAL STRESS VECTOR

The total stress vector at time step n can be expressed as

$$\{\sigma_n\} = \{\sigma_{n-1}\} + \{\Delta\sigma'_n\} + \{1\} \Delta\pi_n \quad (3-2)$$

Substitution of Equation 2-2 into Equation 3-2 yields

$$\{\sigma_n\} = \{\sigma_{n-1}\} + [Dep] \{\Delta\epsilon_n\} + \left(\{1\} - \frac{C_g}{3} [Dep] \{1\} \right) \Delta\pi_n \quad (3-3)$$

3.4 APPROXIMATION OF ABSOLUTE FLUID MOTION

In the previous section, we presented Equation 2-35 describing pore fluid flow in the laminar regime and Equation 2-36 describing flow in the turbulent regime. As shown in Section 6, our experimental work demonstrated that pore fluid transitions rapidly into the turbulent regime under only modest pore pressure gradients. For practical purposes, in large amplitude dynamic loadings, any influence of the mass increment factor, r , is completely obscured by the transition from laminar to turbulent flow. We, therefore, can use Equation 2-36 to represent flow in both the laminar and turbulent regimes.

Substituting the flow parameters for Equation 2-36 into Equation 2-34 gives

$$\pi_{,i} = \frac{\gamma_f}{K} \dot{w}_i + \frac{\beta_f}{K\beta} \dot{w}_i^2 + \frac{\rho_f}{n} \dot{w}_i + \rho_f \ddot{U}_i \quad (3-4)$$

Equation 3-4 can be expressed in the following simple form by using Equations 2-19 and 2-22

$$\pi_{,i} = \rho_f \ddot{U}_i + \frac{1}{k^*} \dot{w}_i \quad (3-5)$$

and

$$k' = \frac{k}{\gamma_f \left(1 + \frac{\beta_f}{\gamma_f} k^{\frac{1}{2}} |w_i| \right)} \quad (3-6)$$

where $k'\gamma_f$ is an equivalent permeability applicable in the turbulent flow regime.

To simplify mathematical derivations, the k' in Equation 3-6 is evaluated at time step $n-1$ and this value is used at time step n . k' is then recomputed at time step n for use during the next time step, $n+1$.

For time step n

$$k' = k'_{n-1} \quad (3-7)$$

At this point we are ready to express the absolute fluid velocity in terms of the pore pressure gradient and skeleton displacement. The apparent fluid velocity, \dot{w}_i , can be expressed in terms of absolute fluid velocity, \dot{U}_i , and skeleton velocity, \dot{u}_i , by differentiating Equation 2-21 with respect to time.

$$\dot{w}_i = n(\dot{U}_i - \dot{u}_i) \quad (3-8)$$

Substitution of Equation 3-8 into Equation 3-5 yields

$$\rho_f \dot{U}_i + \frac{n}{k'} \dot{U}_i = \pi_{,i} + \frac{n}{k'} \dot{u}_i \quad (3-9)$$

By defining the above fluid flow equation at time step $n-k$,

$$\rho_f \dot{U}_i^{n-k} + \frac{n}{k'} \dot{U}_i^{n-k} = \pi_{,i}^{n-k} + \frac{n}{k'} \dot{u}_i^{n-k} \quad (3-10)$$

The field variable at time step $n-k$ can be approximated by the field variables at time steps $n-1$ and n as follows;

$$\ddot{u}_i^{n-\frac{1}{2}} = \frac{1}{\Delta t} (\dot{u}_i^n - \dot{u}_i^{n-1}) \quad (3-11a)$$

$$0_i^{n-\frac{1}{2}} = \frac{1}{2} (\dot{u}_i^n + \dot{u}_i^{n-1}) \quad (3-11b)$$

$$\pi_{,i}^{n-\frac{1}{2}} = \frac{1}{2} (\pi_{,i}^n + \pi_{,i}^{n-1}) \quad (3-11c)$$

$$\dot{u}_i^{n-\frac{1}{2}} = \frac{1}{\Delta t} (\Delta u_i^n) \quad (3-11d)$$

Substituting Equation 3-11 into Equation 3-10 and solving for the absolute fluid velocity at time step n , we obtain

$$\dot{u}_i^n = a_1 \dot{u}_i^{n-1} + a_2 (\pi_{,i}^{n-1} + \pi_{,i}^n) + a_3 \Delta u_i^n \quad (3-12)$$

where

$$\left. \begin{aligned} a_1 &= \frac{2k'\rho_f - n \Delta t}{2k'\rho_f + n \Delta t} \\ a_2 &= \frac{k' \Delta t}{2k'\rho_f + n \Delta t} \\ a_3 &= \frac{2n}{2k'\rho_f + n \Delta t} \end{aligned} \right\} \quad (3-13)$$

Now combining Equations 3-11b, 3-11c, 3-11d, 3-12, and 3-10 and solving for the absolute fluid acceleration at time step $n-\frac{1}{2}$, we obtain

$$\rho_f \ddot{u}_i^{n-\frac{1}{2}} = a_4 \dot{u}_i^{n-1} + a_5 (\pi_{,i}^{n-1} + \pi_{,i}^n) + a_6 \Delta u_i^n$$

where

$$\left. \begin{aligned} a_4 &= -\frac{n}{2k'} (1+a_1) \\ a_5 &= \frac{1}{2} \left(1 - \frac{n}{k'} a_2 \right) \\ a_6 &= \frac{n}{k' \Delta t} \left(1 - \frac{\Delta t}{2} a_3 \right) \end{aligned} \right\} \quad (3-15)$$

At this point, we have defined the motion of the pore fluid in terms of the pore pressure gradients and skeleton motion and can determine all aspects of the skeleton and pore fluid behavior. We are now ready to derive the global equilibrium equations for the bulk mixture and the pore fluid.

3.5 GLOBAL EQUILIBRIUM EQUATION FOR THE BULK MEDIUM

Shown schematically in Figure 3.1 are the total stresses and virtual displacements on the boundary of an infinitesimal element. The total stresses are in equilibrium with the applied boundary tractions. Taking the solid skeleton movement as the virtual displacement, δu_x , the internal and external virtual work must be equal. The internal virtual work at time step n ($t = t_n$) is given by

$$\delta W_I = \int_V \{\delta \epsilon\}^T \{\sigma_n\} dv \quad (3-16)$$

Substituting Equations 3-1 and 3-3 into Equation 3-16,

$$\begin{aligned}
\delta W_I = \{ \delta \bar{u} \}^T & \left[\left(\sum \int_V [B]^T [D^{ep}] [B] dv \right) \{ \Delta \bar{u} \}_n \right. \\
& + \left(\sum \int_V [B]^T (\{1\} - \frac{c_g}{3} [D^{ep}] \{1\}) \langle G \rangle dv \right) \{ \Delta \bar{\pi} \}_n \\
& \left. + \sum \int_V [B]^T \{ \sigma_{n-1} \} dv \right]
\end{aligned} \tag{3-17}$$

The external virtual work at time step n is given by

$$\begin{aligned}
\delta W_E = - \int_V \{ \delta u \}^T \{ F_I \}_n + \int_S \{ \delta u \}^T \{ T \}_n ds \\
= \{ \delta \bar{u} \}^T & \left[- \left(\sum \int_V [N]^T (\rho - n \rho_f) [N] dv \right) \{ \ddot{u} \}_n \right. \\
& \left. - \left(\sum \int_V [N]^T n \rho_f \{ \ddot{u} \}_n dv \right) + \sum \int_S [N]^T \{ T \}_n ds \right]
\end{aligned} \tag{3-18}$$

The absolute fluid acceleration term in Equation 3-18 can be explicitly expressed using the approximate relationships in Equation 3-14.

$$\sum \int_V [N]^T n \rho_f \{ \ddot{u} \}_n dv \approx \{ R_{f1} \}_{n-1/2} \tag{3-19}$$

where

$$\{ R_{f1} \}_{n-1/2} = \sum \int_V [N]^T n \left(a_4 \{ 0 \}_{n-2} + a_5 (\{ \pi, i \}_{n-2} + \{ \pi, i \}_{n-1}) + a_6 \{ \Delta u \}_{n-1} \right) dv$$

(3-20)

Substituting Equation 3-19 into 3-18,

$$\delta W_E = \{\delta \bar{u}\}^T \left[- \left(\sum_V [N]^T (\rho - n\rho_f) [N] dv \right) \{\ddot{\bar{u}}\}_n \right. \\ \left. - \{R_{f1}\}_{n-1/2} + \left(\sum_S [N]^T \{T\}_n ds \right) \right] \quad (3-21)$$

Since internal and external virtual work are equal,

$$\delta W_I = \delta W_E \quad (3-22)$$

Now, global equilibrium equations for the bulk mixture are obtained by substituting Equations 3-17 and 3-21 into Equation 3-22.

$$[M_t] \{\ddot{\bar{u}}\}_n + [K_t] \{\Delta \bar{u}\}_n + [C] \{\Delta \bar{\pi}\}_n = \{P_u\}_n \quad (3-23)$$

where

$$\{P_u\}_n = \{F\}_n - \sum_V [B]^T \{\sigma_{n-1}\} dv - \{R_{f1}\}_{n-1/2}$$

$$[M_t] = \sum_V [N]^T (\rho - n\rho_f) [N] dv$$

$$[K_T] = \sum_V [B]^T [D^{ep}] [B] dv \quad (3-24)$$

$$[C] = \sum_V [B]^T \left(\{1\} - \frac{c_g}{3} [D^{ep}] \{1\} \right) \langle G \rangle dv$$

$$\{F\}_n = \sum_S [N]^T \{T\}_n ds$$

3.6 GLOBAL EQUILIBRIUM EQUATIONS FOR PORE FLUID

Figure 3.2 shows schematically the complementary virtual pore pressures and skeleton and fluid velocities on the boundary of the infinitesimal

element. The internal fluid movements relative to the solid skeleton are compatible with the specified boundary flux. Thus, taking the complementary virtual stresses as the pore pressure field at a certain time, t , the internal and external complementary virtual work which is done between time t_{n-1} and t_n must be the same. That is,

$$\delta W_I^* = \delta W_E^* \quad (3-25)$$

where the internal complementary work is given by

$$\delta W_I^* = \int_{t_{n-1}}^{t_n} \int_V \delta \pi \, n \, \frac{\partial}{\partial t} (\epsilon_F - \epsilon_V) \, dv \, dt + \int_{t_{n-1}}^{t_n} \int_V \{\delta \pi, i\}^T \{\dot{w}\} \, dv \, dt \quad (3-26)$$

and the external complementary work by

$$\delta W_E^* = \int_{t_{n-1}}^{t_n} \int_S \delta \pi \, \hat{Q} \, ds \, dt \quad (3-27)$$

Substitution of Equations 2-16 and 3-5 into Equation 3-26 yields

$$\begin{aligned} \delta W_I^* = & \int_{t_{n-1}}^{t_n} \left[\int_V \delta \pi^T \left(\alpha - \frac{C_g^2}{9} \{1\}^T [Dep] \{1\} \right) \dot{\pi} \, dv \right. \\ & - \int_V \delta \pi^T \left(\{1\}^T - \frac{C_g}{3} \{1\}^T [Dep] \{\dot{\epsilon}\} \right) dv \\ & + \int_V \{\delta \pi, i\}^T k' \{\pi, i\} \, dv \\ & \left. - \int_V \{\delta \pi, i\}^T \rho_f k' \{\ddot{u}\} \, dv \right] dt \end{aligned} \quad (3-28)$$

The absolute fluid acceleration term in Equation 3-28 can be explicitly expressed using Equation 3-14 as follows;

$$\int_{t_{n-1}}^{t_n} \int_V \{ \pi_i \}^T \rho_f k' \{ \ddot{u} \} dv dt \approx \int_V \{ \delta \pi_i \}^T k' \rho_f \{ \ddot{u} \}_{n-1/2} dv \cdot \Delta t \quad (3-29)$$

And the third term in Equation 3-28 can be integrated with respect to time as below;

$$\int_{t_{n-1}}^{t_n} \int_V \{ \delta \pi_i \}^T k' \{ \pi_i \} dv \cdot dt \approx \int_V \{ \delta \pi_i \}^T k' \left(\frac{1}{2} \{ \Delta \pi \}_n + \{ \pi \}_{n-1} \right) dv \cdot \Delta t \quad (3-30)$$

Now, substituting Equations 3-29 and 3-30 into 3-28 and discretizing by Equation 3-1, we have the following expression;

$$\begin{aligned} \delta W_I^* = & \{ \delta \pi \}^T \left[[E] \{ \Delta \pi \}_n - [C]^T \{ \Delta u \}_n \right. \\ & + [H] \left(\frac{1}{2} \Delta t \{ \Delta \pi \}_n + \Delta t \{ \pi \}_{n-1} \right) \\ & \left. - \sum \int_V [A]^T k' \rho_f \{ \ddot{u} \}_{n-1/2} \cdot dv \cdot \Delta t \right] \end{aligned} \quad (3-31)$$

where

$$[E] = \sum \int_V \langle G \rangle^T \left(\alpha - \frac{Cg^2}{9} \{ 1 \}^T [D \epsilon P] \{ 1 \} \right) \langle G \rangle dv \quad (3-32)$$

$$[H] = \sum \int_V [A]^T k' [A] dv$$

For the external complementary virtual work, discretizing Equation 3-27 by Equation 3-1 yields

$$\delta W_E^* = \{ \delta \pi \}^T \left[\int_{t_{n-1}}^{t_n} \{ Q \} dt \right] \quad (3-33)$$

where

$$\{ Q \} = \sum \int_S \langle G \rangle^T \tilde{Q} ds \quad (3-34)$$

Assuming a linear variation of $\{Q\}$ between time t_{n-1} and t_n , Equation 3-33 can be expressed as

$$\delta W_E^* = \{\delta \bar{\pi}\}^T \left[\frac{\Delta t}{2} \left(\{Q\}_{n-1} + \{Q\}_n \right) \right] \quad (3-35)$$

Now, substituting Equations 3-31 and 3-35 into Equation 3-25, the following global equilibrium equations for the pore fluid are obtained:

$$[C]^T \{\Delta \bar{u}\}_n + \left(-[E] - \frac{\Delta t}{2} [H] \right) \{\Delta \bar{\pi}\}_n = \{P_\pi\}_n \quad (3-36)$$

where

$$\{P_\pi\}_n = \Delta t [H] \cdot \{\pi\}_{n-1} - \{R_{f2}\}_{n-1/2} - \frac{\Delta t}{2} \left(\{Q\}_{n-1} + \{Q\}_n \right) \quad (3-37)$$

and

$$\begin{aligned} \{R_{f2}\}_{n-1/2} = \sum \int [A]^T k' \Delta t \cdot & \left(a_4 \{\dot{u}\}_{n-2} \right. \\ & \left. + a_5 \left(\{\pi_{,i}\}_{n-2} + \{\pi_{,i}\}_{n-1} \right) + a_6 \{\Delta u\}_{n-1} \right) dv \end{aligned} \quad (3-38)$$

3.7 COMBINED GLOBAL EQUILIBRIUM EQUATIONS

Equations 3-23 and 3-36 can be combined in the following matrix form:

$$[M] \{\ddot{\bar{d}}\}_n + [K] \{\Delta \bar{d}\}_n = \{\bar{P}\}_n \quad (3-39)$$

where the mass matrix $[M]$ is

$$[M] = \left[\begin{array}{c|c} [M_t] & [0] \\ \hline - & - \\ \hline [0] & [0] \end{array} \right] \quad (3-40)$$

the stiffness matrix $[K]$ is

$$[K] = \left[\begin{array}{c|c} [K_T] & [C] \\ \hline - & - \\ \hline [C]^T & -[E] - \frac{\Delta t}{2}[H] \end{array} \right]$$

the force vector $\{\bar{P}\}_n$ is

$$\{\bar{P}\}_n = \left\{ \begin{array}{c} \{P_U\}_n \\ \hline \{P_\pi\}_n \end{array} \right\}$$

the acceleration vector $\{\ddot{d}\}_n$ is

$$\{\ddot{d}\}_n = \left\{ \begin{array}{c} \{\ddot{u}\}_n \\ \hline \{\ddot{\pi}\}_n \end{array} \right\}$$

and the displacement increment vector $\{\Delta \bar{d}\}_n$ is

$$\{\Delta \bar{d}\}_n = \left\{ \begin{array}{c} \{\Delta \bar{u}\}_n \\ \hline \{\Delta \bar{\pi}\}_n \end{array} \right\}$$

3.8 LINEARIZED GLOBAL EQUILIBRIUM EQUATIONS

Introducing a time integration method which incorporates both Newmark's β method and Wilson's θ method, the generalized acceleration vector is expressed as

$$\{\ddot{\bar{d}}\}_n = C_1 \{\Delta \bar{d}\}_n + C_2 \{\dot{\bar{d}}\}_{n-1} + C_3 \{\ddot{\bar{d}}\}_{n-1} \quad (3-41)$$

where

$$\begin{aligned} C_1 &= \frac{1}{\beta \theta^3 \Delta t^2} \\ C_2 &= -\frac{1}{\beta \theta^2 \Delta t} \\ C_3 &= 1 - \frac{1}{2\beta \theta} \end{aligned} \quad (3-42)$$

and the generalized velocity vector is expressed as

$$\{\dot{\bar{d}}\}_n = B_1 \{\Delta \bar{d}\}_n + B_2 \{\dot{\bar{d}}\}_{n-1} + B_3 \{\ddot{\bar{d}}\}_{n-1} \quad (3-43)$$

where

$$\begin{aligned} B_1 &= \frac{\gamma}{\beta \theta^3 \Delta t} \\ B_2 &= 1 - \frac{\gamma}{\beta \theta^2} \\ B_3 &= 1 - \frac{\gamma}{2\beta \theta} \Delta t \end{aligned} \quad (3-44)$$

Substituting Equation 3-41 into Equation 3-39 and rearranging, we can obtain the following linearized global equilibrium equations which can be

solved simultaneously at each step:

$$[\tilde{K}]\{\Delta \bar{d}\}_n = \{\tilde{P}\}_n \quad (3-45)$$

where the generalized stiffness matrix $[\tilde{K}]$ is

$$[\tilde{K}] = c_1[M] + [K] \quad (3-46)$$

and the generalized force vector $\{\tilde{P}\}_n$ is

$$\{\tilde{P}\}_n = \{\bar{P}\}_n - [M] c_2 \{\dot{\bar{d}}\}_{n-1} + c_3 \{\ddot{\bar{d}}\}_{n-1}$$

3.9 SUMMARY OF GLOBAL EQUILIBRIUM EQUATIONS

A summary of the global equilibrium equations includes:

1. Bulk Mixture Equilibrium

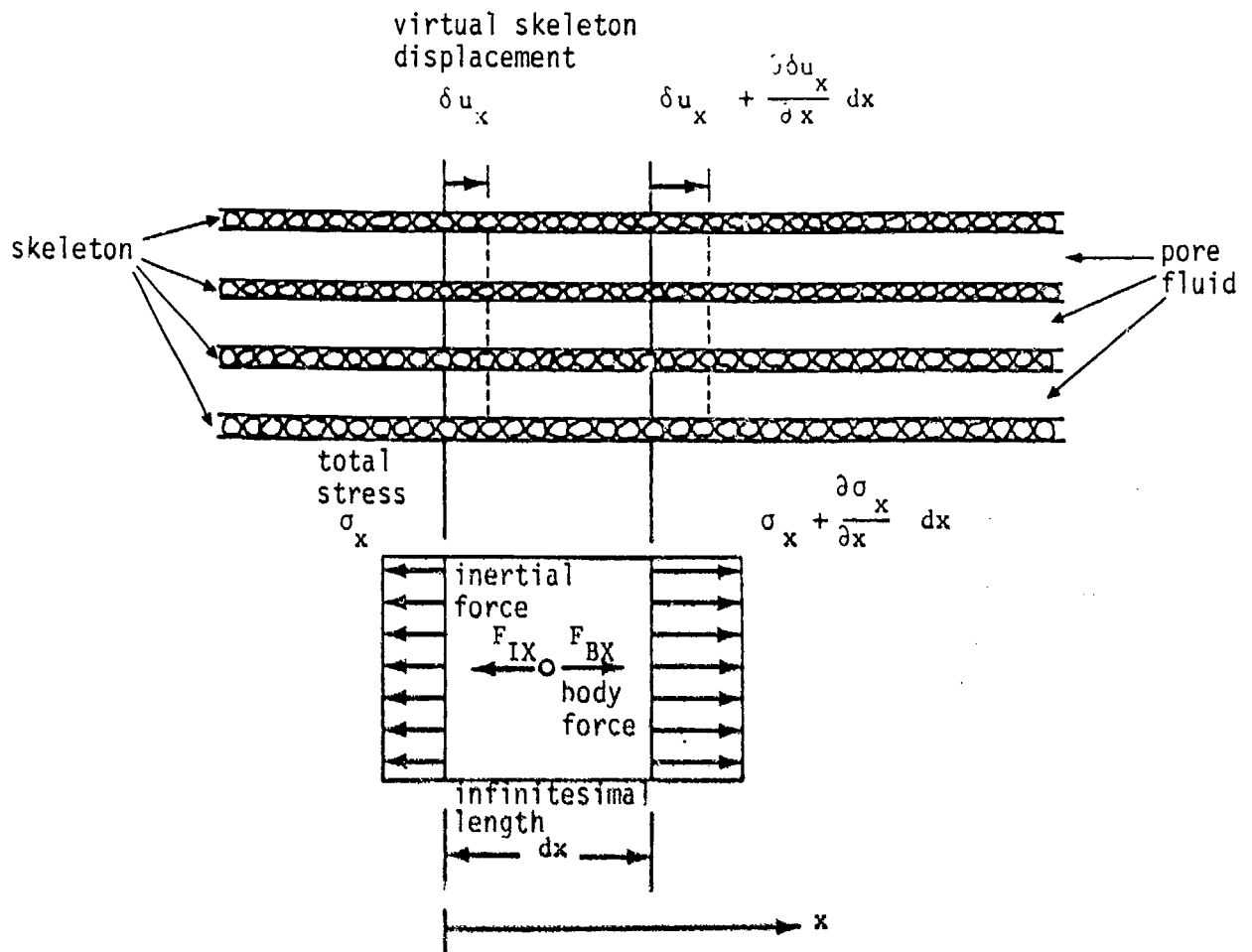
$$[M_t]\{\ddot{u}\}_n + [K_t]\{\Delta u\}_n + [C]\{\Delta \pi\}_n = \{P_u\}_n \quad (3-23)$$

2. Pore Fluid Equilibrium

$$[C]^T\{\Delta u\}_n + -[E] - \frac{\Delta t}{2} [H] \{\Delta \pi\}_n = \{P_\pi\}_n \quad (3-36)$$

3. Combined Equilibrium Equation

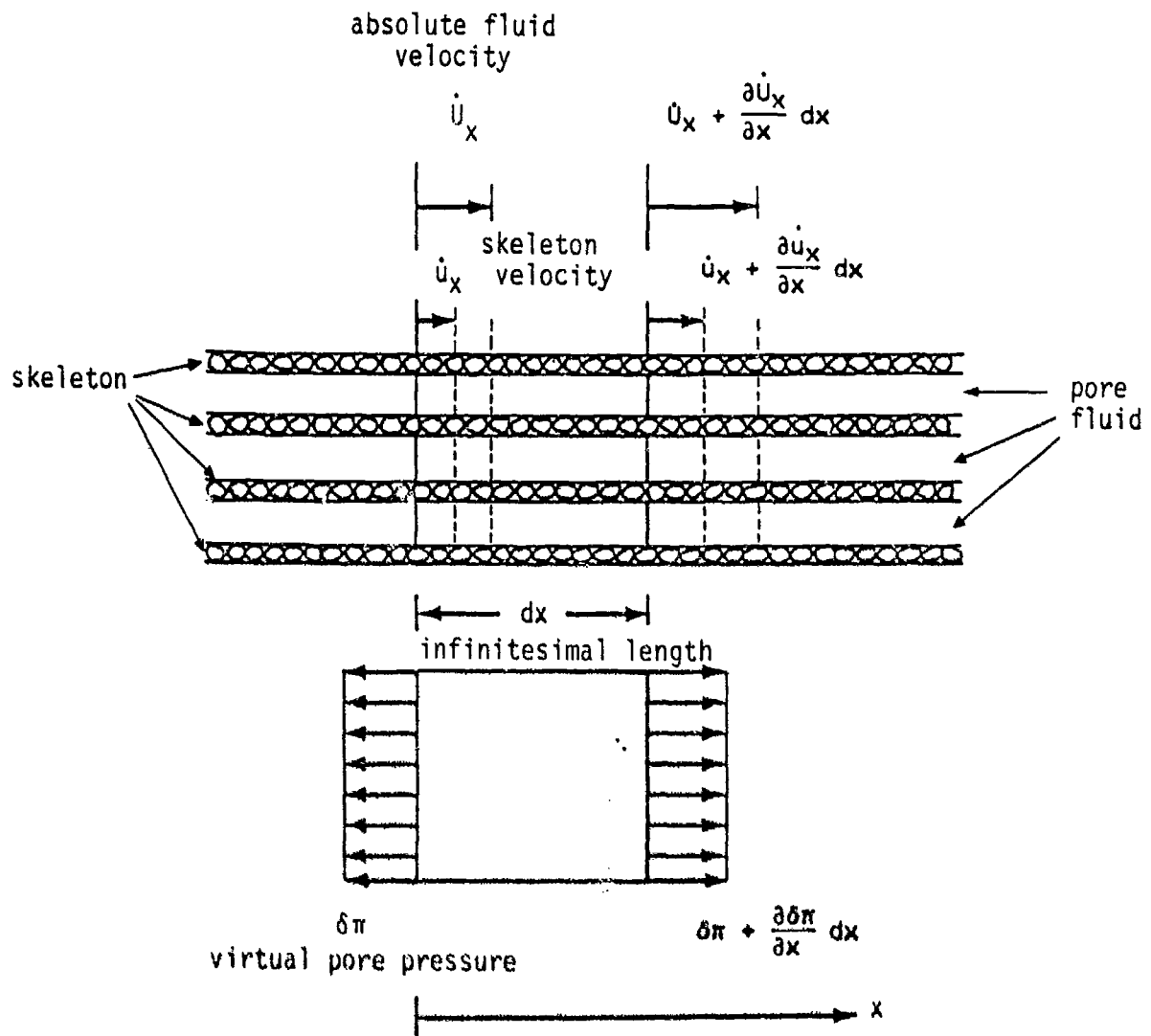
$$[\tilde{K}]\{\Delta \bar{d}\}_n = \{\tilde{P}\}_n \quad (3-45)$$



$$F_{BX} = (\rho dV) b_x$$

$$F_{IX} = (\rho - n \rho_f) dV \ddot{u}_x + n \rho_f dV \ddot{u}_x$$

Figure 3.1. Schematic depiction of total stress and virtual displacement field in x-direction.



$$\delta W_{IX}^* = - \delta \pi n dy dz (\dot{u}_x - \dot{u}_x) dt + \left(\delta \pi + \frac{\partial \delta \pi}{\partial x} dx \right) n dy dz$$

$$\cdot \left[\dot{u}_x + \frac{\partial \dot{u}_x}{\partial x} dx - \dot{u}_x + \frac{\partial \dot{u}_x}{\partial x} dx \right] dt$$

Figure 3.2. Schematic depiction of relative fluid velocity and complementary virtual fluid pressure field in x-direction.

SECTION 4

MPDAP VERIFICATION PROBLEMS

4.1. INTRODUCTION

The formulations described in Section 3 have been implemented in the two-dimensional multiphase finite element code MPDAP. Features of MPDAP include:

1. Special configurations to solve plane strain, axi-symmetric and spherically symmetric problems;
2. Both decoupled and fully coupled compressibility models. The simpler decoupled model treats the mixture and skeleton compressibilities independently (analogous to parallel springs). The fully coupled model includes the influence of grain compression due to pore pressure and the influence of effective stresses on the compressibility of the skeleton (see Blouin and Kim, 1984).
3. Nonlinear pore water and solid grain compressibility models (Kim, Blouin and Timian, 1986).
4. A variety of available material models describing the drained skeleton response. These include:
 - linear elastic;
 - decoupled nonlinear material model which treats volumetric and deviatoric shear response as independent (i.e. no dilatancy) (Kim, Blouin and Timian, 1986);
 - elasto-plastic material model with a nonlinear strength envelope (models dilatancy with an associated flow rule (Kim, Blouin and Timian, 1986); and
 - ARA three invariant plasticity model with strain hardening and softening (models dilatancy with a nonassociated flow rule) (Merkle and Dass, 1986).
5. Single phase, two phase (fully saturated) and three phase (partially saturated) capability;

6. Static, dynamic and quasi-static (consolidation) capability;

7. Calculation efficiency features including:

- a single point stress calculational technique for rapid computation of stresses, strains, and nonlinear constitutive properties (Kim, Blouin and Timian, 1986); and
- use of pore pressure at nodal points to efficiently compute relative pore fluid motions;

8. Nonlinear fluid friction model for both laminar and turbulent pore fluid flow conditions.

A users manual for MPDAP is included in Appendix A. This describes available options and input format.

In this section, we describe four problems used in the initial verification of MPDAP to check both the theoretical formulations and their numerical implementation. These include:

1. an undrained compressibility problem;
2. spherical wave propagation in an elastic single phase material;
3. a linear quasi-static consolidation problem;
4. two phase wave propagation in saturated soil and rock having linear elastic skeletons.

In these problems, the MPDAP calculations are compared with closed form solutions and/or numerical solutions generated with the code TPDAPII. TPDAPII is our previous two phase code, described by Kim, Blouin and Timian (1986), which does not have most of the advanced features incorporated into MPDAP.

4.2. VERIFICATION PROBLEM 1, CONSTRAINED COMPRESSIBILITY OF UNDRAINED SATURATED GRANULAR SOILS.

The first verification problem is to demonstrate analytically that the MPDAP formulations in Section 3 degenerate to the fully coupled solution (Blouin and Kim, 1984) for undrained uniaxial strain loadings as schematically shown in Figure 4.1.

To simplify the analytical derivation, three degrees of freedom are introduced; the first degree of freedom represents the solid skeleton displacement and the second and third degrees of freedom represent pore fluid pressures. Under uniaxial strain static undrained loading conditions, the general MPDAP formulation (Equation 3-39) degenerates to the following simple equation:

$$\begin{bmatrix} [K_T] & [C] \\ [C]^T & -[E] \end{bmatrix} \begin{Bmatrix} \{\Delta U\} \\ \{\Delta \pi\} \end{Bmatrix} = \begin{Bmatrix} \{P_U\} \\ \{P_K\} \end{Bmatrix} \quad (4-1)$$

For the single element with unit length, Equation 4-1 can be expressed as

$$\begin{bmatrix} K_S & \frac{1}{2}a & -\frac{1}{2}a \\ -\frac{1}{2}a & \frac{1}{3}\alpha' & \frac{1}{6}\alpha' \\ \frac{1}{2}a & -\frac{1}{6}\alpha' & -\frac{1}{3}\alpha' \end{bmatrix} \begin{Bmatrix} u_1 \\ \pi_2 = \pi_0 \\ \pi_3 = \pi_0 \end{Bmatrix} = \begin{Bmatrix} \sigma_v \\ 0 \\ 0 \end{Bmatrix} \quad (4-2)$$

where

$$a = 1 - \frac{K_S}{K_G} \quad (4-3)$$

$$\alpha' = \frac{1}{K_m} - \frac{K_s}{K_g^2} \quad (4-4)$$

M_s = constrained modulus of skeleton

u_1 = skeleton displacement

π_0 = pore fluid pressure

σ_v = applied total stress

Solving Equation 4-2 for the pore fluid pressure, we have

$$-\pi_0 = \sigma_v \frac{1}{a + \frac{\alpha'}{a} M_s} \quad (4-5)$$

Substitution of Equation 4-3 and 4-4 into 4-5 yields

$$-\pi_0 = \sigma_v \frac{1}{1 + \beta_m} \quad (4-6)$$

where

$$\beta_m = \frac{K_g^2 M_s + K_m K_s^2 - M_s K_m K_s - K_g K_m K_s}{K_m K_g (K_g - K_s)} \quad (4-7)$$

Equation 4-6 is identical to the closed form solution derived by Blouin and Kim (1984).

4.3. VERIFICATION PROBLEM 2, ELASTIC SPHERICAL WAVE PROPAGATION IN A SINGLE PHASE MEDIUM.

The purpose of this verification problem is to check the global equilibrium equations for the bulk mixture (Equation 3-23) in the one-dimensional spherical coordinate system when the pore fluid is not present.

Figure 4.2 shows a 12 inch hollow spherical hole in an infinite elastic medium subjected to a 100 psi internal step load. Material properties and time-steps used for the calculations are included in Figure 4.2. In Figure

4.3, radial stress profiles at 5.5 msec are plotted. The MPDAP calculations give good agreement with the closed form solution except for some smearing of stresses at the shock wave front. This smearing could be minimized by reducing the element and time step sizes.

4.4. VERIFICATION PROBLEM 3, ONE-DIMENSIONAL LINEAR CONSOLIDATION.

This verification problem is used to check the quasi-static flow portion of the MPDAP formulations against Terzaghi's closed form consolidation solution.

A fully saturated soil deposit is assumed to overlay a rigid impermeable base. The soil deposit is subjected to a step loading at the ground surface, which is assumed to be a free-draining boundary. The initial excess pore pressure distribution is assumed to be constant throughout the deposit. Twenty equally spaced 4-node elements are used with a non-dimensional time increment factor $\Delta T = 0.005$. Plotted in Figure 4.4 is the profile of the normalized excess pore water pressure at time factor $T = 0.5$, at which time about 75% of the excess pore pressure is dissipated on average throughout the soil deposit. The calculated excess pore water pressures show close agreement with Terzaghi's exact solution.

4.5. VERIFICATION PROBLEM 4, ONE-DIMENSIONAL WAVE PROPAGATION IN SATURATED LINEAR ELASTIC SOILS AND ROCKS.

Two series of one-dimensional calculations of a vertically propagating planar compression wave were performed using MPDAP on idealized saturated soil and rock. The input loading, as shown in Figure 4.5, was a short rise time triangular pulse with a peak stress of 5,000 psi and a positive phase duration of 10 msec. The loading pulse was applied to the saturated sand and rock having the properties listed in Figure 4.5. The load was applied to an impermeable boundary at the ground surface.

Three permeability values were used in each series of calculations on the two materials, 0.001, 0.1, and 1.0 in/s. Results of the MPDAP calculations are compared to identical calculations using TPDAPII in Figures 4.6 through

4.8 for the rock and 4.9 through 4.11 for the soil. Each series of calculations compares pore pressure and effective stress profiles from the TPDAPII and MPDAP calculations at times of 10 msec and 20 msec after application of the boundary stress. Each figure (parts a through d) shows the profiles for one of the three assumed permeabilities. The decoupled compressibility option in MPDAP was used because TPDAPII does not have a fully coupled compressibility model.

Overall, the comparisons between the two sets of calculations is excellent. As would be expected, effective stresses in the soil are very small compared to the pore pressures because of the high compressibility of the soil skeleton. The effective stresses in the rock are higher than the pore pressures because the rock skeleton is stiffer than the solid grain-pore water mixture.

The only major discrepancy occurred in the highest permeability soil calculations shown in Figure 4.11. In the MPDAP calculation, both pore pressure and effective stress profiles showed high frequency oscillations. These are believed to occur because of the high contrast between the soft skeleton stiffness and the stiff bulk mixture modulus. The high permeability, in effect, creates an even higher contrast between these two. Further analysis will be required to better define and correct this problem. For practical values of permeabilities (less than 0.1 in/s), the oscillations are not a problem.

The high frequency oscillations in some of the calculations at the impermeable ground surface may be associated with waves of the second kind. They occur in both the MPDAP and TPDAPII calculations and are most noticeable at the highest permeability, as would be expected for waves of the second kind.

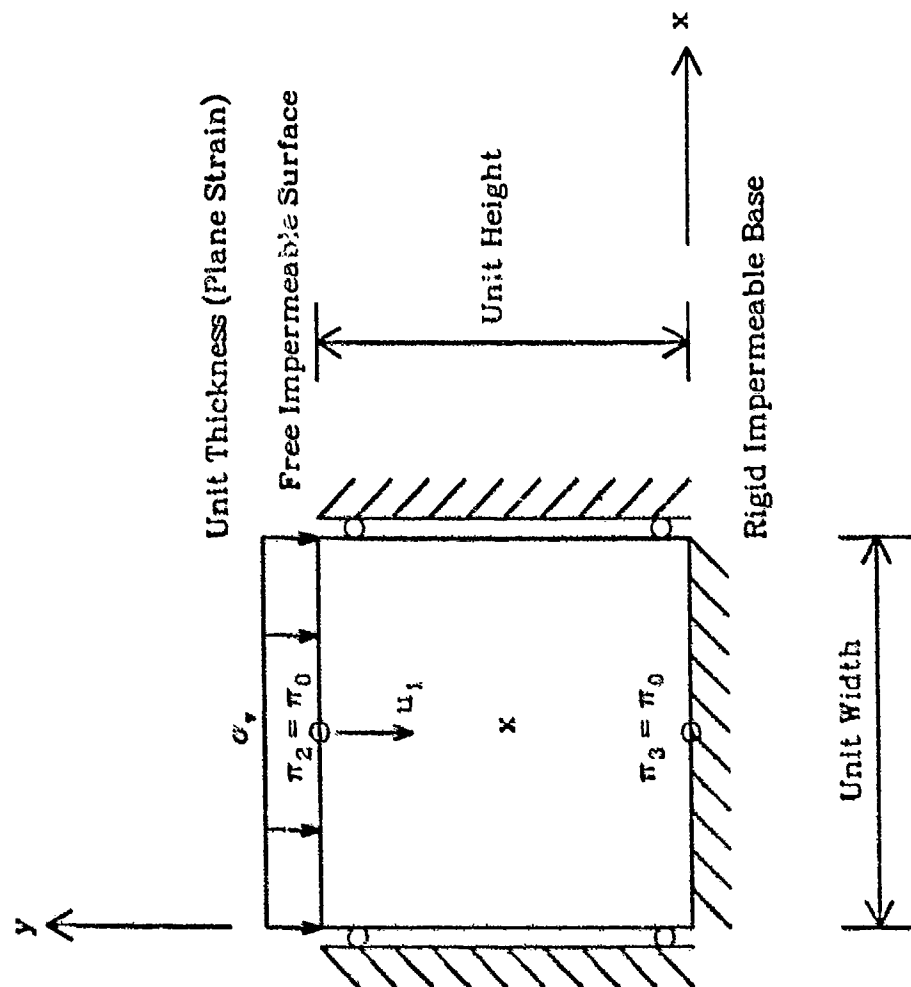
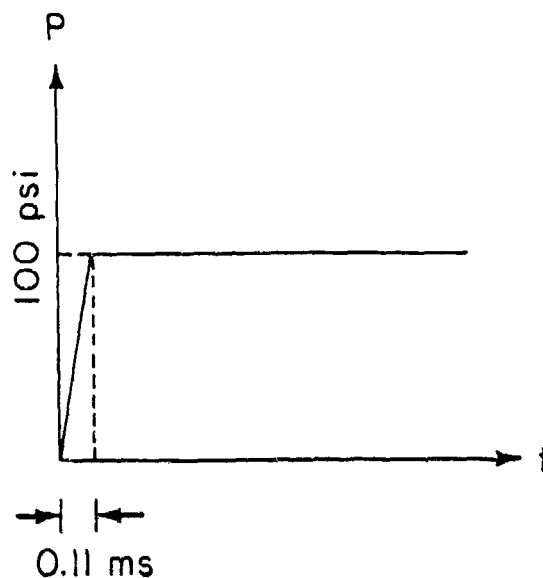
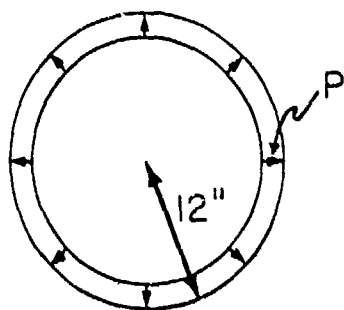


Figure 4.1. A single element subjected to undrained uniaxial strain loading.



Time Step

$$\Delta t = 0.022 \text{ Msec}$$

Young's Modulus

$$E = 12,457 \text{ psi}$$

Poisson's Ratio

$$\nu = 0.25$$

Mass Density

$$\rho = 1.88 \times 10^{-4} \text{ lb-sec}^2/\text{in}^4$$

Figure 4.2. Verification problem 2, elastic spherical wave propagation in one-phase medium.

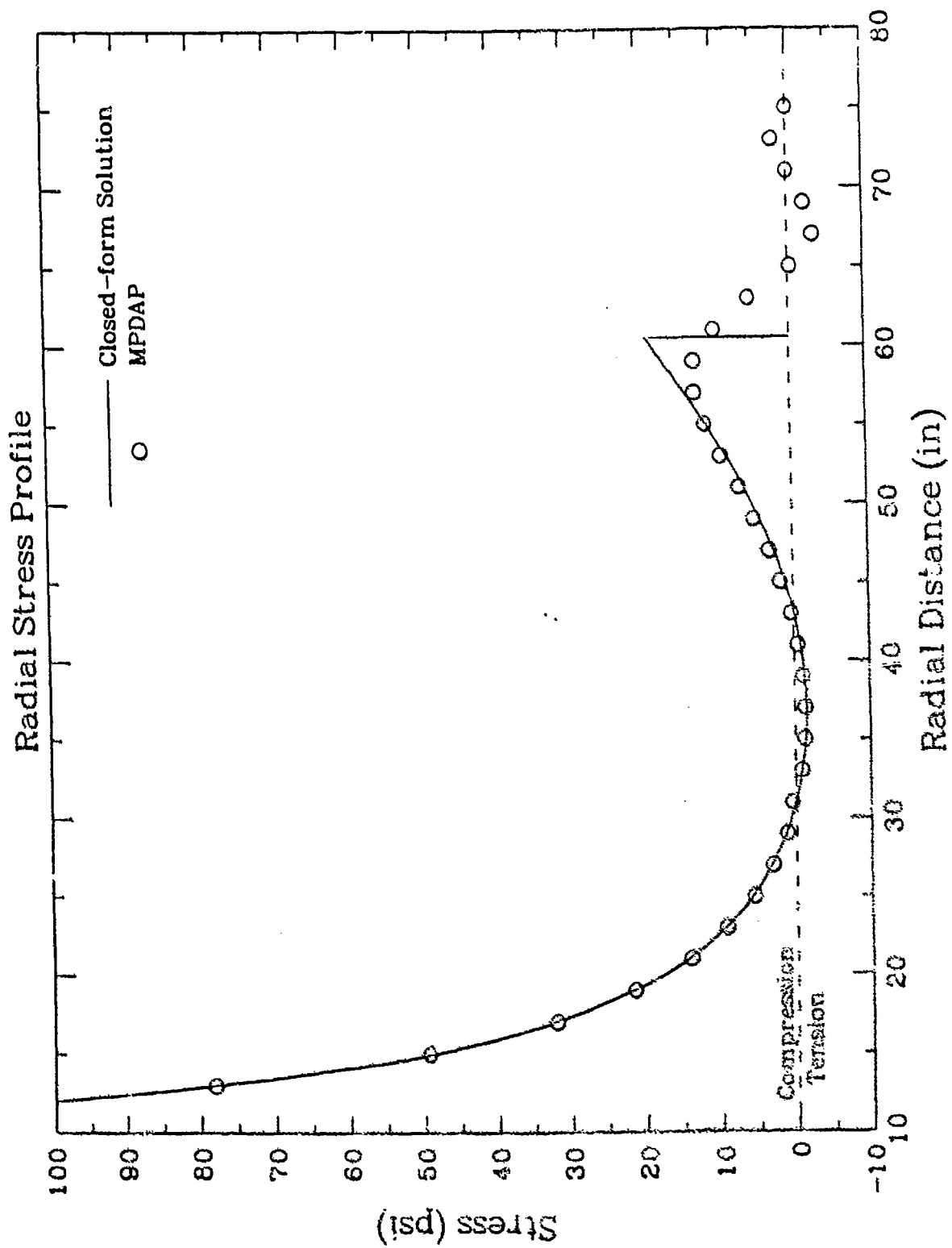


Figure 4.3. Radial stress profile at 5.5 msec, verification problem 2.

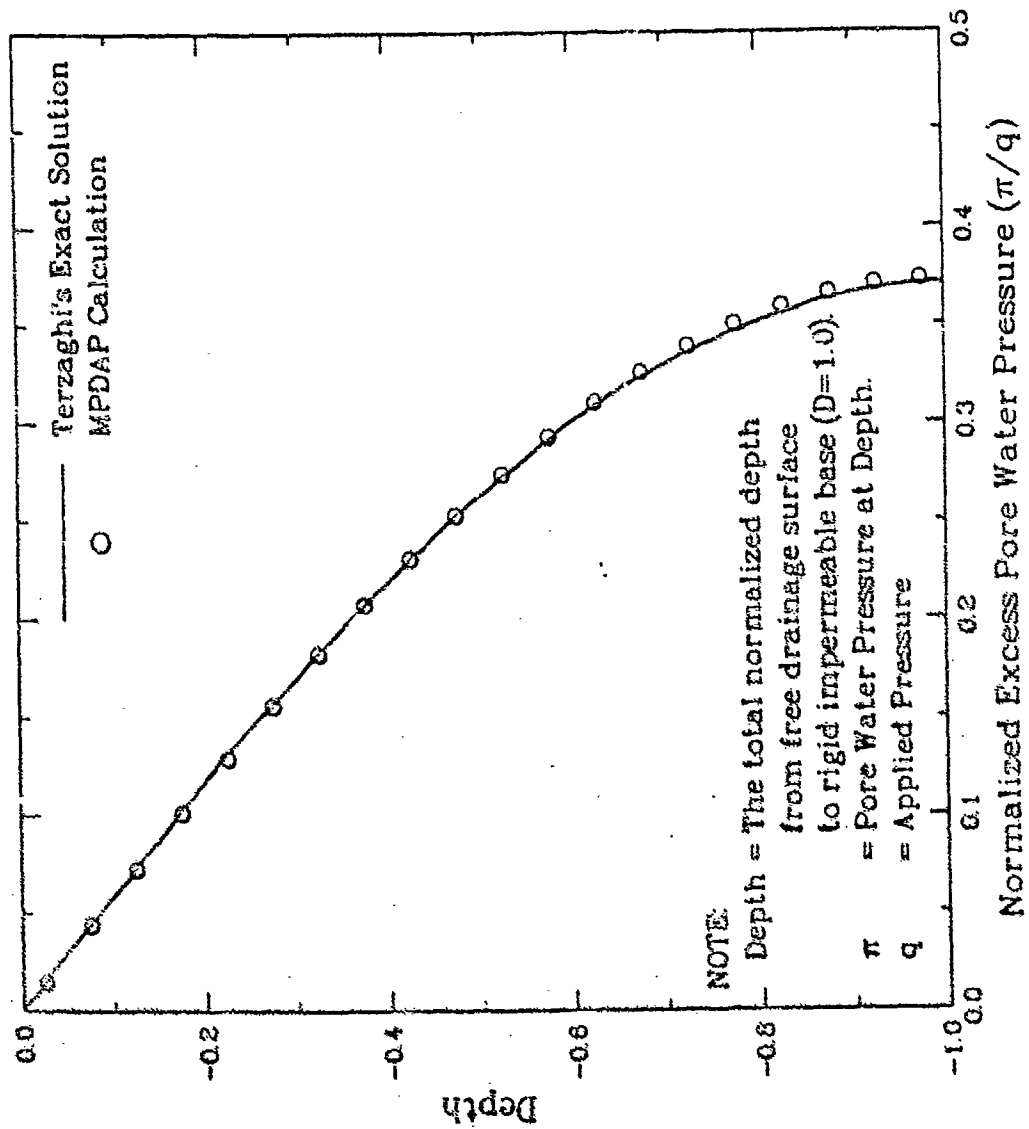
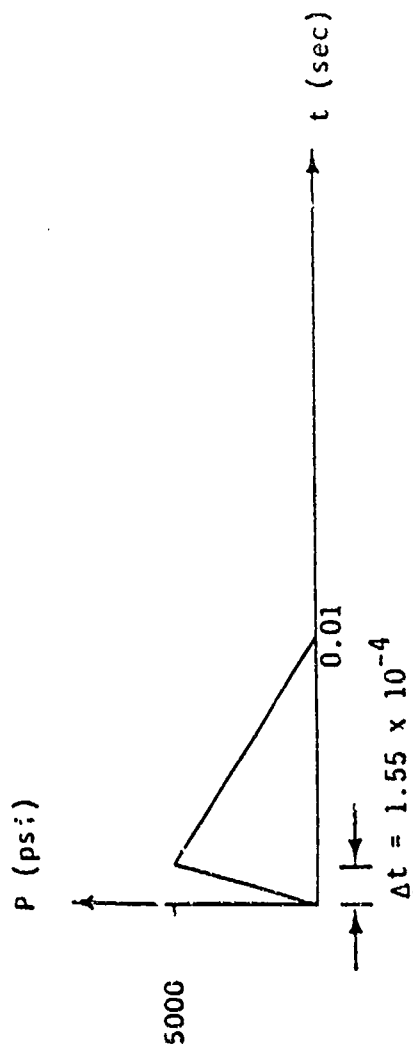


Figure 4.4. Normalized excess pore water pressure profiles at time factor $T = 0.5$, verification problem 3.



ASSUMED MATERIAL PROPERTIES

<u>Pore Water</u>	
Bulk Modulus	0.29×10^6 psi
<u>Solid Grains</u>	
Bulk Modulus	5.0×10^6 psi
Specific Gravity	2.67
<u>Drained Skeleton Properties</u>	
Bulk Modulus	3000 psi
Constrained Modulus	6000 psi
Poisson's Ratio	0.20
Porosity	0.35
<u>Permeability</u>	
	.001, 0.1, 1.0 in/s
<u>Soil</u>	
	$.625 \times 10^6$ psi
	1.250×10^6 psi
	0.20
	0.35
<u>Rock</u>	

Figure 4.5. Loading time history and material properties used in 1-D plane strain elastic wave propagation through saturated soil and rock.

TWO-PHASE DYNAMIC ANALYSIS (MPDAP VS TPDAP-II)
 $K = 0.001$ FOR ROCK AT 10 MSEC

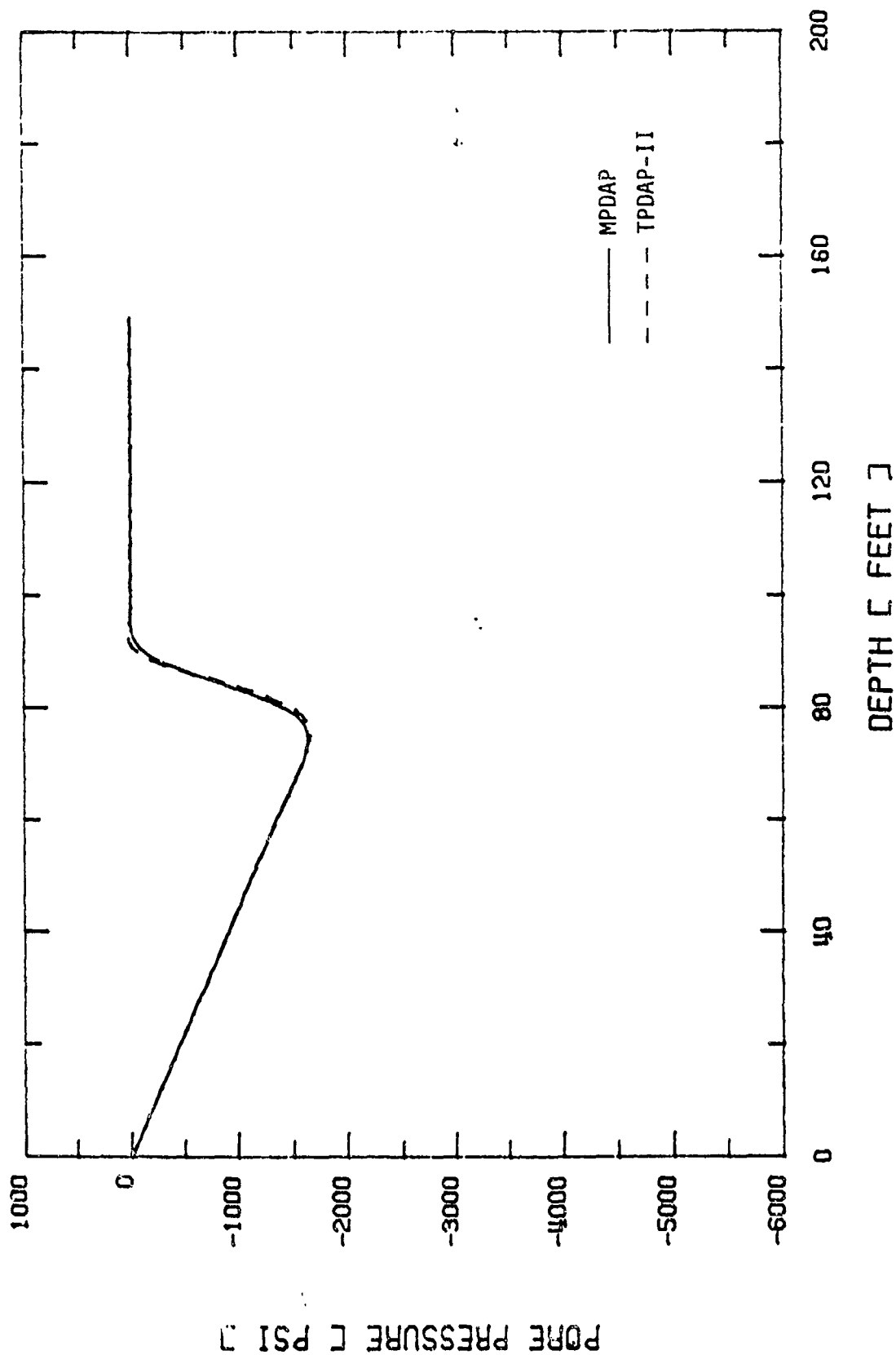


Figure 4.6a. Pore Fluid pressure profile at 10 msec, rock with $k = 0.001$ in/sec.

TWO-PHASE DYNAMIC ANALYSIS (MPDAP VS TPDAP-II)
 $K = 0.001$ FOR ROCK AT 10 MSEC

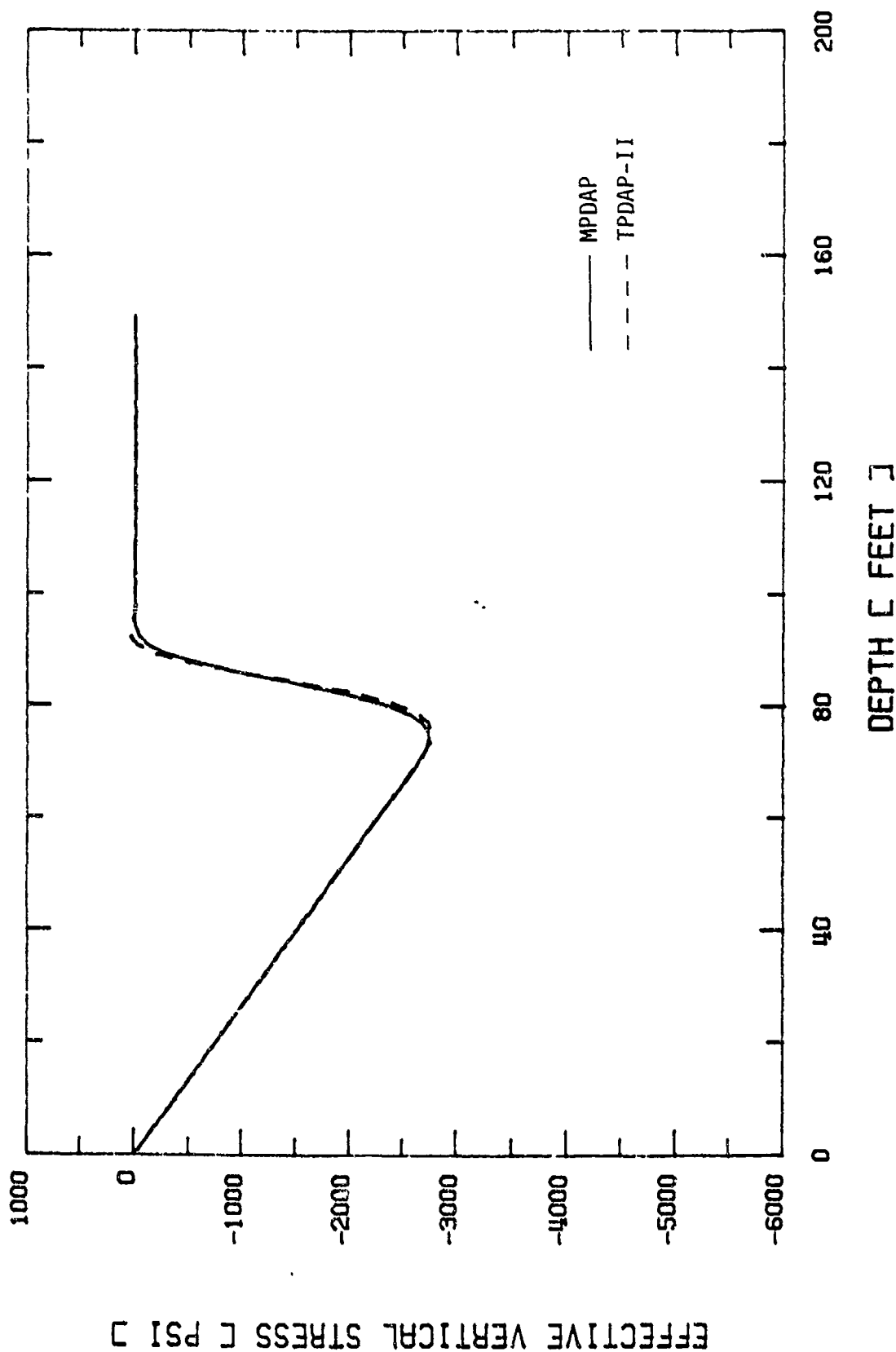


Figure 4.6b. Effective vertical stress profile at 10 msec, rock with $k = 0.001$ in/sec.

TWO-PHASE DYNAMIC ANALYSIS (MPDAP VS TPDAP-II)
 K = 0.001 FOR ROCK AT 20 MSEC

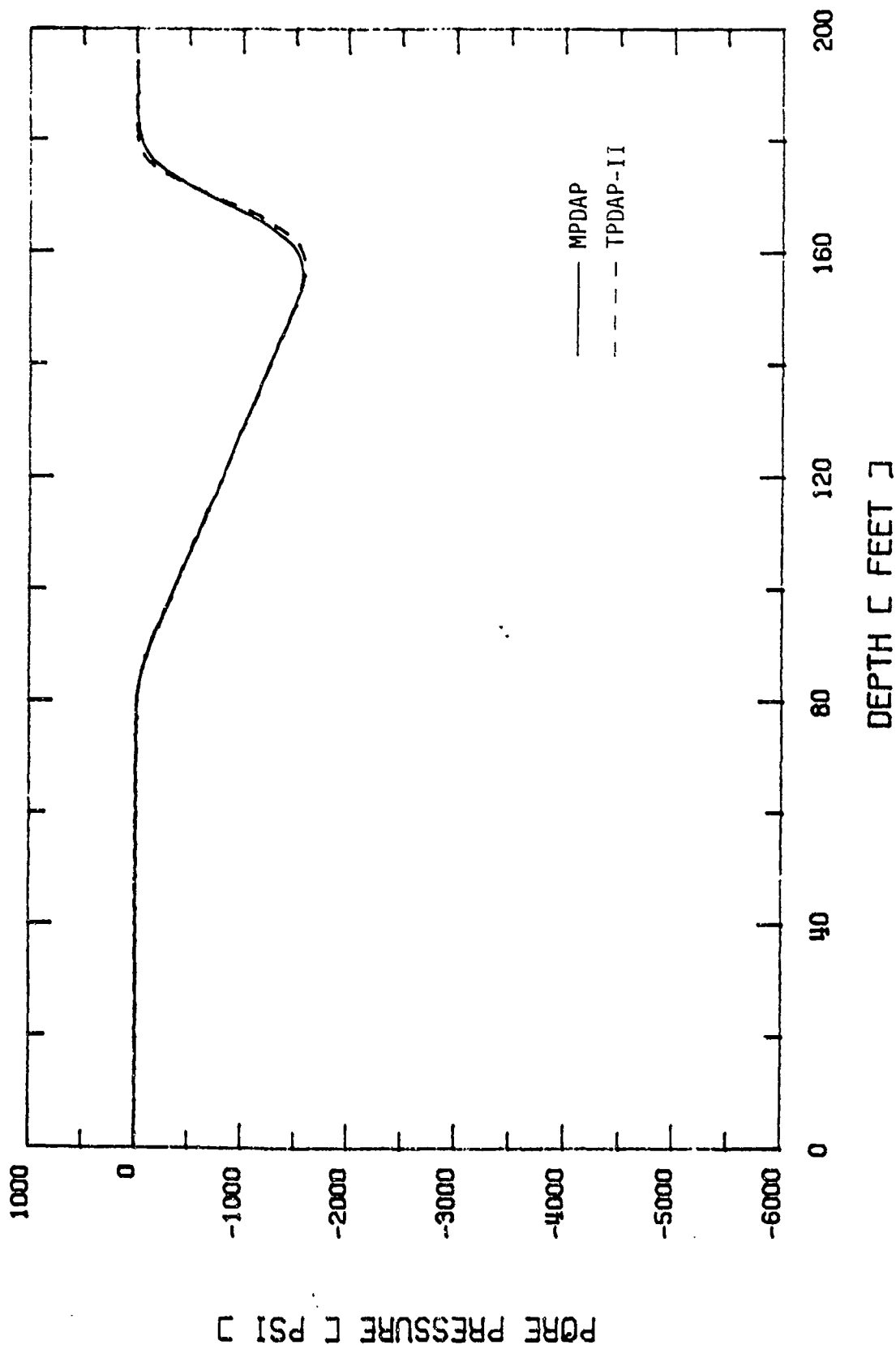


Figure 4.6c. Pore fluid pressure profile at 20 msec, rock with $k = 0.001$ in/sec.

TWO-PHASE DYNAMIC ANALYSIS (MPDAP VS TPDAP-II)
 $K = 0.001$ FOR ROCK AT 20 MSEC

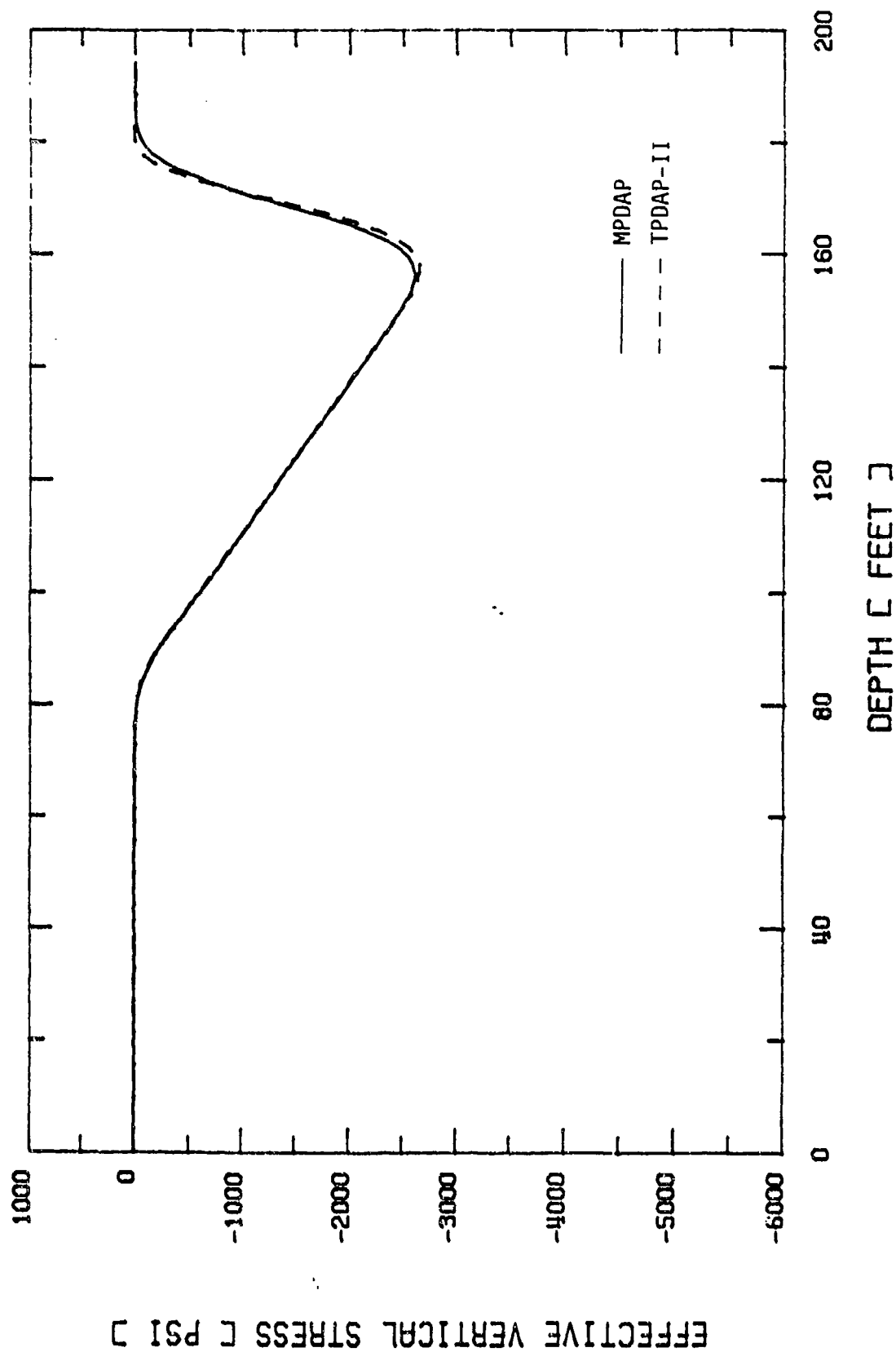


Figure 4.6d. Effective stress profile at 20 msec, rock with $k = 0.001$ in/sec.

TWO-PHASE DYNAMIC ANALYSIS (MPDAP VS TPDAP-II)
 $K = 0.1$ FOR ROCK AT 10 MSEC

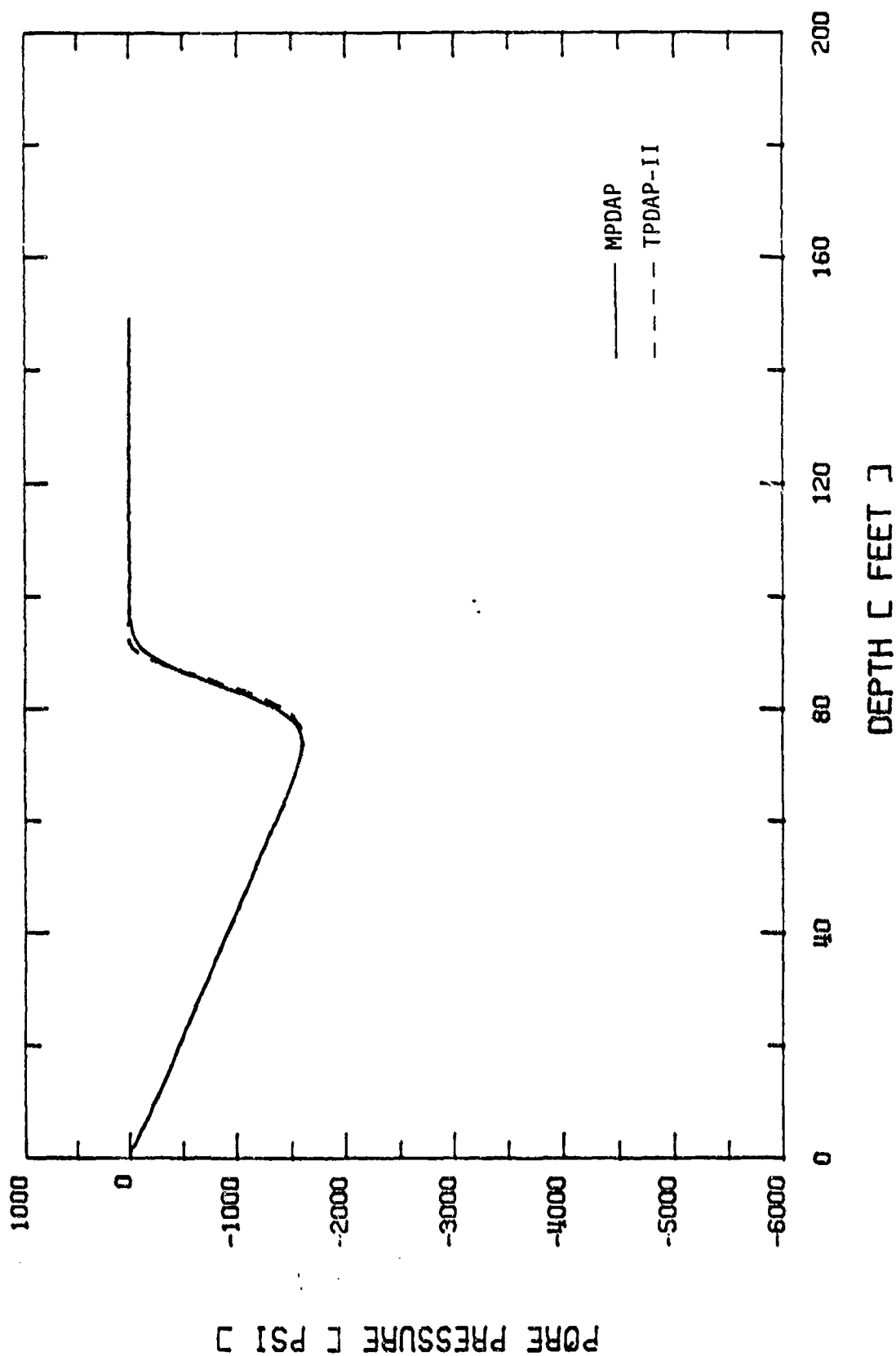


Figure 4.7a. Pore fluid pressure profile at 10 msec, rock with $k = 0.1$ in/sec.

TWO-PHASE DYNAMIC ANALYSIS (MPDAP VS TPDAP-II)
 K = 0.1 FOR ROCK AT 10 MSEC

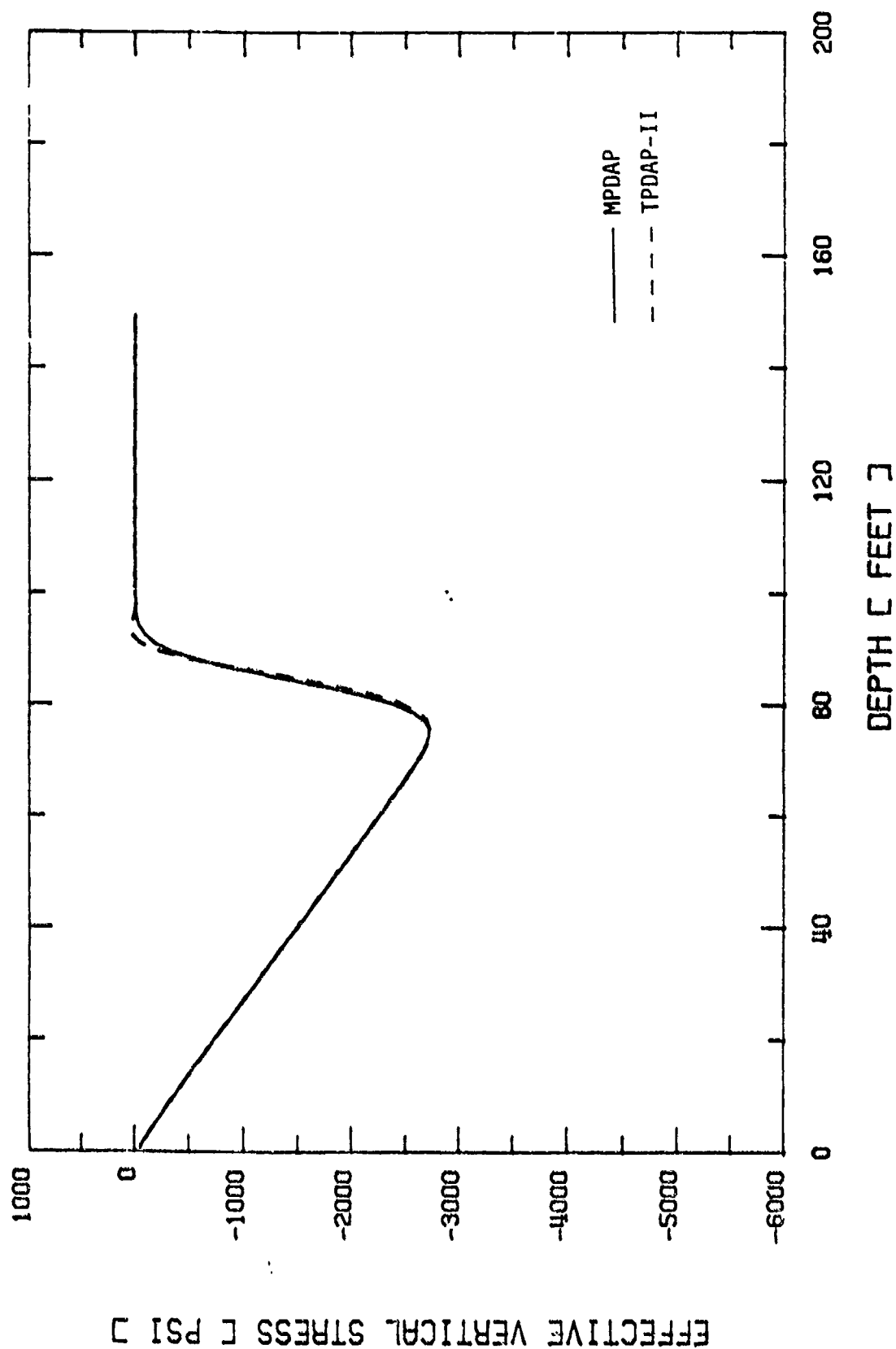


Figure 4.7b. Effective stress profile at 10 msec, rock with $k = 0.1$ in/sec.

TWO-PHASE DYNAMIC ANALYSIS (MPDAP VS TPDAP-II)
 K = 0.1 FOR ROCK AT 20 MSEC

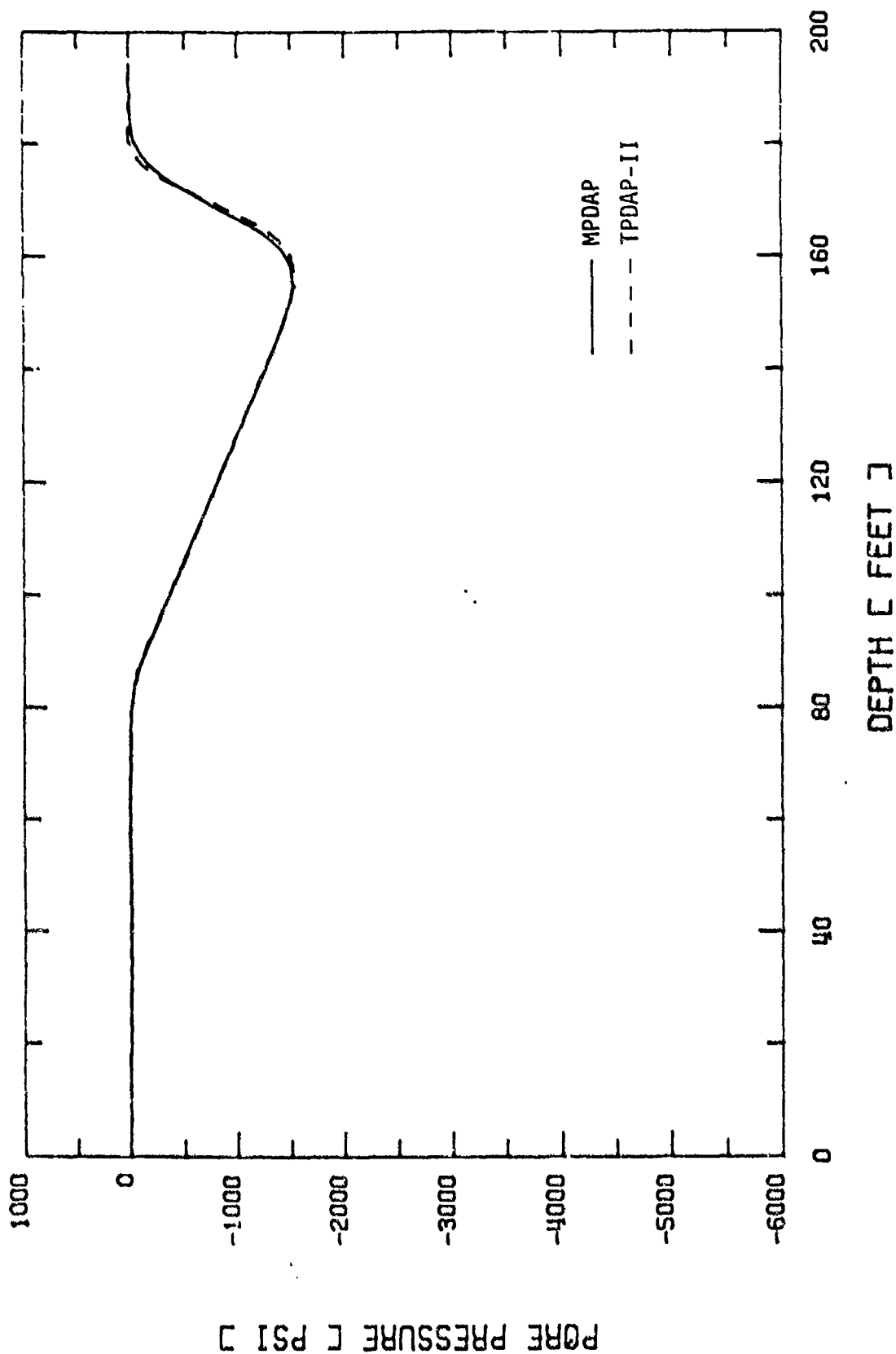


Figure 4.7c. Pore fluid pressure profile at 20 msec, rock with $k = 0.1$ in/sec.

TWO-PHASE DYNAMIC ANALYSIS (MPDAP VS TPDAP-II)
 $K = 0.1$ FOR ROCK AT 20 MSEC

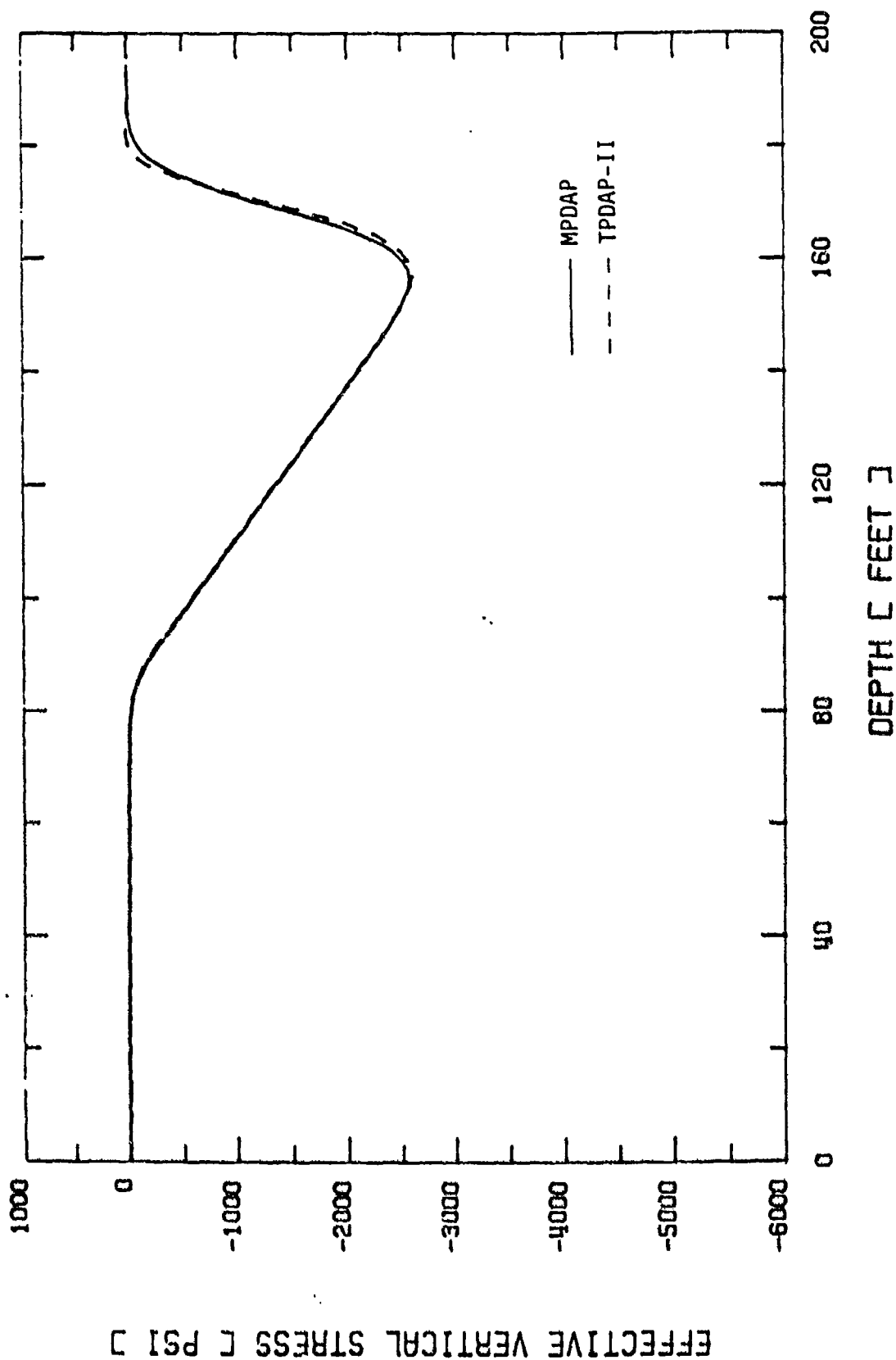


Figure 4.7d. Effective stress profile at 20 msec, rock with $k = 0.1$ in/sec.

TWO-PHASE DYNAMIC ANALYSIS (MPDAP VS TPDAP-II)
 $K = 1.0$ FOR ROCK AT 10 MSEC

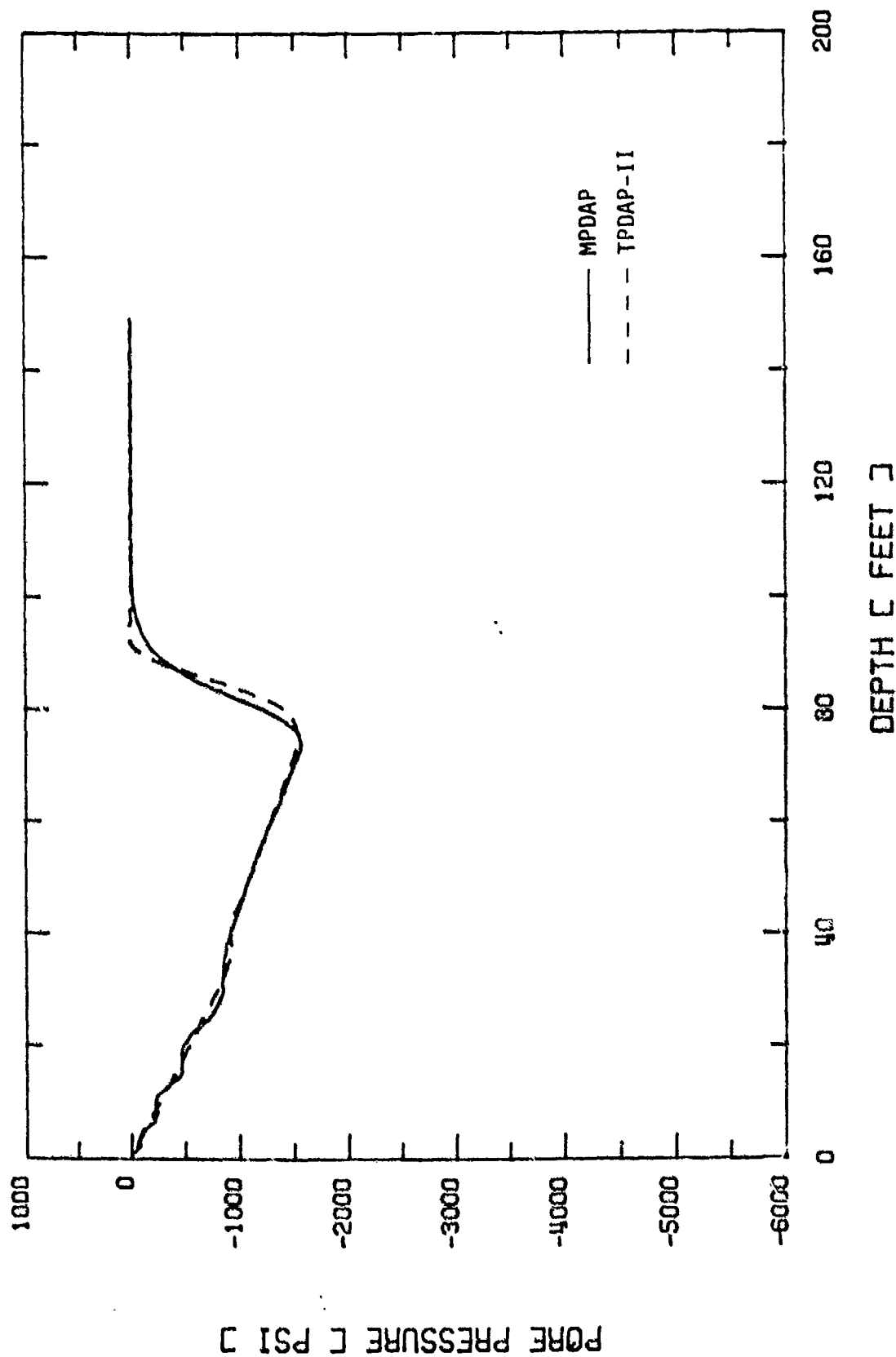


Figure 4.6a. Pore fluid pressure profile at 10 msec, rock with $k = 1.0$ in/sec.

TWO-PHASE DYNAMIC ANALYSIS (MPDAP VS TPDAP-II)
 $K = 1.0$ FOR ROCK AT 10 MSEC

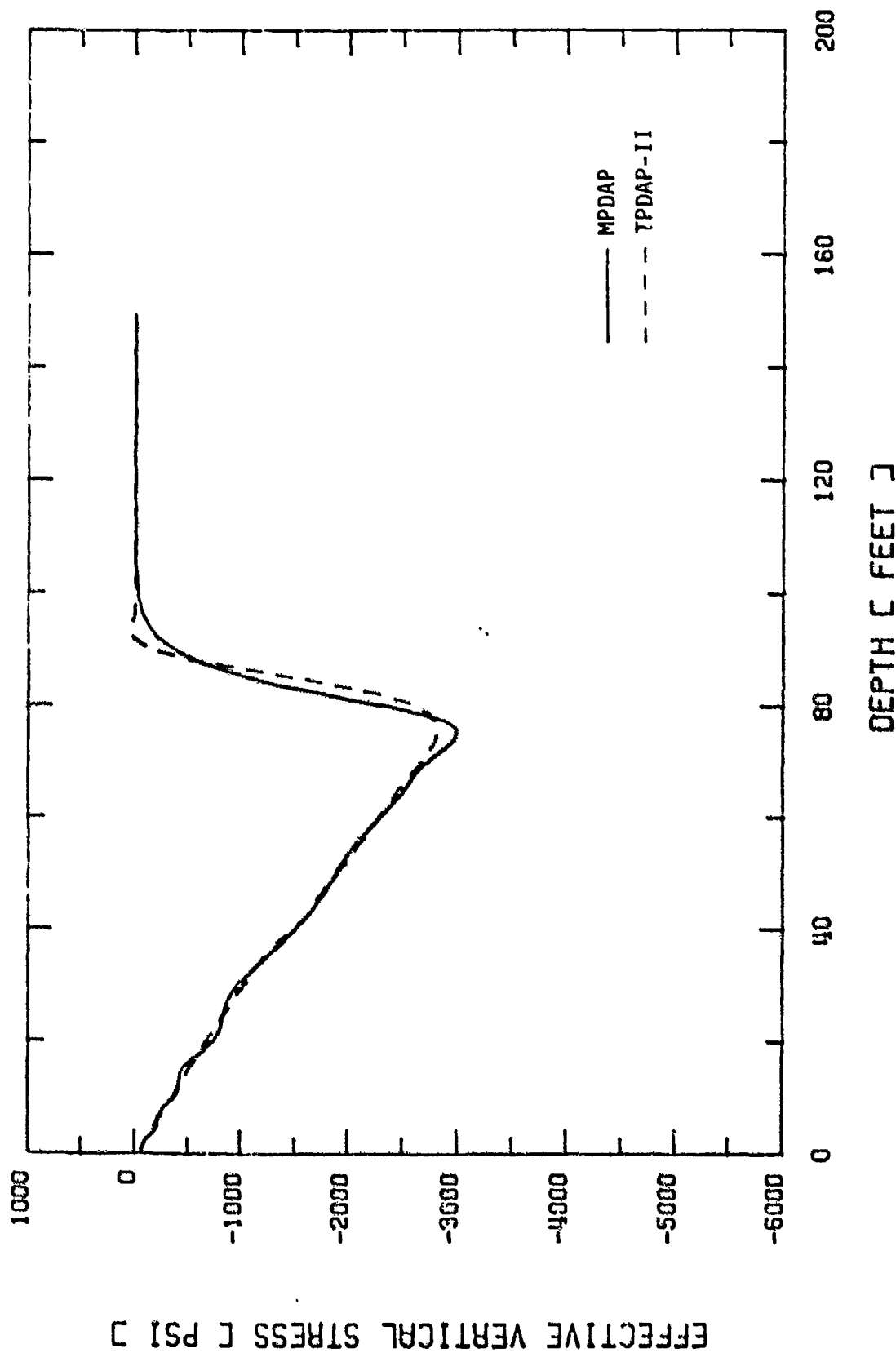


Figure 4.8b. Effective stress profile at 10 msec, rock with $k = 1.0$ in/sec.

TWO-PHASE DYNAMIC ANALYSIS (MPDAP VS TPDAP-II)
 $K = 1.0$ FOR ROCK AT 20 MSEC

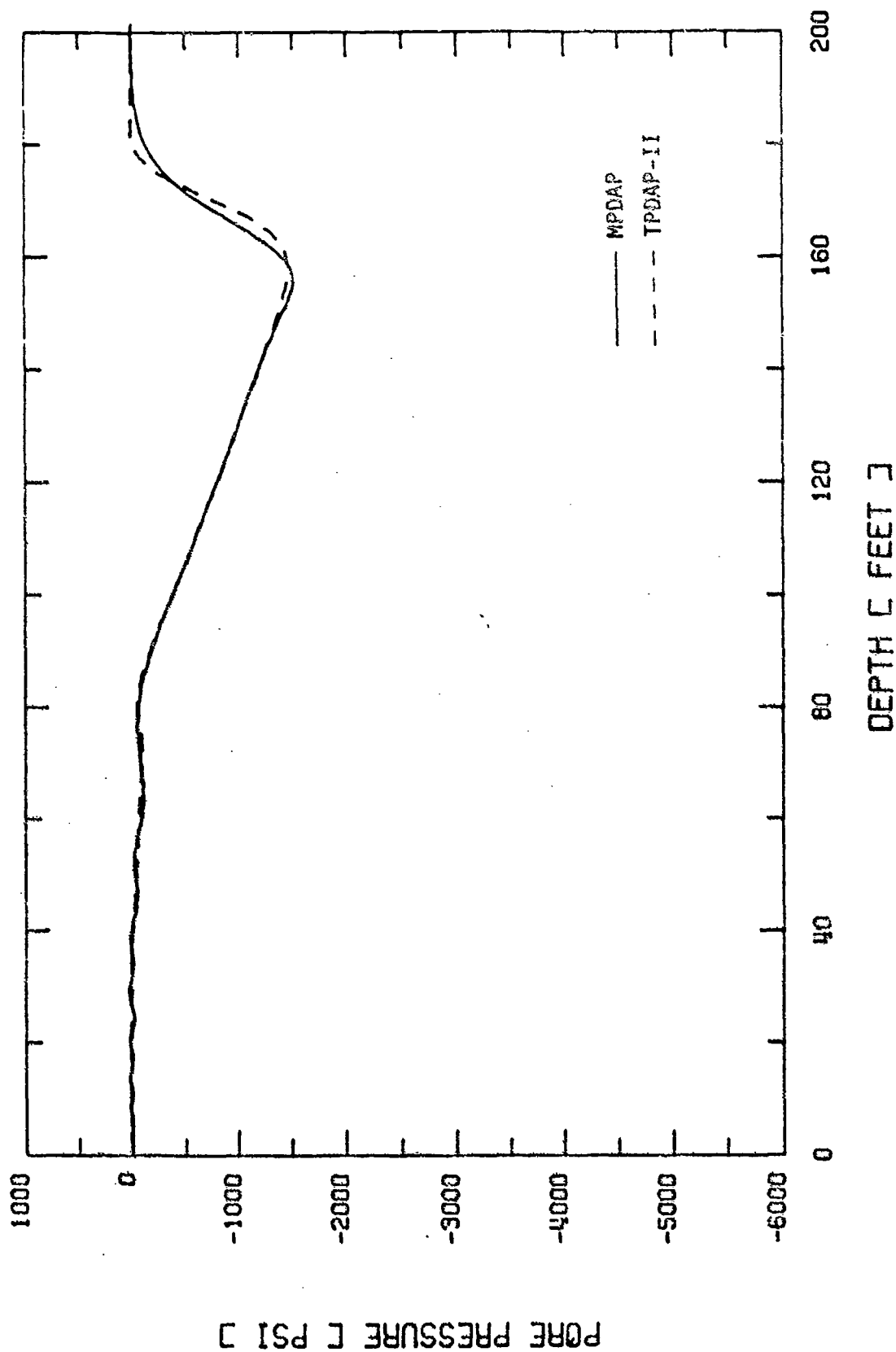


Figure 4.8c. Pore fluid pressure profile at 20 msec, rock with $k = 1.0$ in/sec.

TWO-PHASE DYNAMIC ANALYSIS (MPDAP VS TPDAP-II)
 $K = 1.0$ FOR ROCK AT 20 MSEC

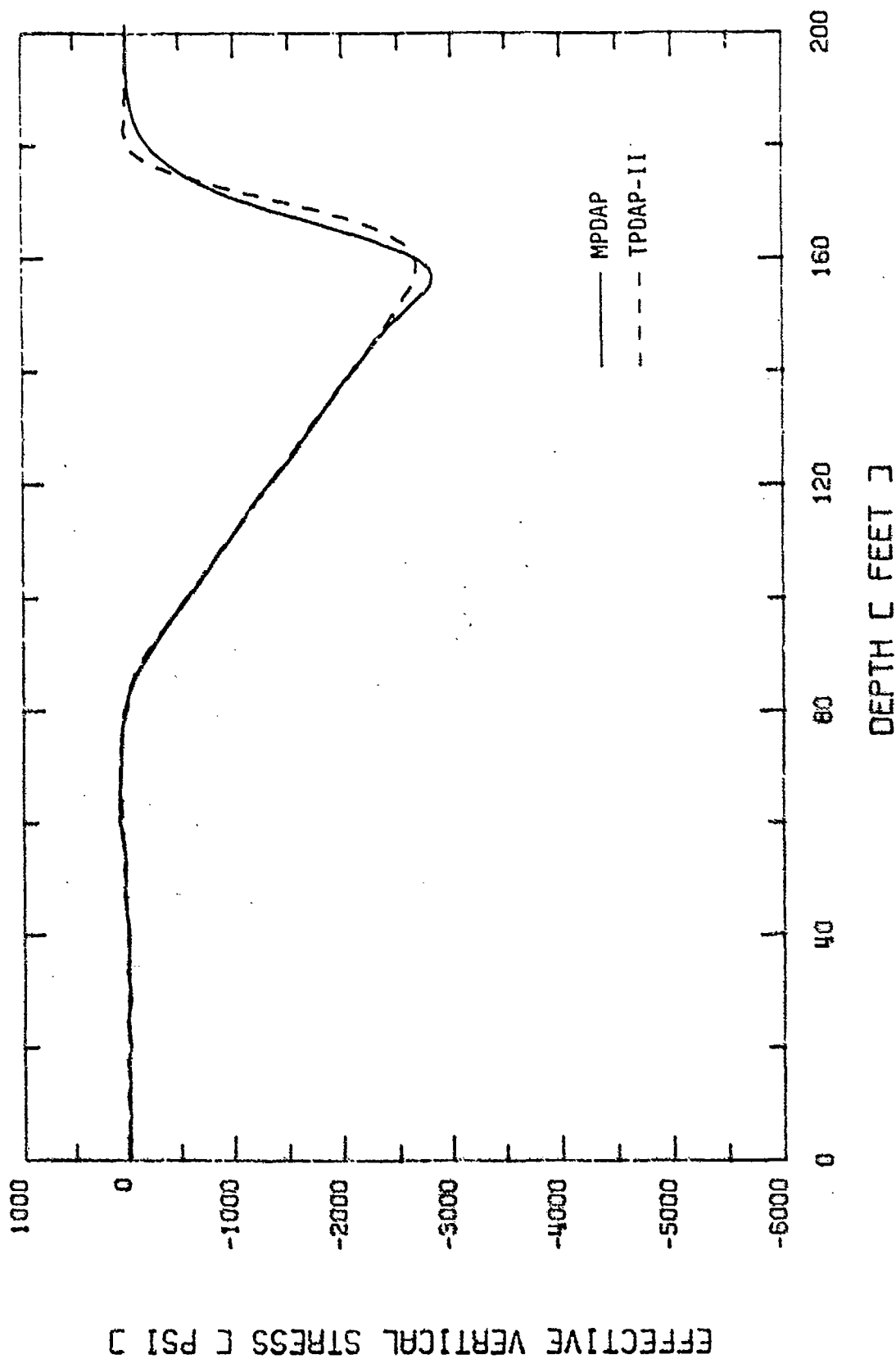


Figure 4.8d. Effective stress profile at 20 msec, rock with $k = 1.0$ in/sec.

TWO-PHASE DYNAMIC ANALYSIS (MPDAP VS TPDAP-II)
 $k = 0.001$ FOR SOILS AT 10 MSEC

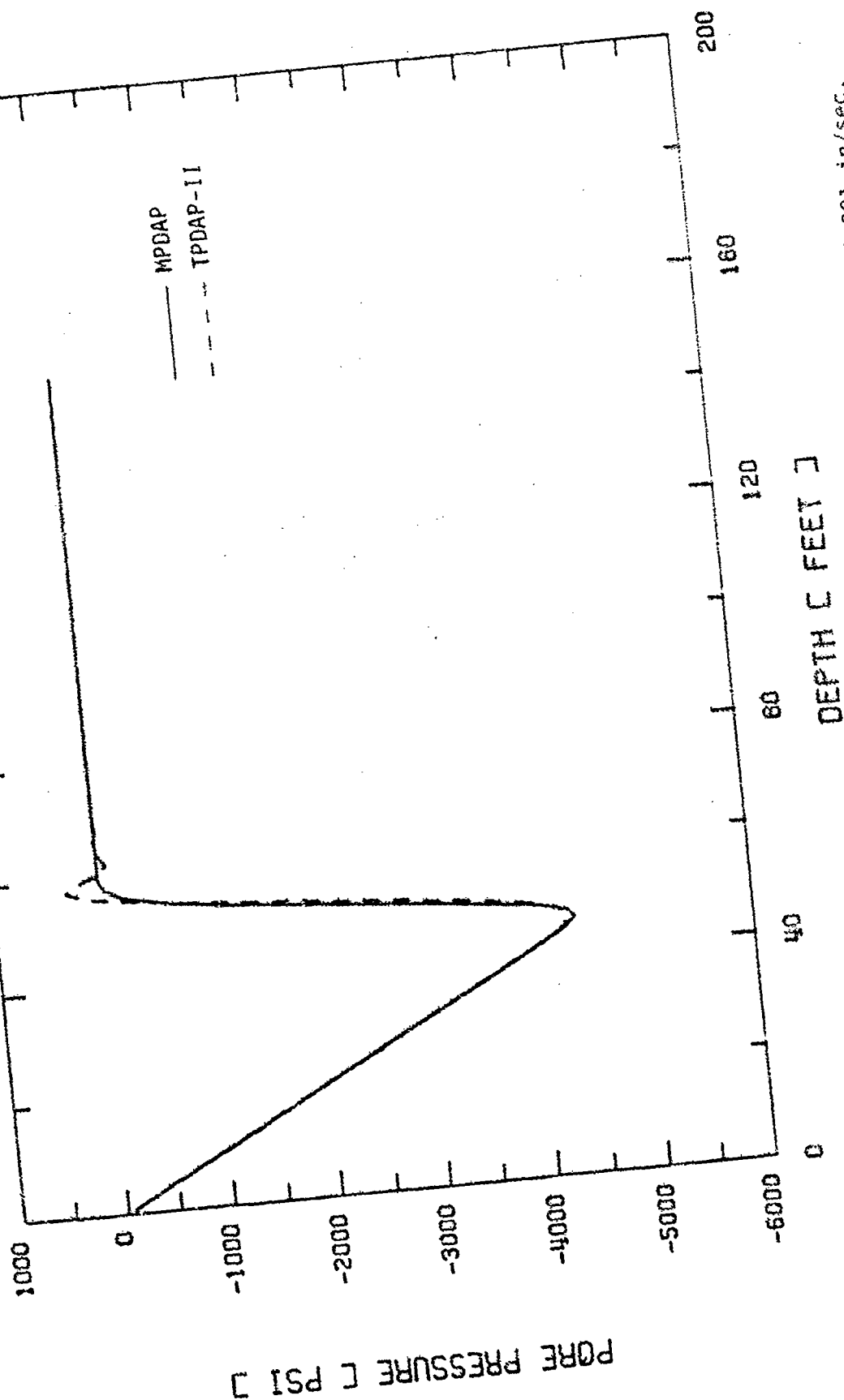


Figure 4.9a. Pore fluid pressure profile at 10 msec, soil with $k = 0.001$ in/sec.

TWO-PHASE DYNAMIC ANALYSIS (MPDAP VS TPDAP-II)
 $K = 0.001$ FOR SOILS AT 10 MSEC

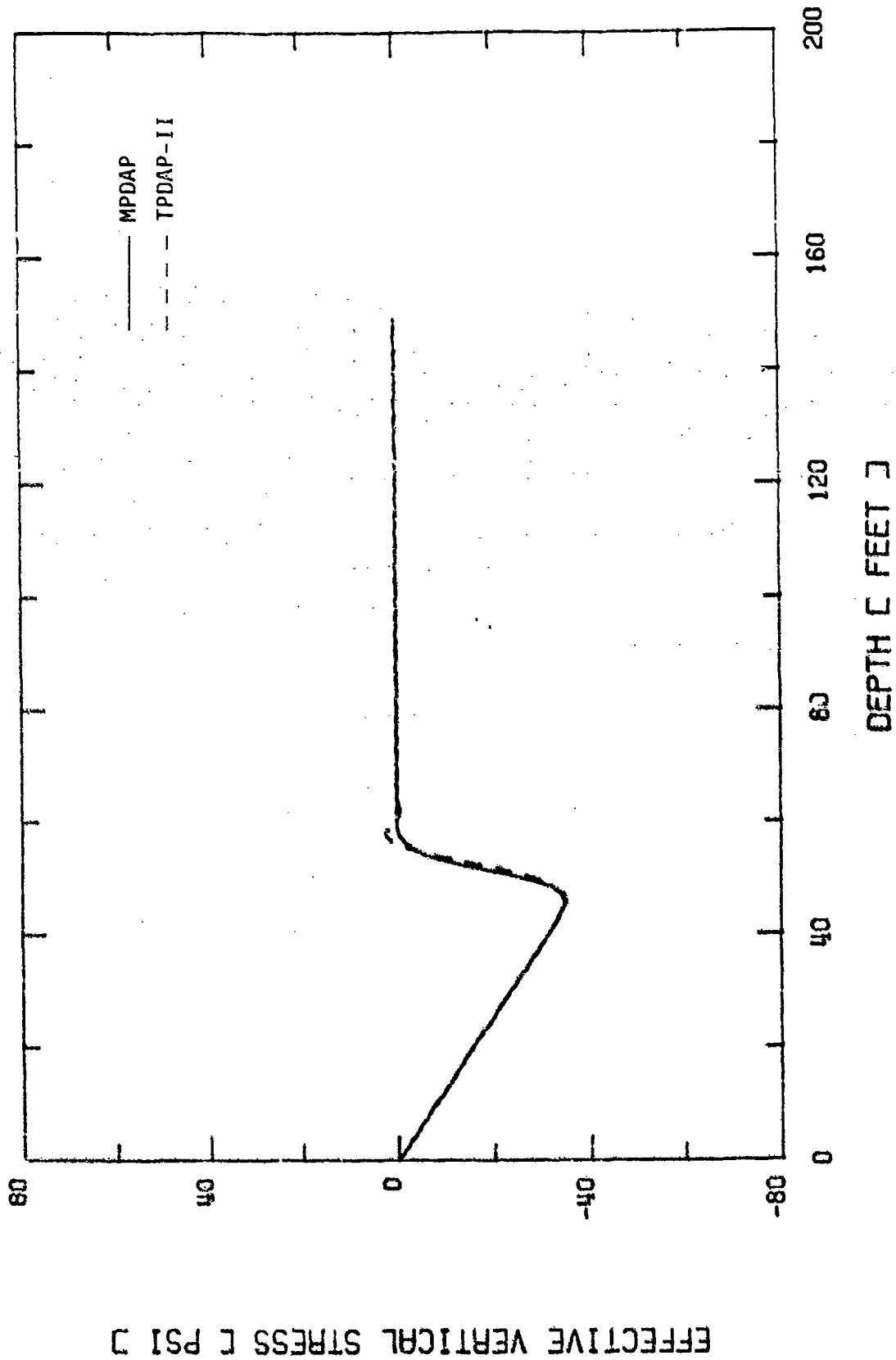


Figure 4.9b. Effective stress profile at 10 msec, soil with $k = 0.001$ in/sec.

TWO-PHASE DYNAMIC ANALYSIS (MPDAP VS TPDAP-II)
 $K = 0.001$ FOR SOILS AT 20 MSEC

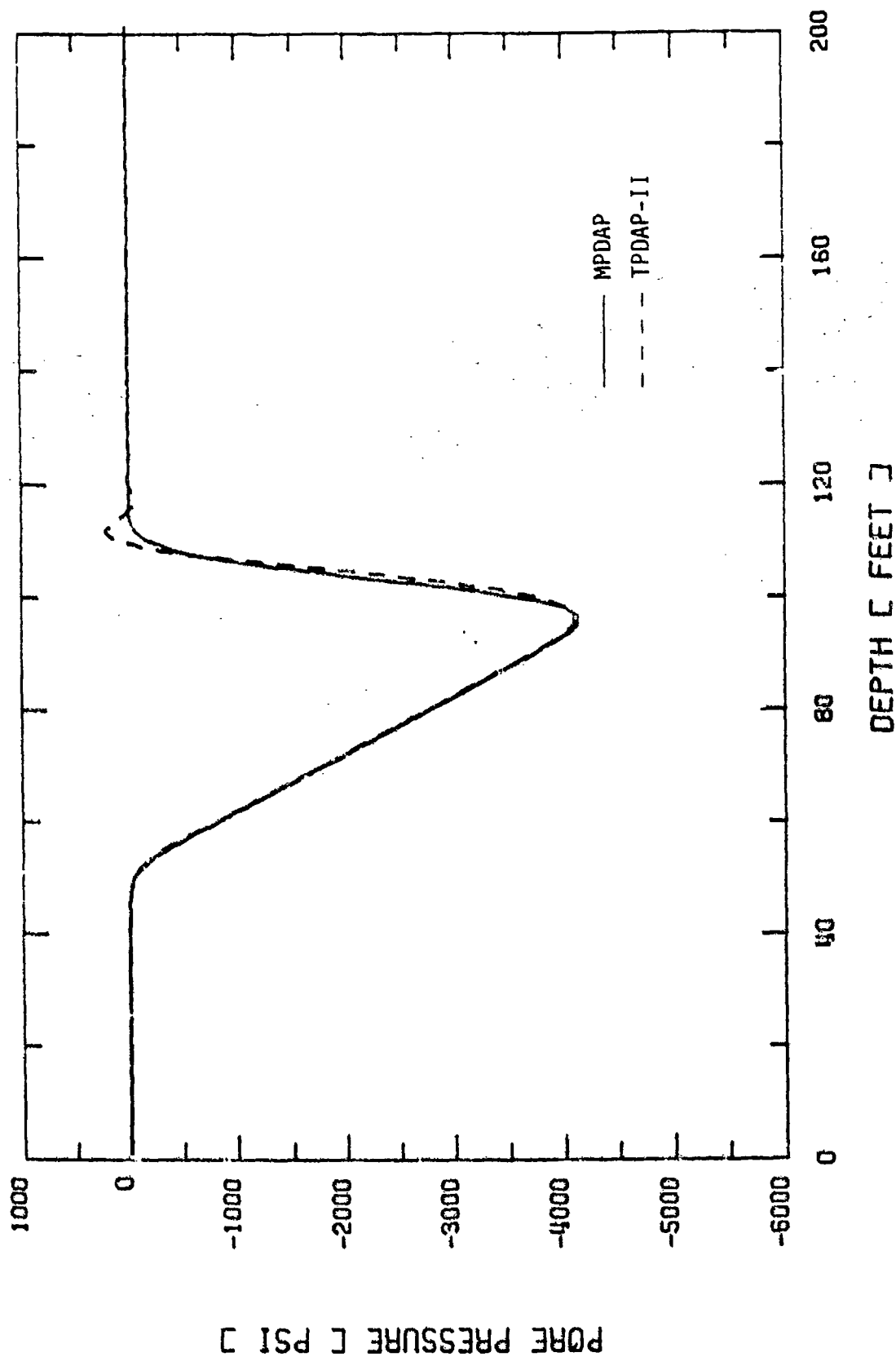


Figure 4.9c. Pore fluid pressure profile at 20 msec, soil with $k = 0.001$ in/sec.

TWO-PHASE DYNAMIC ANALYSIS (MPDAP VS TPDAP-II)
 $K = 0.001$ FOR SOILS AT 20 MSEC

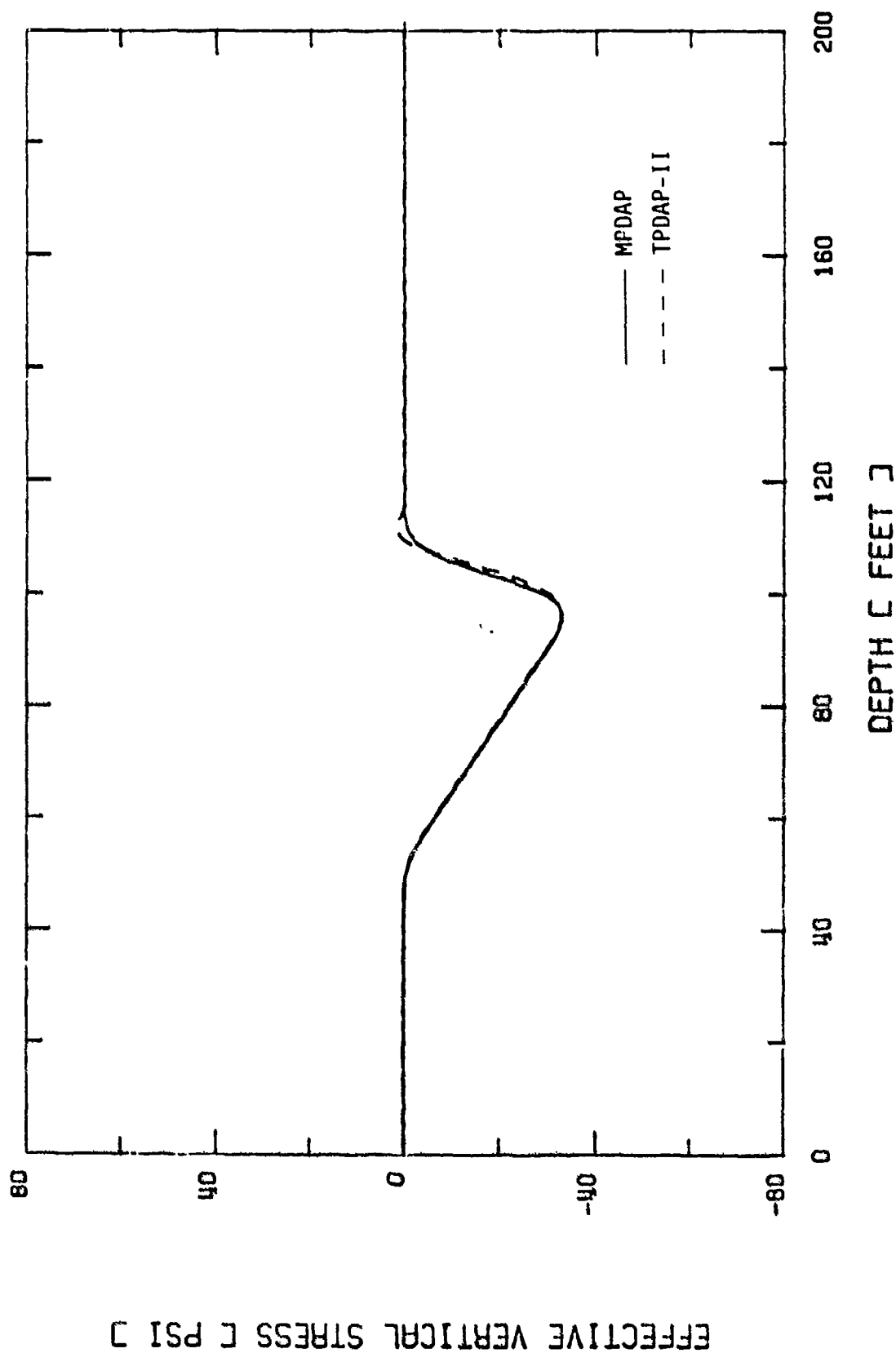


Figure 4.9d. Effective stress profile at 20 msec, soil with $k = 0.001$ in/sec.

TWO-PHASE DYNAMIC ANALYSIS (MPDAP VS TPDAP-II)
 K = 0.1 FOR SOILS AT 10 MSEC

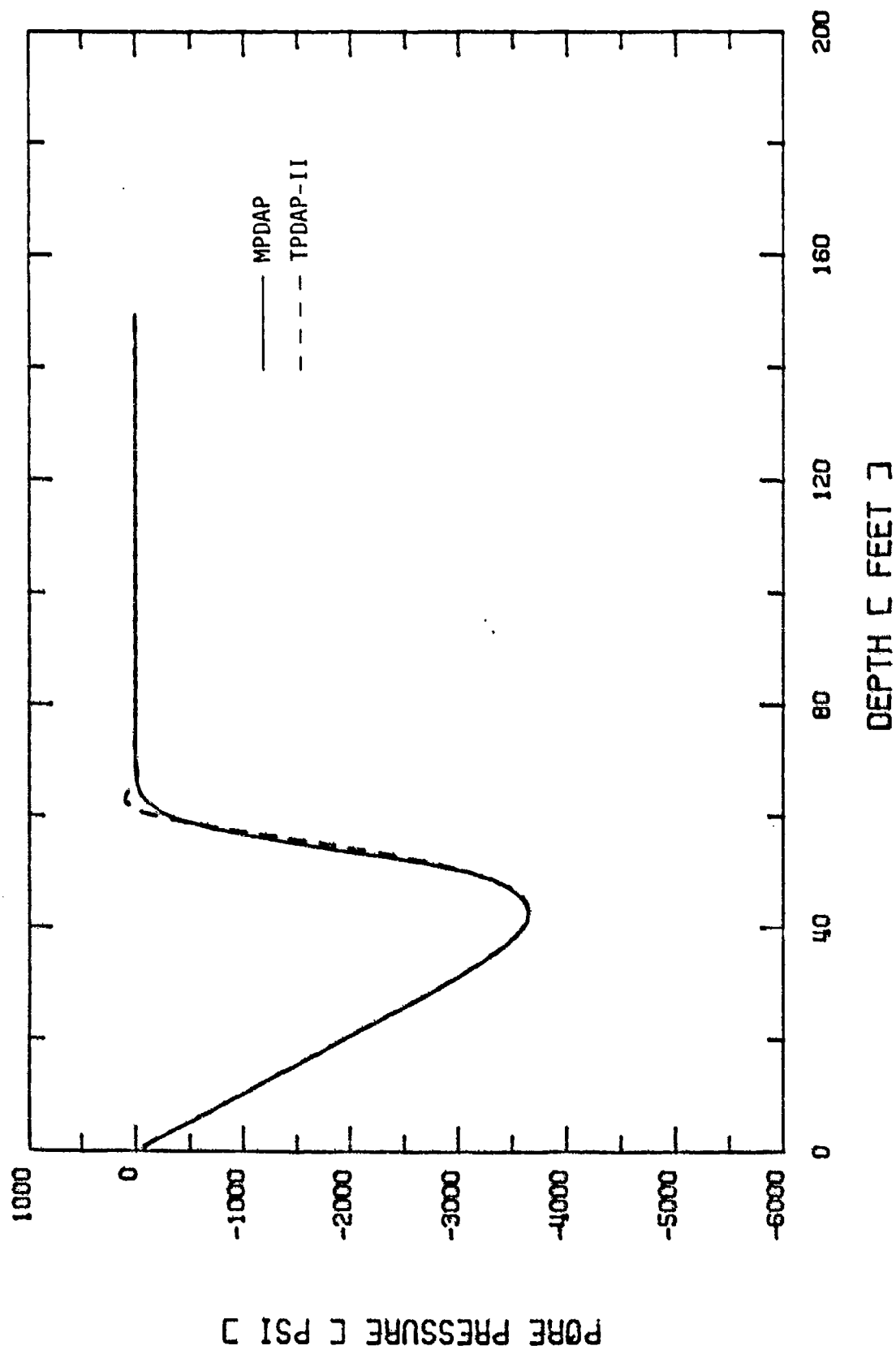


Figure 4.10a. Pore fluid pressure profile at 10 msec, soil with $k = 0.1$ in/sec.

TWO-PHASE DYNAMIC ANALYSIS (MPDAP VS TPDAP-II)
 $K = 0.1$ FOR SOILS AT 10 MSEC

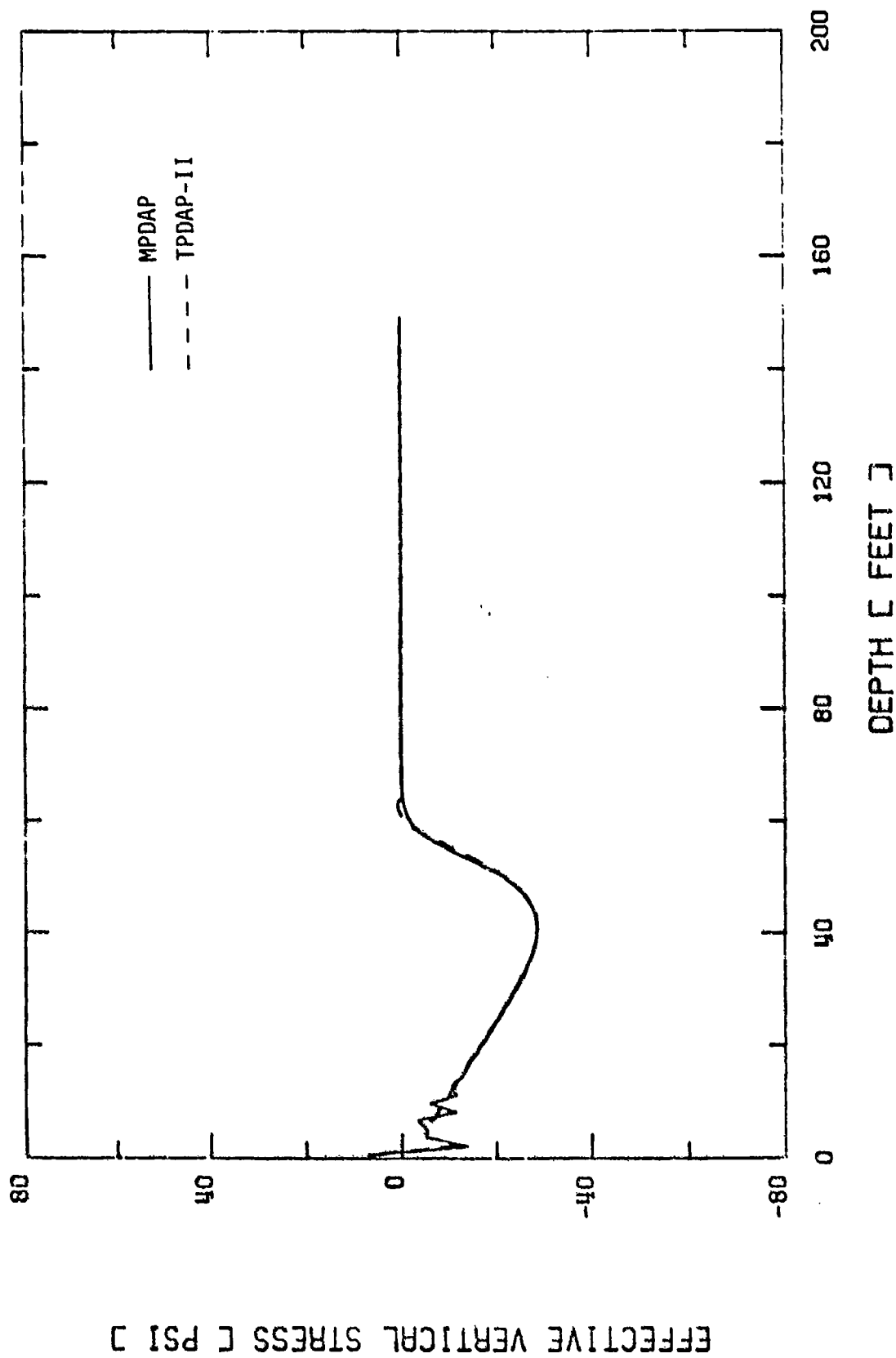


Figure 4.10b. Effective stress profile at 10 msec, soil with $k = 0.1$ in/sec.

TWO-PHASE DYNAMIC ANALYSIS (MPDAP VS TPDAP-II)
 $K = 0.1$ FOR SOILS AT 20 MSEC

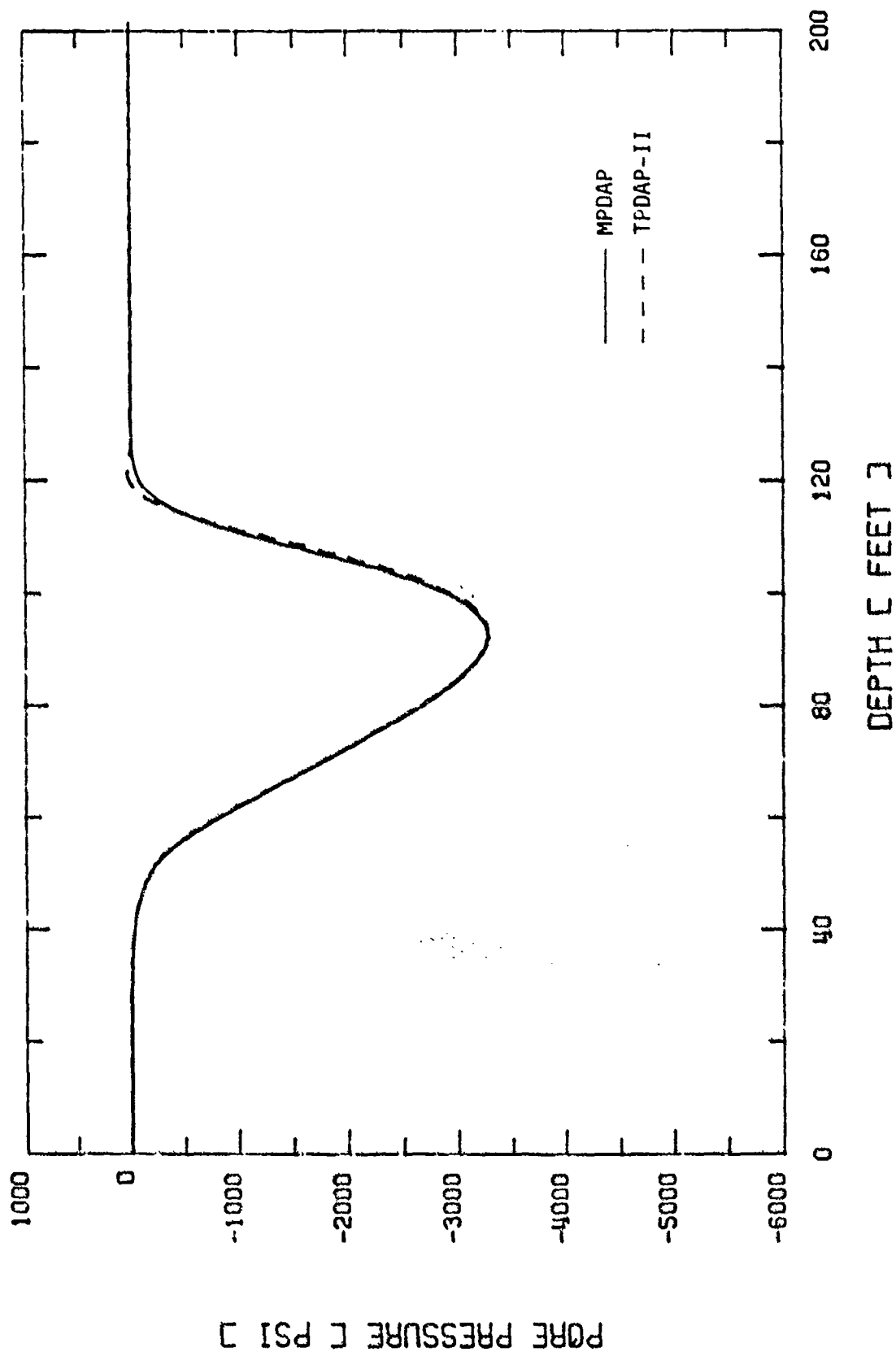


Figure 4.10c. Pore fluid pressure profile at 20 msec, soil with $k = 0.1$ in/sec.

TWO-PHASE DYNAMIC ANALYSIS (MPDAP VS TPDAP-II)
 $K = 0.1$ FOR SOILS AT 20 MSEC

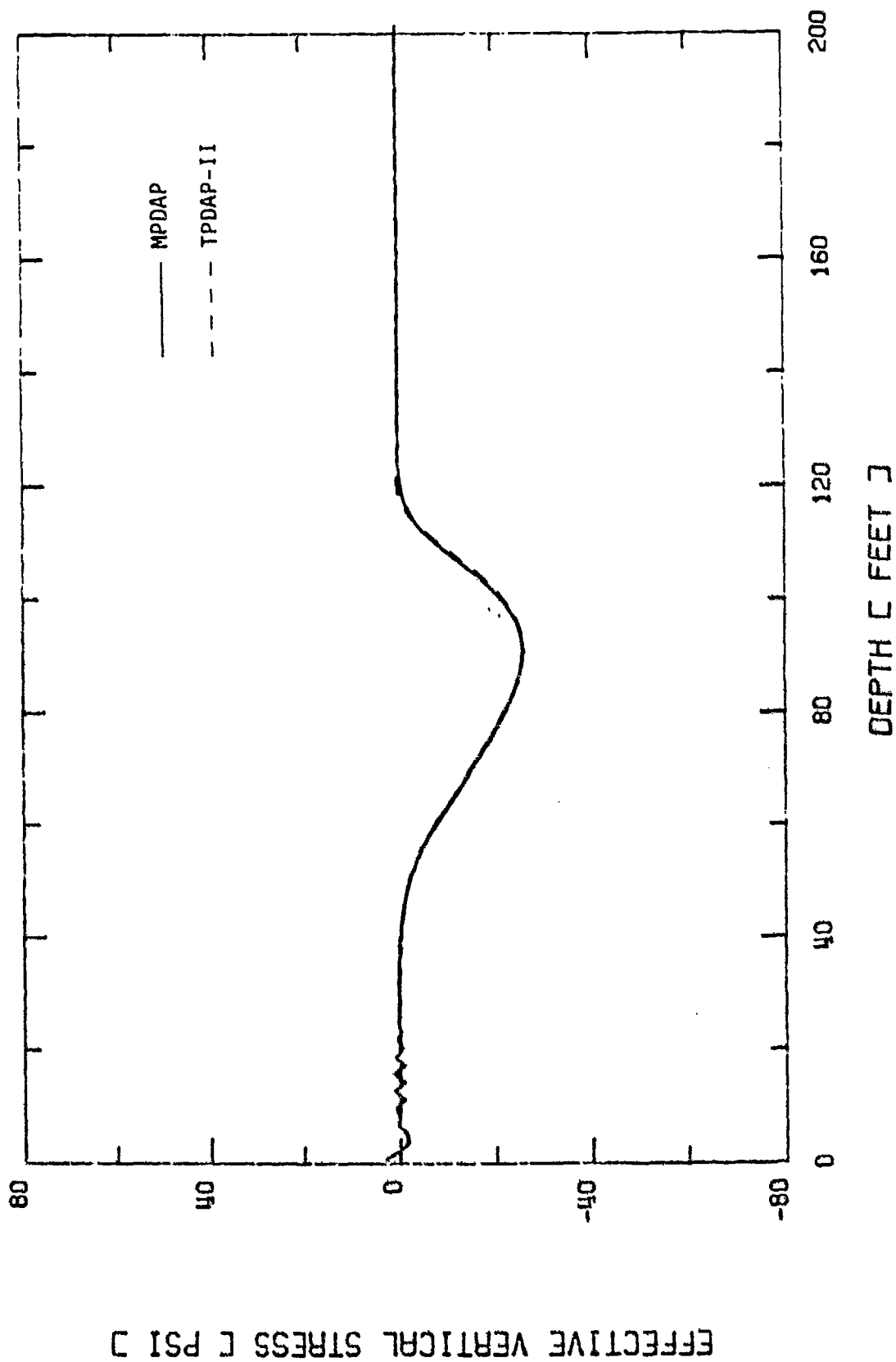


Figure 4.10d. Effective stress profile at 20 msec, soil with $k = 0.1$ in/sec.

TWO-PHASE DYNAMIC ANALYSIS (MPDAP VS TPDAP-II)
 $K = 1.0$ FOR SOILS AT 10 MSEC

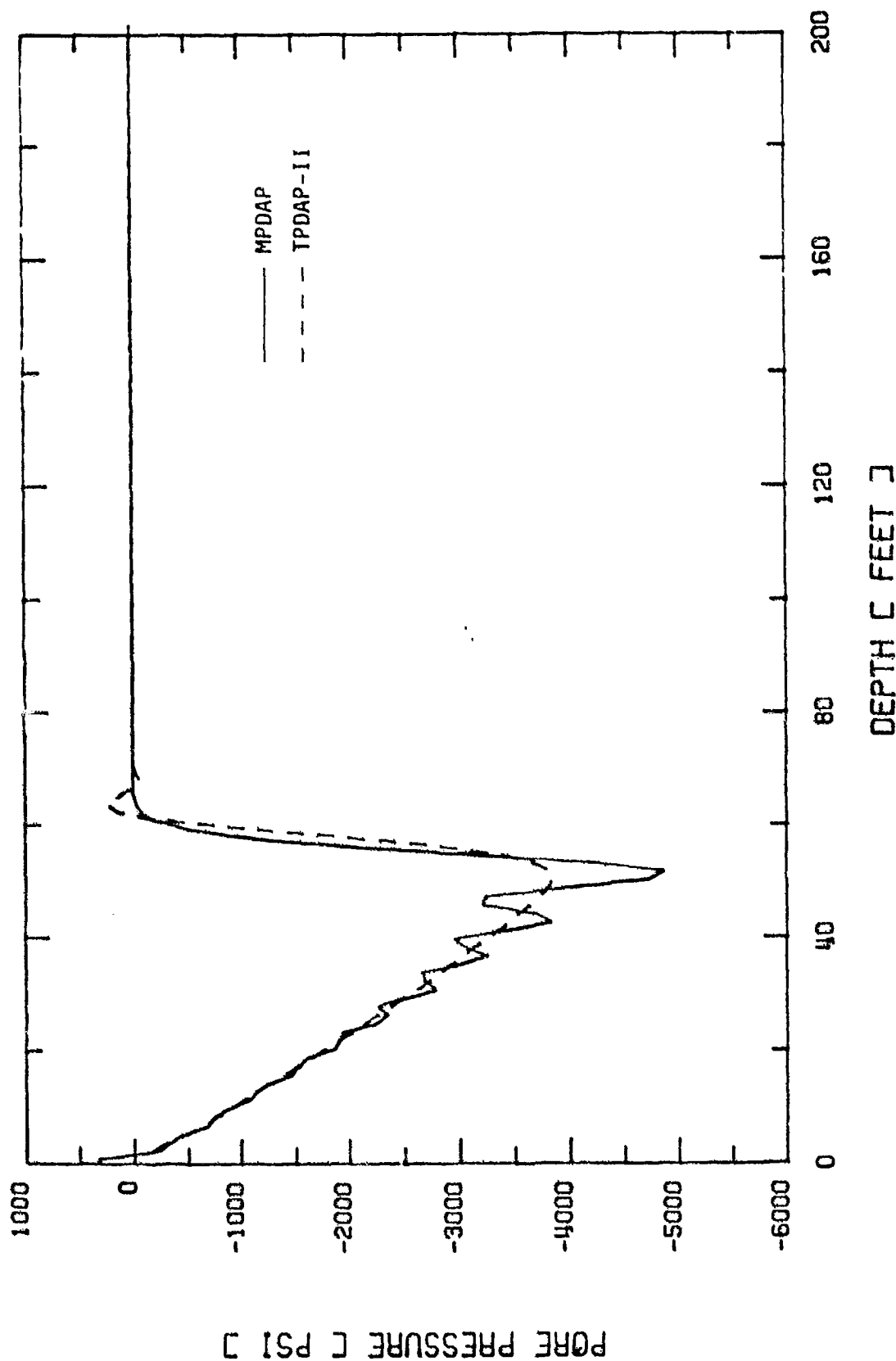


Figure 4.11a. Pore fluid pressure profile at 10 msec, soil with $k = 1.0$ in/sec.

TWO-PHASE DYNAMIC ANALYSIS (MPDAP VS TPDAP-II)
 $K = 1.0$ FOR SOILS AT 10 MSEC

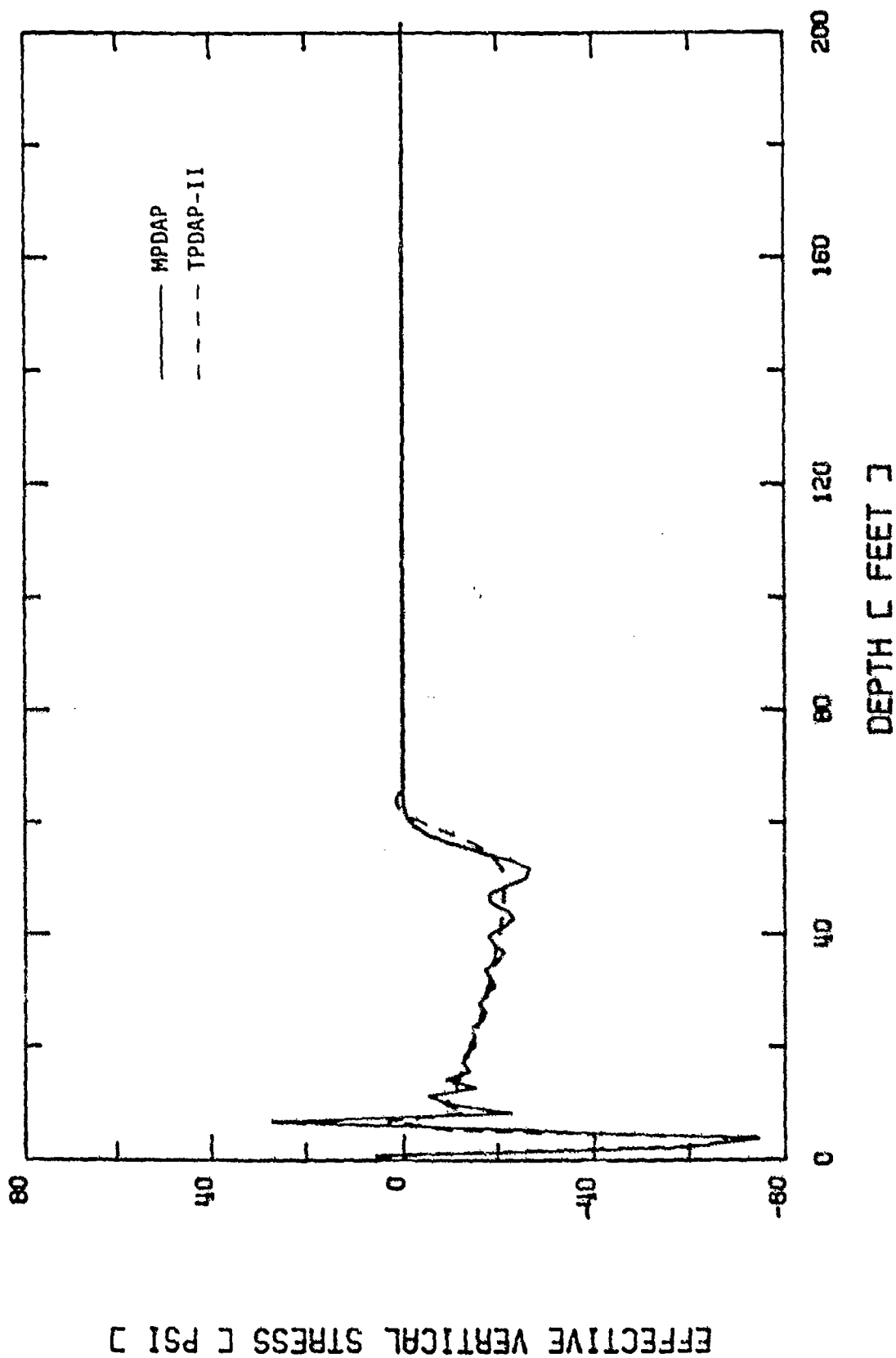


Figure 4.11b. Effective stress profile at 10 msec, soil with $k = 1.0$ in/sec.

TWO-PHASE DYNAMIC ANALYSIS (MPDAP VS TPDAP-II)
 K = 1.0 FOR SOILS AT 20 MSEC

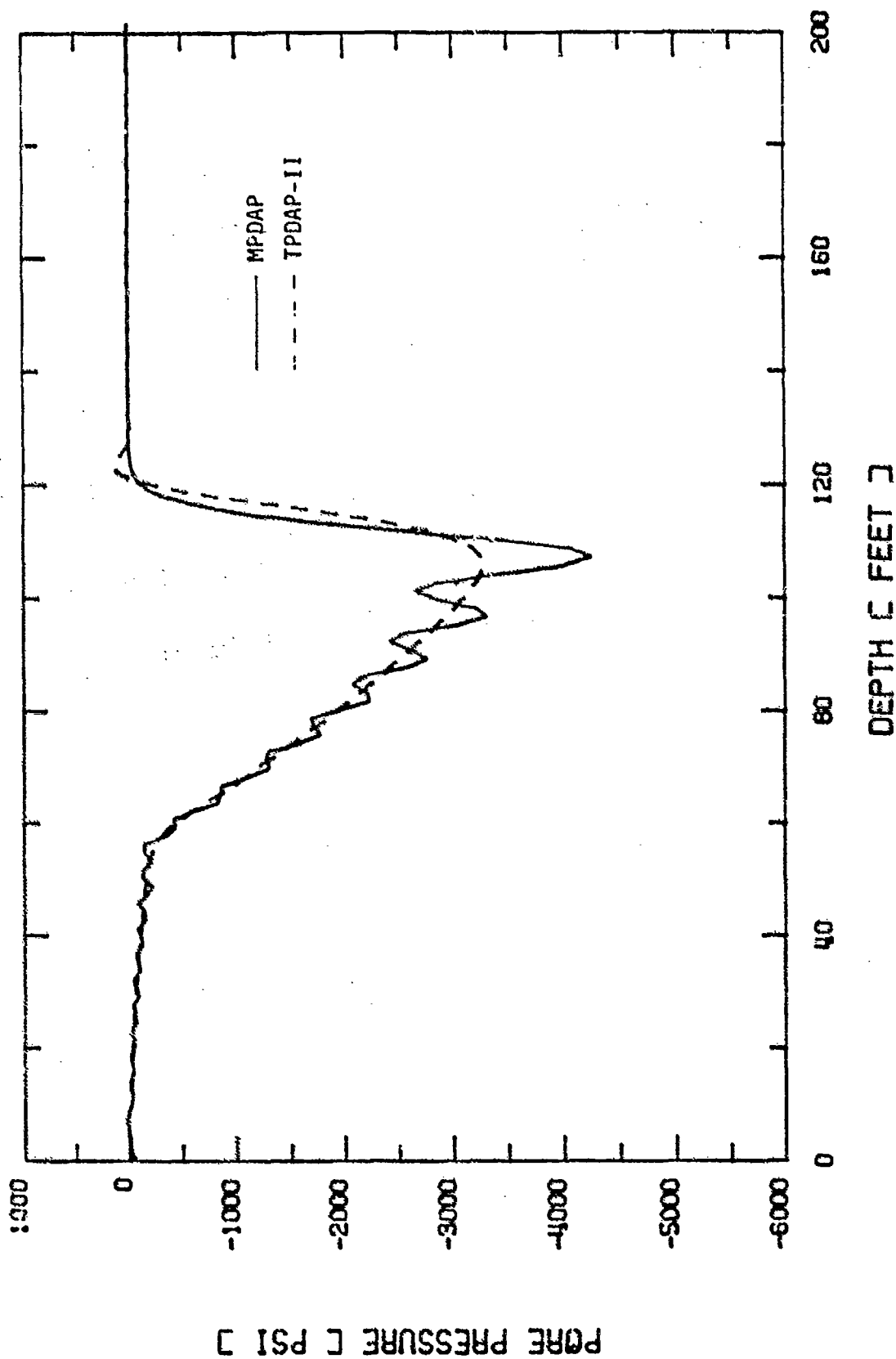


Figure 4.11c. Pore fluid pressure profile at 20 msec, soil with $k = 1.0$ in/sec.

TWO-PHASE DYNAMIC ANALYSIS (MPDAP VS TPDAP-II)
 $K = 1.0$ FOR SOILS AT 20 MSEC

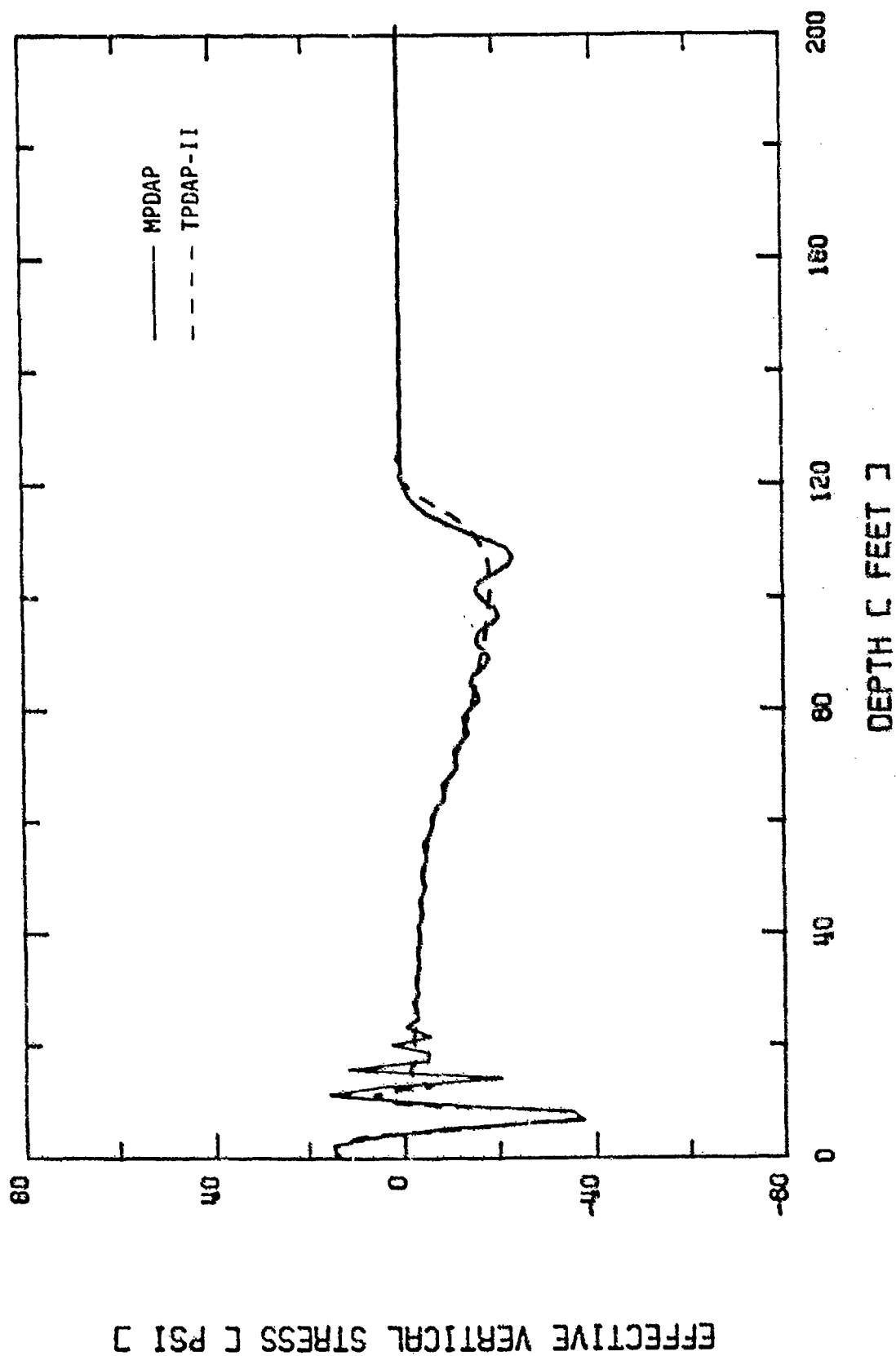


Figure 4.11d. Effective stress profile at 20 msec, soil with $k = 1.0$ in/sec.

SECTION 5

NUMERICAL AND THEORETICAL TREATMENT OF WAVES OF THE FIRST AND SECOND KIND

5.1. INTRODUCTION

Kim, Blouin and Timian (1987) presented both a theoretical and numerical treatment of wave propagation and damping in saturated porous media. In Section 4 of that report, a closed form solution for wave propagation velocity and damping in fully saturated porous media having elastic skeleton properties was derived for a fully coupled model with linearly compressible solid grains and pore water. This solution demonstrated the existence of two types of compression waves, termed waves of the first and second kinds. It also provided a means of benchmarking and verifying multiphase code calculations and a means of planning and guiding a further investigation of these two types of waves using our finite element two-phase codes.

During the past year, we have expanded on this initial study. We performed a numerical investigation of waves of the second kind in saturated porous rock to determine some of the characteristic properties of waves of the second kind. In addition, the method of characteristics was used to verify and expand our previous theoretical derivation for a general, rather than a harmonic, loading function. Results of these numerical and theoretical studies are described in this section.

5.2. NUMERICAL CALCULATIONS OF WAVES OF THE FIRST AND SECOND KIND

The general theoretical solution for compressional wavespeeds and damping was incorporated into the numerical code TWAVE, described by Kim, Blouin and Timian (1987). TWAVE was used in a parametric study of the influence of excitation frequency and variations in material properties on propagation velocity and damping. Compressional wave velocity for waves of the first kind, as shown in Figure 5.1, was found to vary as a function of the frequency-permeability product, with a zone where wavespeed transitions from a lower

bound value to a higher bound value with increasing values of the product. Damping is seen to be at a maximum where the rate of change in wavespeed is greatest. As shown in Figure 5.2, waves of the second kind also have a transition in wavespeed from near zero at low values of the frequency-permeability product to an upper bound value at higher values of the product.

These theoretical predictions were also observed in a set of numerical calculations performed by TPOAPII. A series of 3 one-dimensional calculations, similar to those described in Section 4.5, for a vertically propagating planar compression wave were performed for three different permeabilities. Permeabilities were selected so that the frequency-permeability product fell in the lower bound, upper bound and transitional wavespeed regimes. The input loading was the same as described in Figure 4.5 and consisted of a short rise time triangular pulse with a peak stress of 5,000 psi and a positive phase duration of 10 msec. The loading pulse was applied to saturated soil having the properties also listed in Figure 4.5. Snapshots of the pore water pressure profiles at four different times, from 10 to 40 msec, are shown in Figure 5.3. Three calculations are shown for permeabilities of 0.001, 0.1 and 10 in/s.

The trends in these calculations are similar to those predicted from the TWAVE closed form solution. The wavespeed increases substantially with increasing permeability. For the lowest permeability, the velocity of the wavefront is about 5300 ft/s and for the highest permeability, it is about 5900 ft/s. The wavespeed computed for this material according to the decoupled undrained modulus described by Blouin and Kim (1984) is about 5200 ft/s which agrees very well with the low permeability calculation.

There is a dramatic alteration of the wave shape for the intermediate permeability calculation. The wavefront is smeared and the amplitude is significantly attenuated relative to the calculations in the less permeable and in the more permeable materials. This is a clear indication that excess damping occurs in the transition region between the lower bound and upper bound wavespeeds, as predicted by the TWAVE closed form solution.

An additional calculation was performed using TPDAPII which was tailored to highlight the phenomenology associated with compressional waves of the second kind. In order to accentuate the wave of the second kind, a permeable rock skeleton was used having properties listed in Figure 5.4. The saturated rock was loaded with a downward sinusoidal pressure pulse having a peak pressure of 5000 psi and a frequency of 50 Hz and a half sine duration. Figure 5.4a (Kim and Blouin) shows the pore pressure profiles for both the waves of the first and second kinds at 20 msec. The pore water is in compression in both instances, with the lower amplitude wave of the second kind lagging well behind the wave of the first kind. The effective stress in the rock skeleton, shown in Figure 5.4b is in compression in the wave of the first kind, but in tension in the wave of the second kind. The combined wave-forms are shown in Figure 5.4c where it is obvious that the compressional stresses in the pore water of the second wave are balanced by the tensile stresses in the porous skeleton.

Examination of the TPDAPII output for the pore water and skeleton motion shows that in the wave of the first kind, both the pore water and skeleton are moving in the direction of the wave propagation and are both in compression. However, in the wave of the second kind, the motion of the skeleton and pore water are out of phase. The pore water is in compression and is moving in the direction of the wave propagation. The skeleton is in tension and is moving opposite of the direction of propagation. Thus, waves of the second kind appear to consist of a surge of pore water moving through the porous skeleton. It would be very desirable to obtain experimental verification of the waves of the second kind, as well as verification of the dependence of wavespeed for waves of the first kind on the frequency-permeability product.

5.3. THEORETICAL DERIVATION OF FIRST AND SECOND KIND WAVESPEEDS BY THE METHOD OF CHARACTERIZATION

5.3.1. Introduction

Kim, Blouin and Timian's (1997) derivation of wavespeed and damping for waves of the first and second kind utilized a harmonic excitation function. In order to further verify the theoretical existence of waves of the second

kind, we have developed an alternate derivation using the method of characteristics which doesn't rely on a harmonic excitation function. This solution confirms the existence of waves of the second kind in saturated porous media with no fluid friction damping. The wavespeeds obtained in this solution are identical to the upper bound wavespeeds from the more general 1987 solution where the frequency-permeability product tends toward infinity.

5.3.2. Derivation of Wave Propagation in Saturated Media

The four governing field equations for uniaxial strain loading from Kim, Blouin and Timian (1987) (Equations 4-35, 4-36, 4-40 and 4-46) are:

the governing differential equilibrium equation for the bulk mixture:

$$\rho \frac{\partial \dot{u}_z}{\partial t} + \rho_f \frac{\partial \dot{w}_z}{\partial t} - \frac{\partial \sigma_z}{\partial z} = 0 \quad (5-1)$$

the governing differential equation for motion of the pore fluid:

$$\rho_f \frac{\partial \dot{u}_z}{\partial t} + \frac{\gamma_f}{k} \dot{w}_z + \frac{\rho_f}{n} (1+r) \frac{\partial \dot{w}_z}{\partial t} - \frac{\partial \pi}{\partial z} = 0 \quad (5-2)$$

the governing differential equation for continuity of flow:

$$\frac{\partial \dot{w}_z}{\partial z} + (1-C_g K_s) \frac{\partial \dot{u}_z}{\partial z} + \left(C_g^2 K_s - \frac{1}{K_m} \right) \frac{\partial \pi}{\partial t} = 0 \quad (5-3)$$

the governing differential equation for the effective stress law:

$$M_s \frac{\partial \dot{u}_z}{\partial z} + (1-C_g K_s) \frac{\partial \pi}{\partial t} - \frac{\partial \sigma_z}{\partial t} = 0 \quad (5-4)$$

NB. σ and π are both positive in tension

Equation 5-1 through 5-4 are four linear, first order, partial differential equations involving the quantities \dot{u}_z , \dot{w}_z , σ_z , and π , each of which has par-

tial derivatives with respect to z and t . Since we have eight partial derivatives, but only four equations, we need four more equations, which are:

$$d\dot{u}_z = \frac{\partial \dot{u}_z}{\partial z} dz + \frac{\partial \dot{u}_z}{\partial t} dt \quad (5-5)$$

$$d\dot{w}_z = \frac{\partial \dot{w}_z}{\partial z} dz + \frac{\partial \dot{w}_z}{\partial t} dt \quad (5-6)$$

$$d\sigma_z = \frac{\partial \sigma_z}{\partial z} dz + \frac{\partial \sigma_z}{\partial t} dt \quad (5-7)$$

and

$$d\pi = \frac{\partial \pi}{\partial z} dz + \frac{\partial \pi}{\partial t} dt \quad (5-8)$$

Equations 5-1 through 5-8 can be written in matrix form as follows:

$$\begin{bmatrix} 0 & 0 & 0 & \rho_f & -1 & 0 & 0 & 0 \\ 0 & \rho_f & 0 & \frac{\rho_f}{h}(1+r) & 0 & 0 & -1 & 0 \\ 1-C_0K_B & 0 & 1 & 0 & 0 & 0 & 0 & c_0^2K_B - \frac{1}{K_B} \\ K_B & 0 & 0 & 0 & 0 & -1 & 0 & 1-C_0K_B \\ dz & dt & 0 & 0 & 0 & 0 & 0 & 0 \\ 0 & 0 & dz & dt & 0 & 0 & 0 & 0 \\ 0 & 0 & 0 & 0 & dz & dt & 0 & 0 \\ 0 & 0 & 0 & 0 & 0 & 0 & dz & dt \end{bmatrix} \begin{Bmatrix} \dot{u}_{z,z} \\ \dot{u}_{z,t} \\ \dot{w}_{z,z} \\ \dot{w}_{z,t} \\ \sigma_{z,z} \\ \sigma_{z,t} \\ \pi_z \\ \pi_t \end{Bmatrix} = \begin{Bmatrix} 0 \\ -\frac{\gamma_f \dot{u}_z}{h} \\ 0 \\ 0 \\ d\dot{u}_z \\ d\dot{w}_z \\ d\sigma_z \\ d\pi \end{Bmatrix} \quad (5-9)$$

Equation 5-9 provides a means of determining the eight partial derivatives, $u_{z,z}$, $u_{z,t}$, $w_{z,z}$, $w_{z,t}$, $\sigma_{z,z}$, $\sigma_{z,t}$, $\pi_{,z}$ and $\pi_{,t}$ at a point, when w_z is known at the point and the differentials du_z , dw_z , $d\sigma_z$ and $d\pi$ are specified in a given direction

$$dz = cdt \quad (5-10)$$

except when the value of c renders the coefficient matrix singular.

For convenience, let

$$\frac{\rho_f}{n}(1+r) = a \quad (5-11)$$

$$1 - C_g K_S = b \quad (5-12)$$

$$C_g^2 K_S - \frac{1}{K_m} = d \quad (5-13)$$

then the coefficient matrix in Equation 5-9 is

$$\underline{A} = \begin{bmatrix} 0 & \rho & 0 & \rho_f & -1 & 0 & 0 & 0 \\ 0 & \rho_f & 0 & a & 0 & 0 & -1 & 0 \\ b & 0 & 1 & 0 & 0 & 0 & 0 & d \\ M_S & 0 & 0 & 0 & 0 & -1 & 0 & b \\ cdt & dt & 0 & 0 & 0 & 0 & 0 & 0 \\ 0 & 0 & cdt & dt & 0 & 0 & 0 & 0 \\ 0 & 0 & 0 & 0 & cdt & dt & 0 & 0 \\ 0 & 0 & 0 & 0 & 0 & 0 & cdt & dt \end{bmatrix} \quad (5-14)$$

Multiplying each even column of $|\underline{A}|$ by c , and subtracting it from the previous column leaves the values of $|\underline{A}|$ unaltered, so that

$$|\underline{A}| = A = \begin{bmatrix} -c\rho & \rho & -c\rho_f & \rho_f & -1 & 0 & 0 & 0 \\ -c\rho_f & \rho_f & -ca & a & 0 & 0 & -1 & 0 \\ b & 0 & 1 & 0 & 0 & 0 & -cd & d \\ M_S & 0 & 0 & 0 & c & -1 & -cb & b \\ 0 & dt & 0 & 0 & 0 & 0 & 0 & 0 \\ 0 & 0 & 0 & dt & 0 & 0 & 0 & 0 \\ 0 & 0 & 0 & 0 & 0 & dt & 0 & 0 \\ 0 & 0 & 0 & 0 & 0 & 0 & 0 & dt \end{bmatrix} \quad (5-15)$$

Using the elements dt in the 5th through 8th rows as the pivotal elements in a Laplace expansion yields

$$A = (dt)^4 \begin{vmatrix} -c\rho & -c\rho_f & -1 & 0 \\ -c\rho_f & -ca & 0 & -1 \\ b & 1 & 0 & -cd \\ M_S & 0 & c & -cb \end{vmatrix}$$

$$= (dt)^4 \left\{ (+1) \begin{vmatrix} +c\rho_f & +ca & +1 \\ b & 1 & -cd \\ M_S & 0 & -cb \end{vmatrix} + (c) \begin{vmatrix} +c\rho & +c\rho_f & 0 \\ -c\rho_f & -ca & -1 \\ b & 1 & -cd \end{vmatrix} \right\}$$

$$\begin{aligned}
&= (dt)^4 \left[(-c^2 \rho_f b - c^2 a d M_S + c^2 a b^2 - M_S) \right. \\
&\quad \left. + c(c^3 \rho a d - c \rho_f b + c \rho - c^3 \rho_f^2 d) \right] \\
&= (dt)^4 \left[(\rho a d - \rho_f^2 d) c^4 + (-\rho_f b - a d M_S + a b^2 - \rho_f b + \rho) c^2 - M_S \right] \\
&= -(dt)^4 \left[(\rho_f^2 d - \rho a d) c^4 - (a b^2 + \rho - 2 \rho_f b - a d M_S) c^2 + M_S \right] \quad (5-16)
\end{aligned}$$

If we set

$$\rho_f^2 d - \rho a d = -d(\rho a - \rho_f^2) = A' \quad (5-17)$$

$$a b^2 + \rho - 2 \rho_f b - a d M_S = 2B \quad (5-18)$$

$$M_S = C \quad (5-19)$$

then the condition that A vanish, which renders \underline{A} singular, reduces to:

$$A' c^4 - 2B c^2 + C = 0 \quad (5-20)$$

which means that

$$c^2 = \frac{B \pm \sqrt{B^2 - 4A'C}}{2A'} \quad (5-21)$$

This wavespeed solution is identical to the upper bound wavespeed derived by Kim, Blouin and Timian (1987) given in Equation 4-111. The plus sign produces upper bound velocities of waves of the first kind in an undamped medium and the minus sign produces upper bound velocities of waves of the second kind in an undamped medium.

As compatibility checks, we consider two cases: where there is no pore fluid and when there is no skeleton (water only). When there is no pore fluid

$$\begin{array}{lll} \rho_f = 0 & a = 0 & A' = 0 \\ r = 0 & b = 1 & 2B = \rho_s \\ C_g = 0 & d = 0 & C = M_s \\ \rho = (1-n)\rho_g \end{array}$$

and Equation 5-2 reduces to

$$\rho c^2 - M_s = 0 \quad (5-22)$$

so that

$$c^2 = \frac{M_s}{\rho} \quad (5-23)$$

which is the compressional wavespeed in a single phase dry medium.

When there is no skeleton

$$\begin{array}{ll} n = 1 & A' = 0 \\ a = \rho_f & \\ b = 1 & 2B = \frac{\rho_f}{K_f} M_s \\ d = -\frac{1}{K_f} & C = M_s \end{array}$$

and Equation 5-20 reduces to

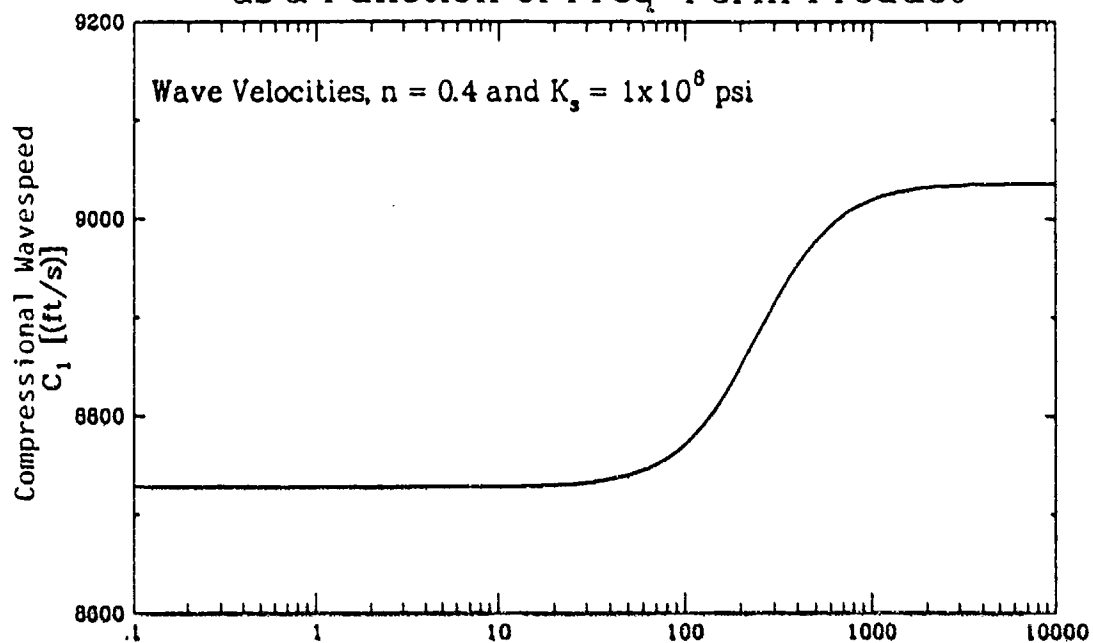
$$\left(\frac{\rho_f}{K_f} c^2 - 1 \right) M_s = 0 \quad (5-24)$$

so that, besides the trivial solution $M_S = 0$,

$$c^2 = \frac{K_f}{\rho_f} \quad (5-25)$$

which is the compressional wavespeed in a pure fluid.

Wave Velocity of Wave of First Kind as a Function of Freq-Perm Product



Specific Damping of Wave of First Kind as a Function of Freq-Perm Product

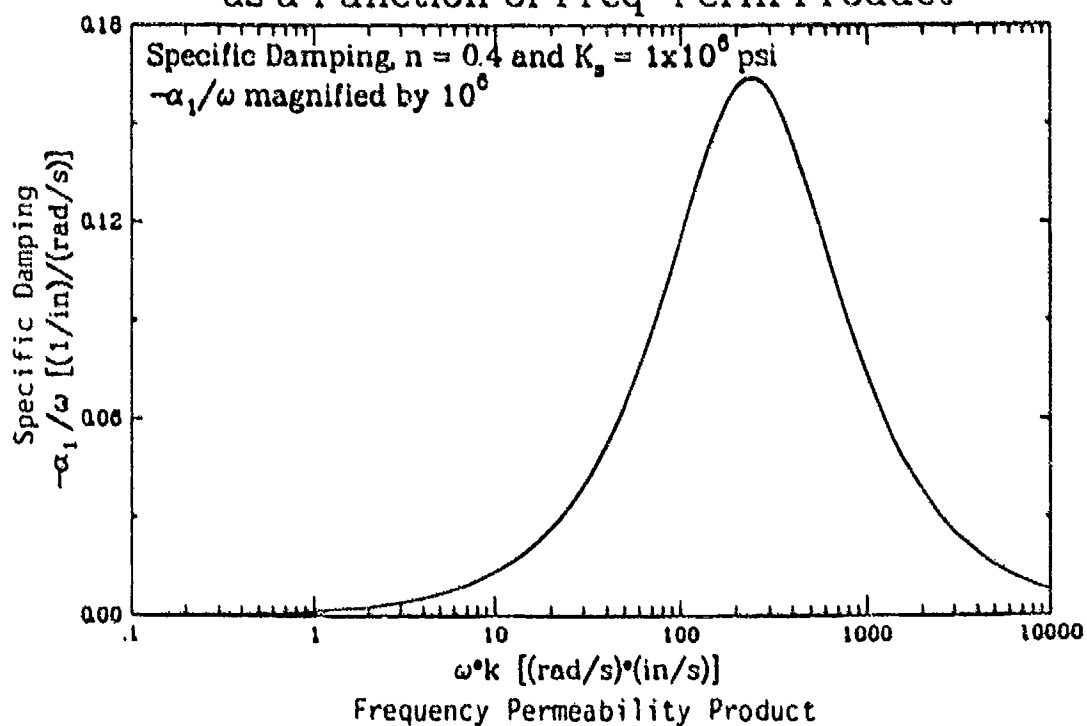
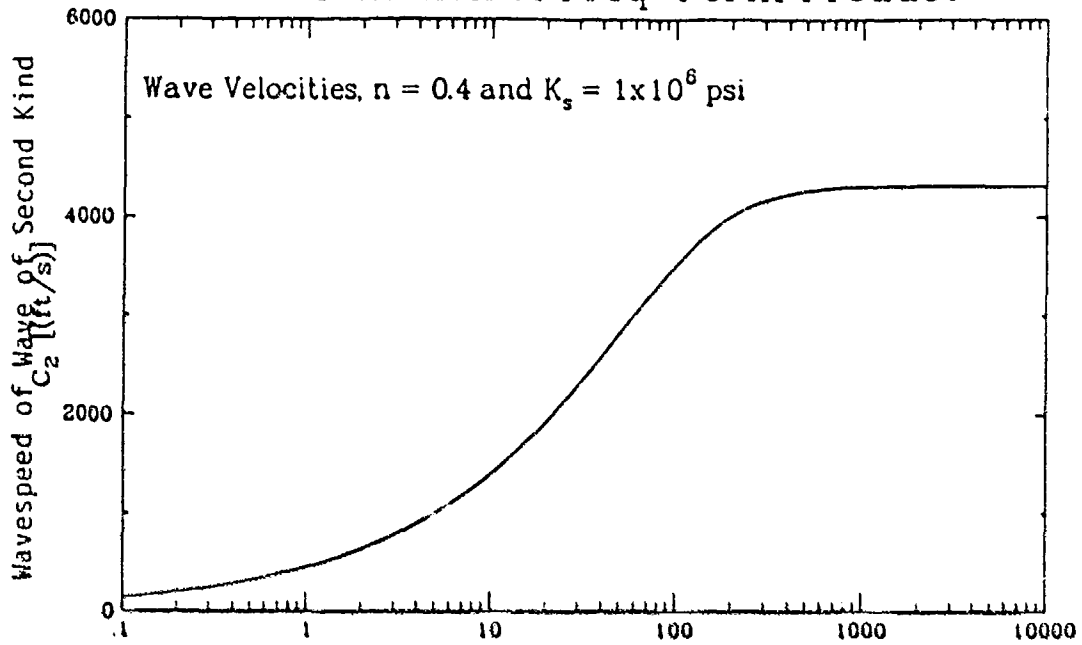


Figure 5.1. Wavespeed and specific damping for waves of the first kind in saturated porous media (Kim, Blouin and Timian, 1987).

Wave Velocity of Wave of Second Kind as a Function of Freq-Perm Product



Specific Damping of Wave of Second Kind as a Function of Freq-Perm Product

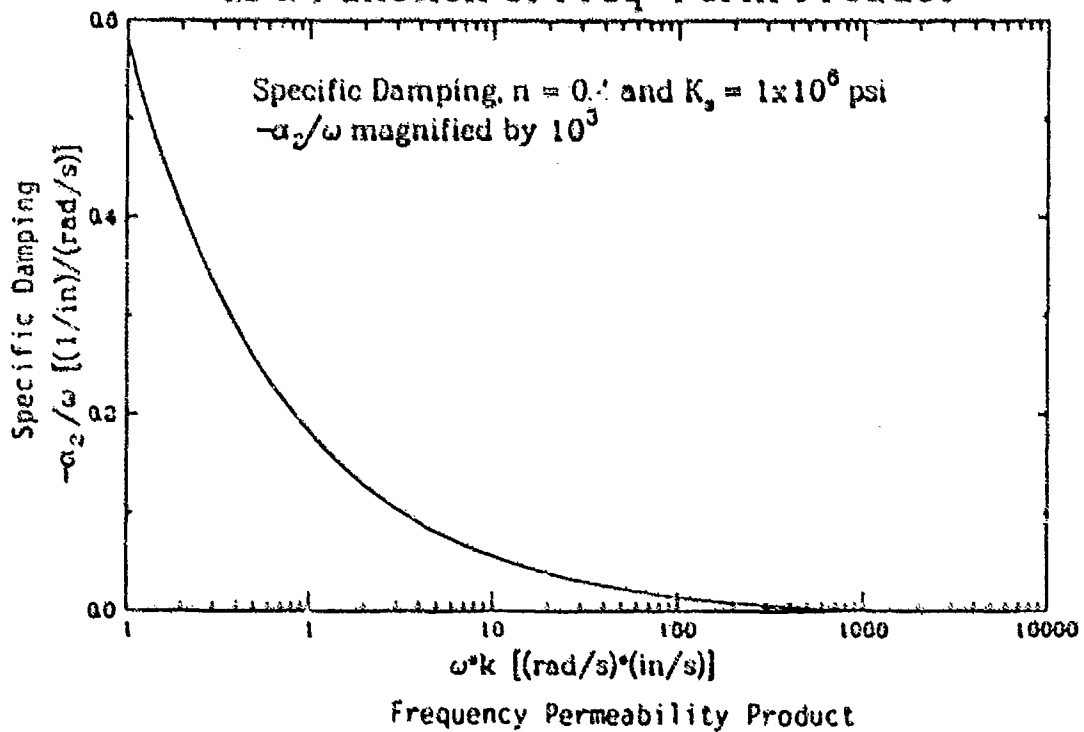


Figure 5.2. Wavespeed and specific damping for waves of the second kind in saturated porous media (Kim, Blouin and Timian, 1987).

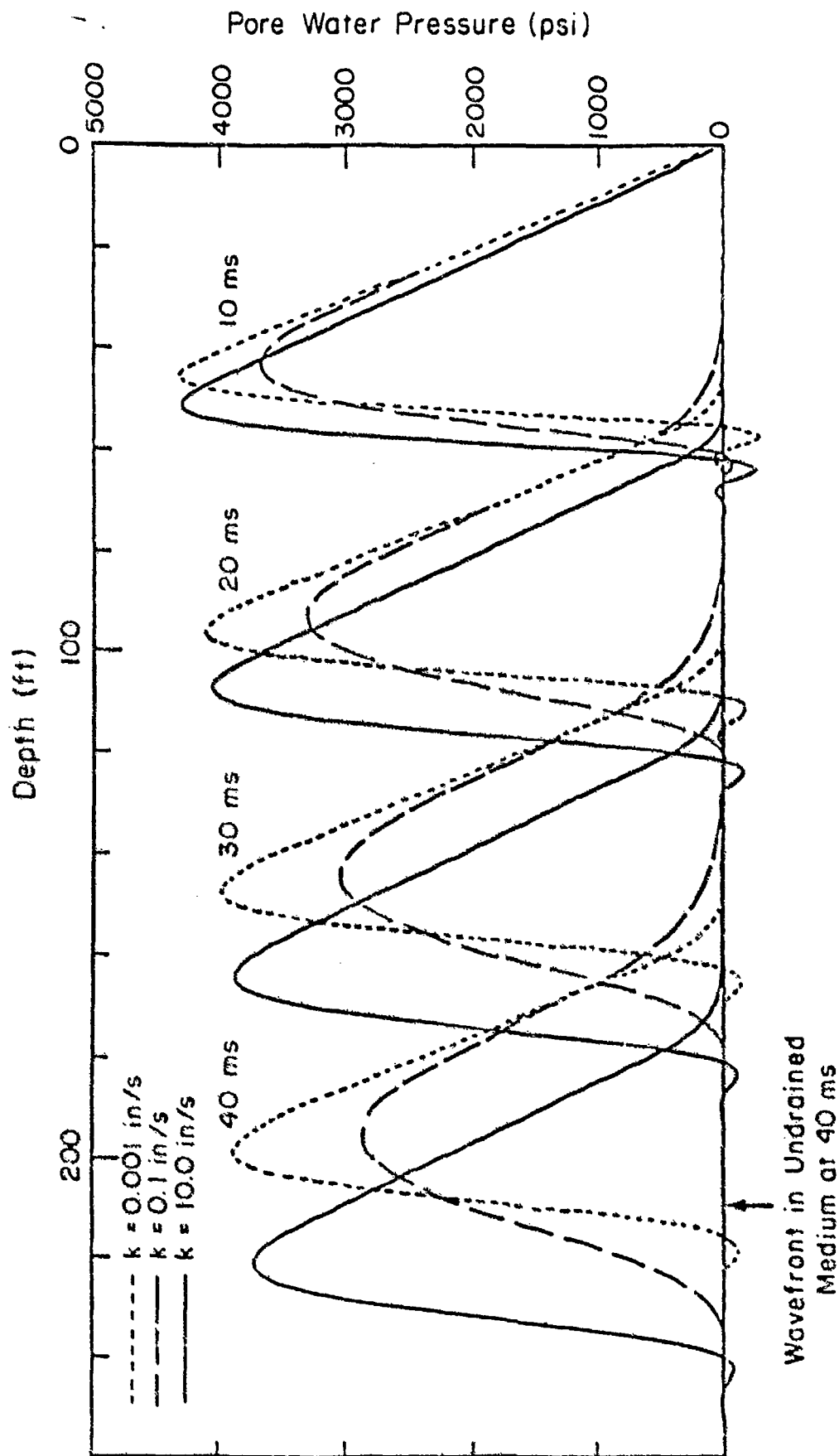


Figure 5.3. Influence of permeability on wavespeed and damping for saturated sand with constant skeleton constrained modulus of 6000 psi and porosity of 35% (Kim, Blouin and Timian, 1987).

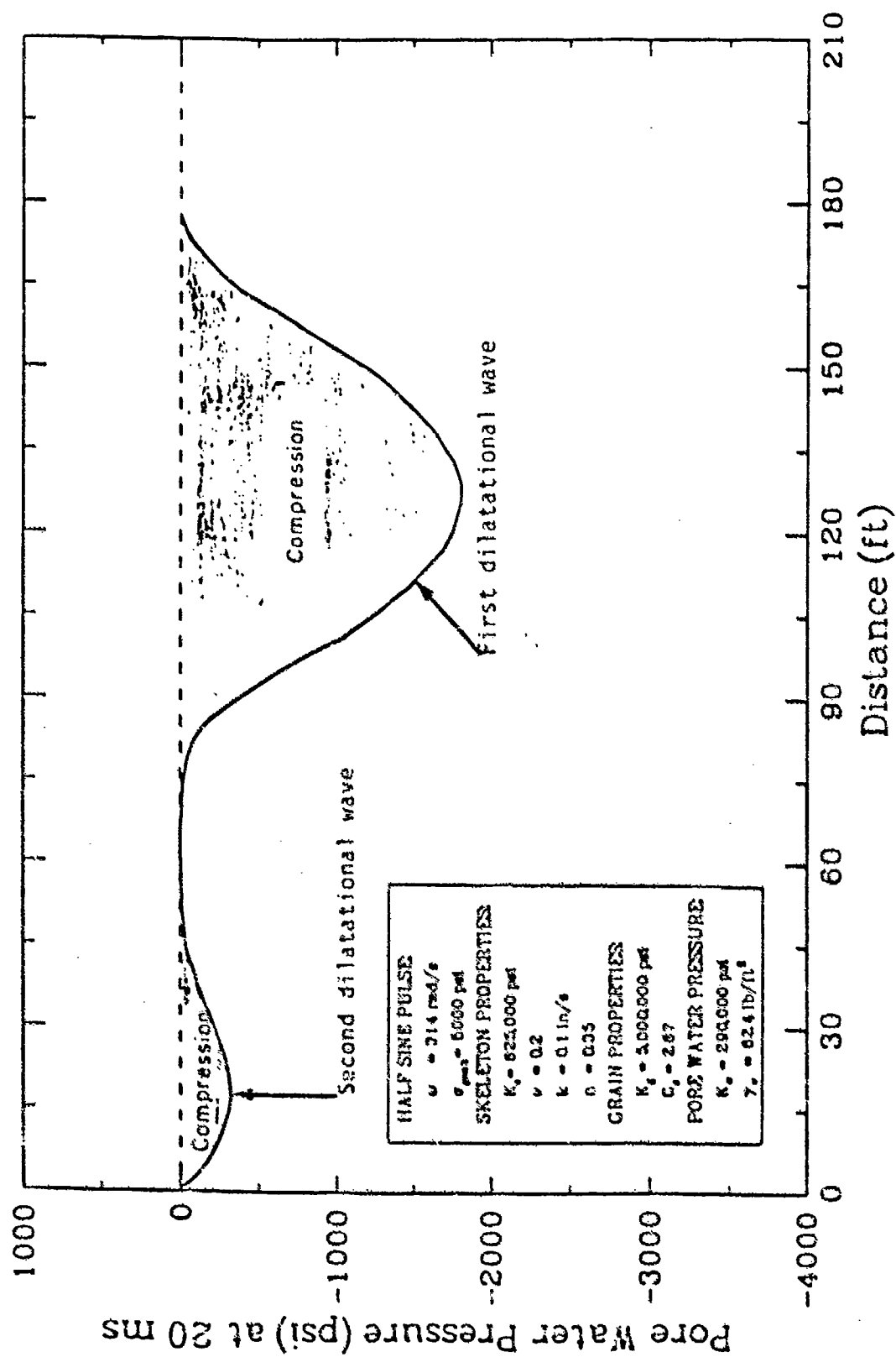


Figure 5.4a. Pore pressure profiles for plane compressional waves of the first and second kind at 20 msec.

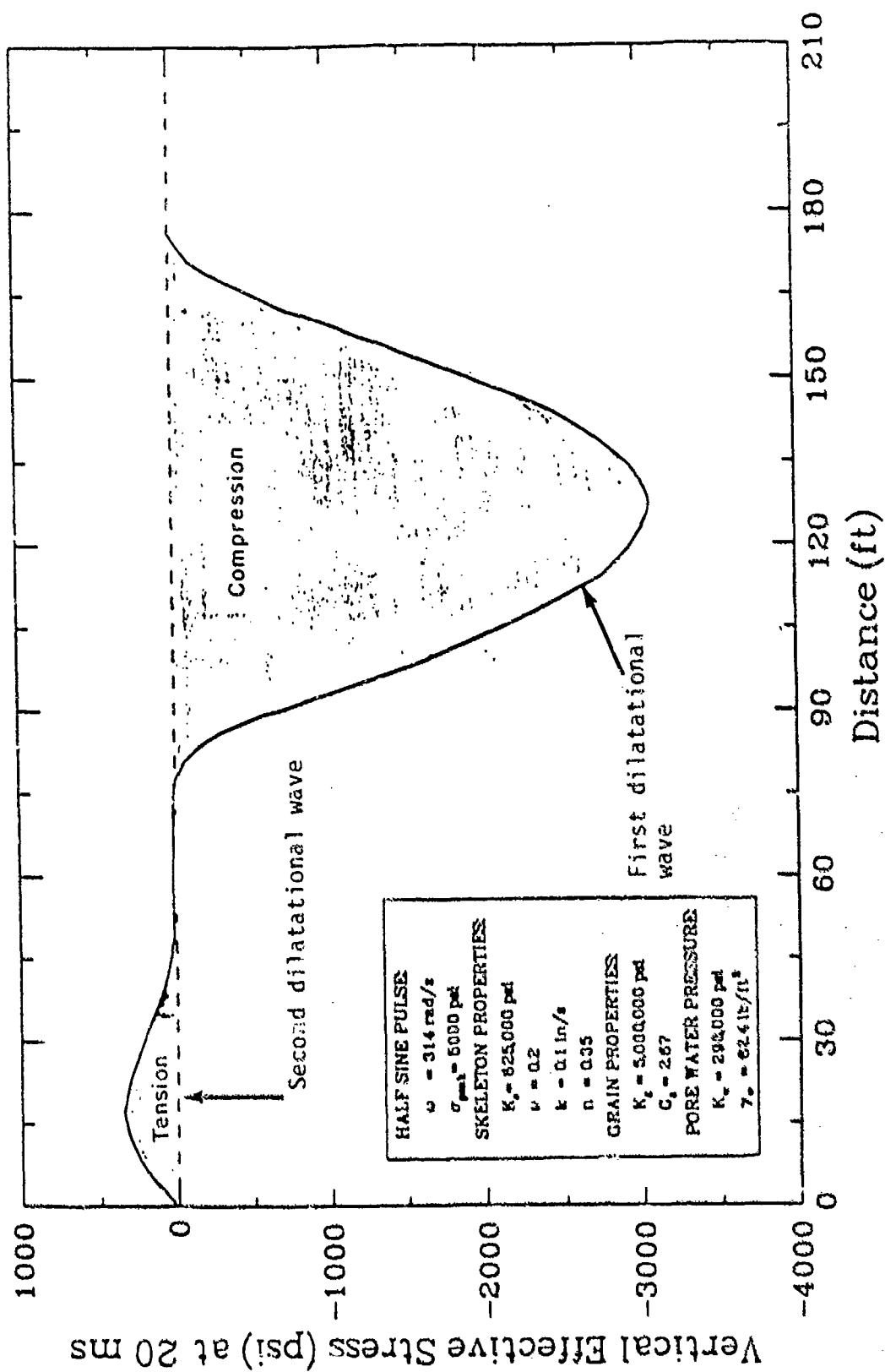


Figure 5.4b. Effective stress profiles for plane compressional waves of the first and second kinds at 20 msec.

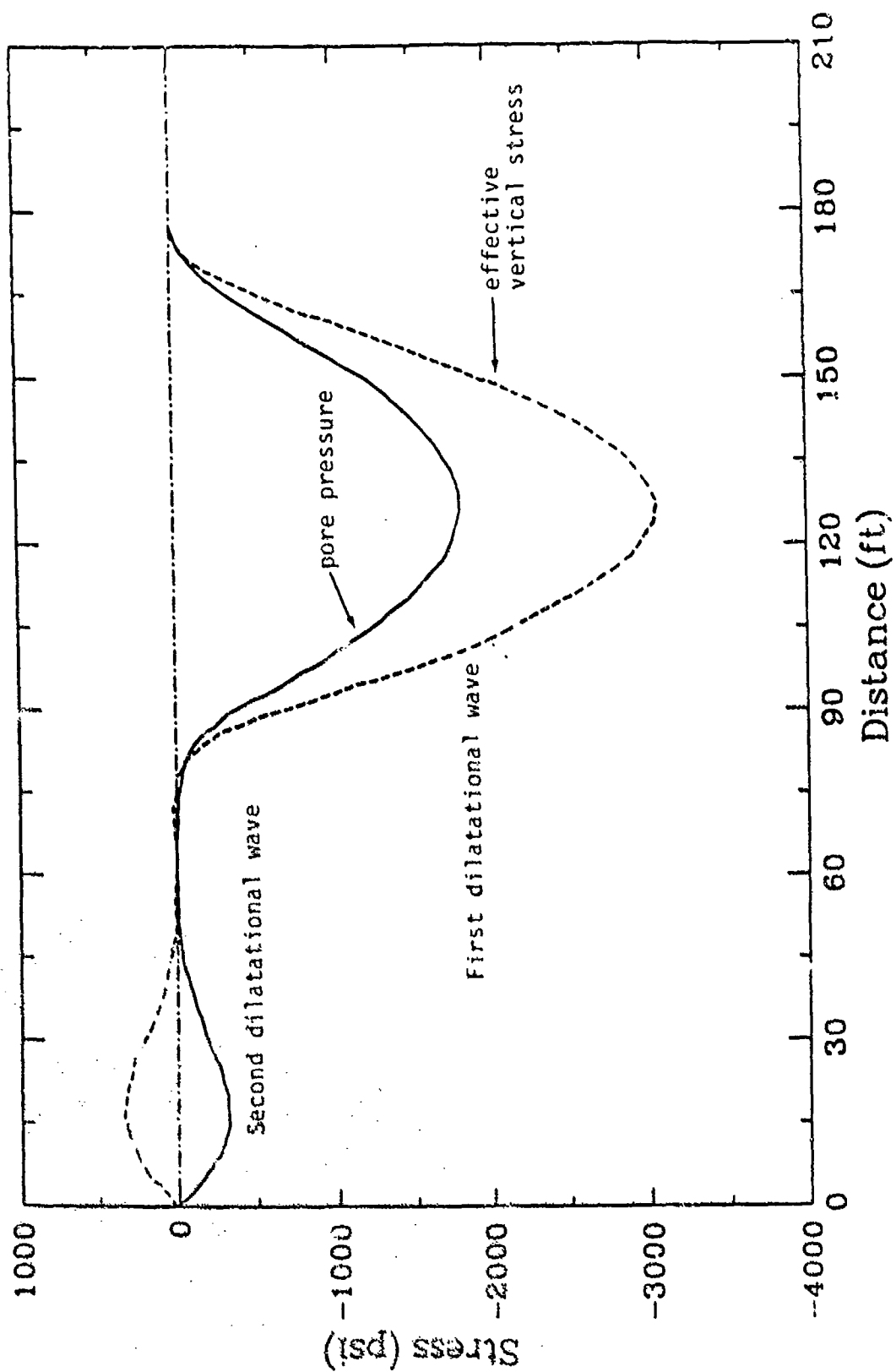


Figure 5.4c. Combined pore pressure and effective stress profiles for plane compressional waves of the first and second kinds at 20 msec.

SECTION 6

EXPERIMENTAL EVALUATION OF FLUID FLOW IN DUCTS AND SOILS

6.1. INTRODUCTION

As described in Section 2.2.2, the equation of motion of the pore fluid (Equation 2.34) is one of the four field equations required to describe multiphase dynamic response. Nearly all previous analysis in this subject area was based on, or heavily influenced by, Biot's pioneering theoretical work on laminar flow (1956, 1962a, 1962b). The experimental findings presented in this section warrant a move away from Biot's formulation of fluid friction, simply because turbulent flow is found to govern the fluid friction equation for the range of pore pressure gradients generated by explosive or rapid dynamic loadings. The consequences of these experimental findings on the theoretical work and its implementation in MPDAP are described in Sections 2 and 3.

Two sets of experimental results are presented in this section: a summary of the steady state and dynamic test results in idealized flat ducts (the experimental analog to Biot's theoretical formulation) and a set of steady state flow data for uniform grained sand over a wide range of flow velocities and pore pressure gradients.

6.2. DYNAMIC FLOW TESTS IN FLAT DUCTS

In order to conduct the dynamic flow tests on the ducts and granular soils, a device was fabricated for conducting high pressure steady state and dynamic flow tests on both ducts and soils. This device, shown schematically in Figure 6.1, is capable of forcing pore fluid through a soil sample or duct with a pressure difference of up to 5000 psi. Originally, the device was designed to be operated by a servo-controlled pump which could produce flow through the sample at a controlled rate or change in rate. During the past year, the device was modified to utilize high pressure nitrogen to propel the piston which forces the pore fluid through the test specimen. In this way,

higher flow velocities could be generated and very rapid changes in flow could be created. Through use of a fast acting valve, pressure gradient rise times as short as 10 msec could be generated. Additional details of this device are presented by Kim, Blouin and Timian (1987).

Using the gas powered modified permeability device, an additional series of 11 steady state flow tests were run at high flow velocities of up to 3700 in/s in the flat duct. The flat duct has a height of 0.04 inches, a width of 0.28 inches and a length of 8.71 inches. These data are shown in Figure 6.2 as pressure gradient normalized by the steady state flow velocity plotted versus the steady state flow velocity. They have been combined with the lower velocity data from Kim, Blouin and Timian (1987) which were mostly run at less than 1800 in/s velocity. The original data fit is also a good match to the higher velocity data. The intercept of the data fit ($a = .0025$) can be used to compute the coefficient of permeability, k , according to Equation 2.36 as

$$k = \frac{\gamma_f}{a} \quad (6-1)$$

as described by Kim, Blouin and Timian (1987). A value of k for kerosene used in these tests is 11.85 in/s. This compares closely to the analytical value of 11.92 m/s computed in the above report.

The slope of the fit to the data in Figure 6.2, b, can be used to compute the turbulent fluid friction coefficient, β_f from Equation 2-36 as

$$\beta_f = b\sqrt{k} \quad (6-2)$$

For the measure slope of $1.5 \times 10^{-5} \text{ lb-s}^2/\text{in}^5$, a value of $\beta_f = 5.16 \times 10^{-5} \text{ lb-s}^{1.5}/\text{in}^{4.5}$ is obtained.

Thus, the steady state flow tests provide us with the first two coefficients of the general dynamic flow Equation 3-4 which can be rewritten as

$$\pi_{,i} = \underbrace{\frac{\gamma_f}{k} \dot{w}_i}_{\text{Frictional Component}} + \underbrace{\frac{\beta_f}{k^{\frac{1}{2}}} \dot{w}_i^2 + \rho_f \ddot{U}_i}_{\text{Inertial Component}} \quad (6-3)$$

In order to completely validate the above flow equation, a series of 12 dynamic flow tests were conducted on the flat duct. Representative data from five of these tests are presented in Figures 6.3 through 6.7. During these dynamic tests, a pore pressure gradient is rapidly applied by the piston driven by the compressed nitrogen. Both the pore pressure gradient and flow are monitored as functions of time as shown in the measured pressure gradient and flow displacement plots of part a of Figures 6.3 through 6.7.

From the measured displacement, the fluid velocity and acceleration are obtained by differentiating with respect to time, as shown in the bottom plot of part b of Figures 6.3 through 6.7. The velocity profile is then substituted into Equation 6-3 to compute the frictional component of the pore pressure gradient using the previously measured friction coefficients, a and b of Equations 6-1 and 6-2. This result is expressed in normalized form as the frictional component of the pressure gradient in the top plot of part b of Figures 6.3 through 6.7.

Using the measured acceleration from Figures 6.3 through 6.7, part b, the inertia force from the last term of Equation 6-3 is computed. The normalized inertial component plus the normalized friction component combine to equal the normalized pressure gradient of unity shown in the plot of Figures 6.3 through 6.7, part b. The total normalized gradients computed from the velocity and acceleration data compare to within about 20% with the actual measured pressure gradients, providing experimental verification of our dynamic pore fluid flow equation (Equations 6-3 and 3-4).

Both the measured pressure gradient and computed frictional component of the pressure gradient are normalized by the measured pressure gradient computed from the velocity and acceleration data in Figure 6.3 through 6.7. Note that during the high early time acceleration, the pressure gradient is

dominated by the inertial component, and as accelerations diminish, the frictional component (dominated by the second term of Equation 6-3) governs. The agreement between the measured pressure gradient and that computed from the velocity and acceleration data is generally within 20% throughout the entire test.

6.3. FLOW TESTS IN SATURATED UNIFORM GRAINED SOIL

A series of flow tests was conducted on a uniform carbonate sand which duplicated the test procedures used for the flat duct flow tests. The objectives of these tests were to:

1. measure the fluid friction flow parameters in actual soil samples;
2. determine where the transition from laminar to turbulent flow occurs in a uniform sand;
3. determine whether Biot's frequency dependent laminar flow parameters are a significant factor in determining the fluid friction in uniform sand; and
4. validate the pore fluid flow equation (Equation 6-3) in saturated soil.

In order to make the appropriate fluid flow measurements in soil, the flat duct was replaced by a cylindrical soil specimen container having a diameter of 0.434 inches and a length of 7.5 inches. A uniform grained carbonate beach sand (Enewetak beach sand) was obtained by sieving so that all of the pretest material was retained on a number 40 sieve and had a grain size ranging from 0.425 to 0.60 mm. This is the same sand used in the grain crushing experiments described by Kim, Blouin and Timian (1987), Section 7. The sample specimens had the following average properties:

dry density, $\gamma_d = 106.0 \text{ lb/ft}^3$
specific gravity, $G_s = 2.81 \text{ gm/cm}^3$
porosity, $n = 39.5\%$

A series of 33 steady state flow tests were run on the uniform beach sand at apparent flow velocities ranging from .4 in/s to 100 in/s and pressure gradients ranging from less than 1 psi/inch to about 250 psi/inch. Data from these tests are presented in Appendix B as apparent flow displacement and pressure gradient both plotted as functions of time. These data are summarized in Table 6.1, where the pressure gradient is also normalized by the absolute flow velocity. Figure 6.8 is a plot of normalized pressure gradient as a function of the absolute flow velocity. The flow data are conveniently fit by a linear relationship, indicating that flow is in the turbulent regime over essentially the entire range of pore pressure gradients. Values of the intercept, a , of Equation 6-1 and the slope, b , of Equation 6-2 were:

$$a = 1.380 \text{ lb-s/in}^4$$

$$b = .2018 \text{ lb-s}^2/\text{in}^5$$

From Equation 6-1, with γ_f for kerosene of 0.0291 lb/in^3

$$k = .0211 \text{ in/s}$$

and from Equation 6-2,

$$\beta_f = .0293 \text{ lb-s}^{1.5}/\text{in}^{4.5}$$

As a check against the steady state test data a conventional constant head permeability test using water as the pore fluid was conducted on a cylindrical Enewetak beach sand sample with a length of 5.35 inches and diameter of 2.50 inches. A value of $k = 0.0383 \text{ in/s}$ was obtained from this test. In order to convert the steady state flow data to the equivalent permeability for water, the following equation is applied.

$$k_{\text{water}} = \left(\frac{\eta_{\text{kerosene}}}{\eta_{\text{water}}} \right) k_{\text{kerosene}} \quad (6-4)$$

For values of dynamic viscosity of $\eta_k = 2.25 \times 10^{-3} \text{ Pa-s}$ and $\eta_w = 1.0 \times 10^{-3} \text{ Pa-s}$, we obtain

$$k_w = .0476$$

which is in good agreement with the value measured in the standard permeability test.

Note that at the highest apparent fluid velocity attained in the soil tests (32 in/s), the equivalent permeability k'_{yf} from Equation 3-6 is about 15% of Darcy's laminar permeability, k . This sharp reduction in permeability illustrates the importance of the influence of turbulent flow on fluid friction.

Several attempts were made to perform dynamic tests on Enewetak sand samples, similar to those reported in Section 6.2 on the flat duct. However, since the apparent flow area of the soil sample was more than 13 times that of the flat duct, we were not able to generate sufficient accelerations in the pore fluid to make meaningful measurements of the influence of inertia.

In order to make meaningful inertia measurements on the soil samples, two modifications to the test apparatus are required. First, a faster acting valve would increase the rate of application of the pore pressure gradient and second, a direct measurement of flow on the low pressure side of the soil sample could increase accuracy of the flow measurements by more than an order of magnitude.

Table 6.1. Summary of steady state flow through Enewetak Beach Sand.

Test No.	Absolute Flow Velocity U_i (in/s)	Pressure Gradient π_i (psi/in)	π_i/U_i	Pressure Level (psi)
U30A8	1.1523	0.66	0.573	5.
U30B8	1.159	0.662	0.571	5.
U30C8	1.156	0.662	0.573	5.
U30D8	2.198	1.32	0.60	10.
U30E8	2.195	1.32	0.601	10.
U30F8	2.166	1.33	0.614	10.
U30G8	4.90	3.34	0.681	25.
U30H8	4.93	3.34	0.678	25.
U30I8	4.93	3.33	0.676	25.
U23D8	4.968	3.48	0.7	25.
U23E8	4.83	3.35	0.694	25.
U23F8	4.52	3.33	0.737	25.
U27G8	8.15	6.8	0.834	50.
U27H8	8.0	6.6	0.825	50.
U27I8	8.09	6.6	0.816	50.
U27D8	13.31	13.3	1.0	100.
U27E8	13.74	13.2	0.96	100.
U27F8	13.31	13.3	1.0	100.
U27A8	21.184	26.5	1.25	200.
U27B8	21.563	26.7	1.238	200.
U27C8	21.372	26.5	1.24	200.
G9F8	21.26	26.5	1.246	200.
U27J8	34.26	53.4	1.559	400.
U27K8	34.5	53.5	1.55	400.
U27L8	34.5	53.4	1.548	400.
U20B8	49.79	106.4	2.137	800.
U20C8	50.74	106.8	2.106	800.
U20D8	50.31	106.8	2.12	800.
U21A8	69.0	187.0	2.7	1400.
U21B8	69.0	187.0	2.7	1400.
U21C8	67.08	185.0	2.76	1400.
U24A8	75.47	225.0	2.98	1690.
U24B8	80.5	245.0	3.04	1840.

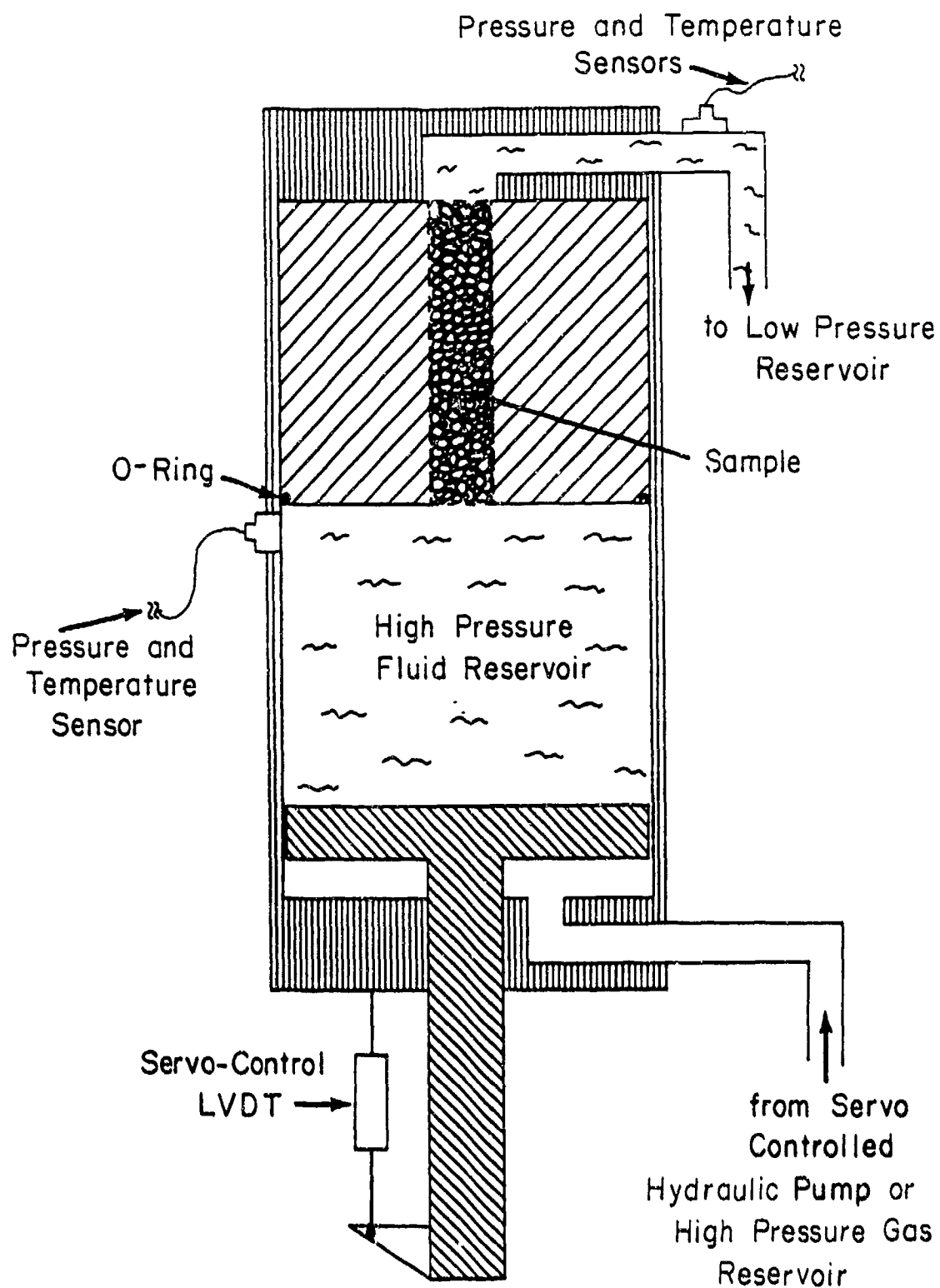


Figure 6.1. Schematic section view of dynamic permeability device.

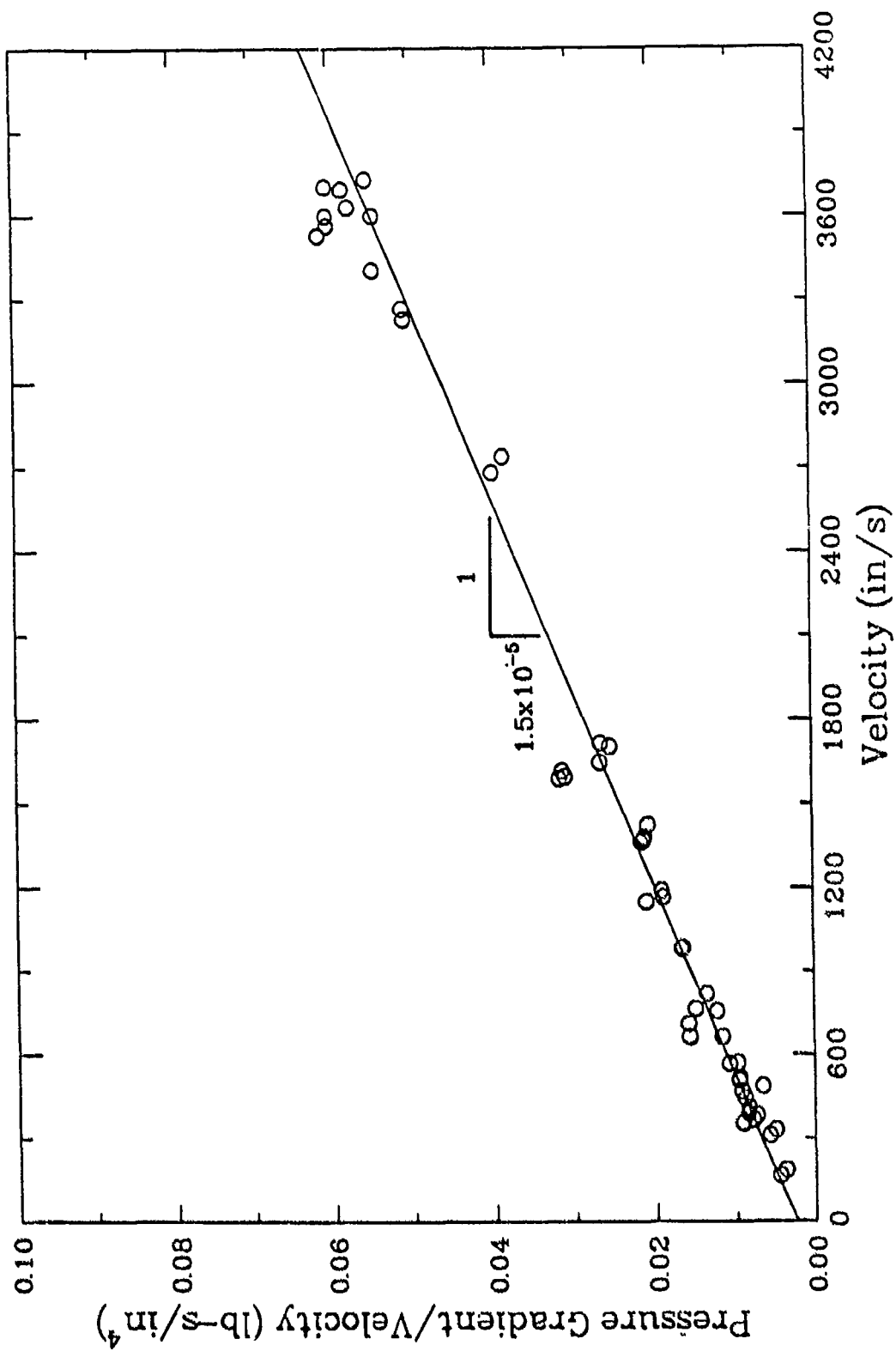


Figure 6.2. Steady state data replotted in order to measure the coefficient of permeability and Ward's constant, flat duct flow test.

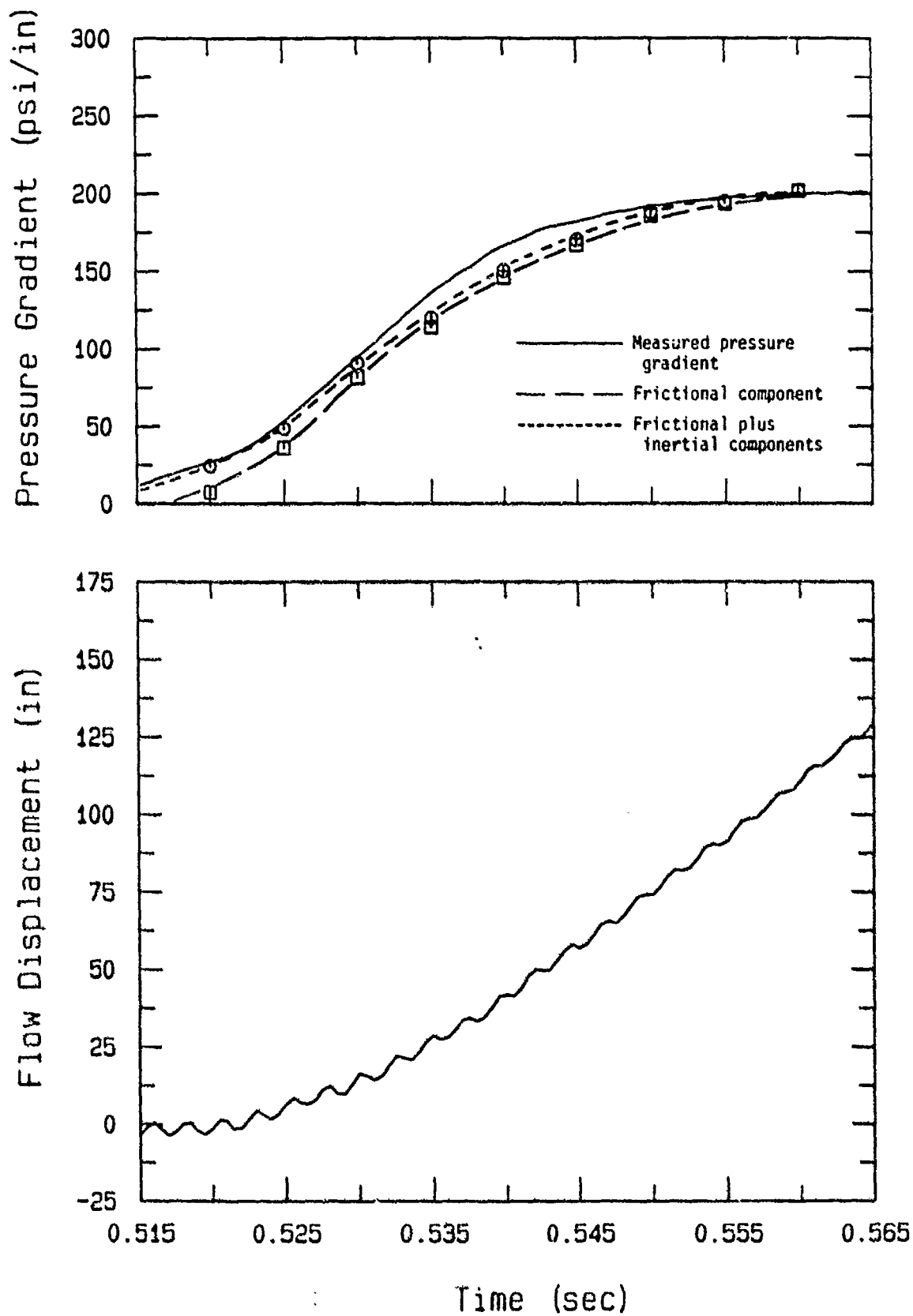


Figure 6.3a. Measured pressure gradient and flow displacement time histories, flat duct test J12A8.

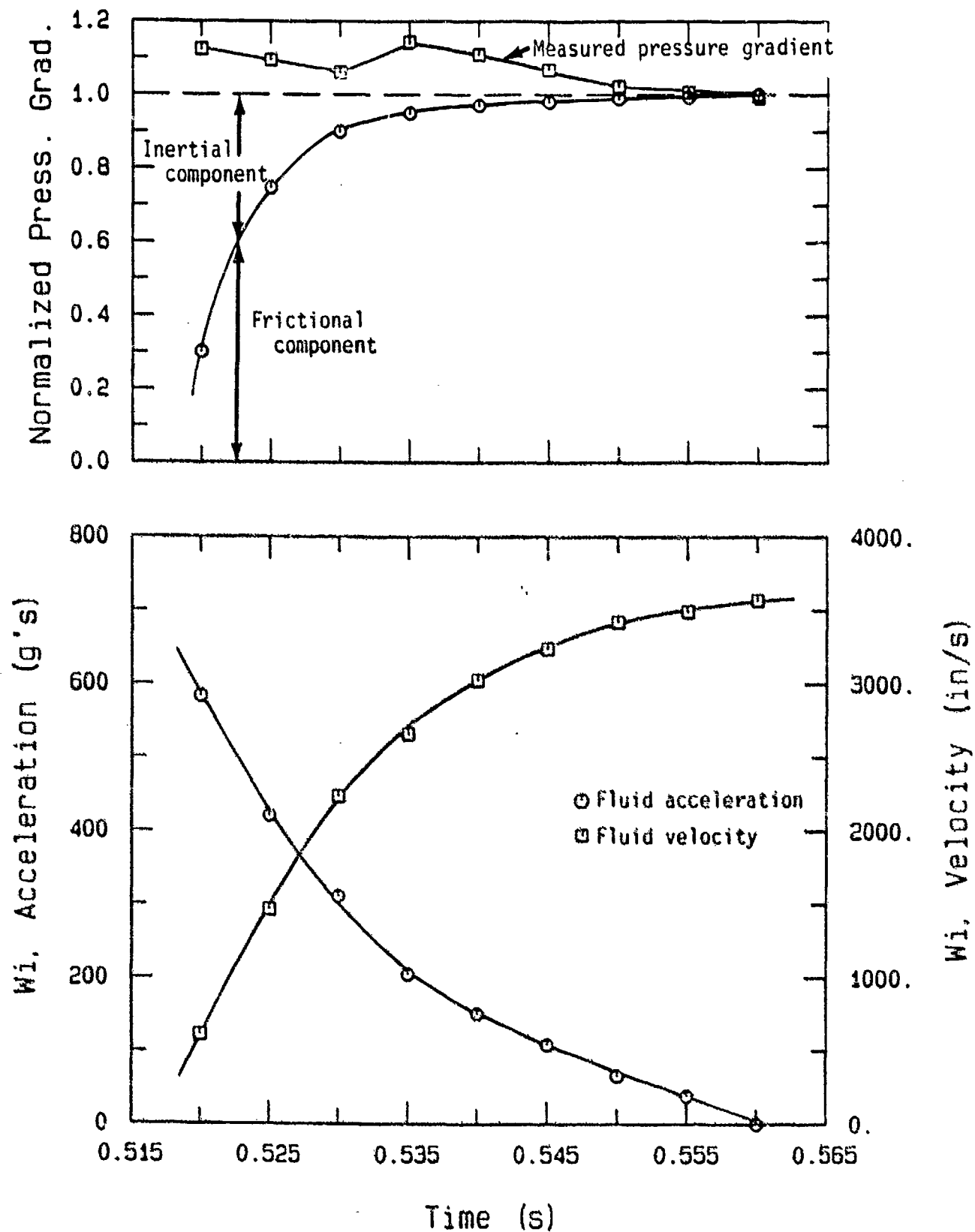


Figure 6.3b. Normalized fluid pressure gradient and fluid motion time histories, flat duct test J12A8.

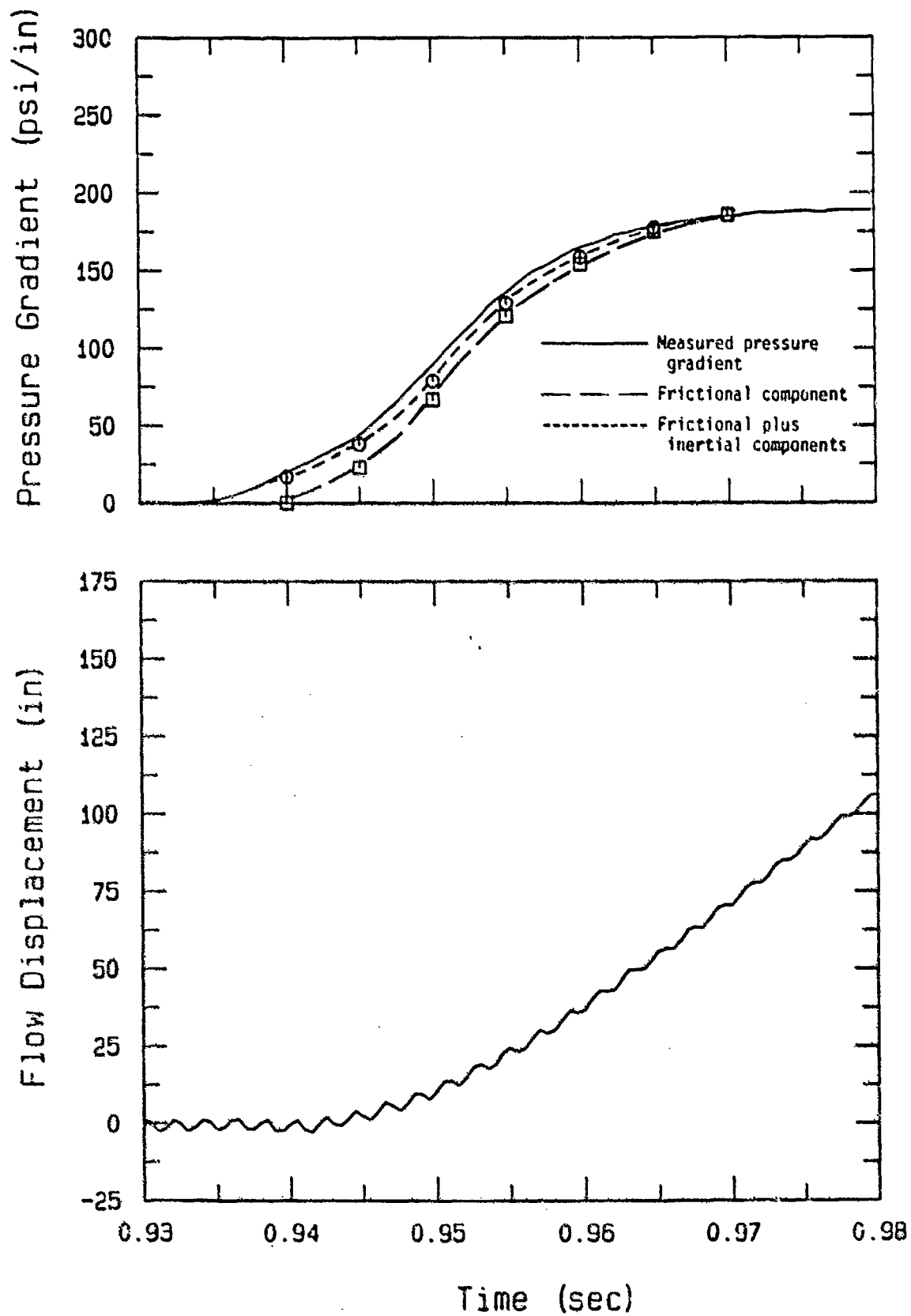


Figure 6.4a. Measured pressure gradient and flow displacement time histories, flat duct test F16A8.

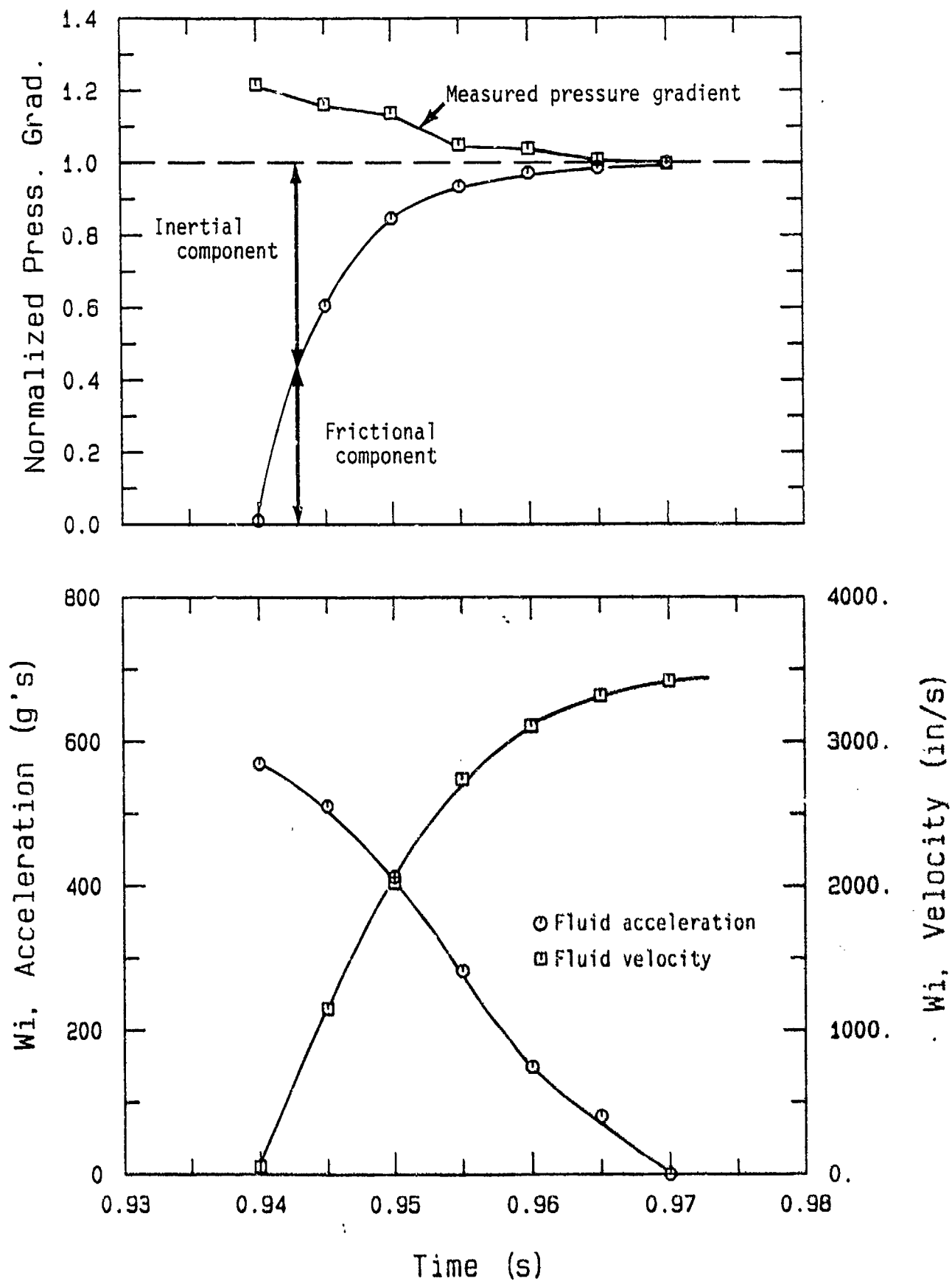


Figure 6.4b. Normalized fluid pressure gradient and fluid motion time histories, flat duct test F16A8.

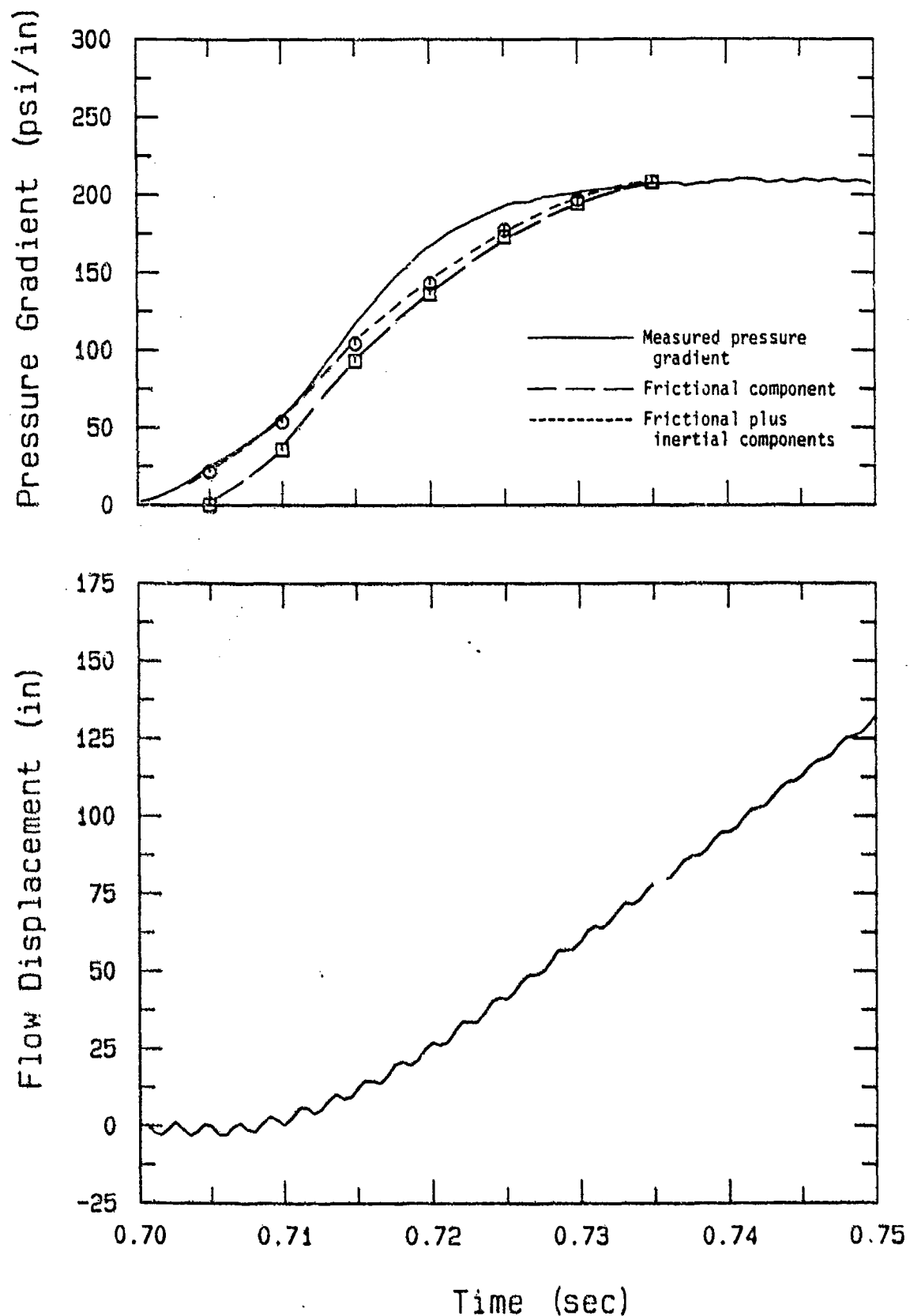


Figure 6.5a. Measured pressure gradient and flow displacement time histories, flat duct test F16B8.

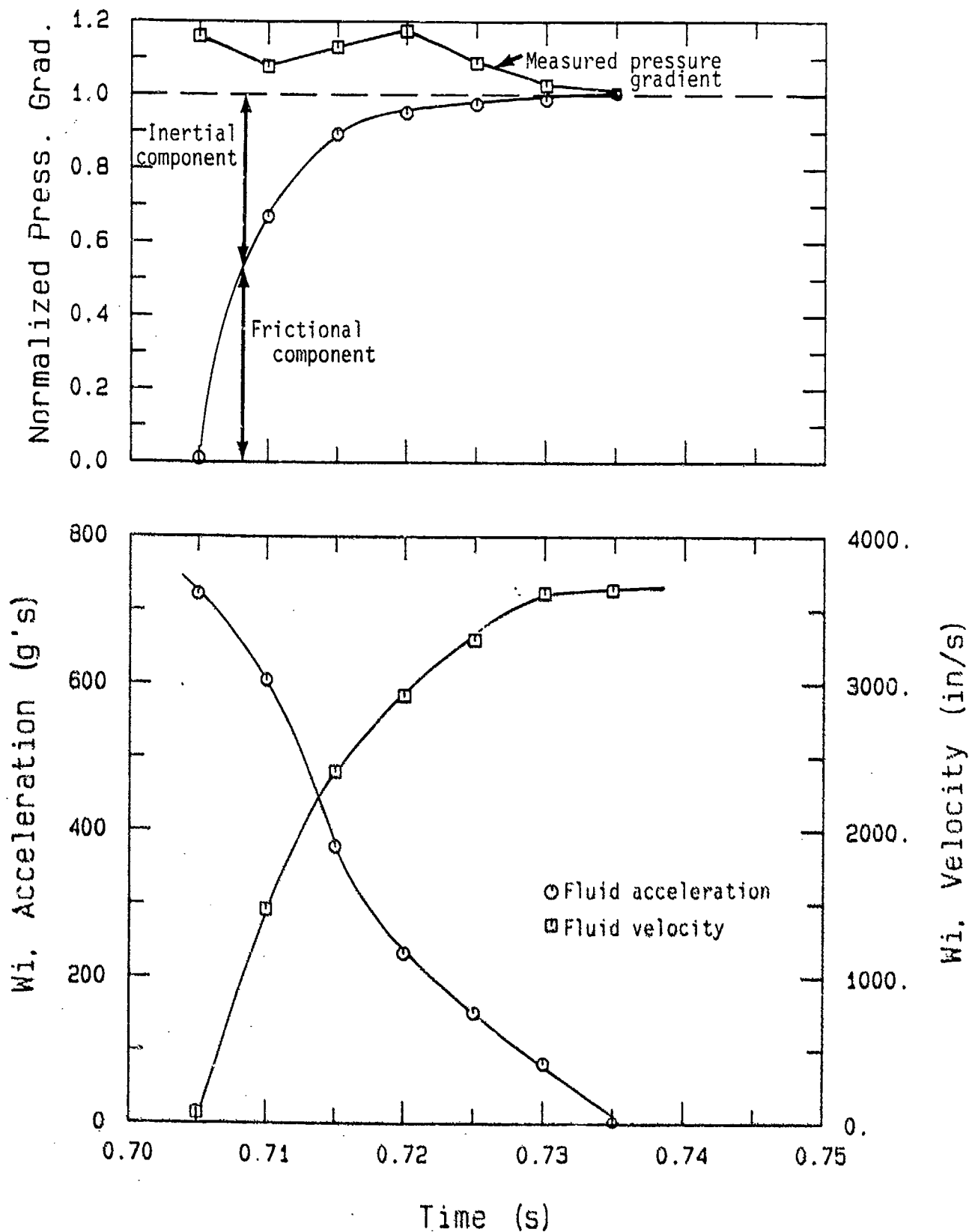


Figure 6.5b. Normalized fluid pressure gradient and fluid motion time histories, flat duct test F16B8.

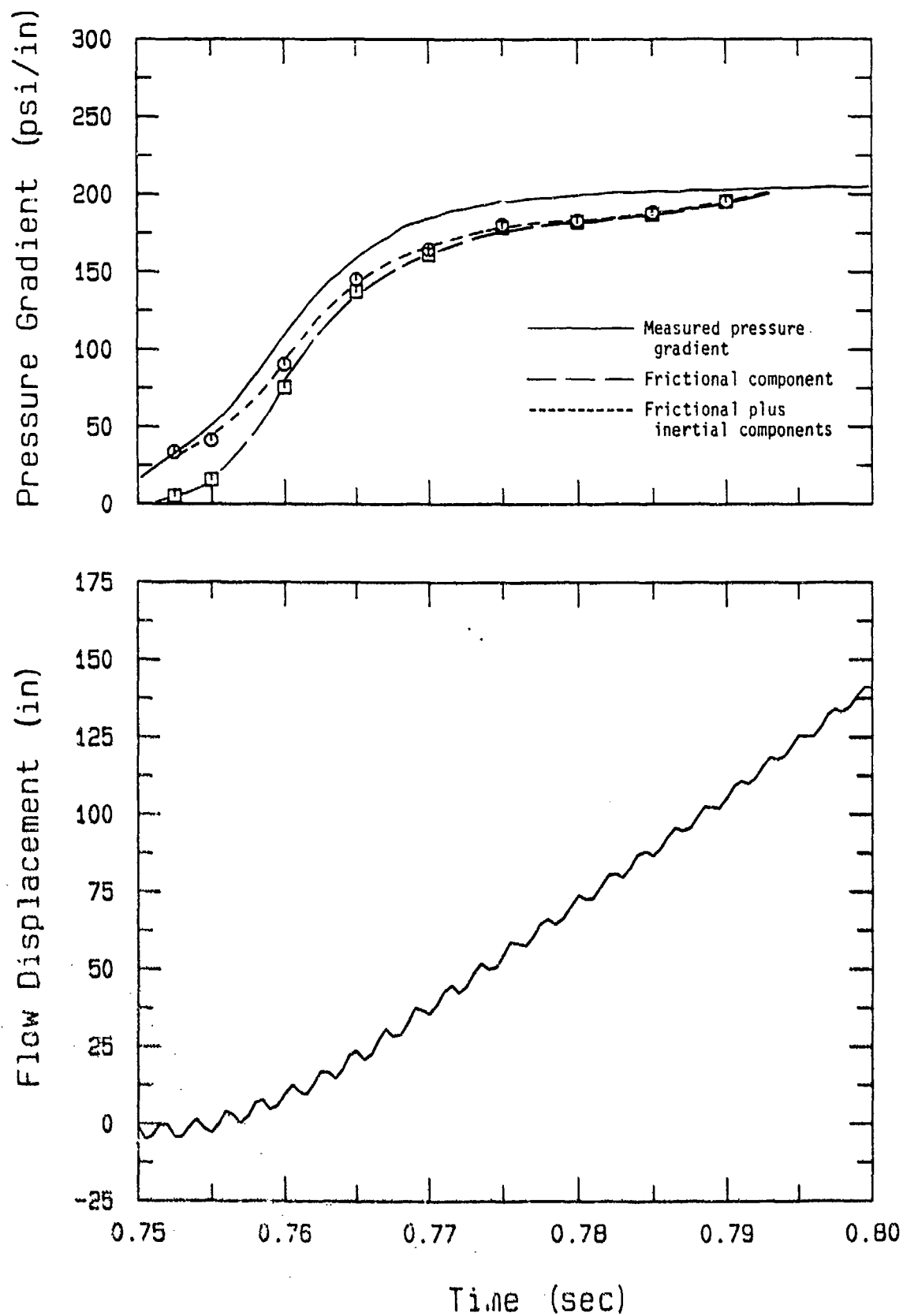


Figure 6.6a. Measured pressure gradient and flow displacement time histories, flat duct test F19A8.

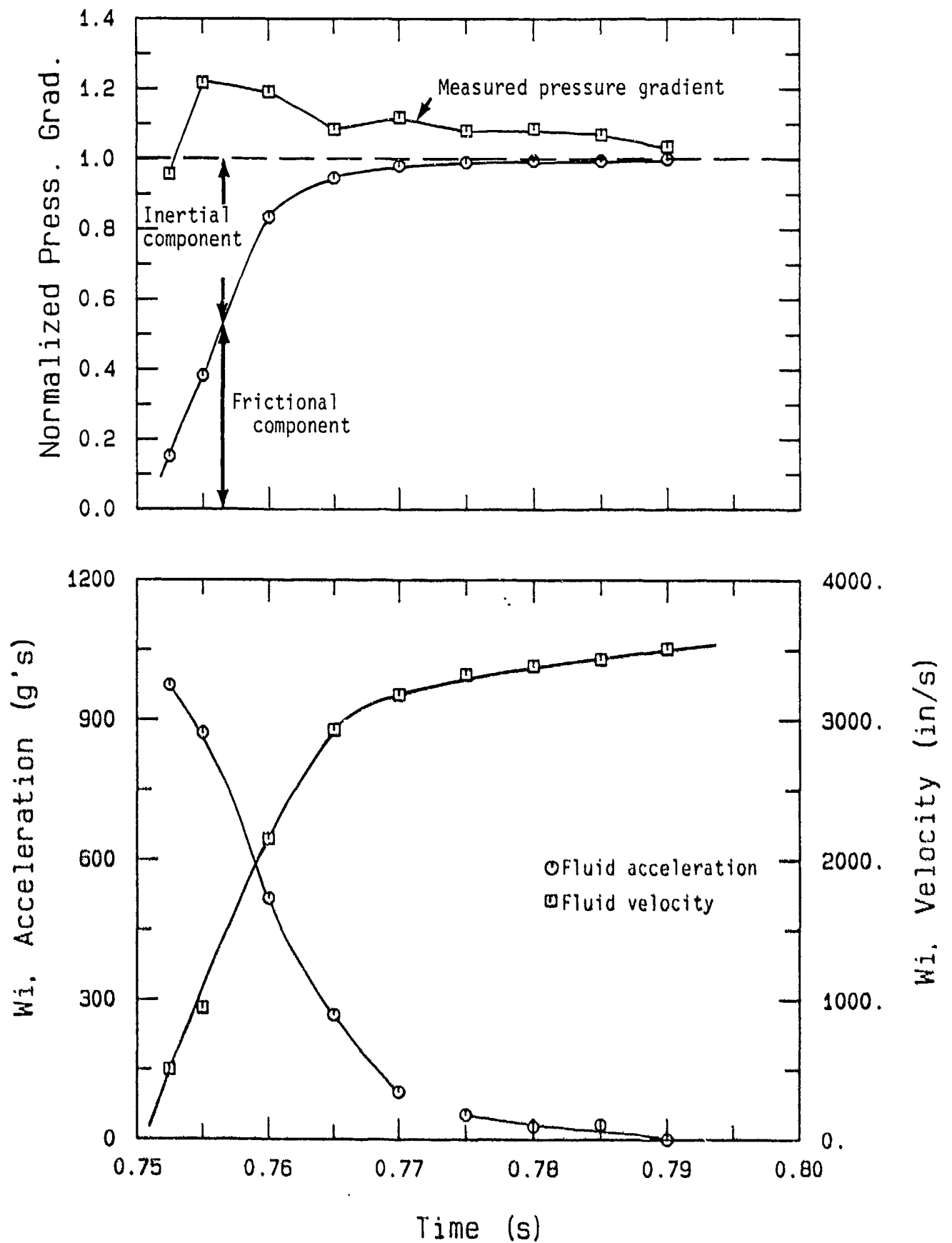


Figure 6.6b. Normalized fluid pressure gradient and fluid motion time histories, flat duct test F19A8.

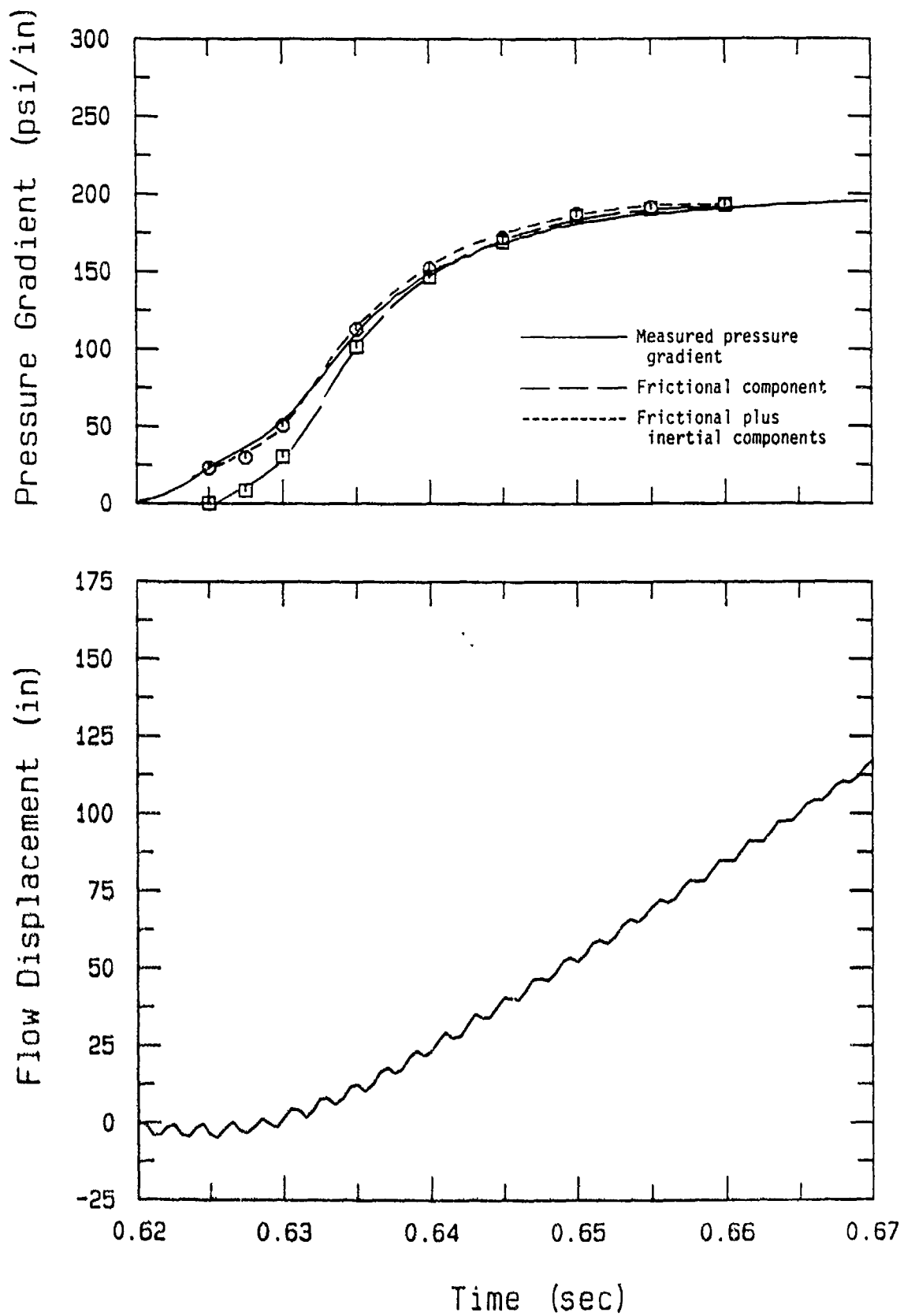


Figure 6.7a. Measured pressure gradient and flow displacement time histories, flat duct test F19B8.

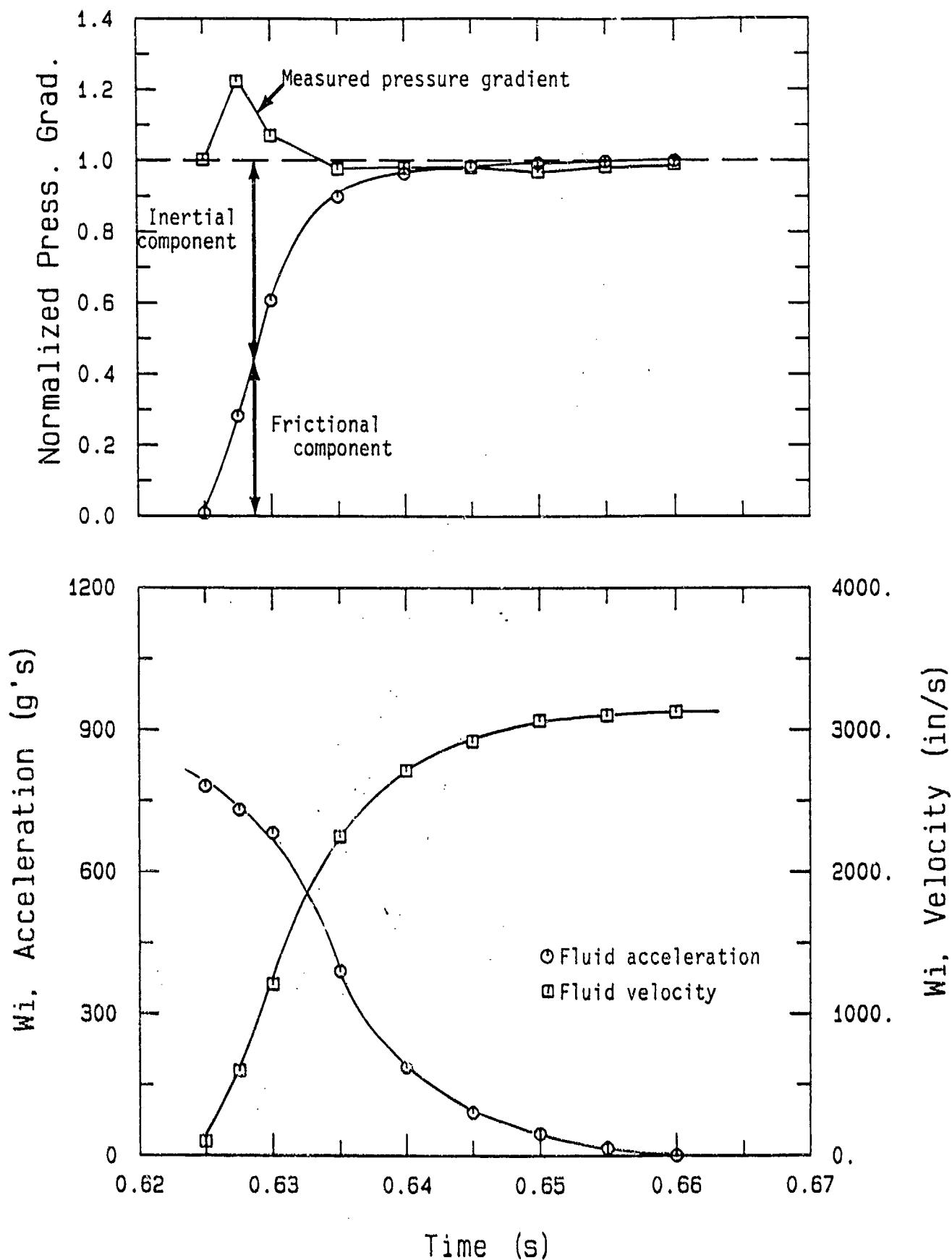


Figure 6.7b. Normalized fluid pressure gradient and fluid motion time histories, flat duct test F19B8.

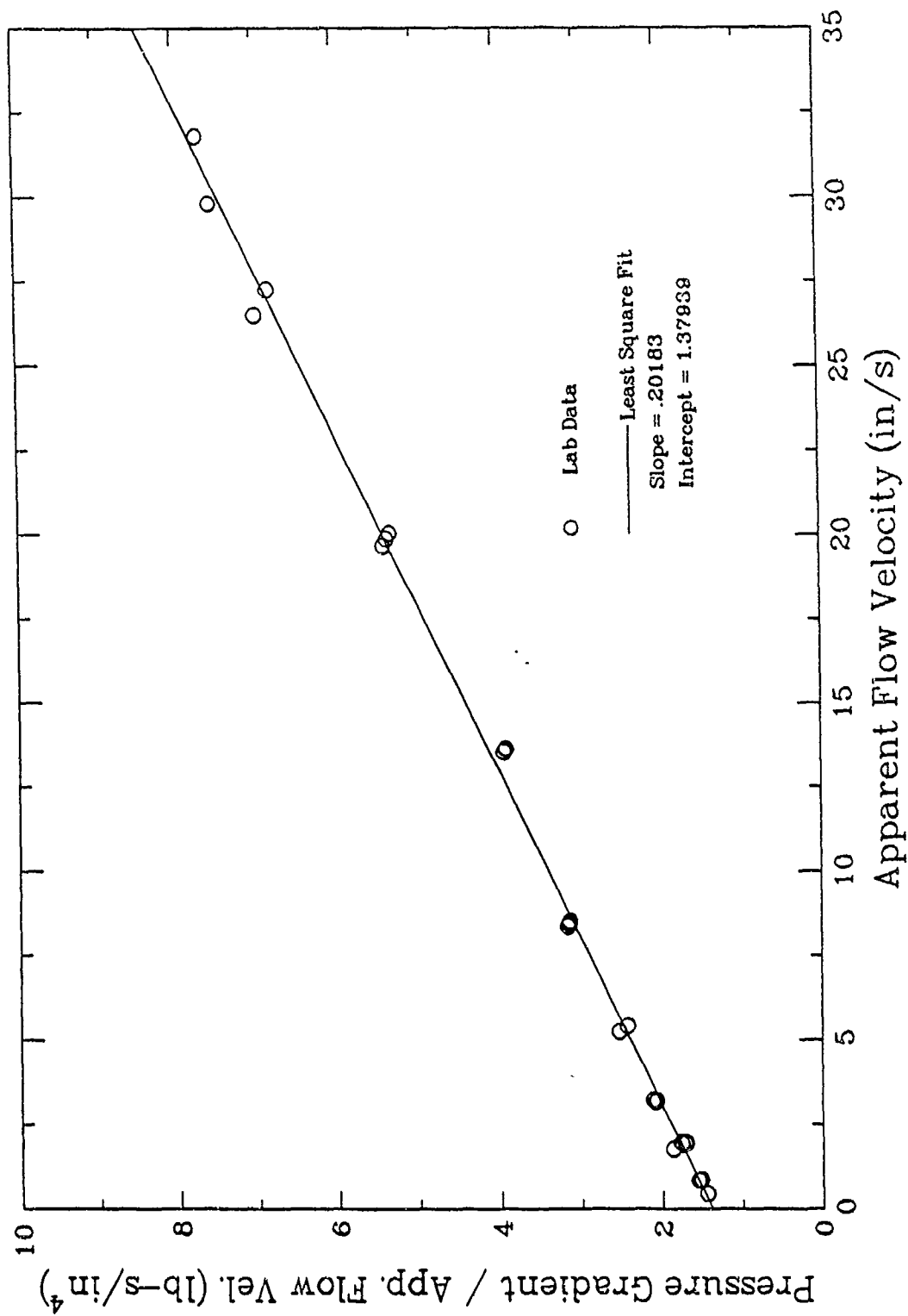


Figure 6.8. Normalized pressure gradient as a function of flow velocity for steady state flow through Enewetak beach sand.

SECTION 7

TWO-PHASE RESPONSE OF SATURATED LIMESTONE

7.1. INTRODUCTION

Applied Research Associates is conducting a series of laboratory tests on Indiana limestone, under sponsorship of Defense Nuclear Agency. The testing program was planned to provide data to formulate and validate two-phase models of the limestone response. In this section, we review these test data in conjunction with the two-phase modeling formulations we have developed under AFOSR sponsorship. The Indiana limestone tests provide a data set against which to evaluate the two-phase model in a much less porous material than we have previously had available.

In addition, a substantial portion of the Indiana limestone testing has been performed along nonconventional specified strain paths. These strain paths are, however, typical of strain paths induced by explosive loadings, and the resulting stress paths provide test data which will challenge modeling efforts.

7.2. LIMESTONE PROPERTIES AND TESTING OUTLINE

The limestone selected for these tests was quarried from the Salem limestone formation by the Elliott Stone Company of Bedford, Indiana. The Salem limestone is a widely used building stone. Table 7.1 lists typical index properties of the Salem limestone. The porosity of the limestone averaged about 13.5%, which is significantly lower than the 36% porosity of the typical Enewetak limestones reported in our previous studies.

Four basic types of tests were run on nominal 2 inch diameter by 4 inch length cylindrical samples of the Salem limestone. These included:

1. Hydrostatic
2. Uniaxial strain
3. Triaxial compression at constant confining pressure
4. Specified strain paths following compression under uniaxial strain.

Both drained and undrained tests with pore pressure measurements were conducted for each test type.

The following subsections highlight the test results and show comparisons to two-phase test simulations using our two-phase models.

7.3. HYDROSTATIC TESTS

A typical drained hydrostatic compression test is shown in Figure 7.1. This is actually a composite of several hydrostatic tests to show unload-reload response. The hydrostat typifies the compression response of the Salem limestone. There is an initial, nearly linear, portion of the loading curve which is essentially elastic and has a high modulus. Bulk moduli of 235 kb are typically measured on the initial part of the loading. At a pressure of over 1 kb, the cementation begins to break down and the pore space begins to be crushed out during a much softer portion of the loading curve. The incremental tangential bulk modulus during this portion of the loading is nearly an order of magnitude softer than the initial modulus. At pressures approaching 4 kb, the limestone begins to show stiffening as approximately half the pore space has been crushed out. Over the 0 to 4 kb pressure range, the initial unloading modulus is approximately equal to the initial loading modulus, and there is a pronounced hook, or heel, as the pressure drops toward zero.

A typical cyclic undrained hydrostatic loading of Salem limestone is shown in Figures 7.2 through 7.4. The test data are compared to a numerical simulation computed using an improved version of the code NKOCP described by Kim, Blouin and Timian, 1987. During the past year, we have modified NKOCP to include a nonlinear unload capability in addition to the original bilinear unload. The NKOCP simulation used the porous skeleton properties obtained from a previous drained test as input. These are combined with our fully coupled two-phase model as described in Section 2.

Figure 7.2 shows the total pressure as a function of volume strain. The initial undrained modulus is significantly higher than the drained modulus, having a value of about 340 kb. Once the sample is loaded beyond the pressure

at which cementation breaks down, there is significant hysteresis due to the nonlinear hysteretic nature of the skeleton. The numerical NKOCP simulation is an excellent match to the test data.

The effective stress response is shown in Figure 7.3. Note that only about half the total pressure is carried by the porous skeleton. The hysteretic nature of the skeleton is apparent, but liquefaction does not occur during the unloading as it did in the more porous Enewetak limestone. However, we would expect liquefaction to occur if the loading had been carried to a higher pressure. Examination of the drained response in Figure 7.1 indicates that above an effective pressure of more than 1.5 kb the unload becomes much more hysteretic which would produce liquefaction in an undrained test. Future tests will be conducted at higher pressure to validate this prediction. The agreement between the measured effective stress response and that simulated by the NKOCP model is again excellent.

Figure 7.4 shows the measured and simulated pore pressure response during the hydrostatic tests. Again, agreement between the two is excellent. There is an apparent negative hysteresis in the pore pressure response which is a result of the rapid unloading of the skeleton and resulting rapid release of compressive strains in the solid grains. This phenomenon is fully explained by Kim, Blouin and Timian, 1987, and highlighted in Section 1 of this report.

7.4. UNIAXIAL STRAIN TESTS

A typical drained uniaxial strain test is plotted in terms of axial stress versus axial strain in Figure 7.5. The skeleton response is similar to that of the hydrostatic drained test (Figure 7.1) but the initial elastic constrained modulus, M , is correspondingly higher at about 420 kb. The cementation breaks down at an axial stress between 1.5 and 2 kb and a nearly linear, but softer portion of the loading occurs as the porosity is crushed out of the sample. The incremental tangential constrained modulus along this portion of the loading, about 50 kb, is nearly an order of magnitude less than the initial modulus. At an axial stress of about 3.5 kb the skeleton begins to stiffen as a significant volume of the pores have been crushed out. The

initial unloading modulus tends to about equal the initial elastic loading modulus, for peak axial stresses of less than about 4 kb. At higher peak stresses, the initial unloading modulus appears to be increasing with increasing peak axial stress. Also note that the uniaxial unloading cannot be maintained back to zero axial stress because of plastic strains occurring during loading of the sample. At some point in the unloading, the axial stress drops to the confining pressure. In order to continue the unload and maintain no lateral strain, it would be necessary to apply axial expansion to the samples, a condition which could not be achieved during these tests. Thus, as noted in Figure 7.5, the last portion of the final unload is actually hydrostatic, rather than uniaxial.

The relationship between the axial stress and the confining stress during the drained uniaxial strain test is shown in Figure 7.6. During the initial elastic loading the apparent Poisson's ratio, ν_a , defined as

$$\nu_a = \frac{\Delta K_0}{1 + \Delta K_0} \quad (7-1)$$

or

$$\nu_a = \frac{\Delta \sigma_r}{\Delta \sigma_a + \Delta \sigma_r} \quad (7-2)$$

where ΔK_0 = the incremental coefficient of lateral earth pressure

$\Delta \sigma_r$ = incremental change in confining stress

$\Delta \sigma_a$ = incremental change in axial stress

is equal to about 0.25. During the portion of the loading beyond the breakdown of cementation, the material responds more nearly hydrostatically, and the apparent Poisson's ratio increases to 0.42. During the uniaxial unload, the apparent Poisson's ratio drops to 0.32. The hydrostatic portion of the final unload begins at a confining stress of about 2 kb.

Stress difference versus axial (or volume) strain is plotted for the uniaxial test in Figure 7.7. At a stress difference of about 1 kb, the

cementation collapses and there is only a slow further increase in stress difference. In terms of stress difference, the unloadings reach a value of zero at which point the sample is under a hydrostatic compressive load, as can be seen in Figure 7.6.

The mean stress versus volume strain from the uniaxial test is shown in Figure 7.8. It is compared to the drained hydrostat from Figure 7.1. During the elastic portion of the loading, and at mean stress above about 3.5 kb, the response is essentially identical to the hydrostat. However, the collapse of the cementation occurred at consistently lower mean stresses in the uniaxial tests because the material is subjected to an additional component of shear stress. This results in a deviation between the two data sets over the intermediate mean stress range.

An undrained uniaxial strain loading of Salem limestone is shown in Figure 7.9 through 7.11. In Figure 7.9, parts a through c, the total axial stress, effective axial stress and pore pressure are plotted against axial strain, respectively. A numerical simulation was generated using NKOCIP in which a set of drained uniaxial test data were used as inputs to NKOCIP. The agreement between the total stress response of the test and the numerical simulation is excellent. There are, however, differences in the effective stress response and the pore pressure response between the test and simulation. These are primarily due to differences in the skeleton properties of the two samples being compared, as is apparent in Figure 7.9b. The softer skeleton in the undrained test resulted in a higher portion of the total stress being carried by the pore pressure in that test.

The relationship between the axial and radial stress during the undrained uniaxial strain loading is shown in Figure 7.10 in terms of both effective and total stress. Because of the stress component carried by the pore fluid, the apparent values of K_0 , in terms of total stress, are significantly higher than values in terms of effective stress.

The stress paths for the undrained uniaxial loading are shown in Figure 7.11 in terms of both effective stress and total stress. The effective stress

closely matches those from drained uniaxial strain tests. It falls just below the drained ultimate strength envelope obtained from triaxial compression tests. The total stress path is much flatter than the effective stress path because of the significant portion of total stress carried by the pore fluid.

7.5. TRIAXIAL COMPARISON TESTS

Data from the drained triaxial compression tests on Salem limestone at constant confining pressure are presented in Figures 7.12 through 7.15. Figure 7.12 shows stress difference versus axial and radial strain for a series of tests at six different confining pressures ranging from 0 to 4 kb. At confining pressures of $\frac{1}{2}$ kb and less the samples fail in a brittle manner. At higher confining pressures the samples fail in a ductile mode with stress difference continuing to increase with increasing axial strain. The initial modulus indicated by the slopes of the stress-strain curves is comparatively high for samples in the brittle failure regime at low confining pressures. Above the point where cementation has been crushed by the initial confining pressure, the initial moduli are softer than those in the brittle regime. The tests at 2 and 3 kb confining pressure exhibit lower initial moduli than the tests at lower confining pressures. As the initial confining pressure is increased further, the modulus increases due to crush out of the pore space by the hydrostatic pressure applied prior to starting the triaxial shearing.

The volume strain response during the triaxial shear portion of the loading is shown in Figure 7.13 for the six tests. In all cases, the samples undergo compressive volume strains during the initial portion of the shearing. As the ultimate failure stress is approached, the rock begins to dilate, as indicated by the incremental volume expansion. The sample at 2 kb confining pressure shows the greatest amount of compression during shear. At higher confining pressures the compressive volume strain tends to decrease, with the sample at 4 kb experiencing nearly a constant volume shear.

The ultimate strength of the Salem limestone from the triaxial tests is plotted in Figure 7.14. For purposes of this figure, ultimate strength is defined either as the maximum stress difference reached during the tests for

samples which failed in the brittle regime, or as the stress difference at 15% axial strain for samples at higher confining pressures in the ductile regime. We have also included test data from Salem limestone obtained by the Waterways Experiment Station (WES) from Zelasko, 1988. The test data define an ultimate failure envelope which is linear below about 2 kb stress difference and has a cohesion of $c = 0.16$ kb and a friction angle of 49° ($\phi = 29^\circ$, in the traditional Mohr-Coulomb stress space). Above a stress difference of 2 kb, the envelope is concave downward toward the mean stress axis.

By plotting the stress difference at which the incremental volume strain changes from compressive to dilatent (i.e. where the slopes become infinite in Figure 7.13), we can plot a contour which defines the onset of dilatency. This is shown in Figure 7.15, and lies just beneath the ultimate failure surface plotted in Figure 7.14. In other words, to reach the ultimate failure surface, the rock must incrementally dilate and the incremental dilation begins when the rock reaches the stress contour shown in Figure 7.15.

The undrained triaxial compression test data are presented in Figures 7.16 through 7.19. The stress difference as a function of axial and radial strains is shown for tests at four confining pressures in Figure 7.16. All samples exhibit very similar behavior with a rapid increase in stress difference until failure at an axial strain ranging from 0.5 to 1.0%. The strength is only slightly dependent on the total confining pressure. There is no further increase in stress difference with increasing axial strain.

The effective stress paths for the four undrained tests are shown in Figure 7.17. The initial effective stresses following the hydrostatic portion of the test are approximately half of the total confining pressure. The maximum effective stress difference in each test agrees reasonably well with the drained ultimate strength envelope from Figure 7.14. In terms of total stress, the strength envelope would exhibit a friction angle of only about 10° , as indicated in Figure 7.17 (vs 49° for the drained envelope). Note that the effective stress paths tend to be concave toward the mean effective stress axis at low confining pressures, but concave toward the stress difference axis at higher confining pressures. This difference in stress indicates that pore pressures are increasing more rapidly in the higher confining pressure tests.

Stress difference as a function of volume strain for the undrained tests is shown in Figure 7.18. As would be expected, there is a slightly compressive volume strain occurring during the initial portion of the loading. Once the effective stresses reach the strength envelope, however, there is a sudden failure and the samples begin to dilate strongly. Dilation occurs throughout the remainder of the test, with no further increase in stress difference.

A corresponding plot of pore pressure as a function of volume strain is shown in Figure 7.19. There is an increase in pore pressure during the initial loading, followed by a sudden leveling off once failure occurs. During the dilatant portion of the test the pore pressure remains nearly constant for the tests at the higher confining pressures and decreases slowly for the 0.5 kb confining pressure test.

The behavior demonstrated by the test data in Figures 7.18 and 7.19 and contradicts what we would expect from effective stress theory and demonstrates a shortcoming of undrained triaxial strength tests. The volume strain is measured at the midpoint of the cylindrical test specimen. At the midpoint, where the shear failure is occurring, the sample is dilating rapidly. Local pore pressures within this shear zone should be dropping rapidly as volume expansion occurs. As pore pressures drop, effective stresses and the stress difference should both increase. Figures 7.16 through 7.19 clearly demonstrate that this does not occur during the latter stages of the undrained tests. We believe the reason that pore pressure doesn't decrease is that total volume strain of the specimen remains nearly constant during shearing. For the total volume strain to remain constant, the ends of the sample, constrained radially by the steel end caps, must be undergoing volumetric compaction while the center is experiencing the measured volumetric expansion.

In essence, we believe that the radial constraint imposed by the sample end caps prevents the sample strength from increasing during the later stages of shear. This is a serious shortcoming of the undrained triaxial test which underestimates the sample strength at higher shear strains and could lead to gross errors in predicting the late time in situ response of saturated porous media.

7.6. STRAIN PATH TESTS

A series of drained and undrained load-unload cycles was performed on Salem limestone following predesignated strain paths. The strain paths were chosen to be representative of strain paths from various depths beneath shallow buried explosive detonations as predicted by finite difference calculations performed by several of the national laboratories. Figure 7.20 is a schematic view of the strain paths. All paths undergo an initial compression under uniaxial strain conditions, then from a designated point on the uniaxial loading curve, one of four paths is followed:

1. Path A: a constant volume path in which axial strain continues in compression while radial strain is allowed to expand at half the rate of axial compression resulting in a constant volume shearing;
2. Path B: a constant axial strain path in which axial strain is held constant while radial expands;
3. Path C: an iso-unloading path in which both axial and radial strains expand at the same rate;NS
4. Path D: a uniaxial strain unload which is the same as that used in the uniaxial strain tests described in Section 7.4.

The actual drained strain paths and resultant stress Paths for paths A, B, and C are plotted in Figures 7.21a, 7.22a and 7.23a, respectively. The Type A constant volume stress paths, shown in Figure 7.21b, show increasing shear stress with decreasing mean stress, approaching the constant volume strength contour (from Figure 7.15) along a path nearly perpendicular to it. Similar tests run by WES to larger shear strains showed some further gain in shear strength as the stress path turned upward and toward the right as it moved along the constant volume contour.

The Type B, constant axial strain stress paths, are shown in Figure 7.22b. These tend to move laterally toward the ultimate strength envelope without further increase in stress difference. In all cases, the stress paths

extend slightly beyond the strength envelope, which indicates that the material has been strengthened somewhat by the compaction process during uniaxial strain loading.

The Type C, iso-unloading stress paths, are shown in Figure 7.23b. These tend to unload down the uniaxial loading stress paths without the sample reaching failure.

Figure 7.24 is an idealized schematic representation of the stress paths resulting from the four prescribed strain paths. The stress paths represent a range of material response which will be difficult to match with most existing models.

Undrained strain paths for samples loaded along Path B (constant axial strain) and Path C (iso-unload) are shown in Figures 7.25 and 7.26. In the stress path for the Type B loading of Figure 7.25b, the effective stress response is very similar to that of the drained tests in Figure 7.22b. Note that both the effective stress path and the total stress path converge on the strength envelope indicating that pore pressure has dropped to zero at this point. Thus, the drained strength envelope serves both the effective stress and total stress response for the Type B strain path.

The effective stress response for the Type C strain path, shown in Figure 7.26b, is also very similar to that of the drained tests shown in Figure 7.23b. Note that pore pressure also drops to zero for this load path prior to complete unloading and that the sample does not undergo failure.

Figure 7.27 shows hypothesized strength envelopes in terms of both effective and total stresses for undrained Type A and B strain paths and triaxial compression tests. These were constructed using NKOC numerical simulations of the initial hydrostatic and uniaxial strain portions of the loadings, then approximating the shear loadings using effective stress theory and adaptation of our two-phase model. This figure demonstrates that:

1. strength envelopes expressed in terms of effective stress do not vary with the strain path and match the envelopes determined from drained tests; and

2. strength envelopes expressed in terms of total stress vary dramatically, being dependent on the strain path.

Because of the dependence of undrained strength on the strain paths, the appropriateness of using equivalent single-phase models for ground shock calculations in saturated media (a common practice) is questioned. Such models cannot make direct compensation for the influence of various strain paths on strength and post failure response.

Table 7.1. Typical Salem Limestone Properties.

	Salem Limestone (Avg. 6 samples)	
Dry Density (lb/ft ³) (kg/m ³)	147.4	2359
Porosity	.135	
Specific Gravity of Grains	2.728	
Permeability (cm/s)	5.3 x 10 ⁻⁵ (1 sample)	
Ultrasonic P Wave Velocity (ft/s) (m/s)	14806	4514
Yield Stress (unconfined) (lb/in ²) (kb)	5540	.382
Ultimate Stress (unconfined) (lb/in ²) (kb)	7752	.535
Young's Modulus (lb/in ²) (kb)	3.9 x 10 ⁶	270
Yield Strain (unconfined) (Axial, %)	.168	
Ultimate Strain (unconfined) (Axial, %)	.261	

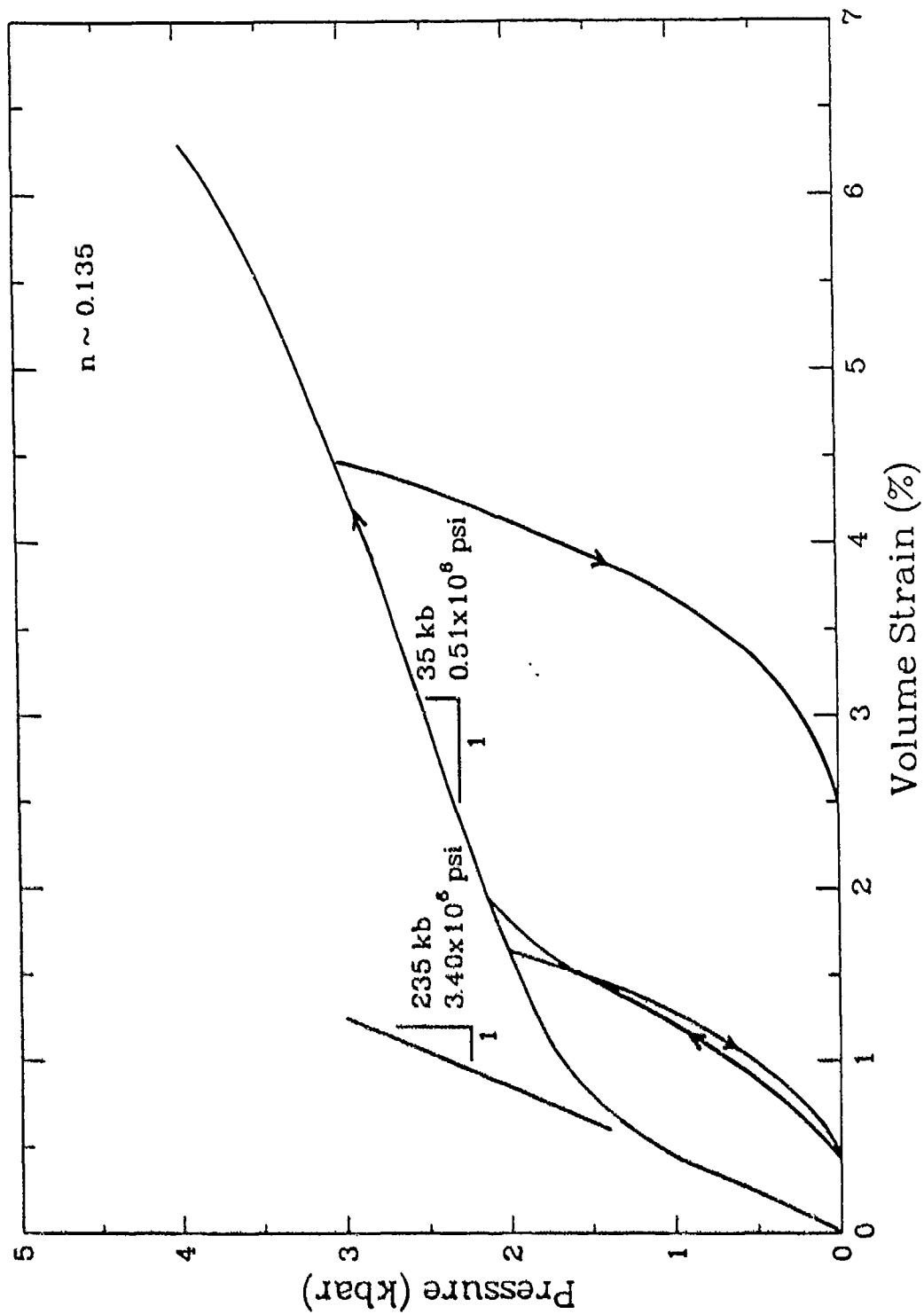


Figure 7.1. Typical drained hydrostat on Salem limestone.

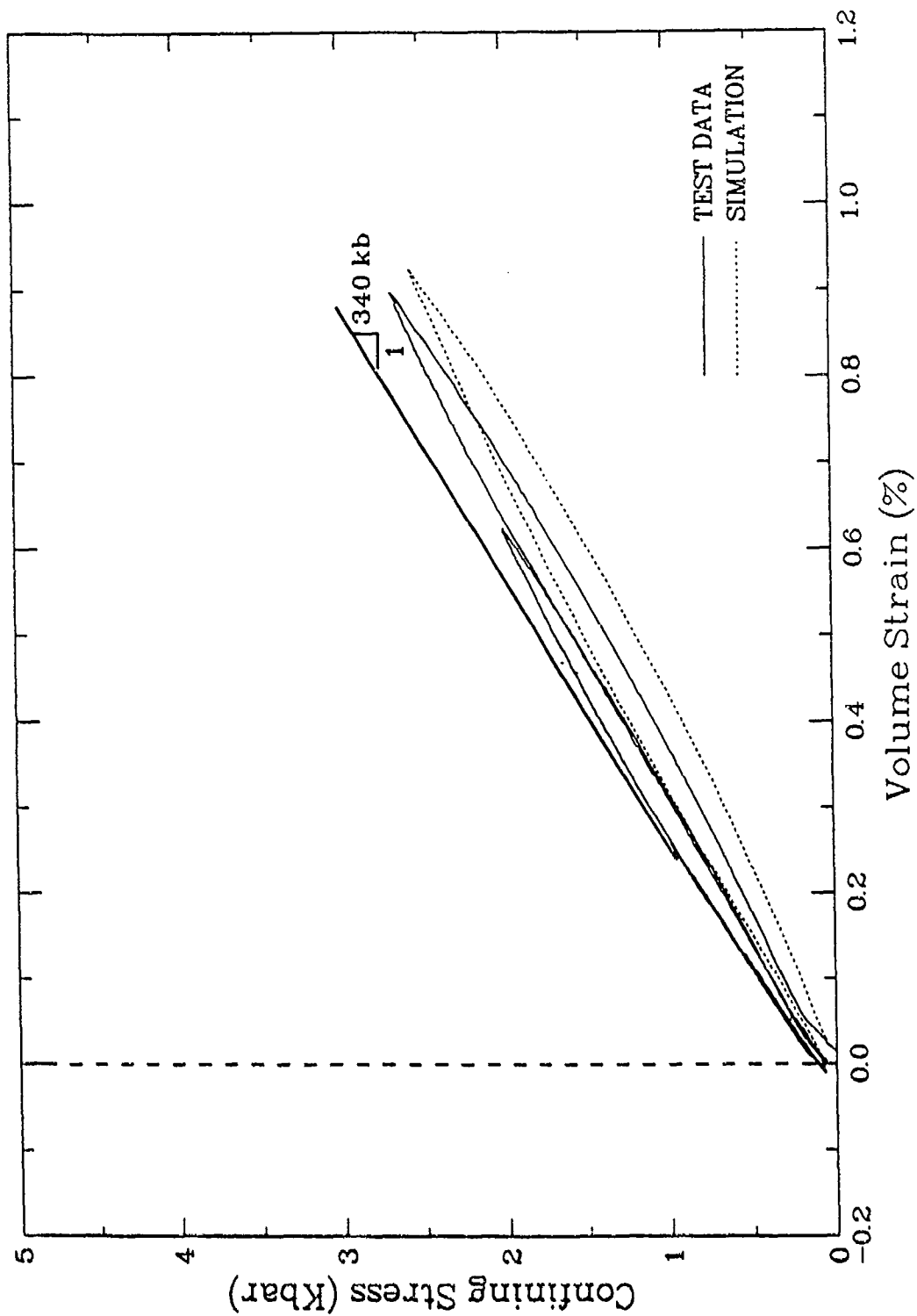


Figure 7.2. Comparison of total stress from an undrained hydrostatic compression test with a two-phase simulation using skeleton properties from drained test data.

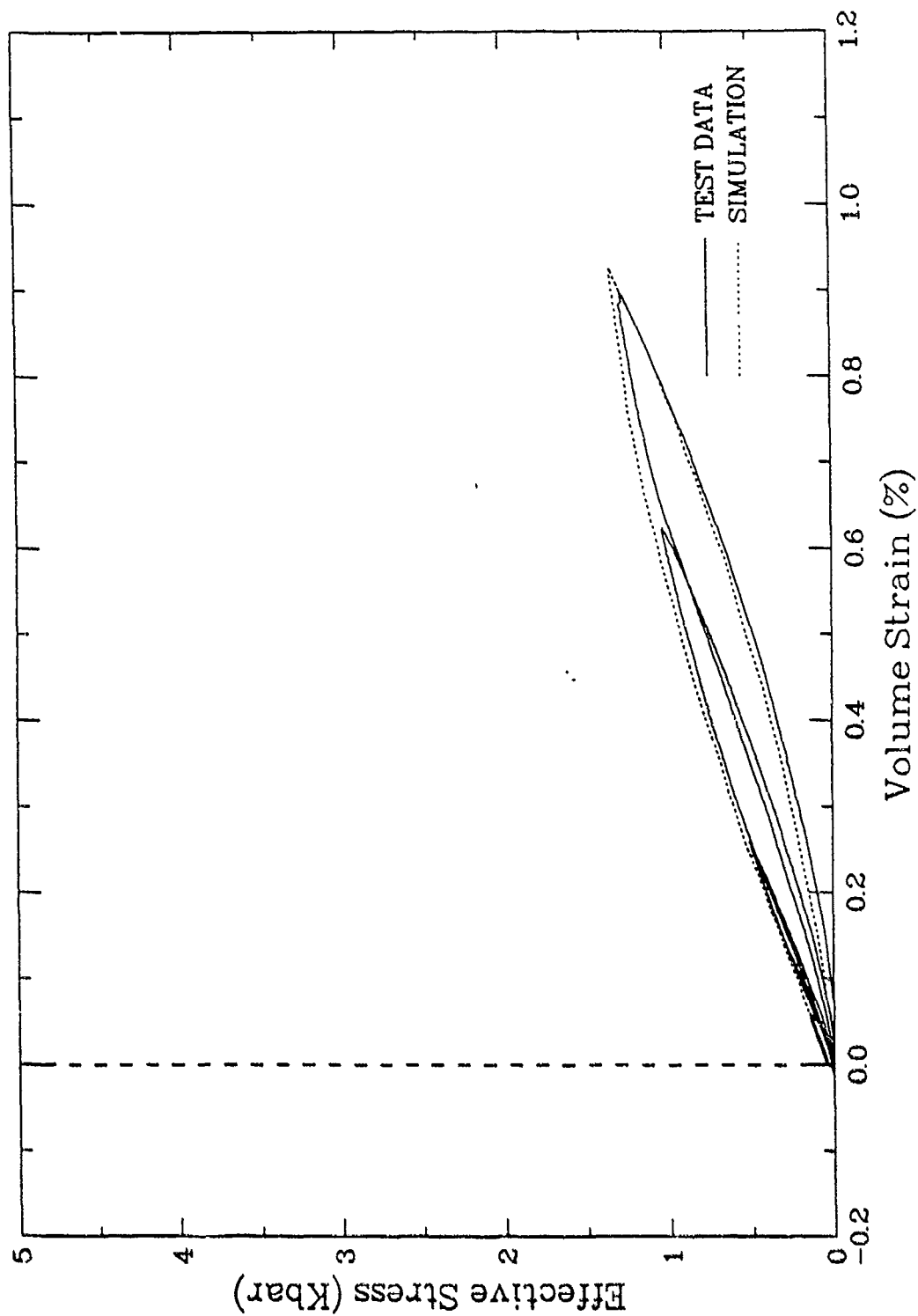


Figure 7.3. Comparison of effective stress from an undrained hydrostatic compression test with a two-phase simulation using skeleton properties from drained test data.

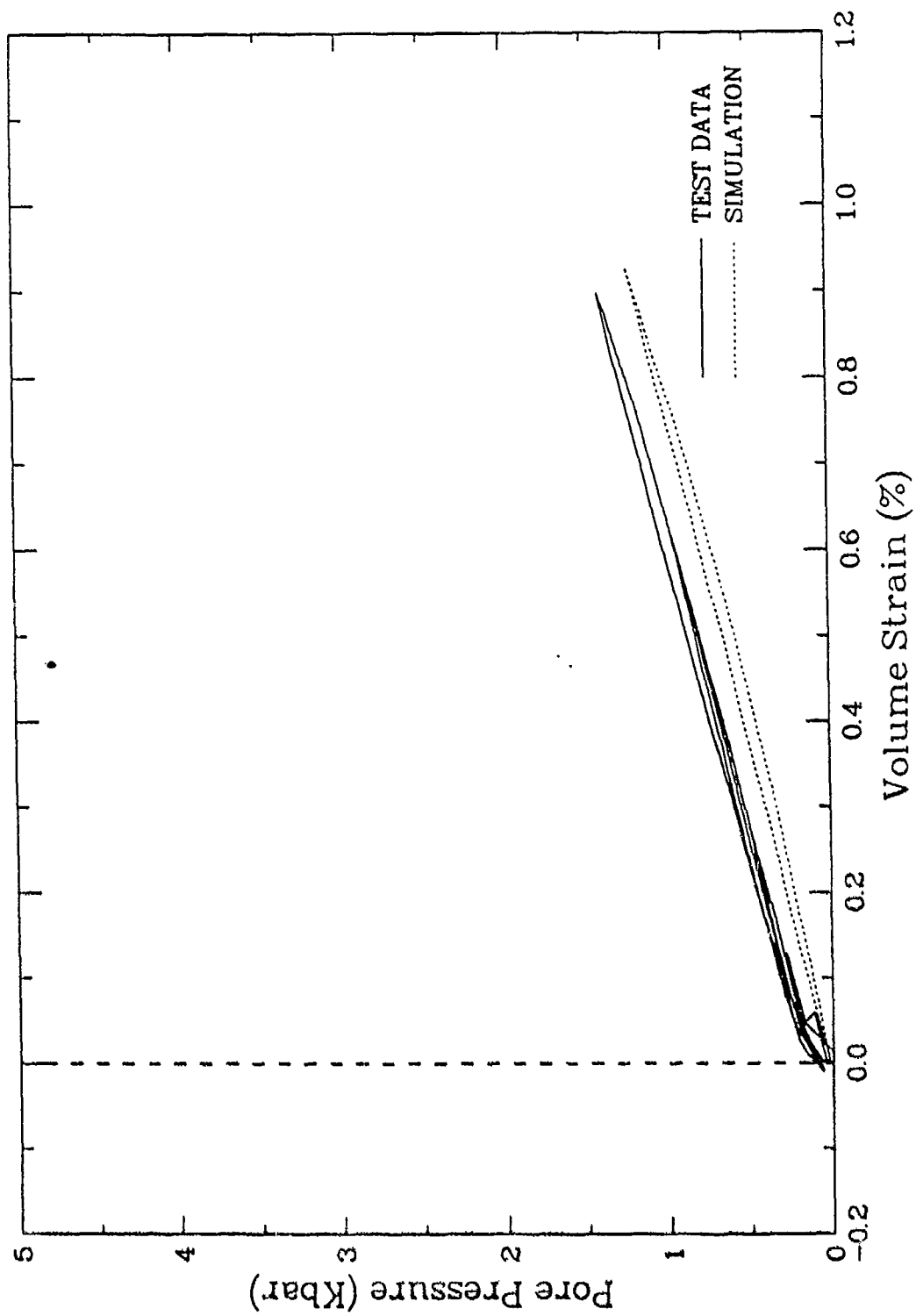


Figure 7.4. Comparison of pore pressure from an undrained hydrostatic compression test with a two-phase simulation using skeleton properties from drained test data.

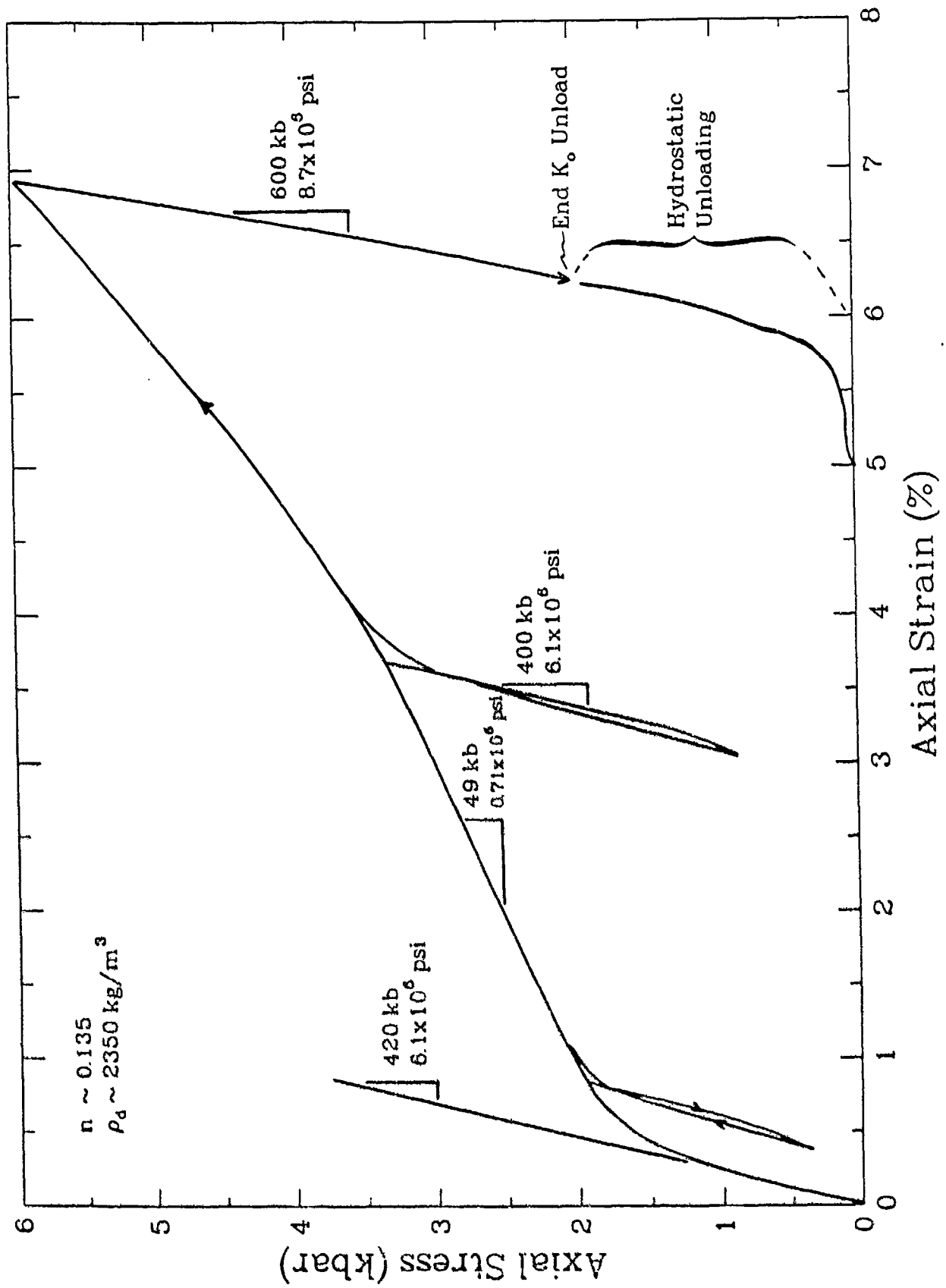


Figure 7.5. Typical drained uniaxial strain loading on Salem limestone.

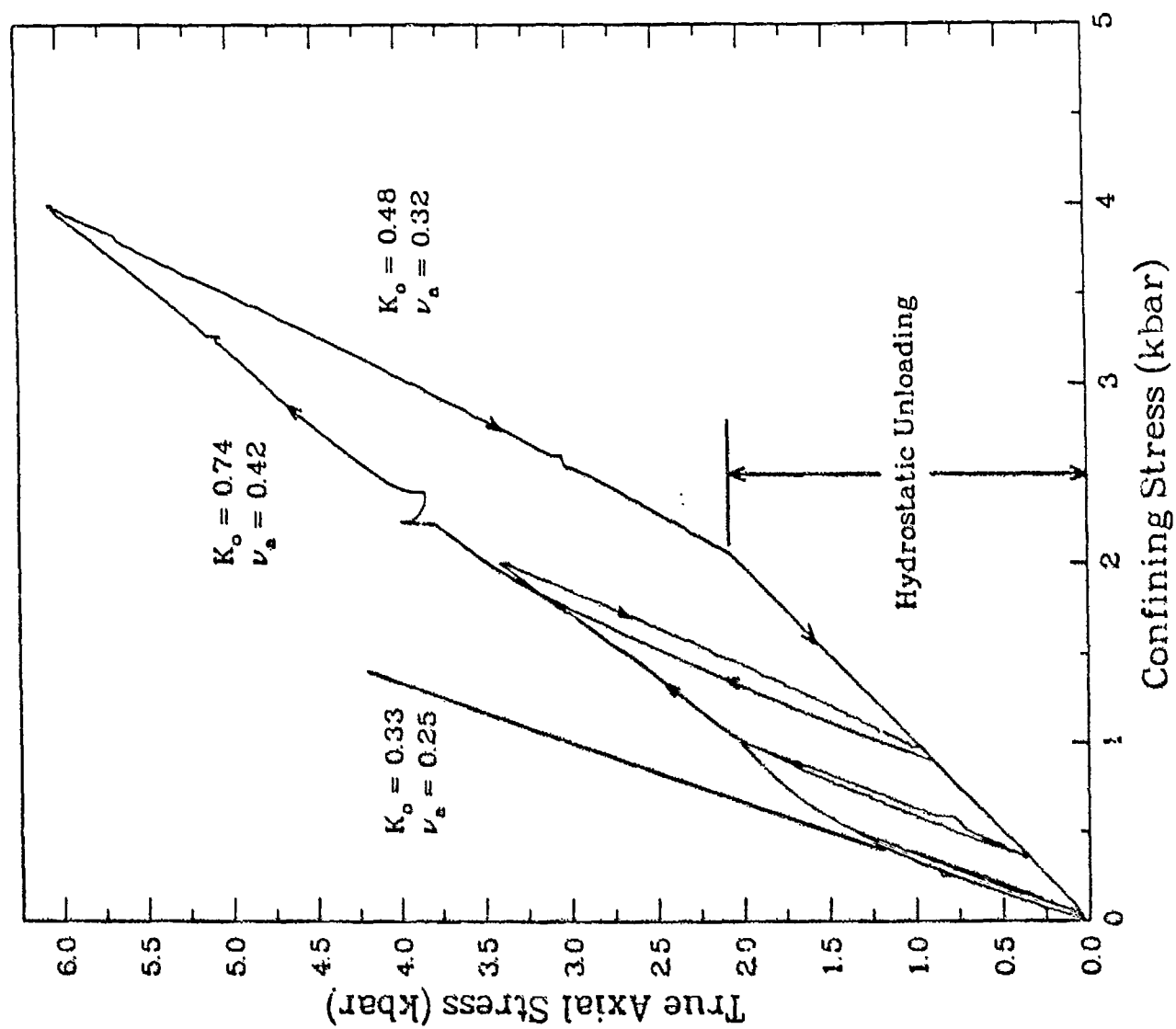


Figure 7.6. Drained uniaxial strain test on Salem limestone; relationship between axial stress and confining stress

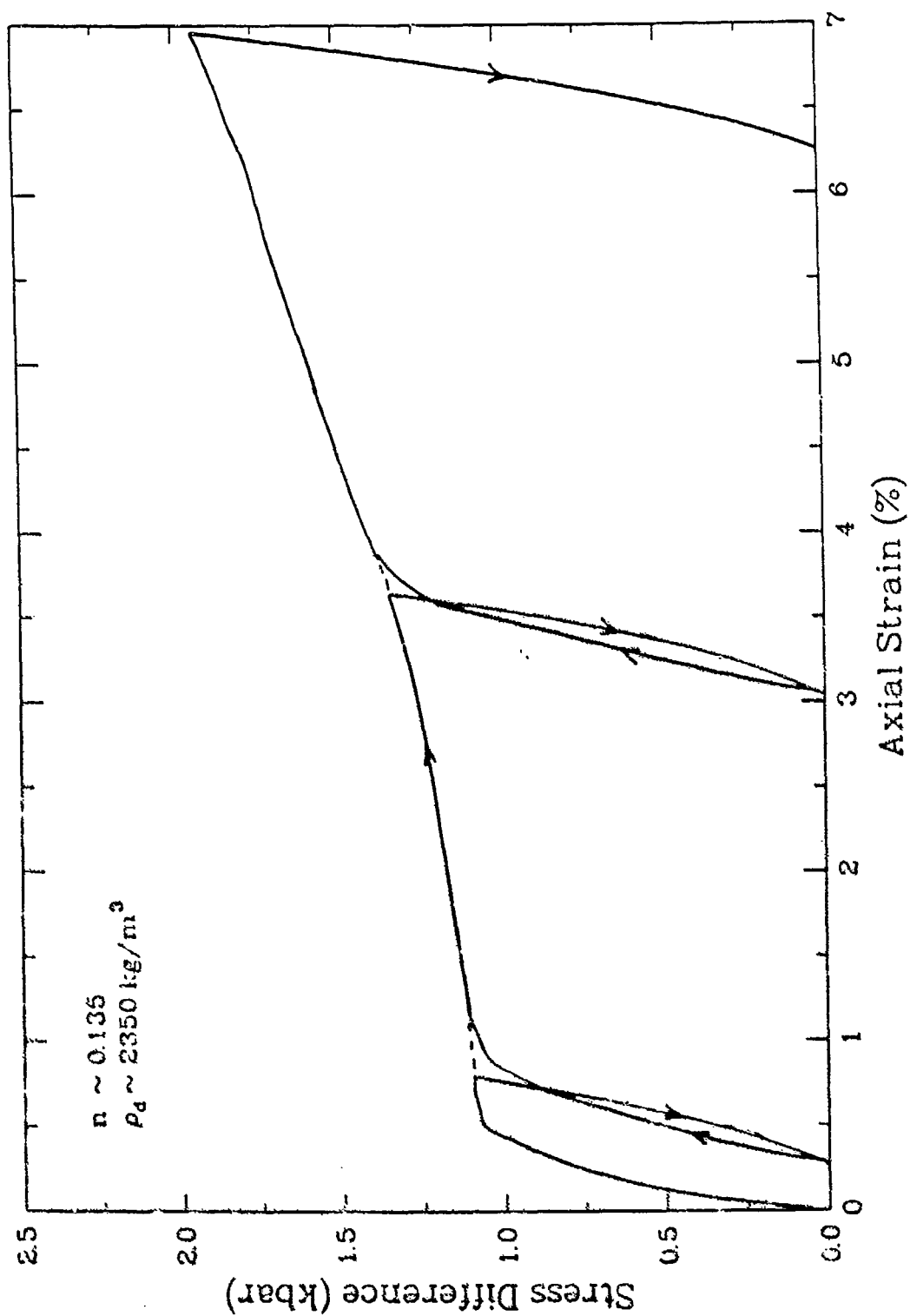


Figure 7.7. Drained uniaxial strain test on Salem limestone; relationship between stress difference and volume strain.

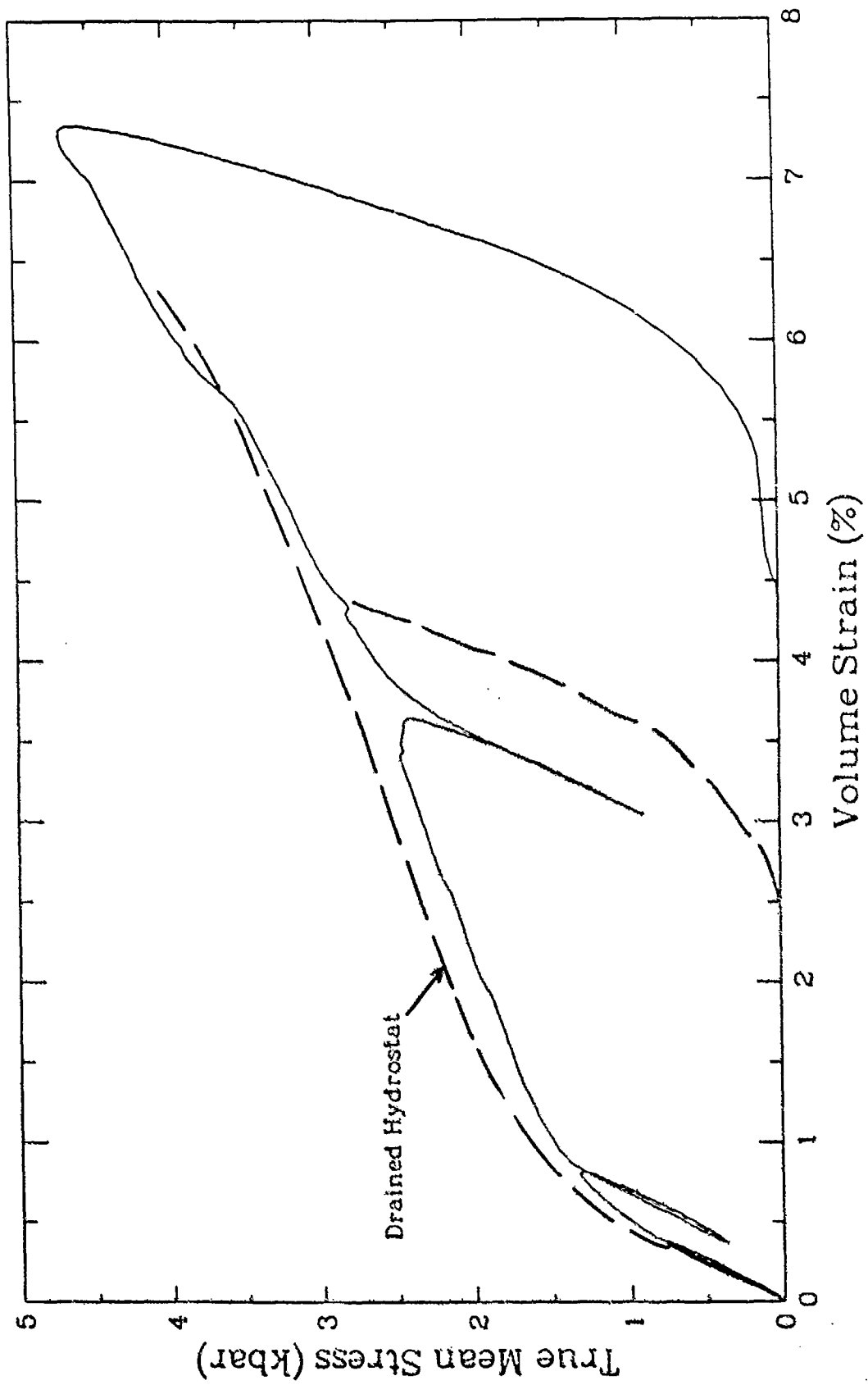


Figure 7.8. Drained uniaxial strain test on Salem limestone; relationship between true mean stress and volume strain.

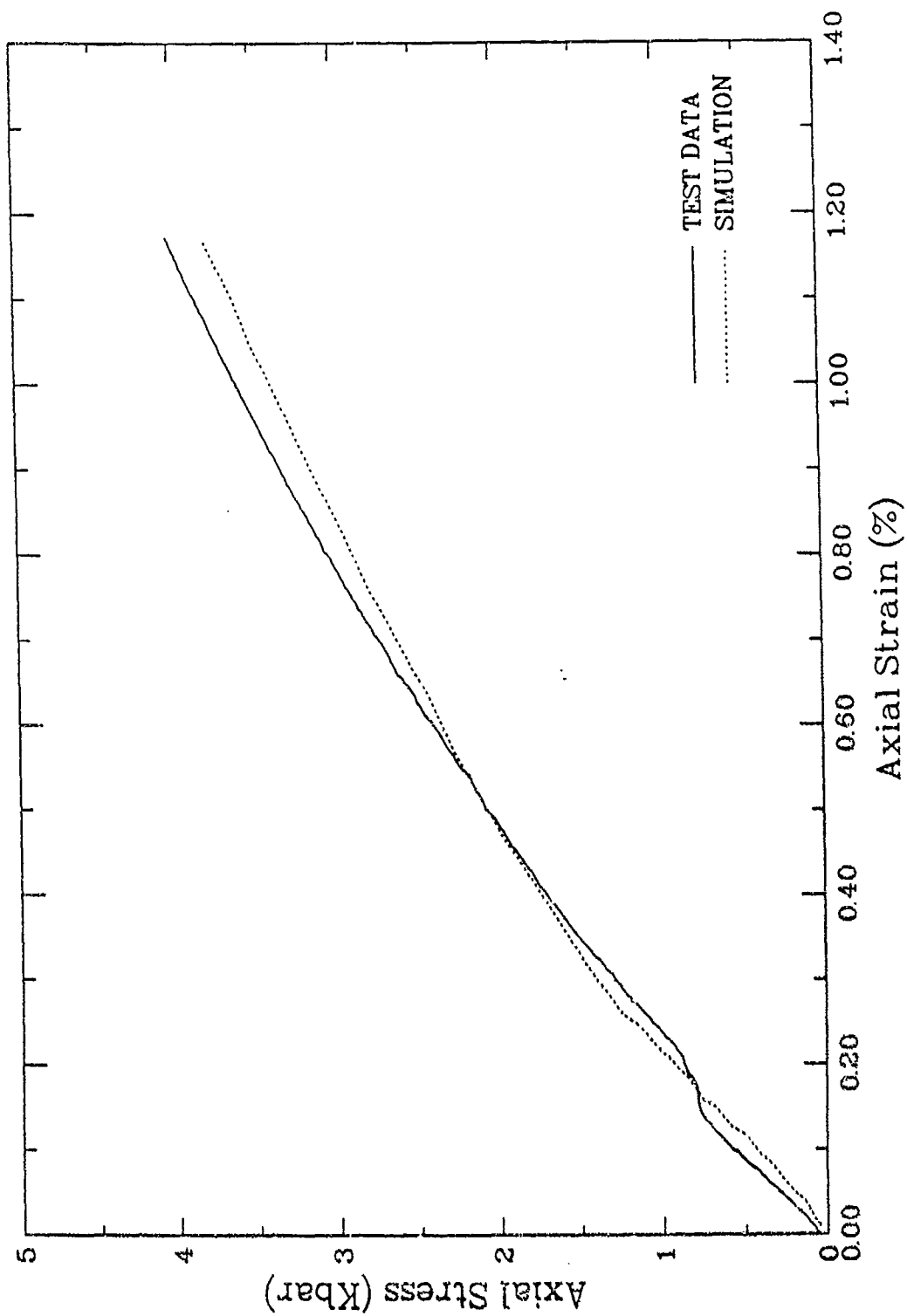


Figure 7.9a. Comparison of total stress from an undrained uniaxial strain test with a two-phase simulation using skeleton properties of Salem limestone from drained test data.

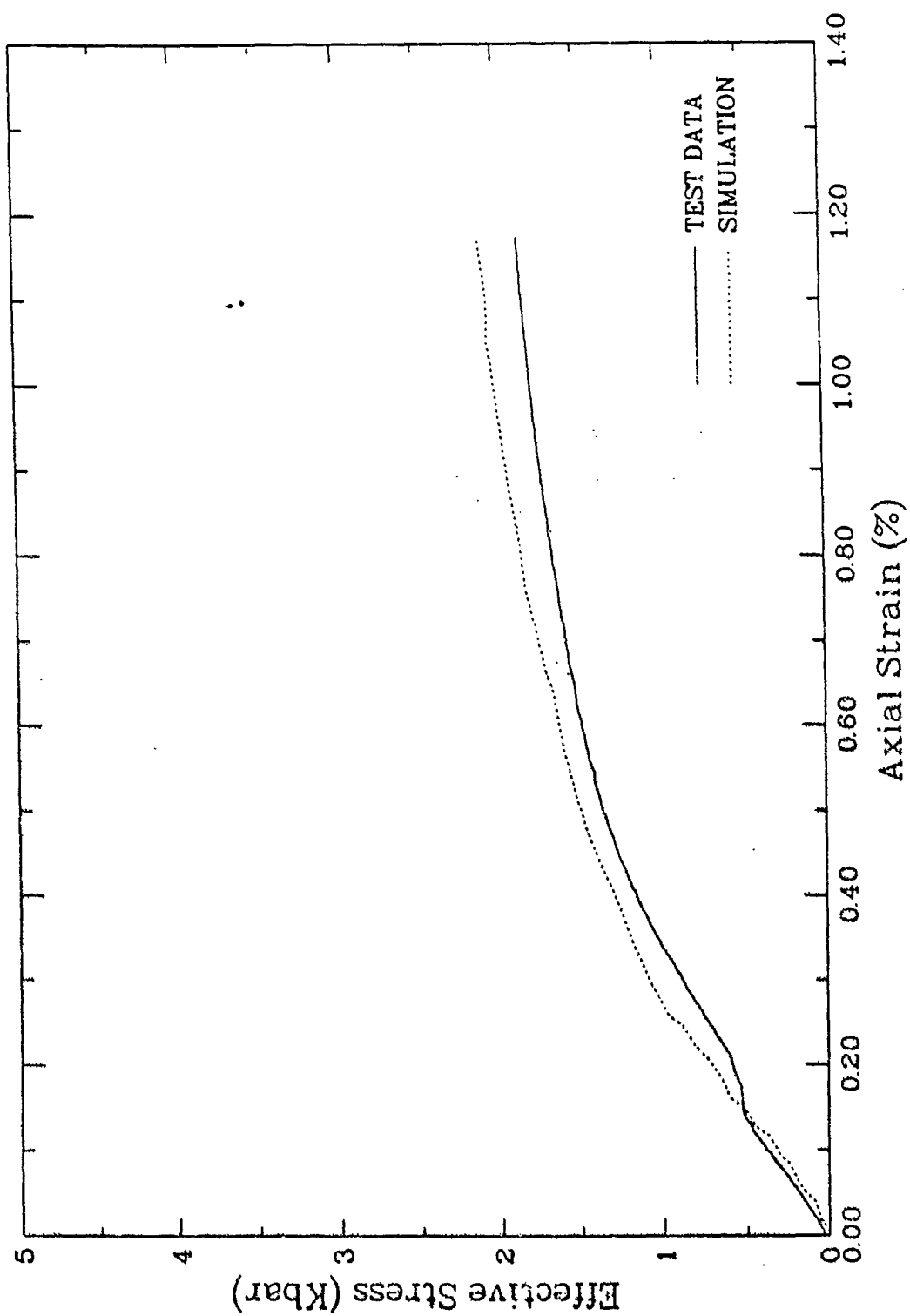


Figure 7.9b. Comparison of effective stress from an undrained uniaxial strain test with a two-phase simulation using skeleton properties of Salem limestone from drained test data.

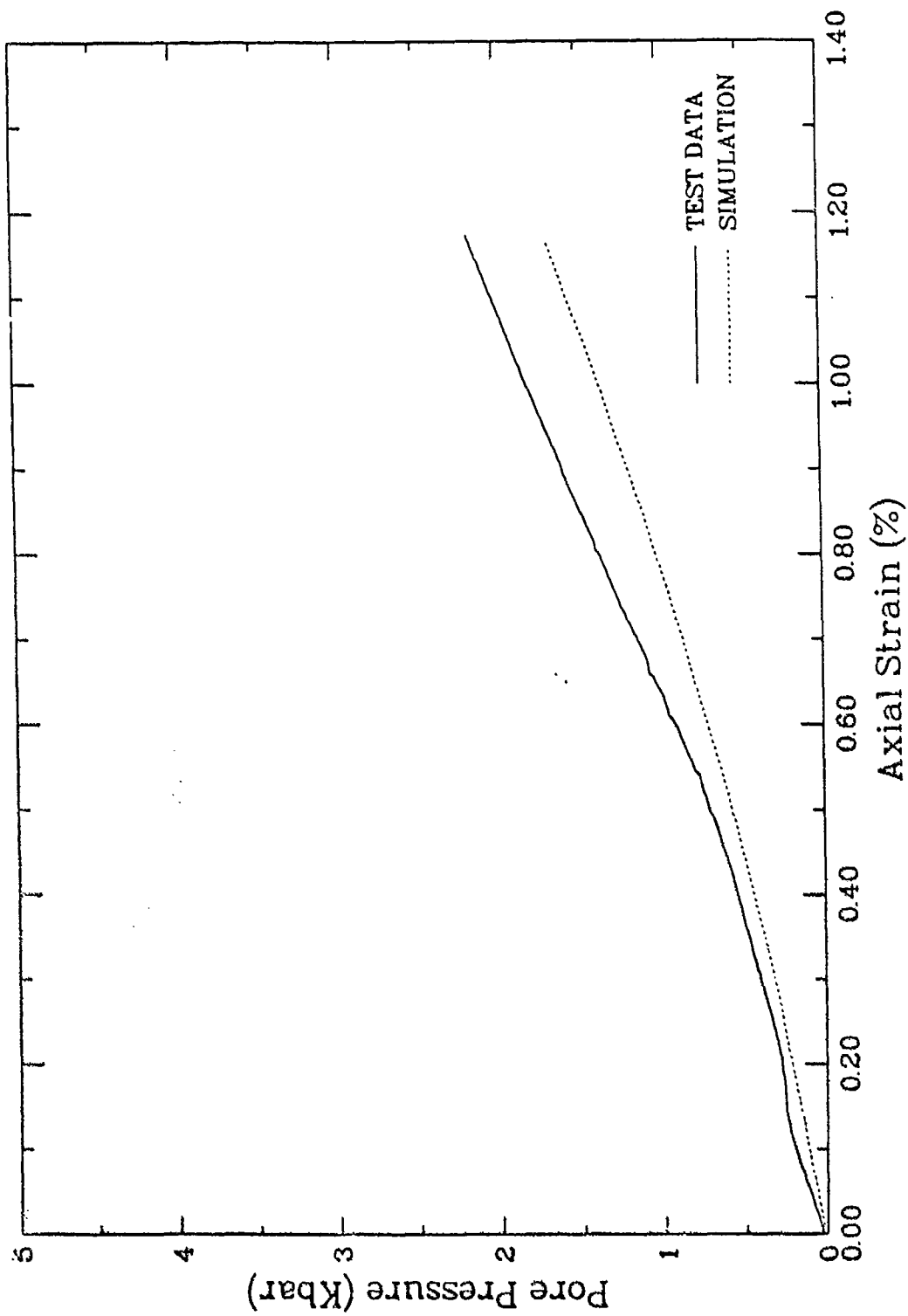


Figure 7.9c. Comparison of pore pressure from an undrained uniaxial strain test with a two-phase simulation using skeleton properties of Salem limestone from drained test data.

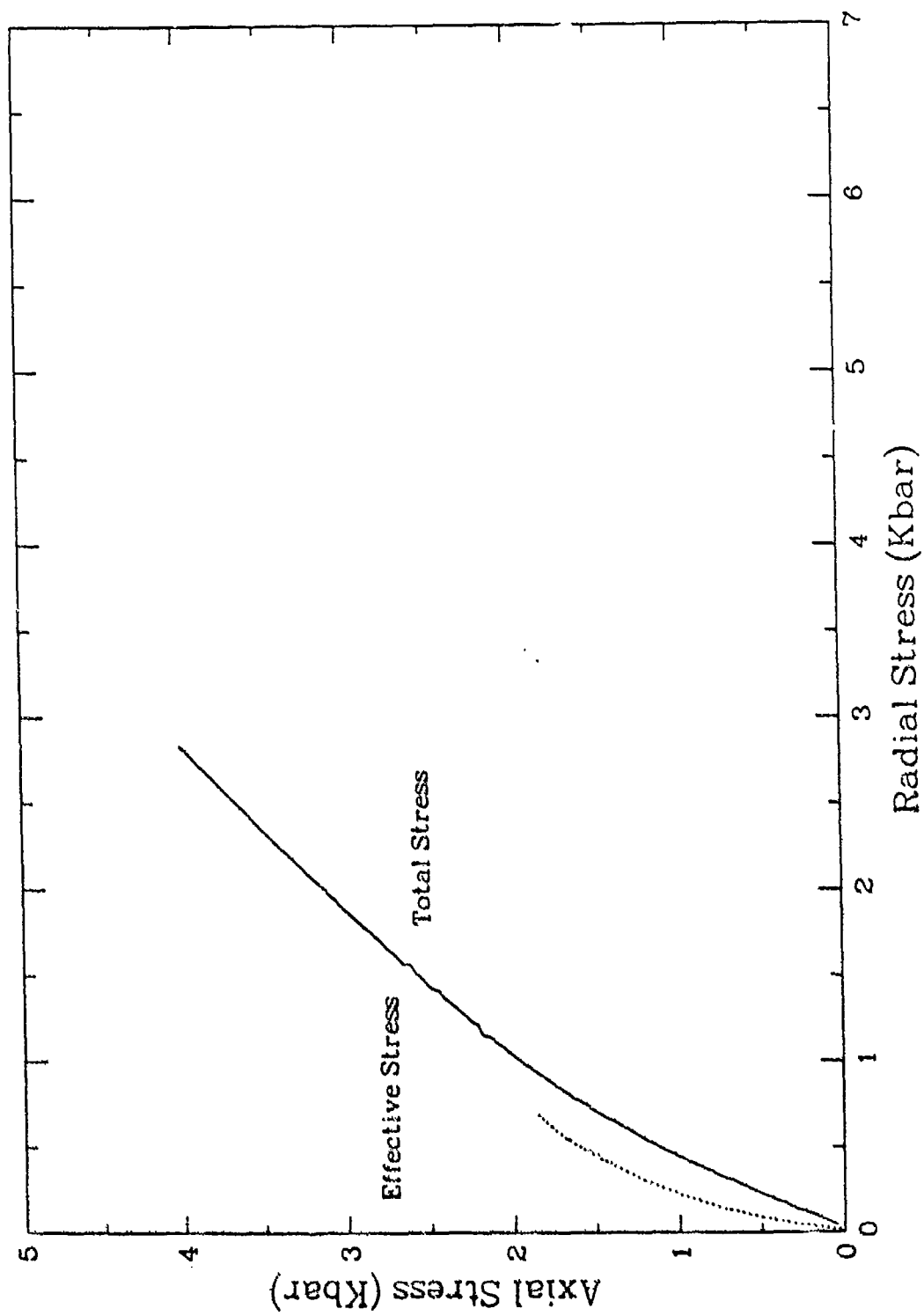


Figure 7.10. Axial stress vs. radial stress during undrained uniaxial strain loading of Salem limestone - Test L11A8.

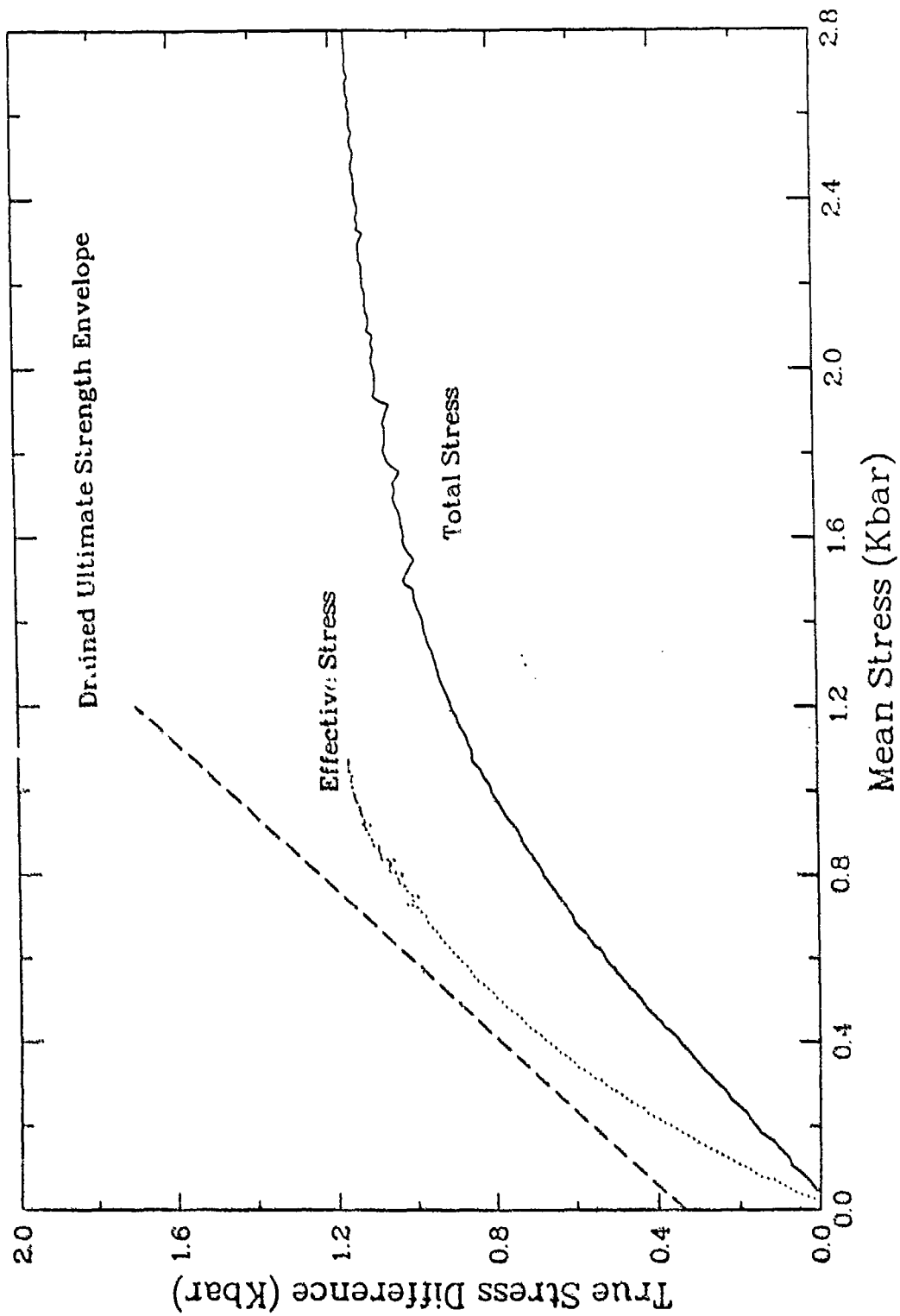


Figure 7.11. Stress paths for undrained uniaxial strain loading of Salem limestone - Test L11A8.

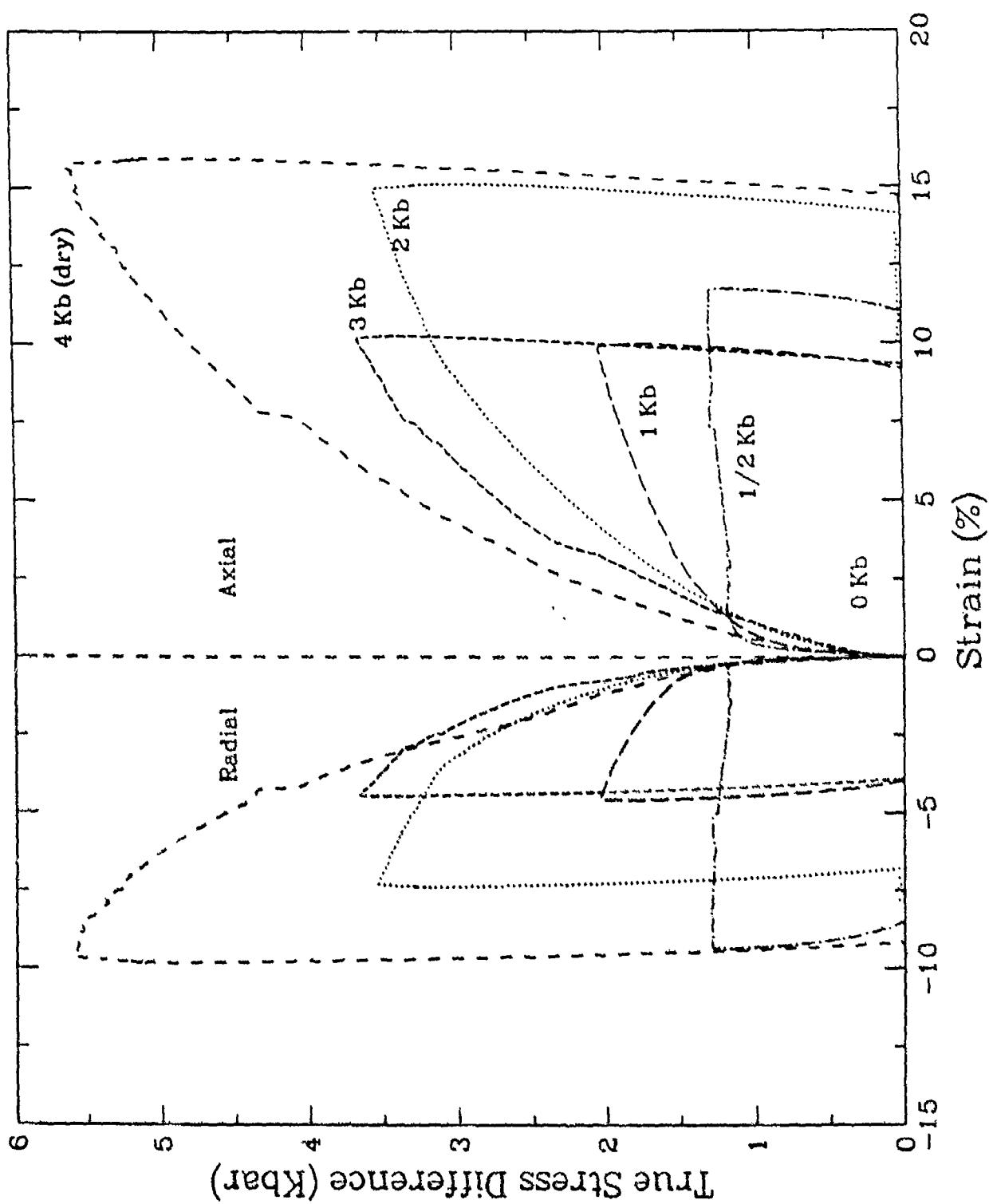


Figure 7.12. Axial-radial strain response of drained Salem limestone in triaxial compression

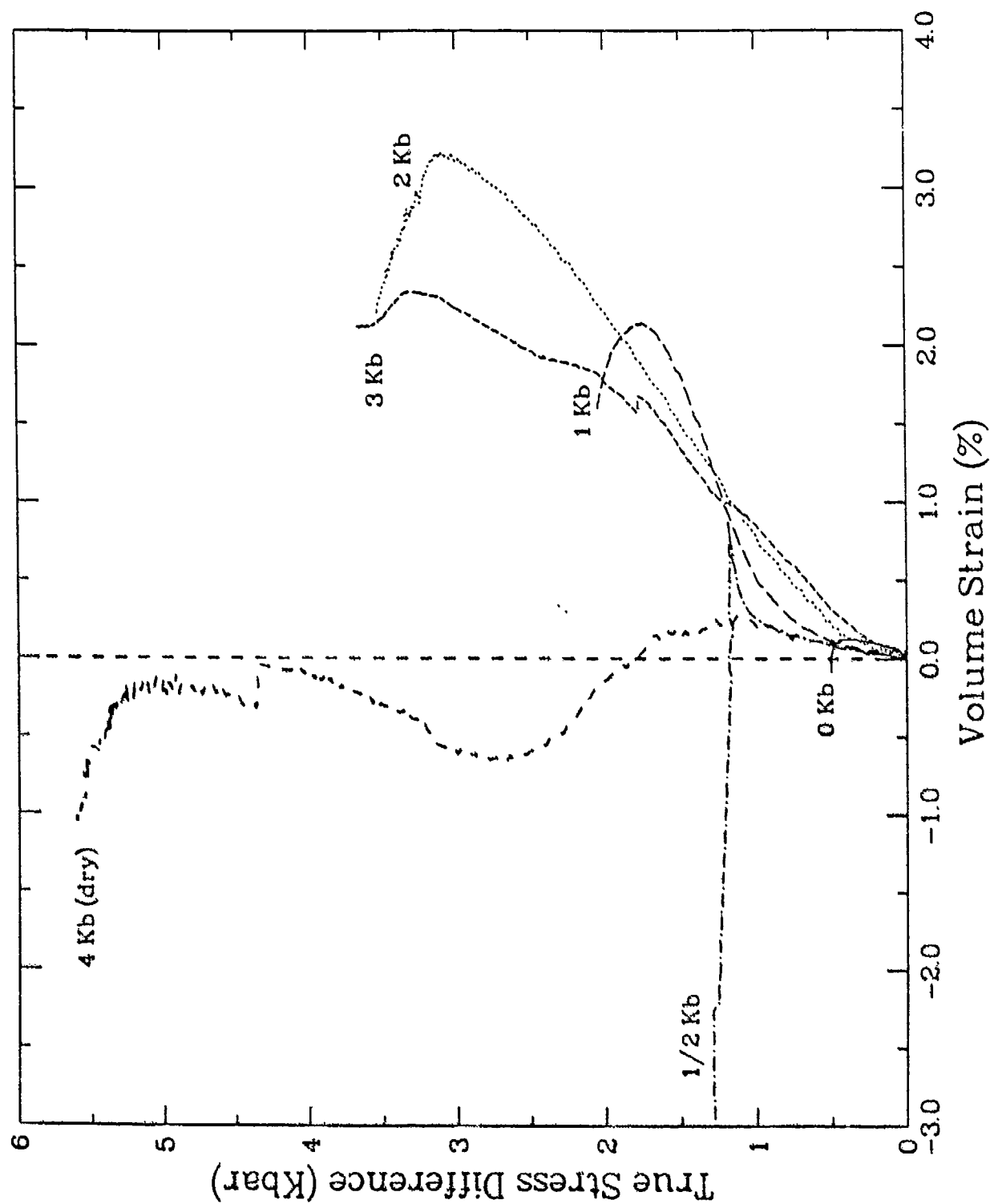
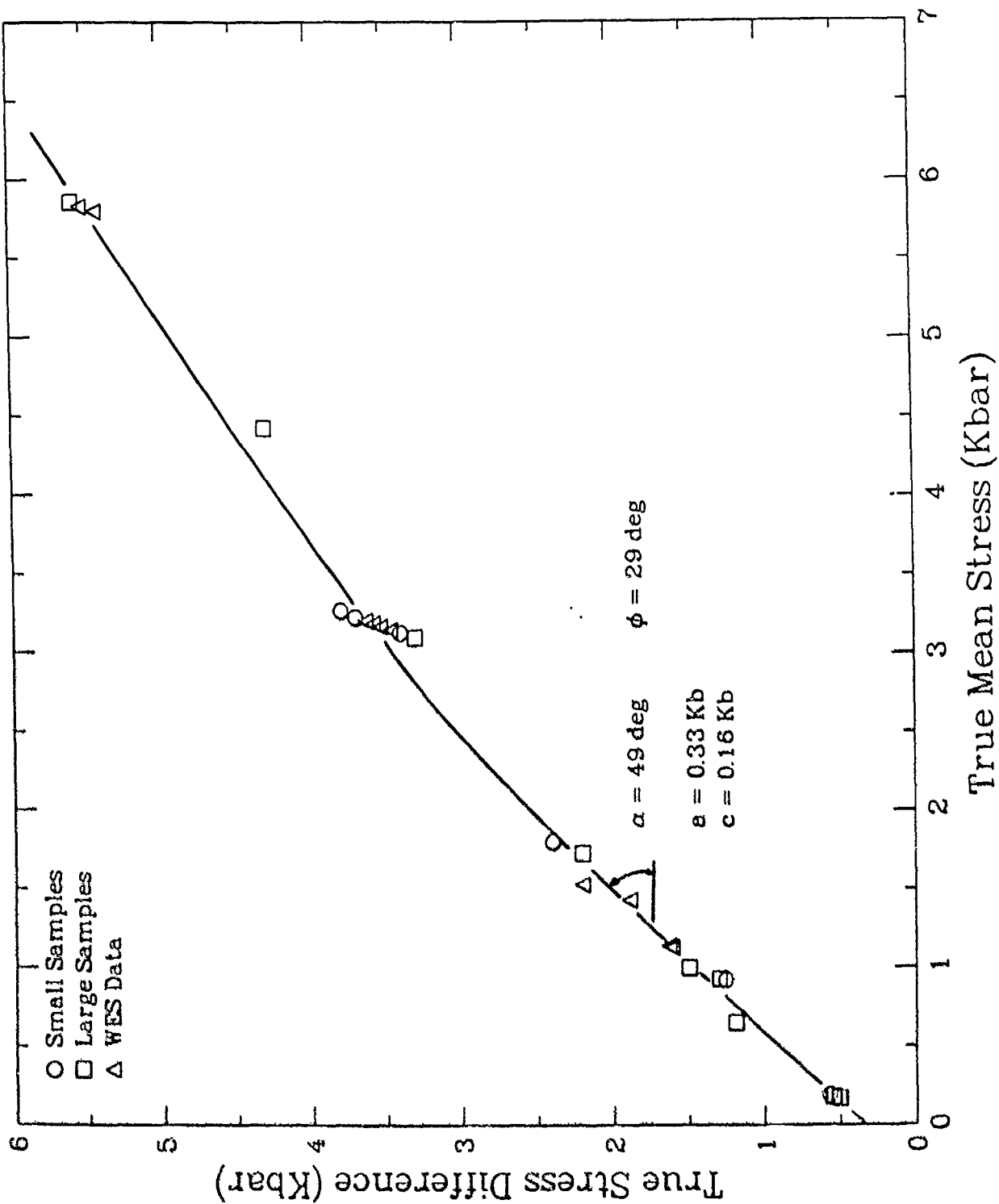


Figure 7.13. Relationship between stress difference and volume strain; Salem limestone in drained triaxial compression.



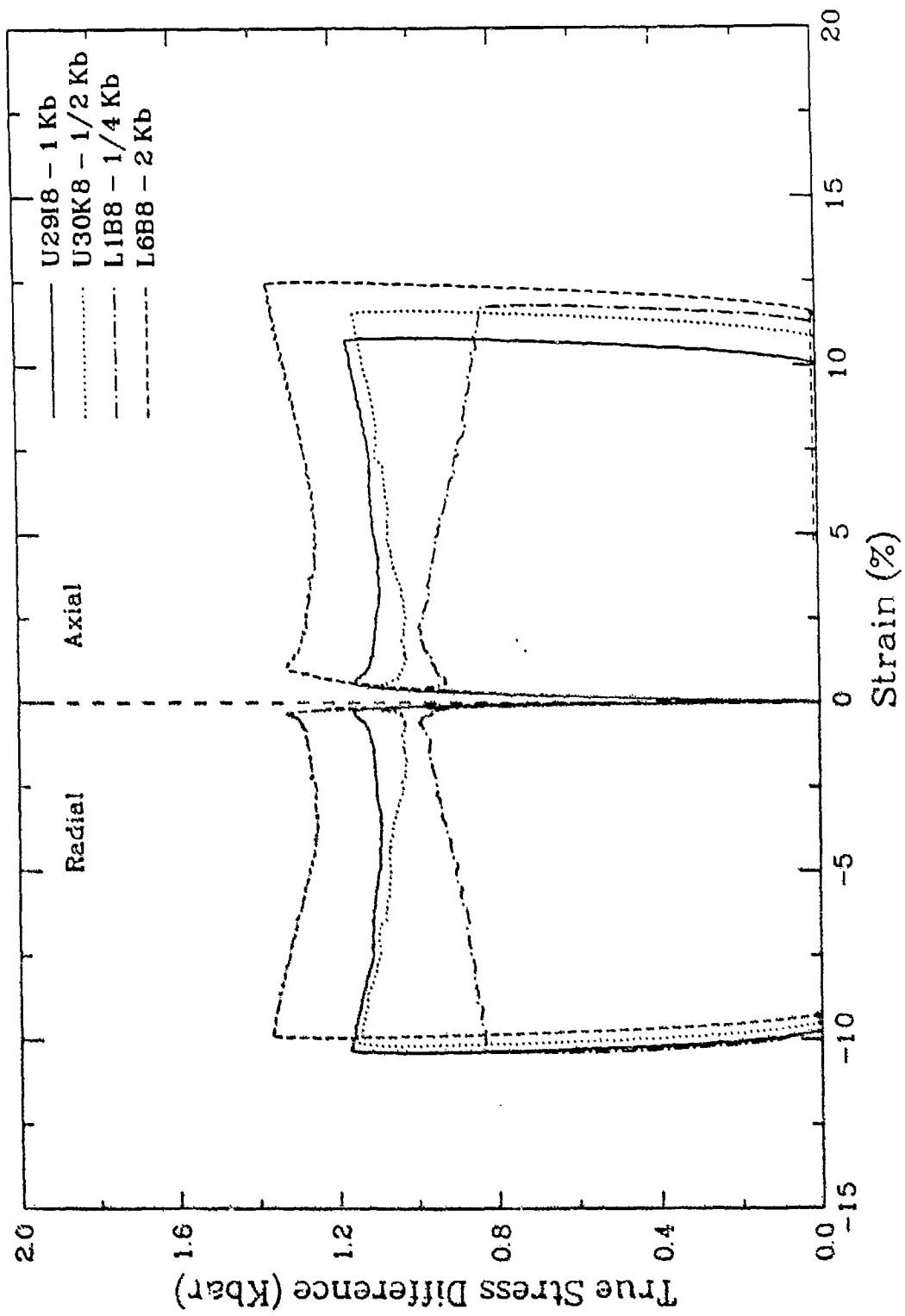


Figure 7.16. Axial and radial strain response of Salem limestone in undrained triaxial compression.

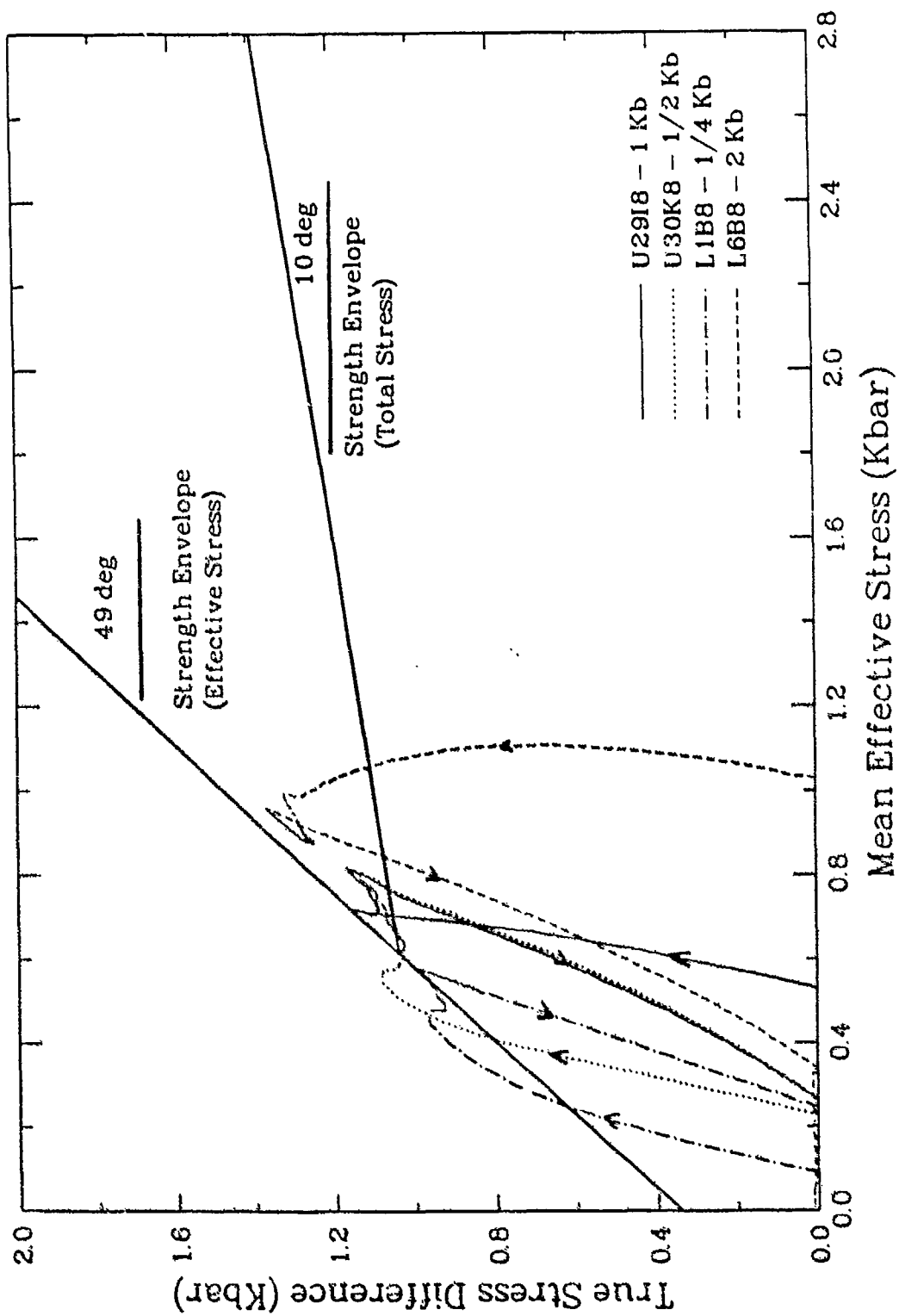


Figure 7.17. Effective stress paths for Salem limestone in undrained triaxial compression.

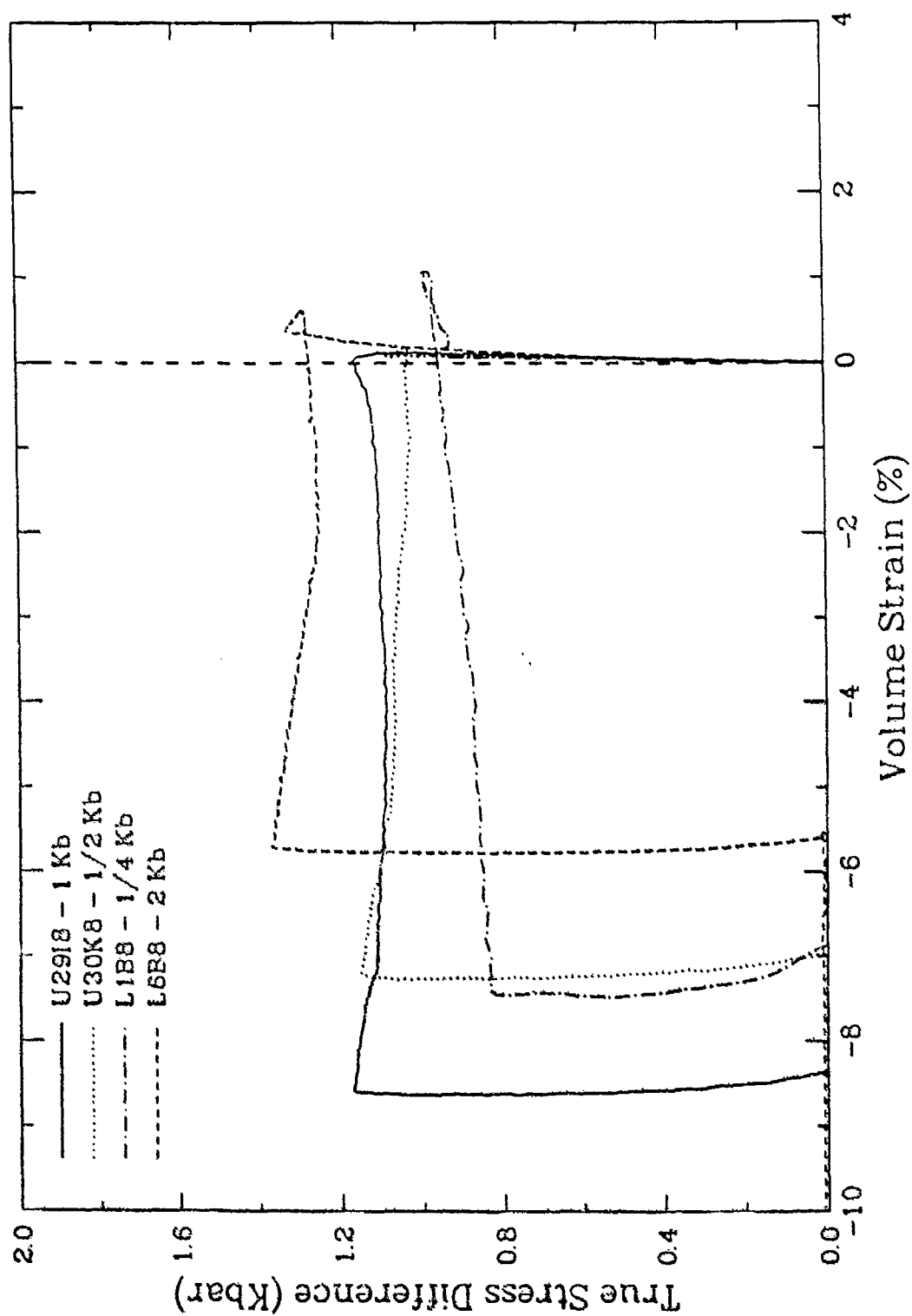


Figure 7.18. Relationship between stress difference and volume strain for Salem limestone in undrained triaxial compression.

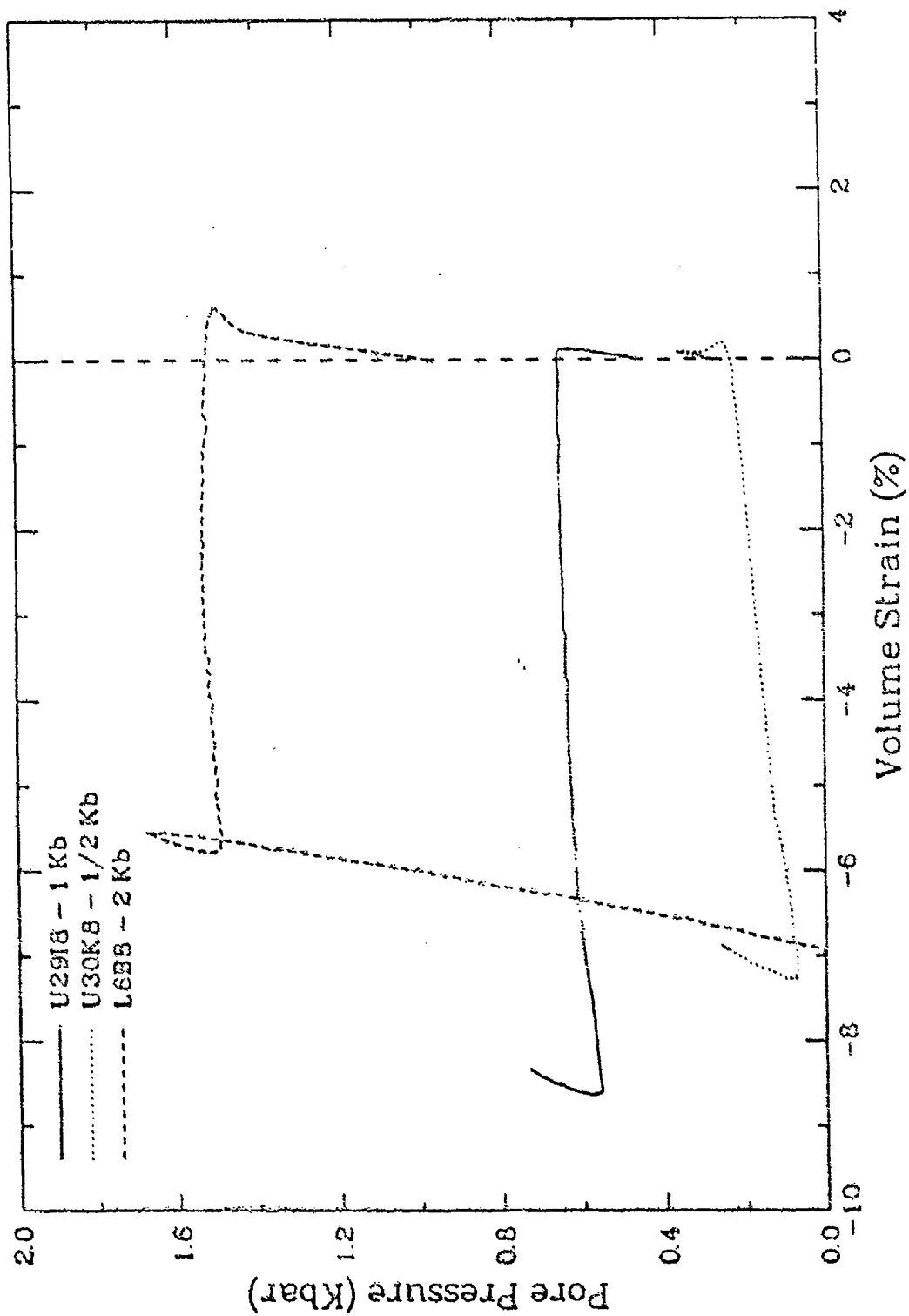


Figure 7.19. Relationship between pore pressure and volume strain for Salem limestone in undrained triaxial compression.

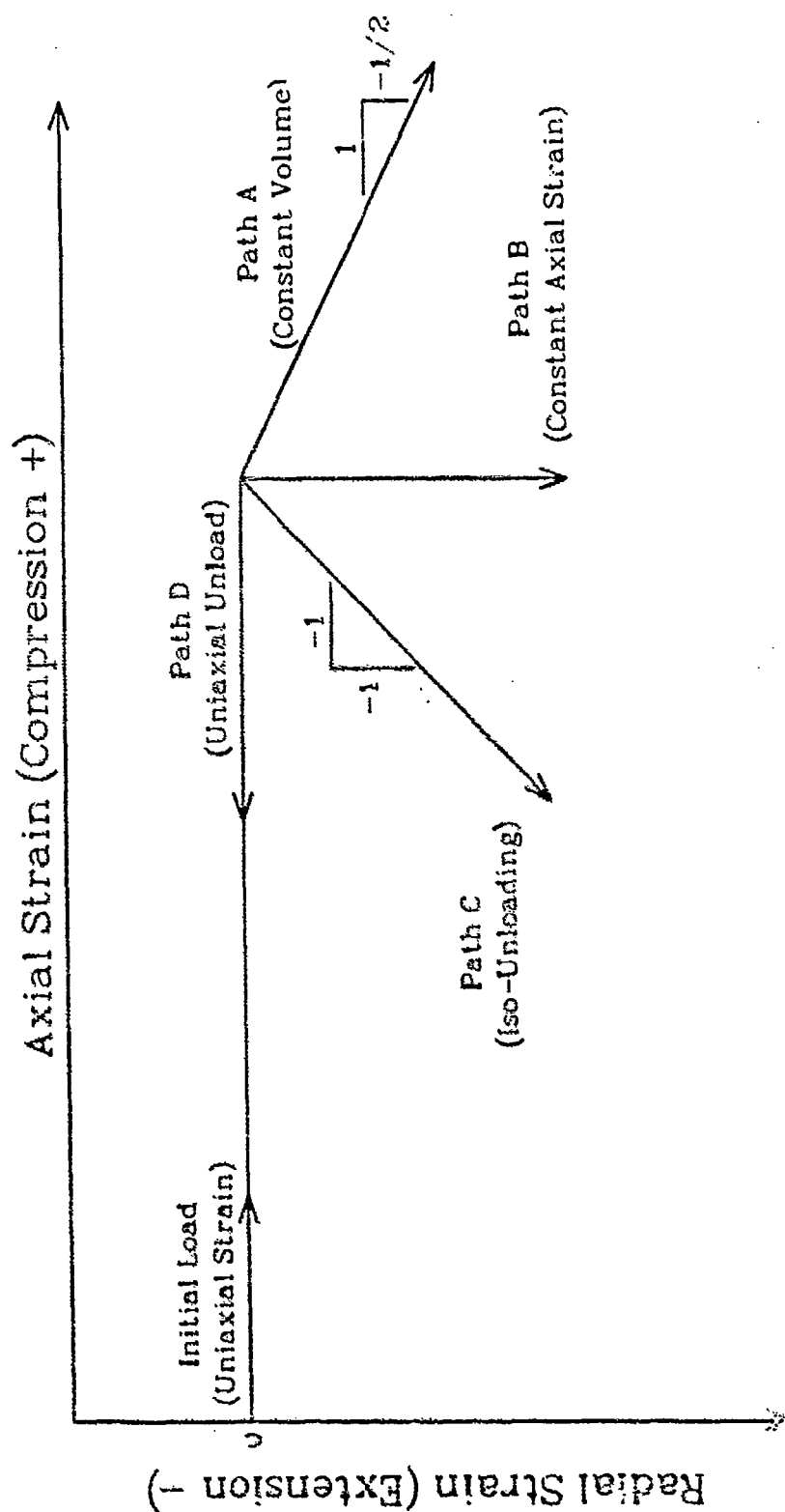


Figure 7.20. Strain paths specified for Salem limestone tests.

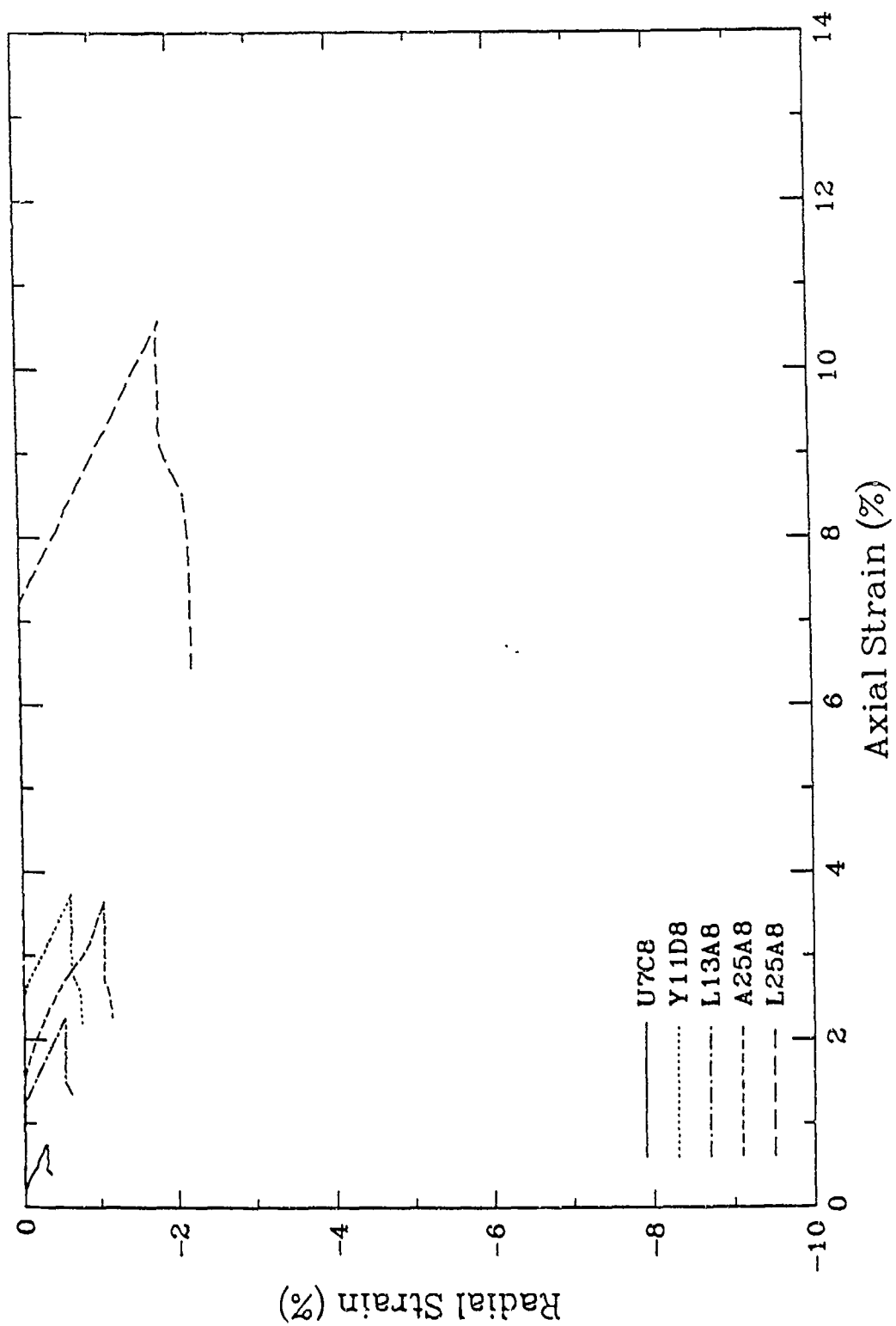


Figure 7.21a. Type A strain paths for drained Salem limestone.

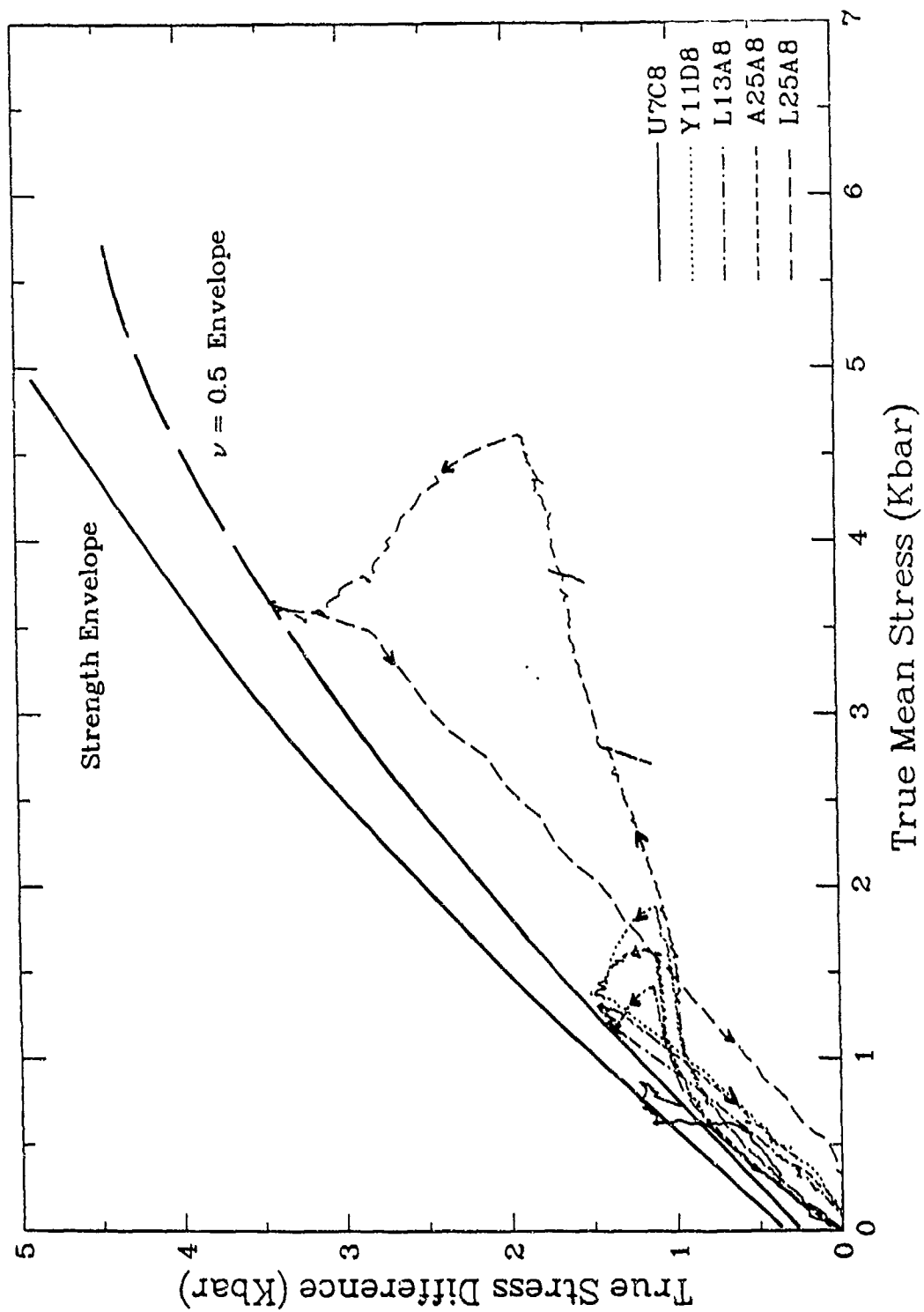


Figure 7.21b. Stress paths for drained Type A strain paths on Salem limestone.

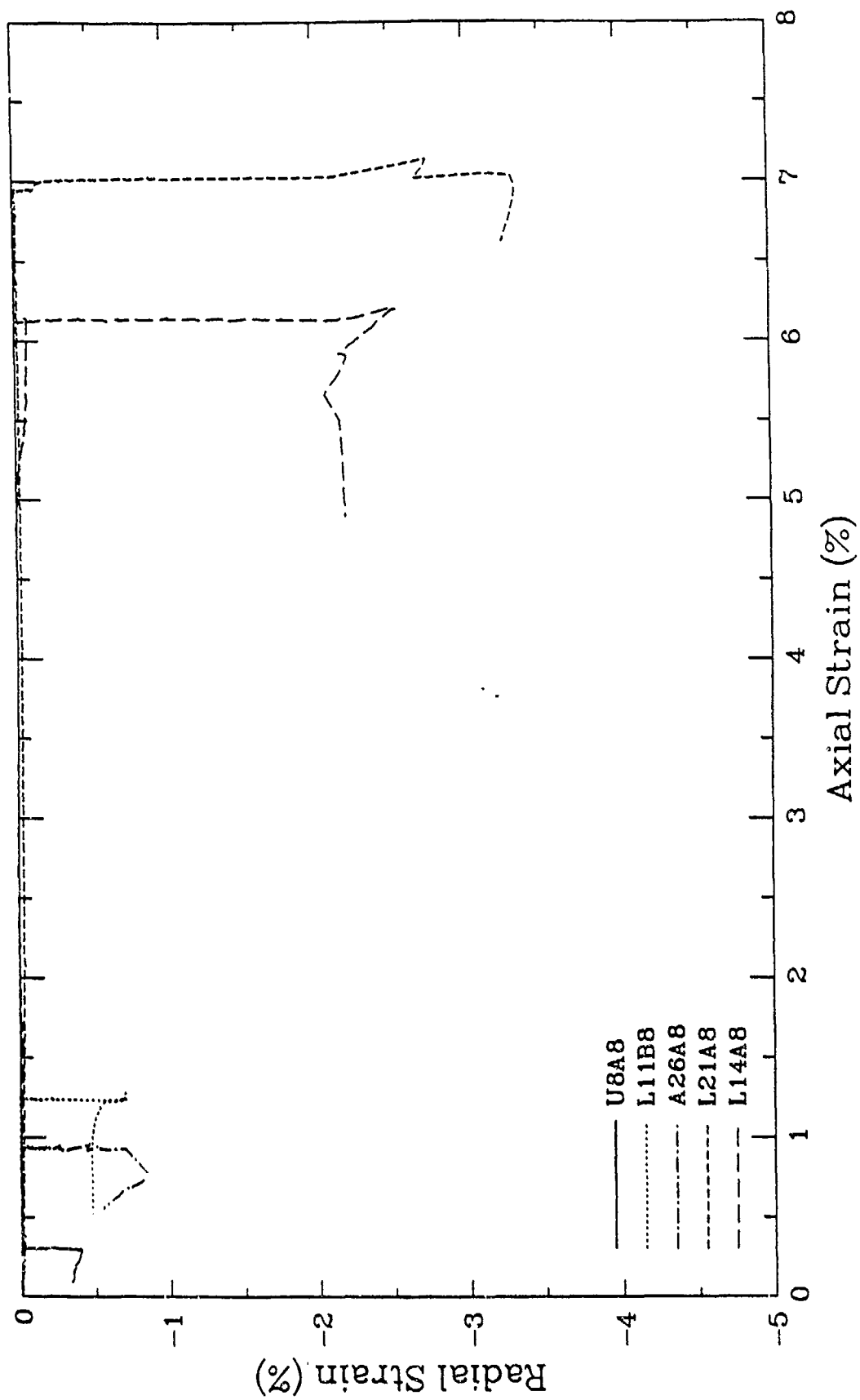


Figure 7.22a. Type B strain paths for drained Salem Limestone.

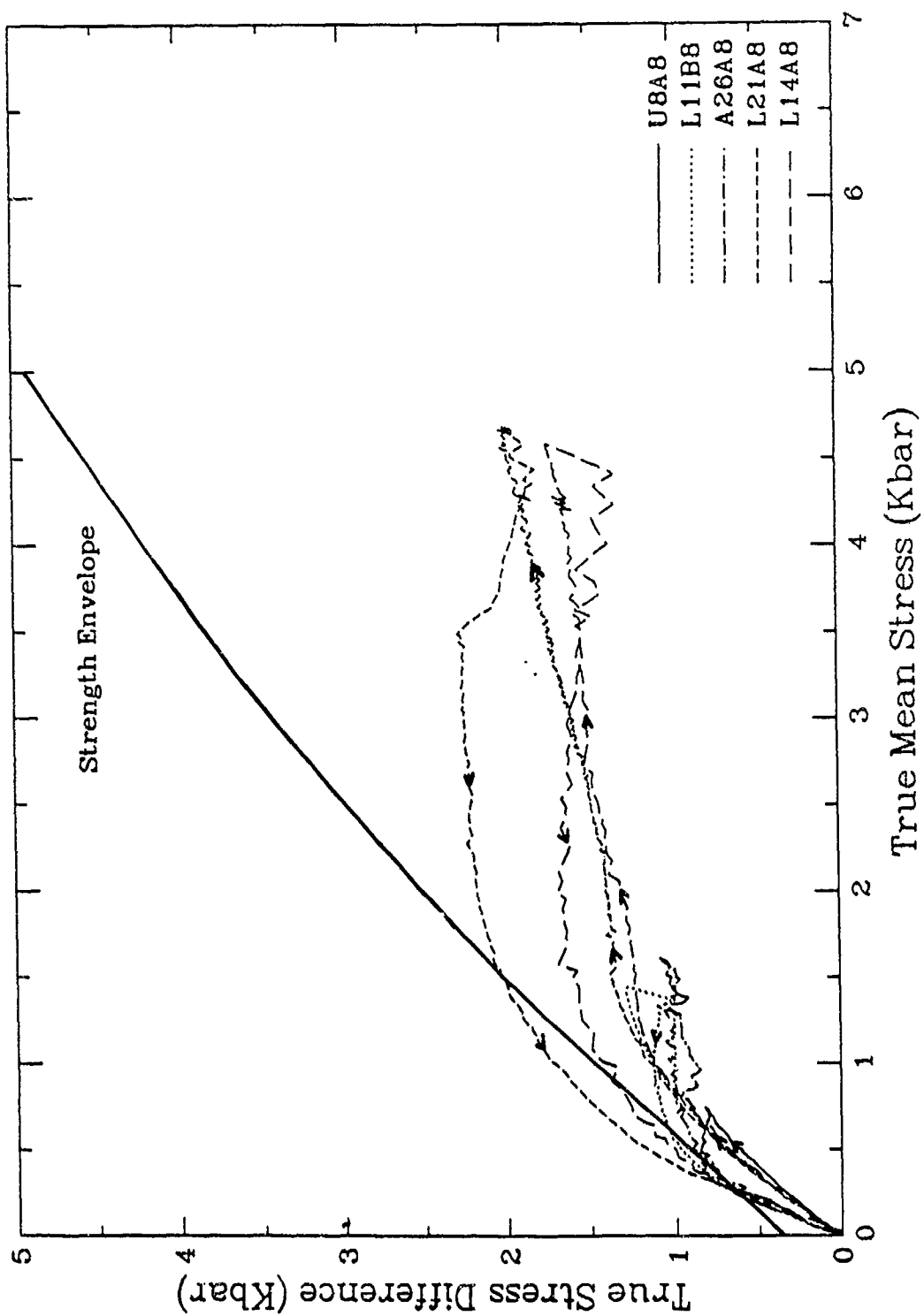


Figure 7.22b. Stress paths for drained Type B strain paths on Salem limestone.

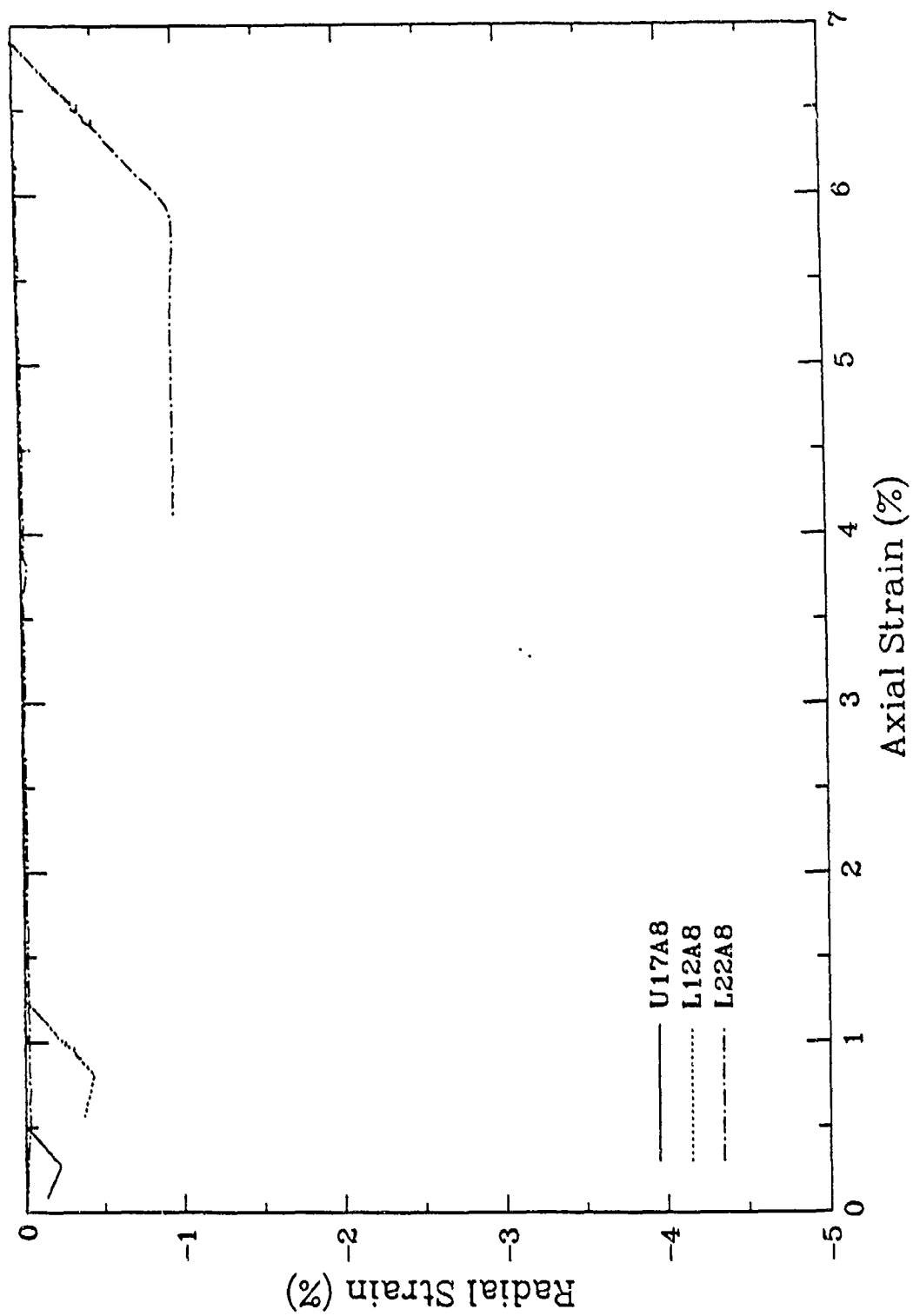


Figure 7.23a. Typc C strain paths for drained Salem limestone.

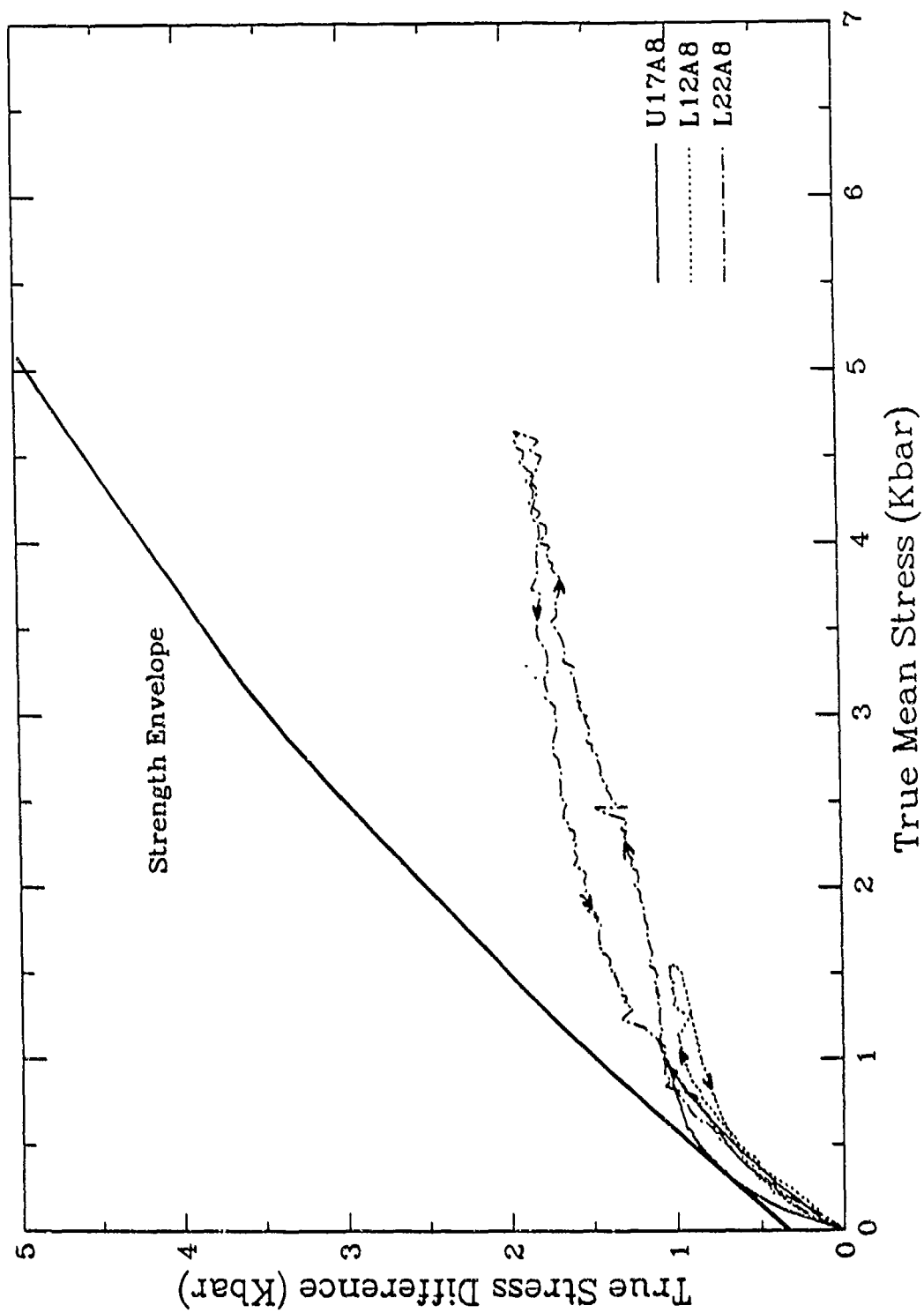


Figure 7.23b. Stress paths for drained Type C strain paths on Salem limestone.

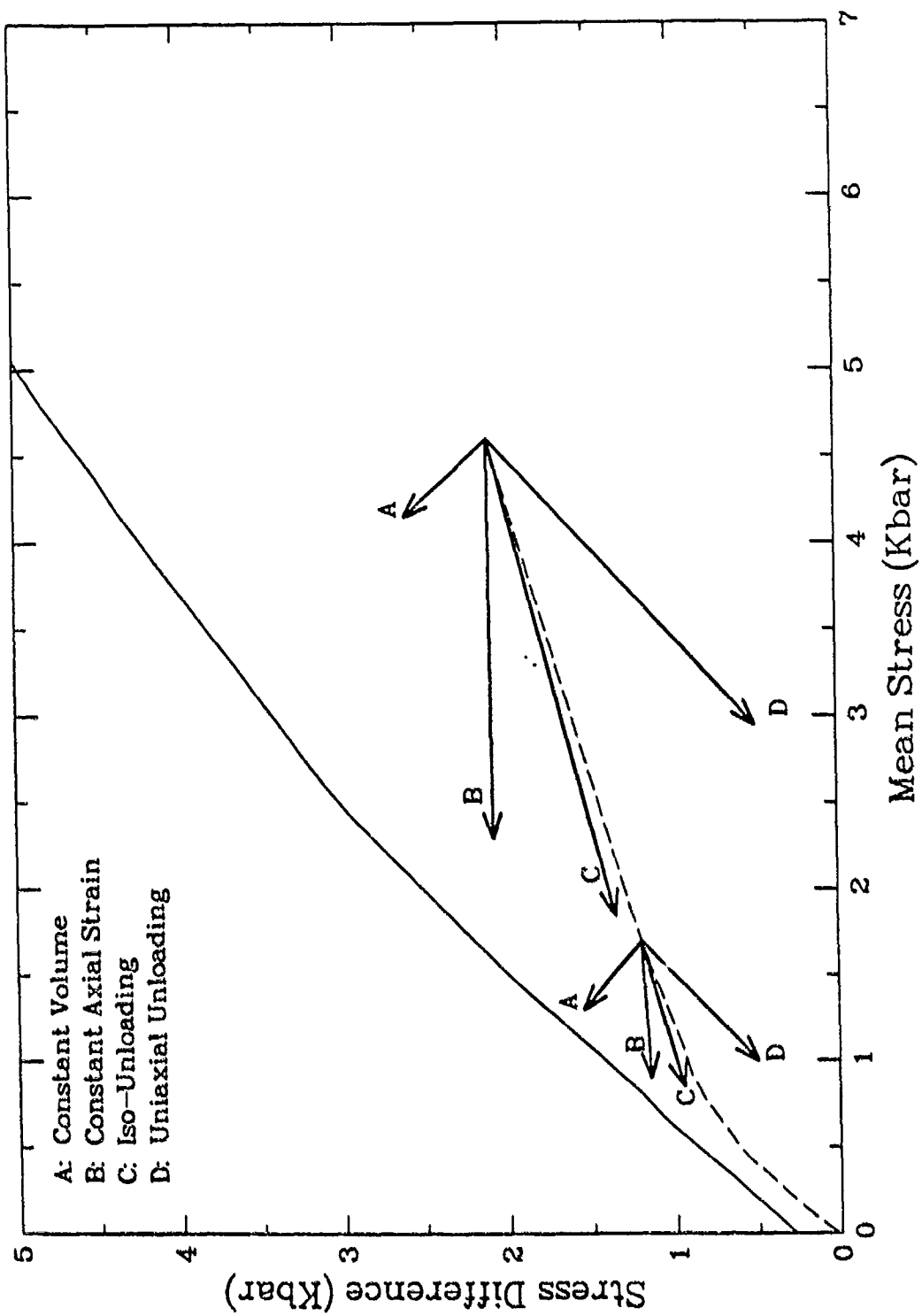


Figure 7.24. Idealized stress paths from strain path tests.

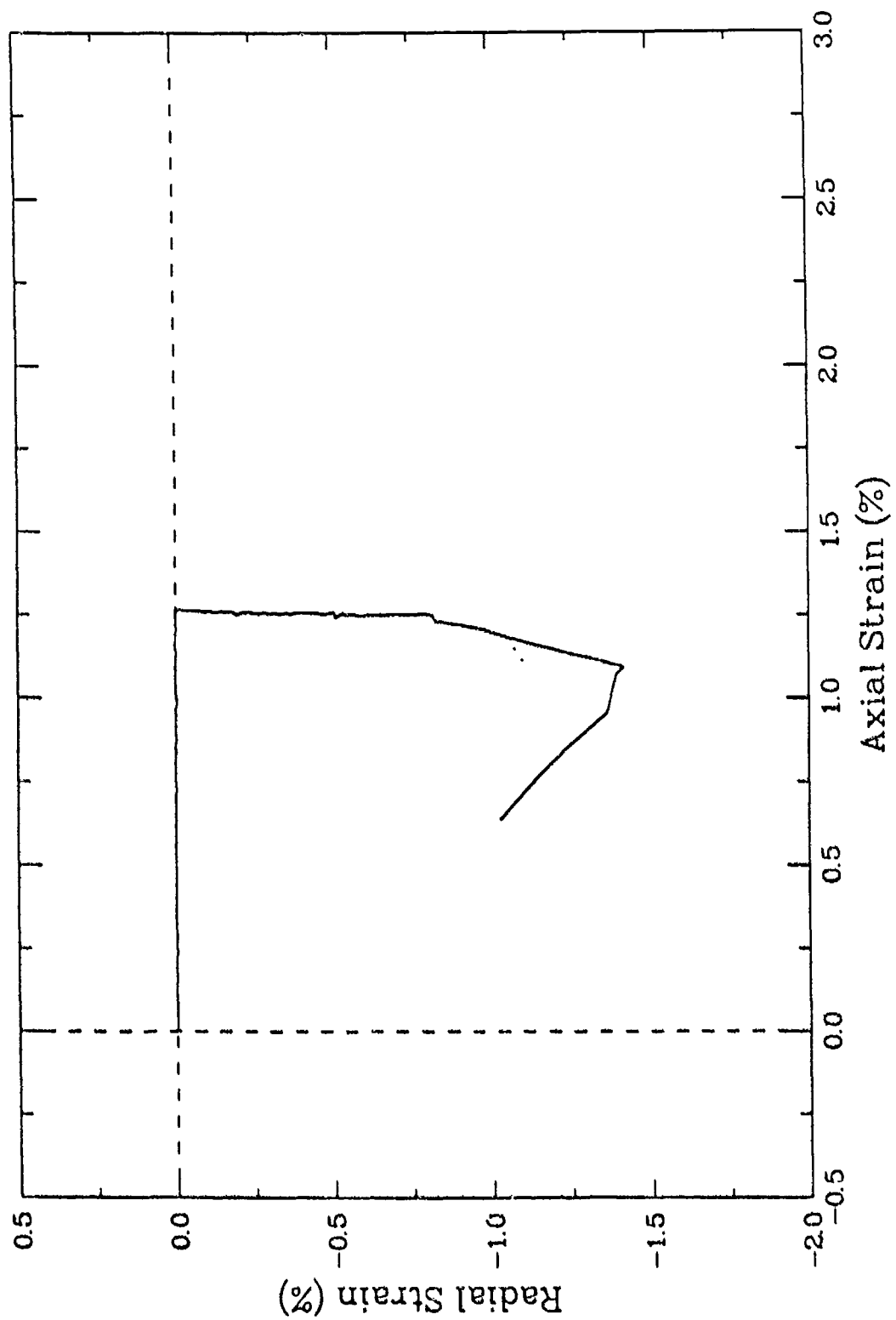


Figure 7.25a. Undrained Type B strain path for Salem limestone.

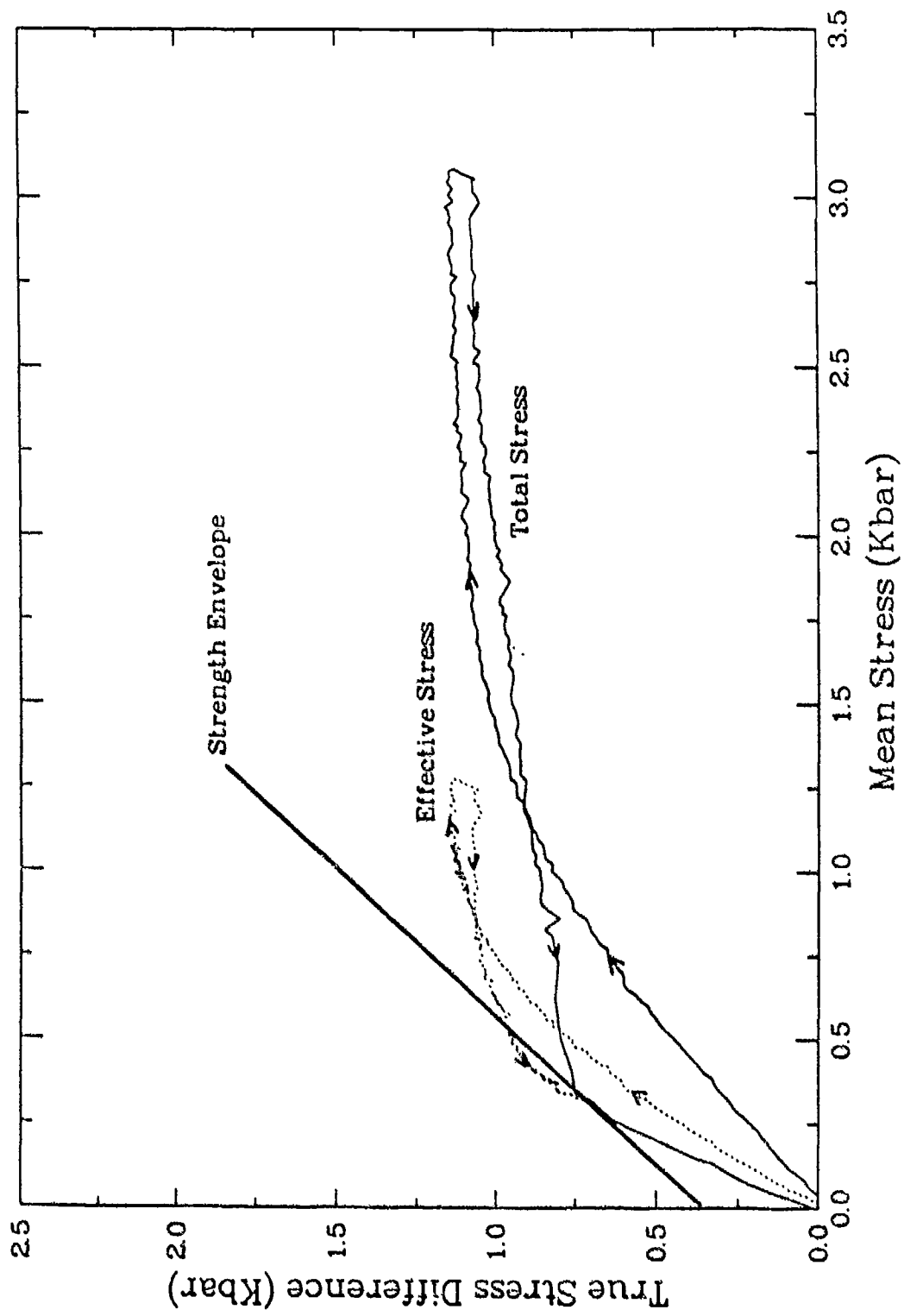


Figure 7.25b. Stress path for undrained Type B strain path test for Salem Limestone.

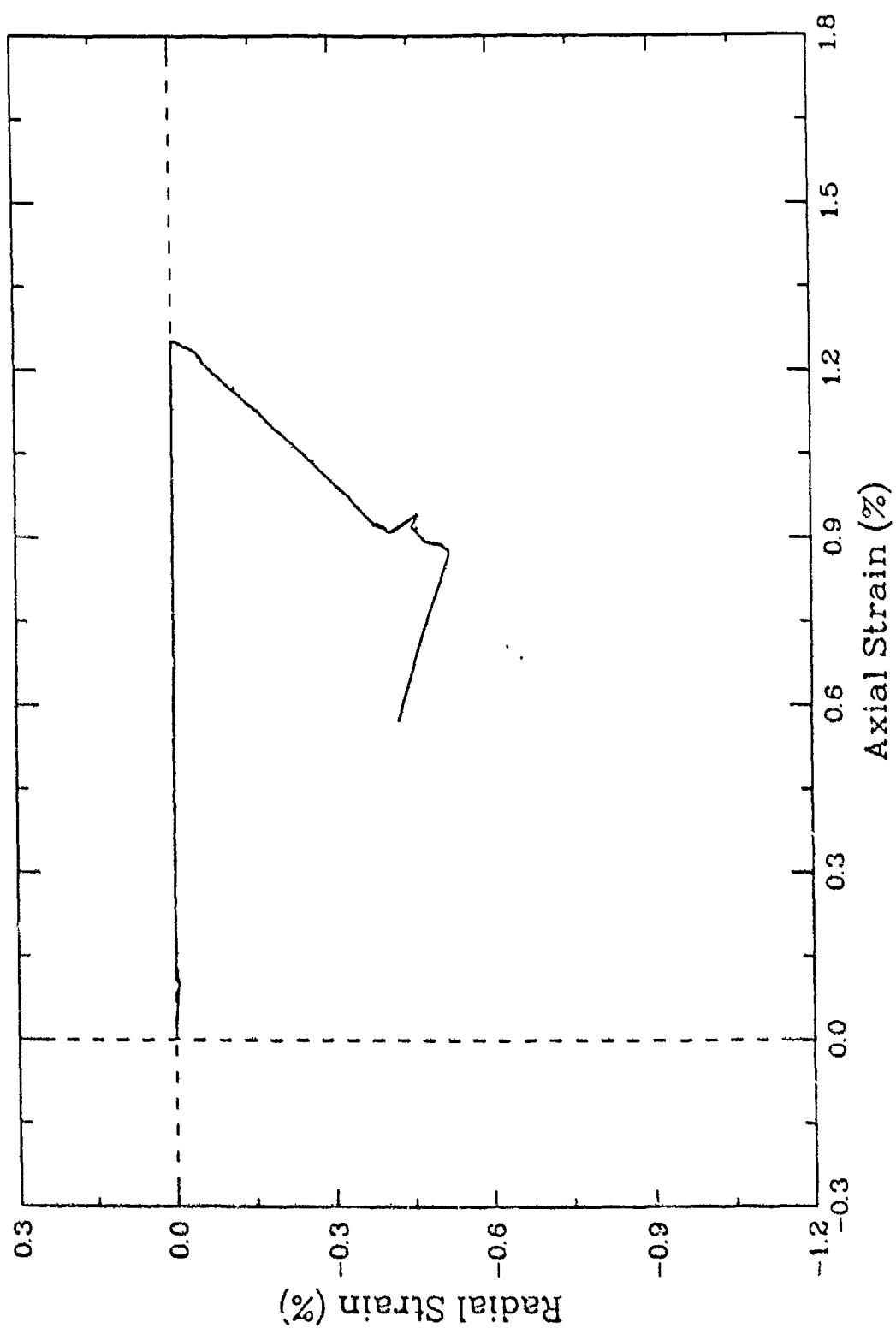


Figure 7.26a. Undrained Type C strain path for Salem limestone.

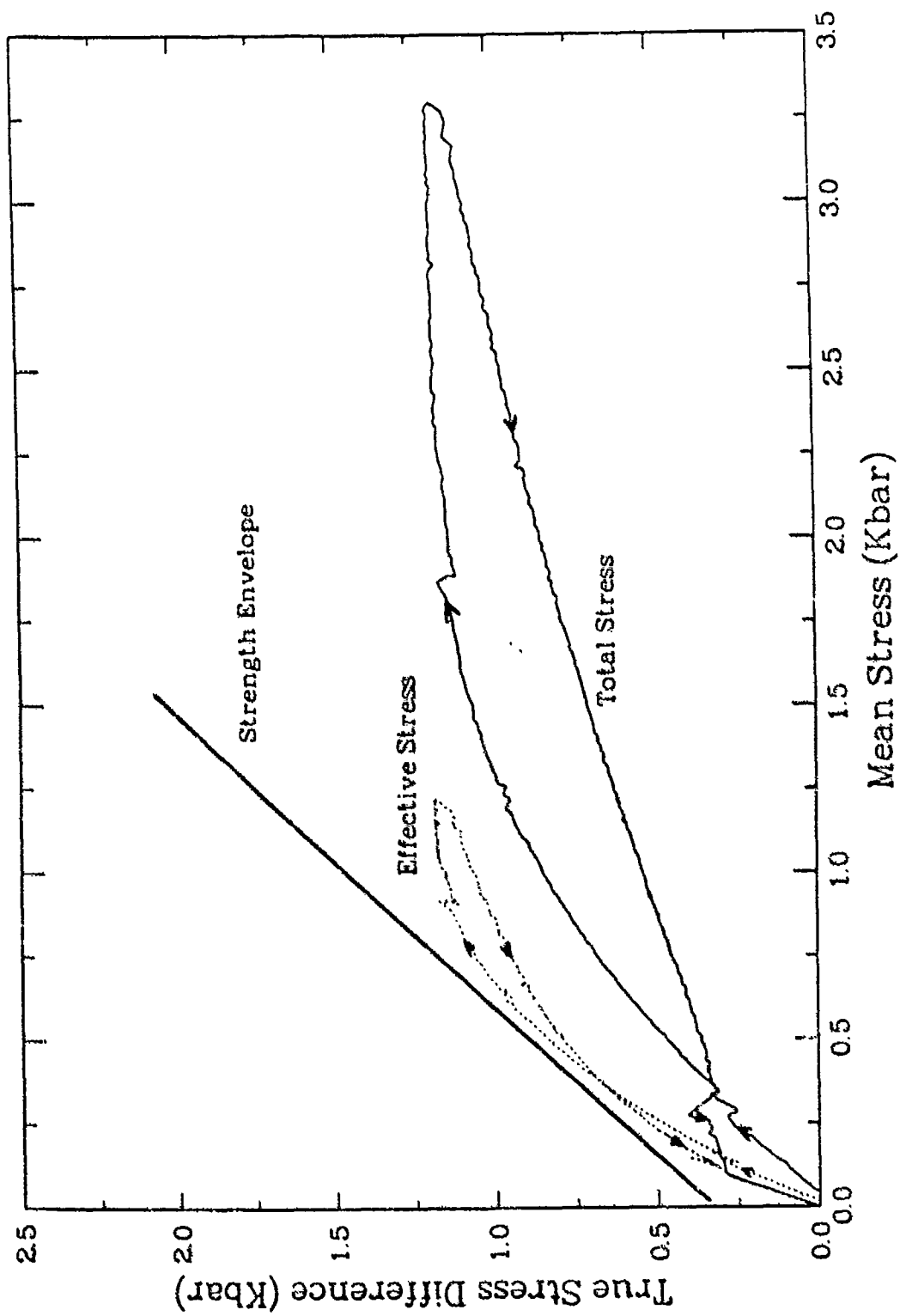


Figure 7.26b. Stress paths for undrained Type C strain path test for Salem limestone.

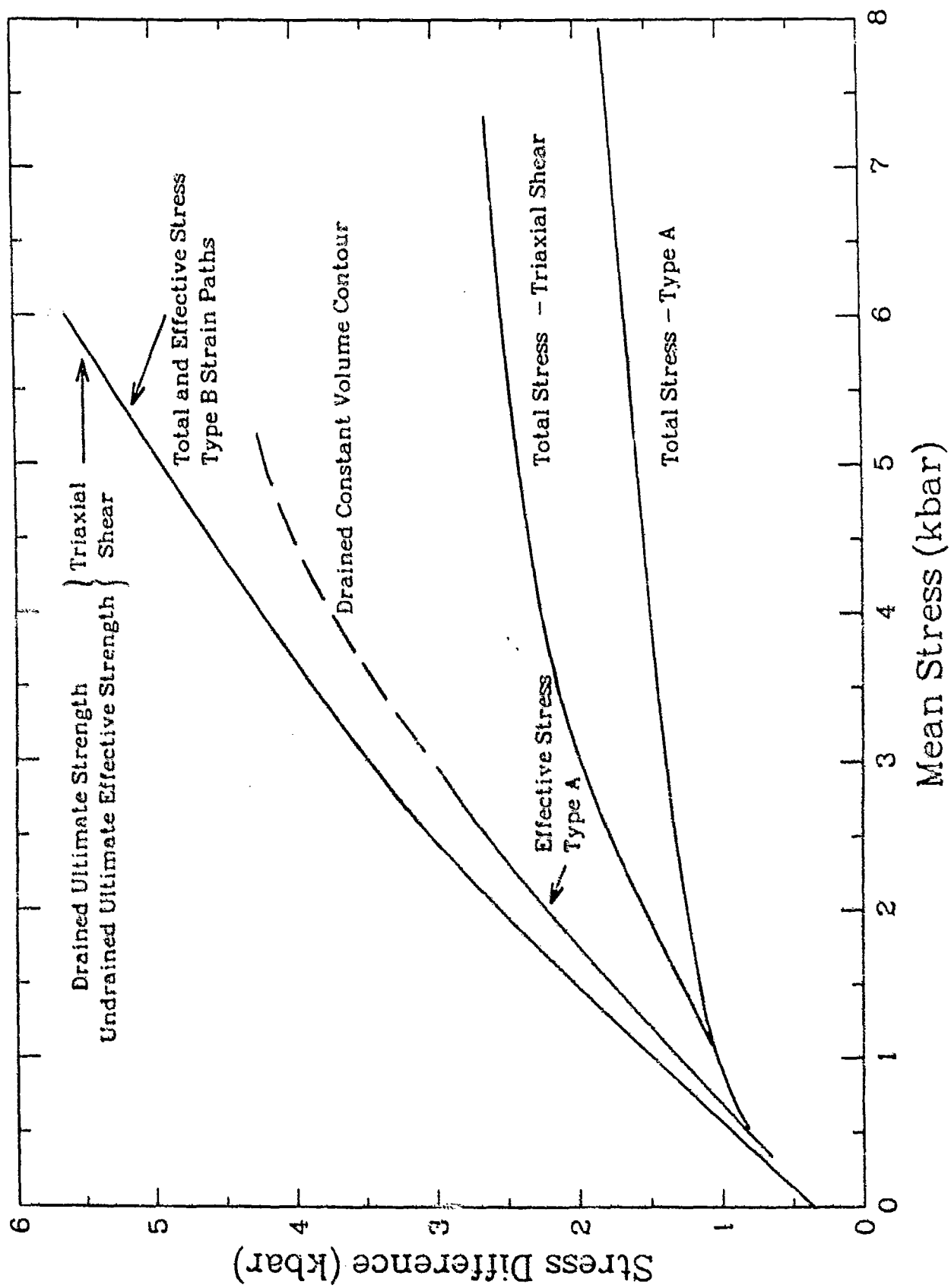


Figure 7.27. Hypothesized strength envelopes for Type A and Type B strain paths on Salem limestone.

LIST OF REFERENCES

- Biot, M.A., "Theory of Propagation of Elastic Waves in Fluid Saturated Porous Solid, I, II", Journal of Acoustical Society of America, Vol. 28, pp. 168-191, 1956.
- Biot, M.A., "Mechanics of Deformation and Acoustic Propagation in Porous Media", Journal of Applied Physics, Vol. 33, pp 1482-1498, 1962a.
- Biot, M.A., "Generalized Theory of Acoustic Propagation in Porous Dissipative Media", Journal of Acoustical Society of America, Vol. 34, pp. 1254-1264, 1962b.
- Blouin, S.E. and K.J. Kim, "Explosion Induced Liquefaction in the Pacific Proving Grounds", Report to Air Force Office of Scientific Research, Washington, D.C., 1983.
- Blouin, S.E. and K.J. Kim, "Undrained Compresssibility of Saturated Soil", Technical Report to Defense Nuclear Agency, Washington, D.C., 1984.
- Blouin, S.E., R.J. Martin, K.A. McIntosh, "Laboratory Investigation of the Mechanical Properties of Enewetak Sand," Report to Air Force Office of Scientific Research, Washington, D.C., 1984.
- Blouin, S.E. and J.D. Shinn II, "Explosion-Induced Liquefaction," Report to Air Force Office of Scientific Research, Washington, D.C., 1983.
- Bridgman, P.W., The Physics of High Pressure, Dover Publications, Inc., New York, N.Y., 1931.
- Ghaboussi, J. and E.L. Wilson, "Variational Formulation of Dynamics of Fluid-Saturated Porous Elastic Solids," Journal of the Engineering Mechanics Division, ASCE, Vol. 98, pp. 946-963, 1972.
- Kim, K.J., "Finite Element Analysis of Nonlinear Consolidation", PhD thesis, University of Illinois, Urbana-Champaign, 1982.
- Kim, K.J. and S.E. Blouin, "Response of Saturated Porous Nonlinear Materials to Dynamic loadings", Report to Air Force Office of Scientific Research, Washington, D.C., 1984.
- Kim, K.J., S.E. Blouin, and D.A. Timian, "Experimental and Theoretical Response of Multiphase Porous Media to Dynamic Loads", Annual Report No. 1 to Air Force Office of Scientific Research, Washington, D.C., 1986.
- Kim, K.J., S.E. Blouin, and D.A. Timian, "Experimental and Theoretical Response of Multiphase Porous Media to Dynamic Loads", Annual Report No. 2 to Air Force Office of Scientific Research, Wasington, D.C., 1987.

LIST OF REFERENCES (concluded)

- Hoek, E. and E.T. Brown, Underground Excavations in Rock, The Institution of Mining and Metallurgy, London, England, 1982.
- Mendelson, A., "Plasticity: Theory and Application", The MacMillan Company, New York, N.Y., 1968.
- Merkle, D.H. and W.C. Gass, "Fundamental Properties of Soils for Complex Dynamic Loadings: Development of a Three Invariant Constitutive Model", Report to Air Force Office of Scientific Research, Washington, D.C., 1985.
- Rischbieter, F., et.al., "Studies of Soil Liquefaction by Shock Wave Loading", Fifth International Symposium on Military Applications of Blast Simulation, Vol. III, Royal Swedish Fortifications Administration, Stockholm, Sweden, 1977.
- Simmons, G. and H. Wang, Single Crystal Elastic Constants and Calculated Aggregate Properties: A Handbook, Second Edition, The MIT Press, Cambridge, MA, and London, England, 1971.
- Ward, J., "Turbulent Flow in Porous Media", ASCE Journal of Hydraulic Division, American Society of Civil Engineers, NY5, pp. 1-12, 1964.

CARD 1

IBATCH (I5)

IBATCH = 0 Terminal interactive job
1 Batch job

CARD 2

Main Title (up to 80 characters)

CARD 3

Subtitle (up to 80 characters)

CARD 4 General Options

NF, NTCSF, ISFG, IP, NLNR, NFG, ICOPL (715)

Options in Dynamic Analysis

NF = 1 One-phase solid dynamic analysis
2 One-phase fluid dynamic analysis
3 Multiphase dynamic analysis

Analysis Type

NTCSF = 1 Static analysis
2 Consolidation analysis
3 Dynamic analysis

Initial Stress Conditions

ISFG = 0 No initial stress
1 Specified effective stress and pressure
2 Specified effective stress
3 Specified pore pressure
4 Imposed excess pore pressure

Stress and Strain Conditions

IP = 1 Plane stress
2 Plane strain
3 Axial symmetry
4 Spherical symmetry

Skeleton Material Model

NLNR = 0 Linear elastic material model
1 Decoupled elastoplastic model
4 Uniaxial strain model
5 Generalized Hoek and Brown rock model
6 ARA 3-Invariant model

Loading Type

NFG = 1 Specified base accelerations (not available)
2 Specified pressure time history
3 Specified velocity time history (not available)
4 Both pressure and velocity time histories (not available)

Fluid - Grain - Skeleton Compressibility model

ICOPL = 0 Decoupled model
1 Fully coupled model

CARD 5 Global Calculation Parameters

NCYCL, DT, NUPDAT, ITER (I5, F10.0, 2I5)

NCYCL: Number of cycles (total number of time steps)
DT: Global time step (duration of each cycle)
NUPDAT: Number of cycles between updates to global stiffness matrix
(ITER = 0 for NUPDAT > 1)
ITER: Number of updates of global stiffness matrix within each
cycle (NUPDAT = 1)

CARD 6 Mesh and Material Parameters

NUMNF, NUMEL, NUMMAT, NHSIZE, NPSIZE (5I5)

NUMNP: Number of nodes
NUMEL: Number of elements
NUMMAT: Number of different materials
NHSIZE: Maximum number of hysteretic variables (for ARA 3-Invariant
model, use NHSIZE = 14)
NPSIZE: Maximum number of material parameters (for ARA 3-Invariant
model, use NPSIZE = 100)

CARD 7 Pressure Loading Functions

NUMLP, NUMLH, NUMTP, NTYPE, DTXX (4I5, F10.0)

NUMLP: Total number of degrees of freedom at which input pressure
time history are specified
NUMLH: Number of input pressure time histories
NUMTP: Number of pressure time pairs in every input pressure time
history
NTYPE = 0: Constant time increments in pressure time history
1: Specified times in pressure time history
DTXX: Constant time increment in the input pressure time
history (NTYPE = 0)

CARD 8 Output Stress and/or Motion Profile Specifications

A. NPFL, NDC, NSG, NPRINT, NPEL, NPMT (6I5)

NPFL = 0 Both motions at all nodes and stresses at all elements
1 Motions and stresses at specified nodes and elements respectively
2 Motions at all nodes
3 Stresses at specified elements
4 Stresses at all elements

NDC = 0 Write stress/displacement profile output to hard disc
1 Write stress/displacement profile output to floppy disc

NSG = 0 Write stress/displacement profile output in one file
1 Write stress/displacement profile output in specified files

NPRINT: Number of cycles between each output profile

NPEL: Number of elements in output stress profile

NPMT: Number of nodes in output motion profile

NOTE: If NDC = 1 and NSG = 0, the program writes displacement/stress profiles on hard disk under the name "DISTR"

B. If NPFL = 1 or 3, otherwise go to Card 8C.

NPRT(I), I = 1, NPEL (free format)

NPRT(I): List specified element numbers in sequential order

C. If NPFL = 1, otherwise go to next card

NMP(I), I = 1, NPMT (free format)

NMP(I): List specified node numbers in sequential order

CARD 9 Output Stress and/or Motion Time History Specifications

A. NTHS, NHPEL, NHPMT (3I5)

Time history options

NTHS = 0 Do not print time history data, go to next card
1 Motion time histories
2 Stress time histories
3 Both motion and stress time histories

NHPEL: Number of elements at which stress time histories are required

NHPMT: Number of nodes at which motion time histories are required

B. If NTHS = 2 or 3, otherwise go to 9C.

NHPRT(I), I = 1, NHPEL (free format)

NHPRT(I): List specified element numbers in sequential order

C. If NTHS = 1 or 3, otherwise go to next card

NHPN(I), I = 1, NHPMT (free format)

NHPN(I): List specified node numbers in sequential order

CARD 10 Numerical Time-Integration Options

TETA, BETA, GAMA, ALPA, (4F10.0)

TETA: θ
 BETA: β Refer to Table 1.
 GAMA: γ
 ALPA: α

TABLE 1. Values of β and θ for $\gamma = 1/2^*$ ($\alpha = 0$ by Default)

Integration Method (1)	β (2)	θ (3)
Explicit second central difference	0	1.0
Fox-Goodwin	1/12	1.0
Linear Acceleration	1/6	1.0
Newmark's constant acceleration	1/4	1.0
Wilson	1/6	2.0
Stiff linear acceleration	1/6	1.5

* $\gamma = 1/2$ indicates no damping

$\gamma > 1/2$ introduces numerical damping and $\beta = (\gamma + 1/2)^2/4$

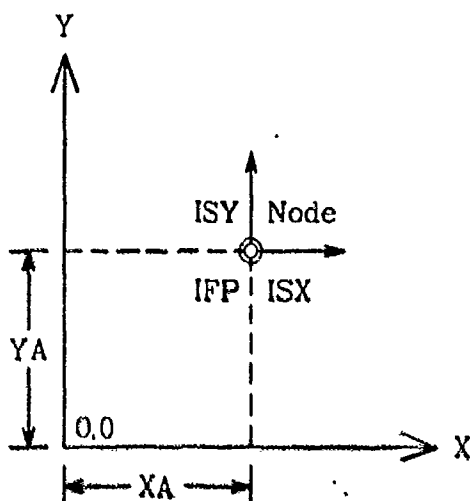
α Method available soon

For more information, see: Ghaboussi and Wilson, "Variational Formulation of Dynamic of Fluid Saturated Porous Elastic Solids," ASCE Engineering Mechanics Journal, August 1972.

CARD 11 Nodal Coordinates and Degree of Freedom Specifications

For each node:

NODE, ISX, ISY, IFP, XA, YA (4I5, 2F10.0)



NODE: Node Number

ISX: Specifies skeleton X Degrees of Freedom (DOF)

ISY: Specifies skeleton Y DOF

IFP: Specifies DOF for pore fluid pressure

ISX, ISY = 0 Free to move in specified direction

1 Fixed in specified direction

IFP = 0 Unknown pore fluid pressure

1 Zero pore fluid pressure

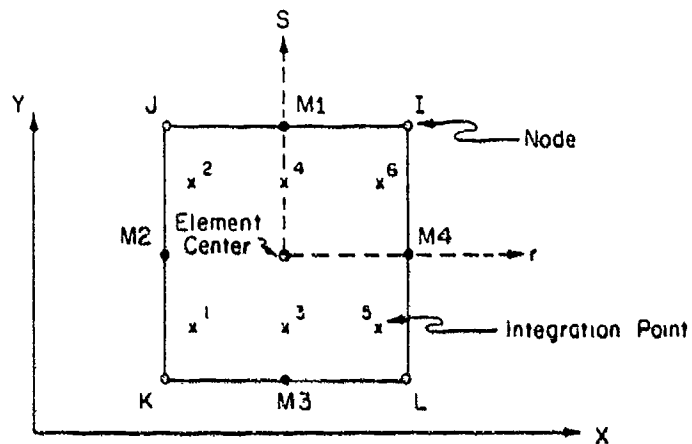
XA: X Coordinate

YA: Y Coordinate: Note for IP = 4 (1-D spherical analysis) set the mesh height equal to 1.0.

CARD 12 Element Specifications

For each element;

NEL, MAT, KS, KF, INTR, INTS, I, J, K, L, M1, M2, M3, M4 (14I5)



NEL:	Element number
MAT:	Material property number
KS = 0	Element has solid phase
1	Element has no solid phase
KF = 0	Element has fluid phase
1	Element has no fluid phase
INTR:	Number of integration points in r-direction
INTS:	Number of integration points in s-direction
I,J,K,L:	Node numbers at element corner
M1,M2,M3,M4:	Node numbers at element midside

CARD 13 MATERIAL PROPERTIES

A. Title (up to 80 characters)

B. General Property

POR, GF (Free Format)

POR: Initial porosity

GF: Unit weight of pore fluid

C. Permeability Property

NP, RK, BETHF (free format)

NP = 0: Constant permeability

= 1: Nonlinear permeability

RK : Darcy's coefficient of permeability

BETHF: Ward's fluid friction coefficient for turbulent flow

D. Grain Property

NG, BKG, ROG, CO, VO, S, PB (free format)

NG = 0: Constant grain modulus

1: Nonlinear grain modulus

BKG: Initial bulk modulus of grain

ROG: Initial mass density of grain

CO: Initial wave velocity at relatively low pressure

VO: Initial Poisson's ratio

S: Experimentally determined constant relating
loading wave velocity to peak particle velocity
(generally about equal to 1.5 for most rocks and
minerals)

PB: Threshold pressure beyond which materials tend to
behave like fluids

E. Fluid Property

NW, BKW, ROF, SO, HC, PAO, T (free format)

NW = 0: Constant fluid modulus

1: Nonlinear modulus

BKW: Initial bulk modulus of pore fluid

ROF: Initial mass density of pore fluid

SO: Initial degree of saturation

HC: Coefficient of solubility (Henry's constant)

PAO: Initial pore air pressure (absolute)

T: Pressure difference between the air and pore water due to
surface tension

F. Skeleton Property

a. General Property

NS, BKS, GS, TENS, STIFAC, SHEFAC, PMN (free format)

NS = 0: Linear elastic modulus

1: Nonlinear modulus

BKS: Initial bulk modulus of skeleton

GS: Initial shear modulus of skeleton

TENS = 0.0: No tension cut-off

1.0: Tension cut-off

STIFAC: Factor which reduces normal stiffness once tensile strength is exceeded (example: reduced modulus = original modulus/STIFAC)

SHEFAC: Factor which reduces shear stiffness once shear strength is exceeded (see example above)

PMN: Tensile strength (tensile stress is positive)

b. Material Model Specification

MODNO (free format)

MODNO = 0: Linear elastic material model

1: Decoupled elasto-plastic model

4: Uniaxial strain model

5: Generalized Hoek and Brown rock model

6: ARA 3-Invariant model

c. Decoupled Elasto-Plastic Model (DCOUP)

If MODNO is not equal to 1, go to next card group.

1. Shear Stress-Strain Behavior

GP, A, B (free format)

GP: Plastic shear modulus

A: a (constant defining proportional elastic limit)

B: b (fraction of plastic shear modulus after failure)
(refer to Model DCOUP by Kim, Blouin and Timian, 1986)

****DESCRIBE VOLUMETRIC BEHAVIOR****

2. NLPC (I5)

3. P_1, B_{L1}

P_2, B_{L2}

- -

- -

P_n, B_{Ln}

"NLPC" cards with format (2F10.0)
for each card

4. NUPC (I5)

5. P_1, B_{U1}

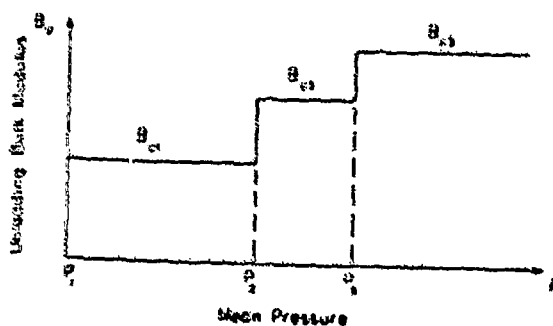
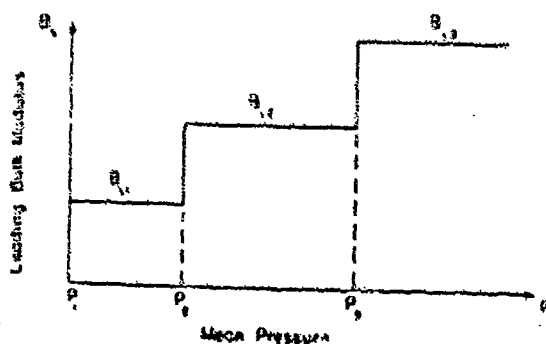
P_2, B_{U2}

- -

- -

P_n, B_{Un}

"NUPC" cards with format (2F10.0)
for each card

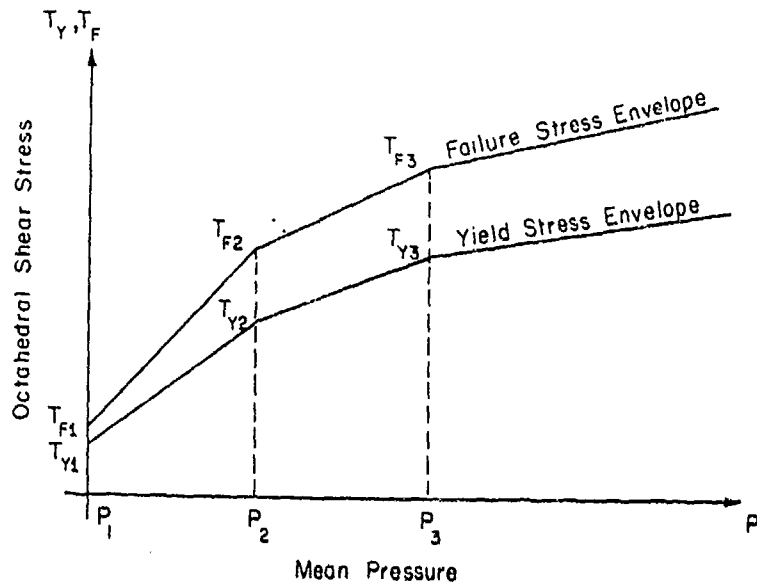


NLPC: Number of pressure/modulus pairs describing
the loading bulk modulus
BL_i: Loading bulk modulus at mean pressure P_i
NUPC: Number of pressure/modulus pairs describing
the unloading bulk modulus
BU_i: Unloading bulk modulus at mean pressure P_i

****DESCRIBE DEVIATORIC BEHAVIOR****

6. NTPC (15)

7. P_1, T_{Y1}, T_{F1}
 P_2, T_{Y2}, T_{F2}
 $- \quad - \quad -$
 $- \quad - \quad -$
 P_n, P_{Yn}, P_{Fn} } "NTPC" cards with format (3F10.0) for each card



NTPC: Number of pressure/yield stress/failure stress points describing the yield and failure envelopes as a function of mean pressure

T_{Yi}, T_{Fi} : Octahedral shear stress at yield and failure, respectively, at mean pressure P_i

d. Uniaxial Strain Model (UNIAX) Reference: Kim and Blouin, 1986

If MODNO is not equal to 4 go to next card group

1. POSNR, EQNO, C, D, SVMALL (free format)

POSNR: Poisson's ratio

EQNO = 1: Unloading modulus as a function of effective vertical stress

2: Unloading modulus as a function of previous maximum effective vertical stress (σ_v' max)

3: Unloading modulus computed by $M_u = C (\sigma_v'$ max)^D

C,D: Material parameters defining unloading modulus when EQNO = 3

2. NLPC (I5)

3. S_1, M_{11}

- -
- -

S_n, M_{Ln}

"NLPC" cards with format (2F10.0) for each card

4. NUPC (I5)

5. S_1, M_{U1}

- -
- -

S_n, M_{Un}

"NUPC" cards with format (2F10.0) for each card

NLPC: Number of vertical stress-loading constrained modulus pairs

M_{Li} : Loading constrained modulus at vertical stress S_i

NUPC: Number of vertical stress-unloading constrained modulus pairs

M_{Ui} : Unloading constrained modulus at vertical stress S_i

e. Generalized Hoek and Brown Rock Model

If MODNO is not equal to 5, go to next card group.

RN, ALPHA, BETA, RLKAPA, RLK (free format)

RN: n
 ALPHA: α
 BETA: β
 RLKAPA: κ
 RLK: K

Note that the strength parameters, n , α , β , κ , and K are described in detail by Kim and Blouin, 1986.

f. ARA 3 - Invariant Model, Reference: Merkle and Dass, 1985)

If MODNO is not equal to 6, go to next card group.

1. APEX, ATMO (free format)

APEX: Tensile strength measured along the octahedral normal stress axis
 ATMO: Atmospheric pressure (0.1013 MPa)

2. AKUR, AN, APOI (free format) Elastic Constants

AKUR: Constant for Young's modulus (K_{ur})
 AN: Constant for Young's modulus (n)
 APOI: (Poisson's ratio (ν))

3. AR, ACRV (free format) Compressive Yielding and Hardening Parameters

AR: Cap axes ratio
 ACRV: Number of c and p data set

4. AACC(1), AAPC(1)
AACC(2), AAPC(2) Free Format "ACRV" cards

,
 ,
 ,

AACC: Hardening constant (c)
 AAPC: Hardening constant (p)

5. AEY, AMY, AETA1 (free format) Expansive Yielding and Hardening Parameters

AEY: Yield constant (E)
 AMY: Yield exponent (m)
 AETA1: Failure constant (n_1)

6. ATG, ARG, ASG (free format) Plastic Potential Constant

ATG: t
 ARG: R
 ASG: S

7. APBAR, AL (free format) Work Hardening Constant

APBAR: \bar{p}
 AL: l

Note that the peak expansive plastic work, $w_{p,peak}$, is related to initial confining stress as

$$w_{p,peak} = \bar{p} \cdot p_a \left(\frac{\sigma_{3c}}{p_a} \right)^l$$

8. AALPH, ABETA (free format)

AALPH: Work hardening constant (α)
 ABETA: Work hardening constant (β)

Note that the hardening parameter, q , is related to the initial confining stress as

$$q = \alpha + \beta \left(\frac{\sigma_{3c}}{p_a} \right)$$

and the program MPDAP computes the hardening parameters a and b as follows:

$$a = \eta_1 \cdot \left(\frac{e \cdot p_a}{w_{p,peak}} \right)^{\left(\frac{1}{q} \right)}$$

and

$$b = \frac{1}{q \cdot w_{p,peak}}$$

CARD 14 Initial In Situ Effective Stress Conditions

If ISFG from Card 4 equals 1 or 2, otherwise go to next card
For each element

SXX, SYY, SZZ, SXY (4F10.0)

Initial effective skeleton stresses

SXX = σ_x' (normal stress in x direction)

SYY = σ_y' (normal stress in y direction)

SZZ = σ_z' (normal stress in z direction)

SXY = τ_{xy} (shear stress in xy plane)

CARD 15 Initial Pore Fluid Pressures

If ISFG from Card 4 equals 1, 3, or 4, otherwise go to next card

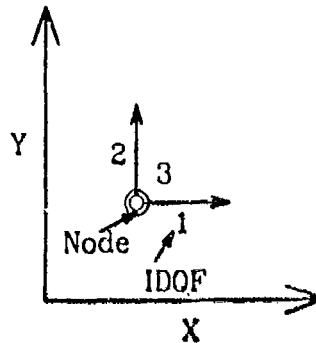
PRF(I) I = 1, NUMEL (F10.0)

PRF: List of initial pore fluid pressures in each element, specified sequentially from 1 to NUMEL.

Note that tensile stresses are positive.

CARD 16 Input Loading: For specified pressure and flow time histories
(Card 4, NFG = 2)

- A. Header (80 characters)
- B. For each of the NUMLP nodes (Card 7) at which a load is applied:
NODE, IDOF, LHNO, CINT (3I5,E10.3)
- C. TD(I), I = 1, NUMTP (7E10.0) for (NTYPE = 1)
- D. For each of the NUMLH (Card 7) loading time histories:
DYL(I), I = 1, NUMTP (7E10.0)
- E. Comment Card (80 characters) - to separate loadings



NODE: Node number

IDOF = 1 Total force acting on a given node in the x direction
2 Total force acting on a given node in the y direction
3 Flow at the given node

LHNO: Load history number (one of NUMLH load histories)

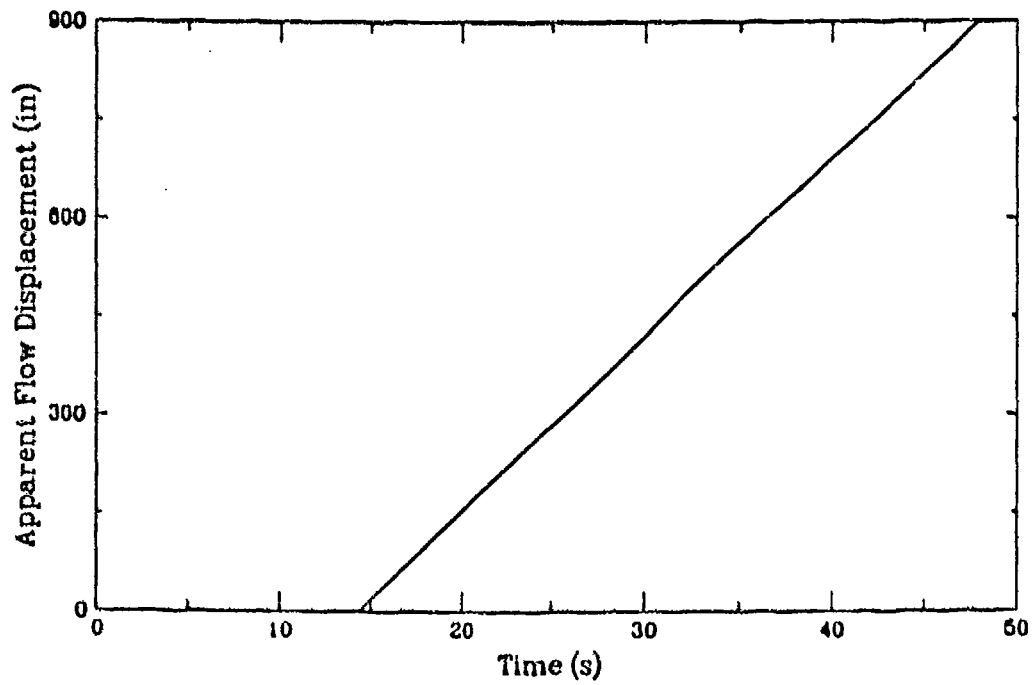
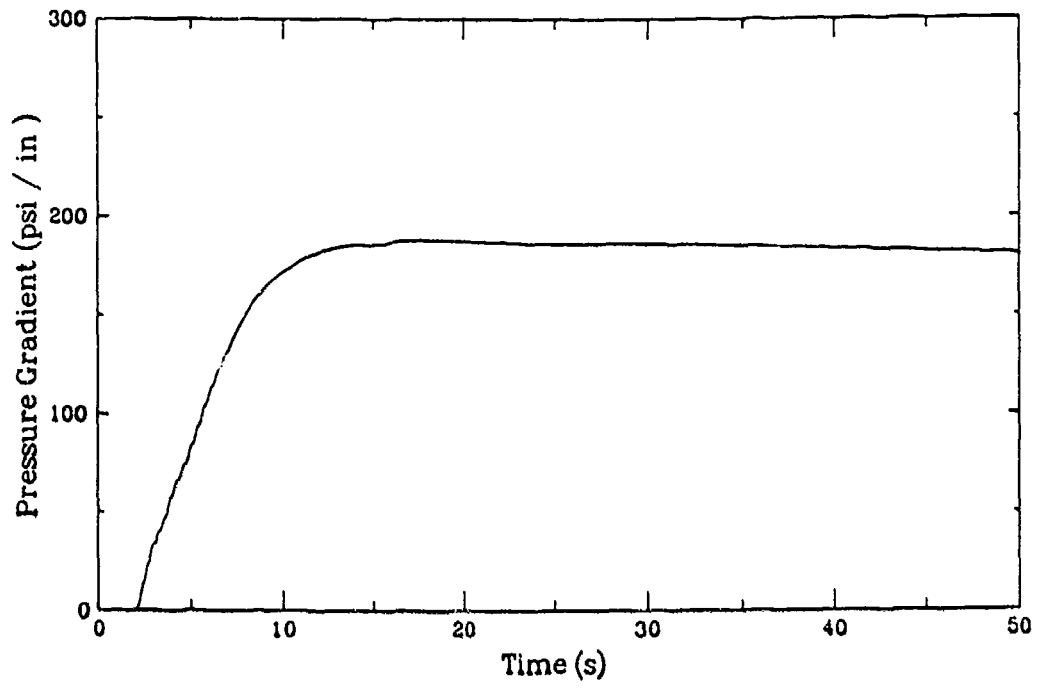
CINT: Load intensity factor (used to convert pressure or flow on a given node, based on contributing area)

TD(I): Set of specified times used in all the pressure loading histories

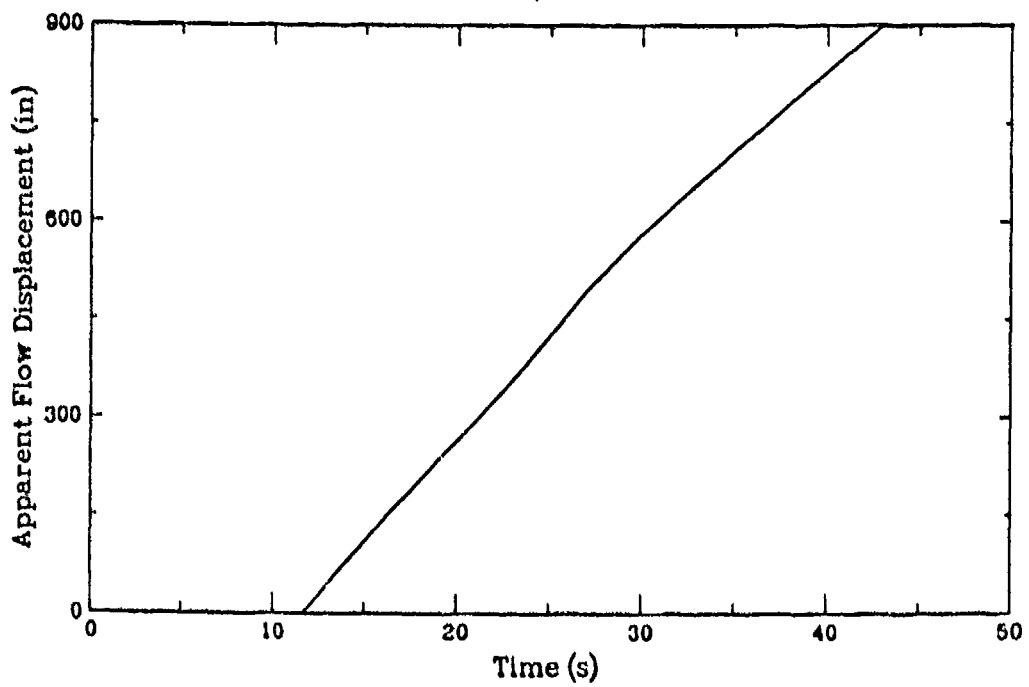
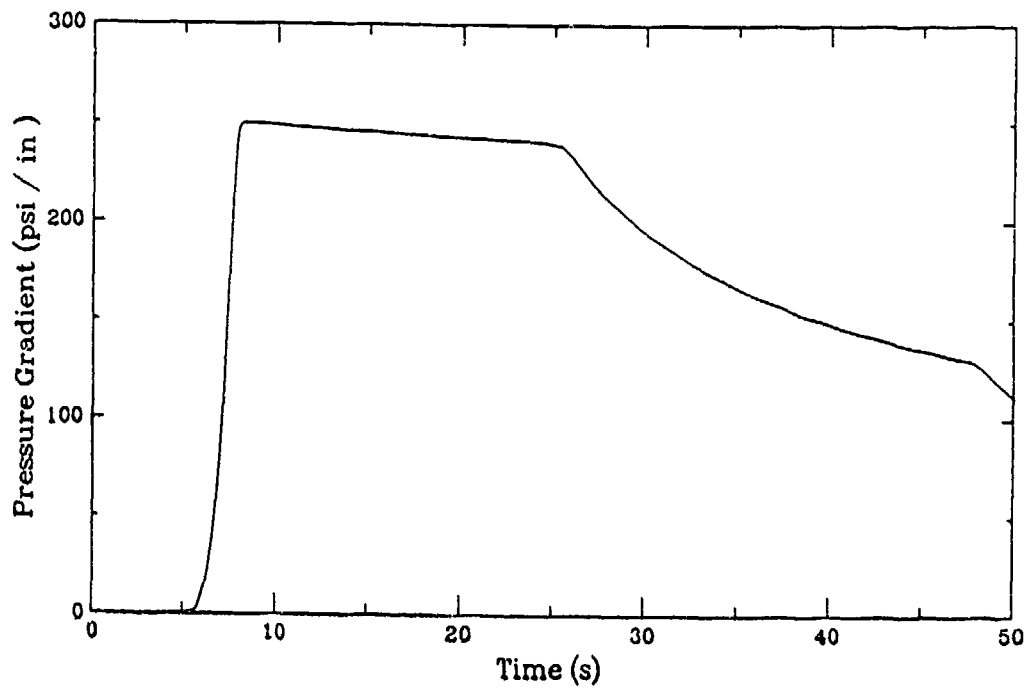
DYL(I): A set of pressure/flow magnitudes input for each loading history at corresponding times TD(I)

APPENDIX B
STEADY STATE FLOW DATA THROUGH
ENEWETAK BEACH SAND

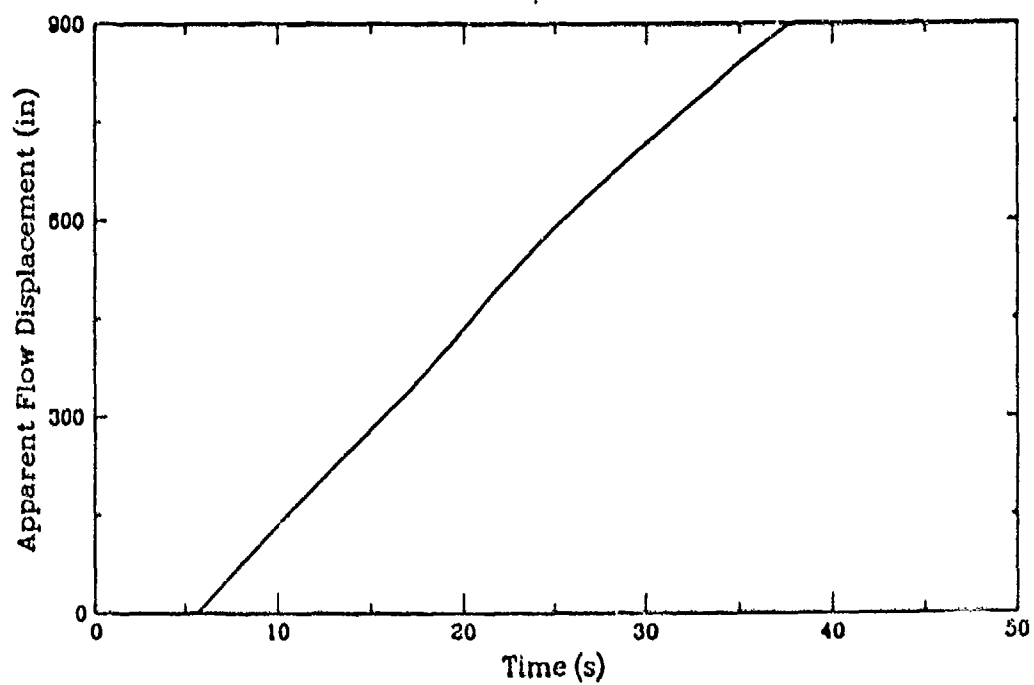
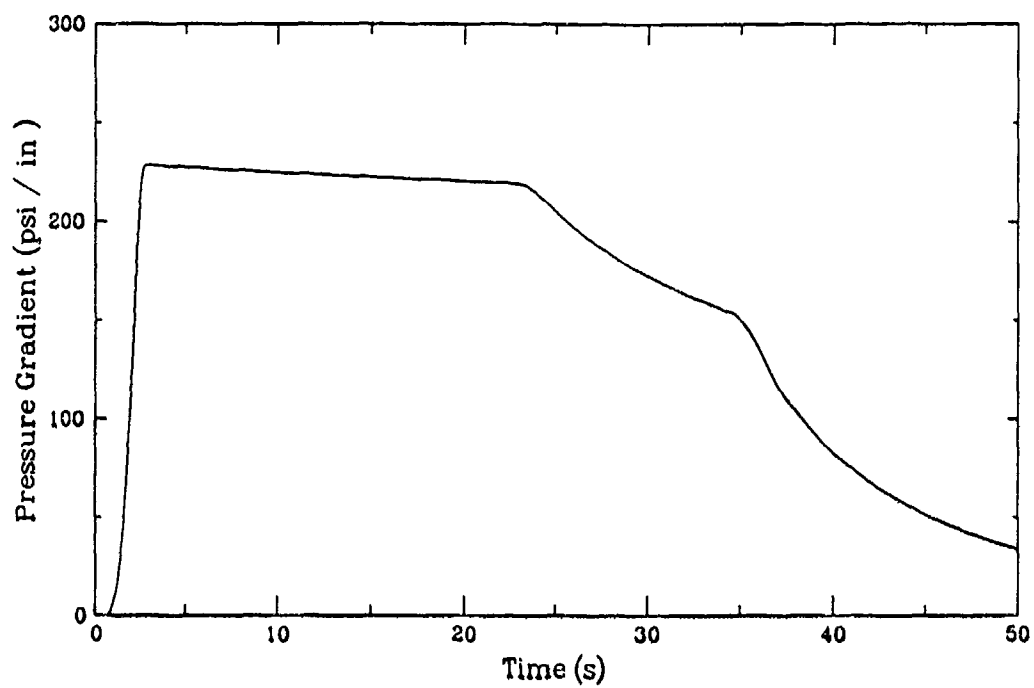
U21C8



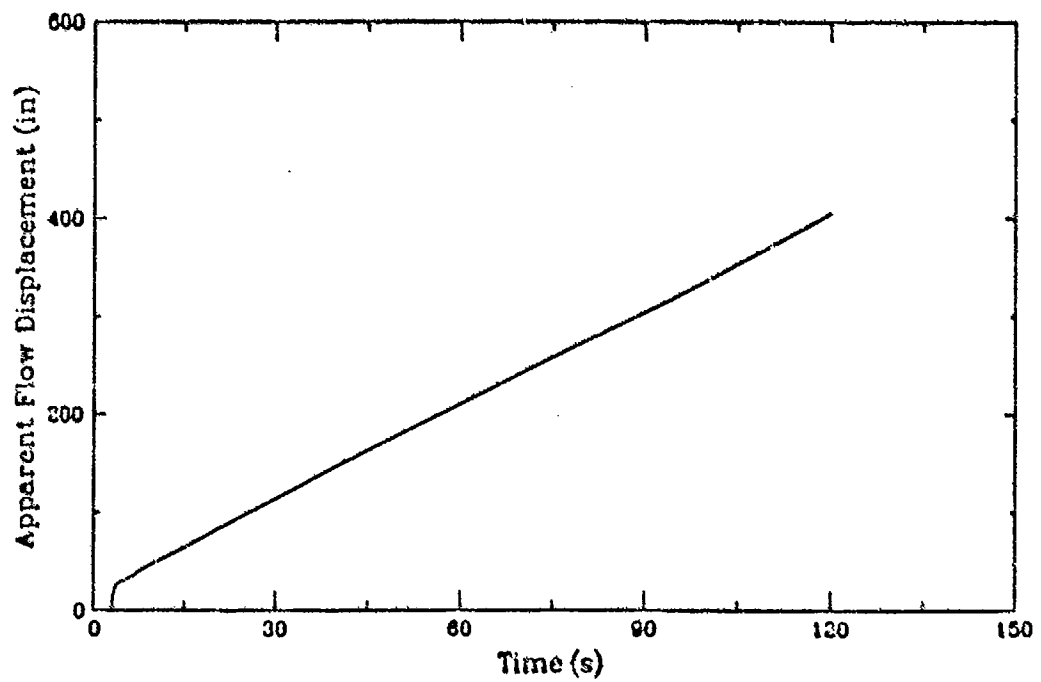
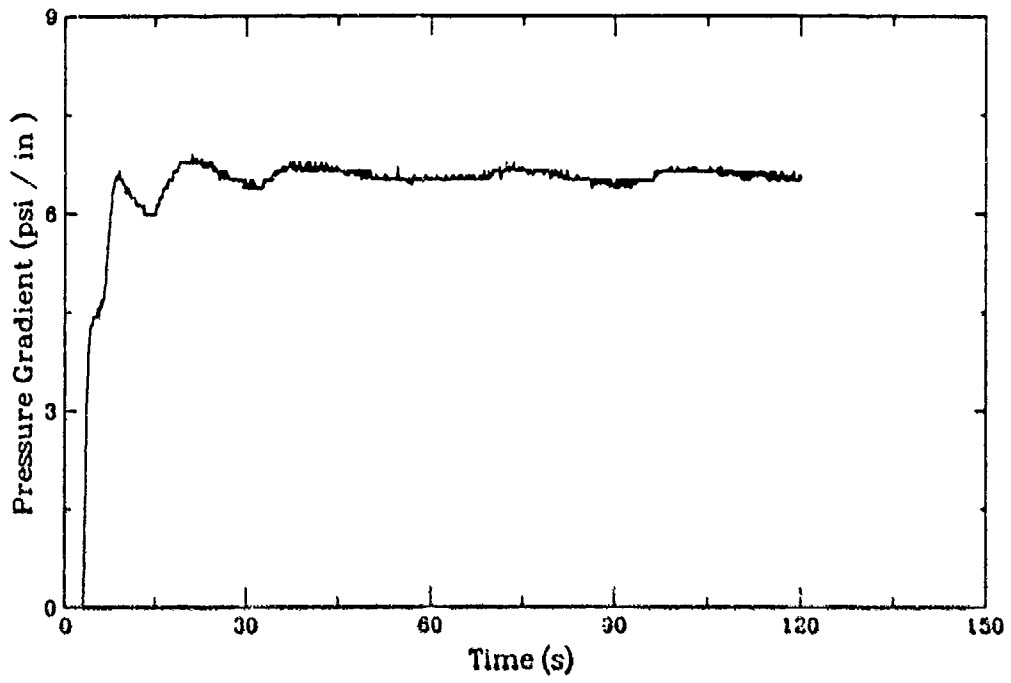
U24A8



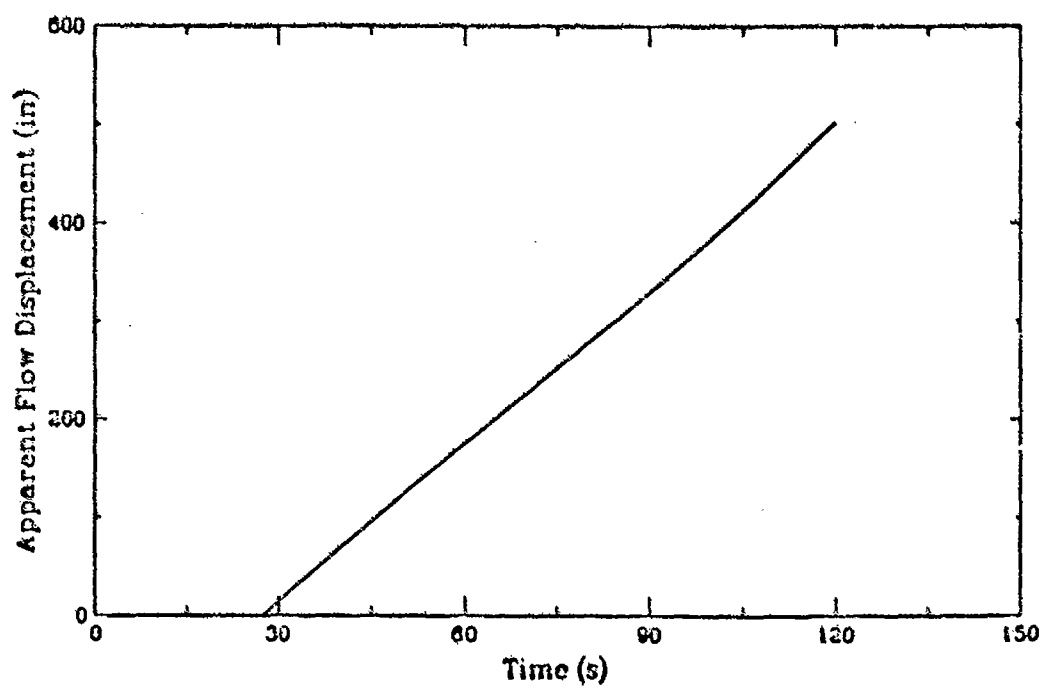
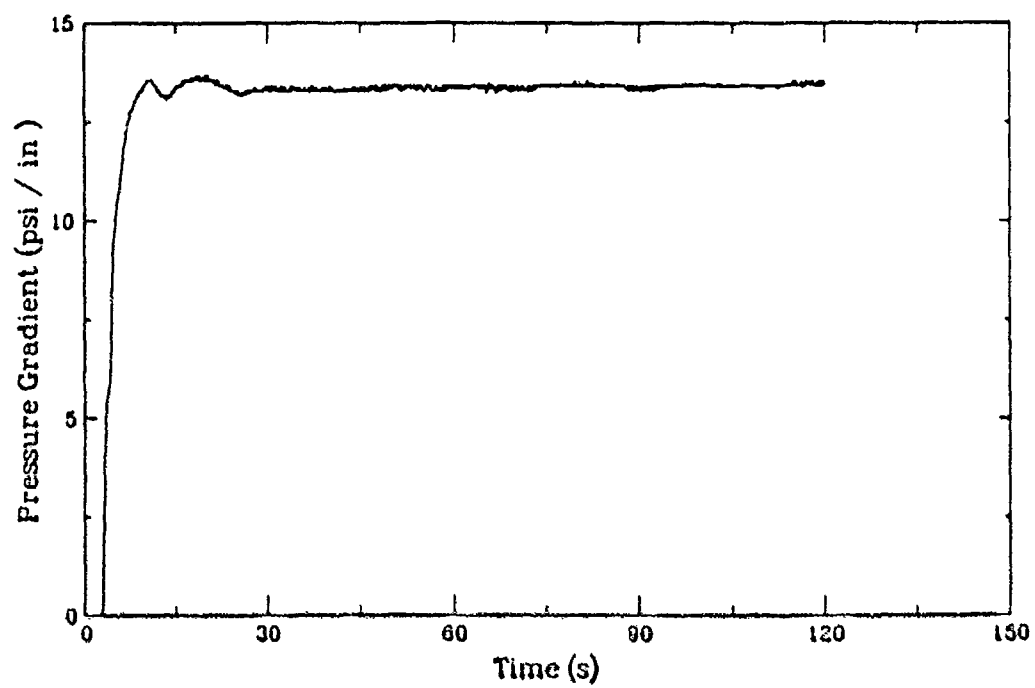
U24B8



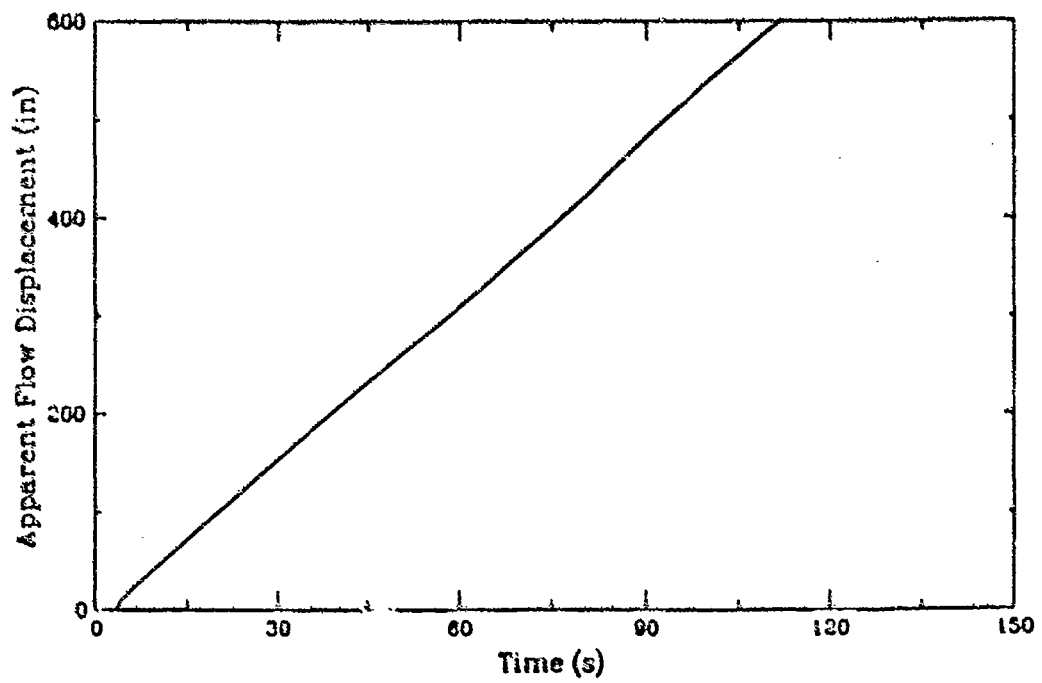
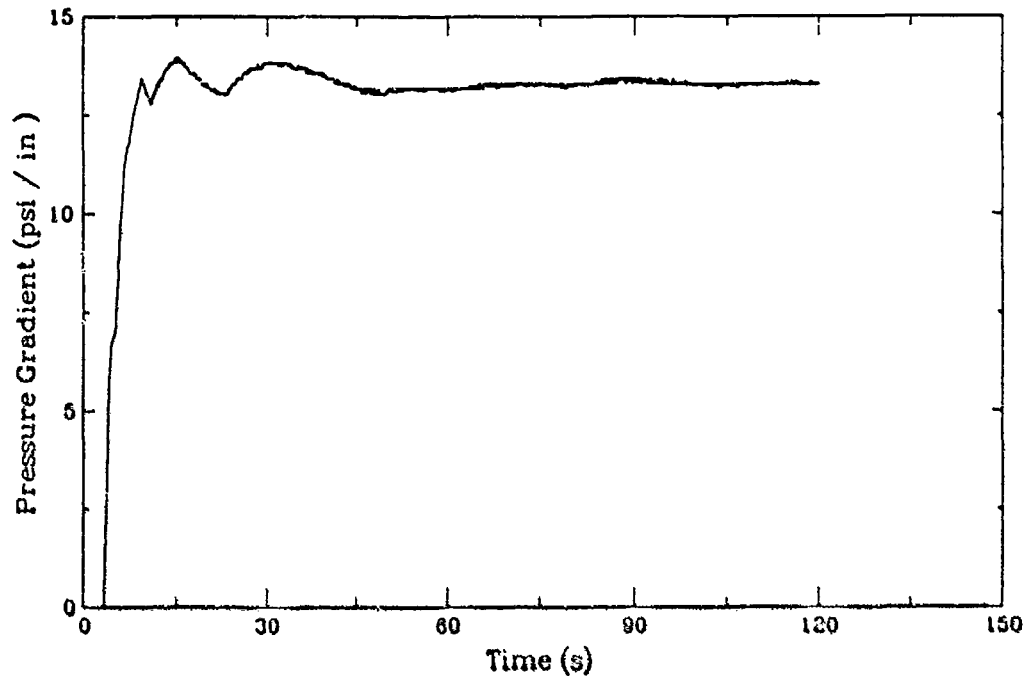
U2718



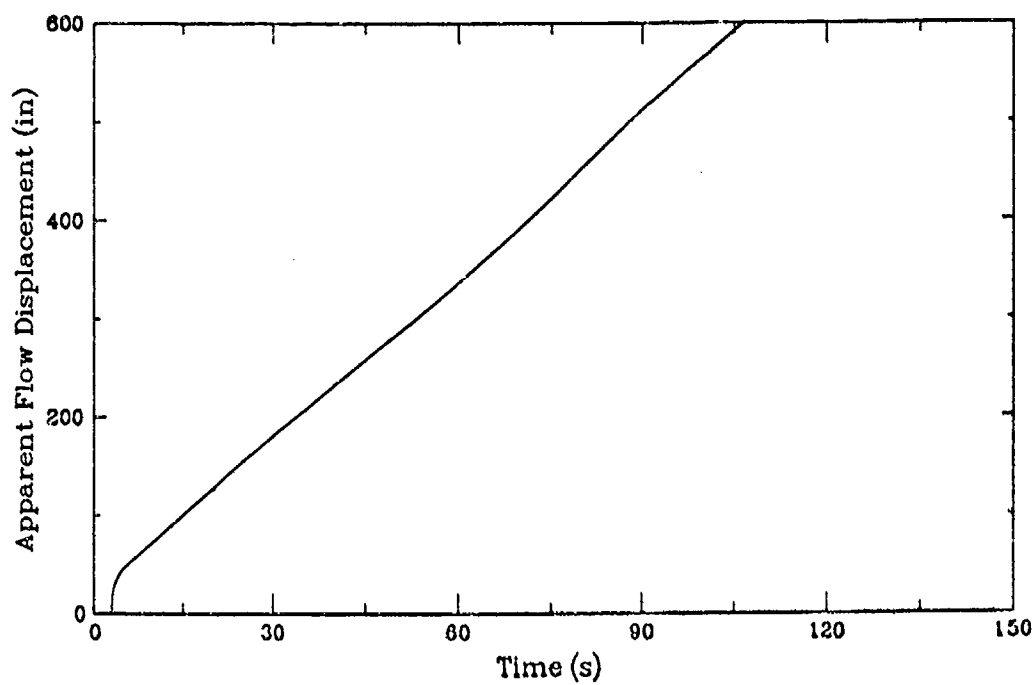
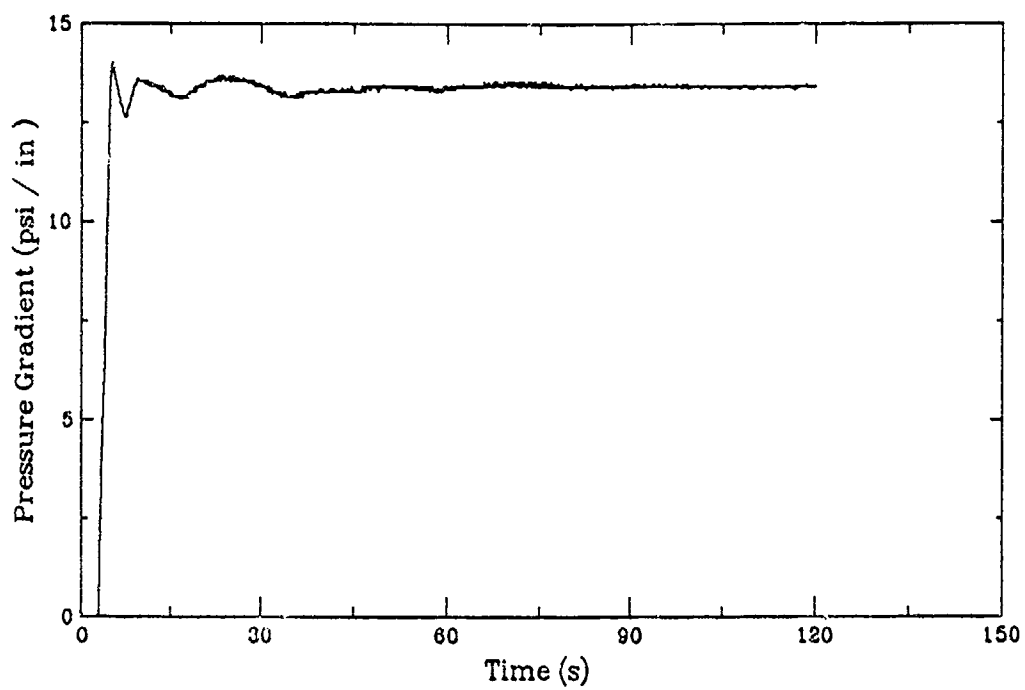
U27D8



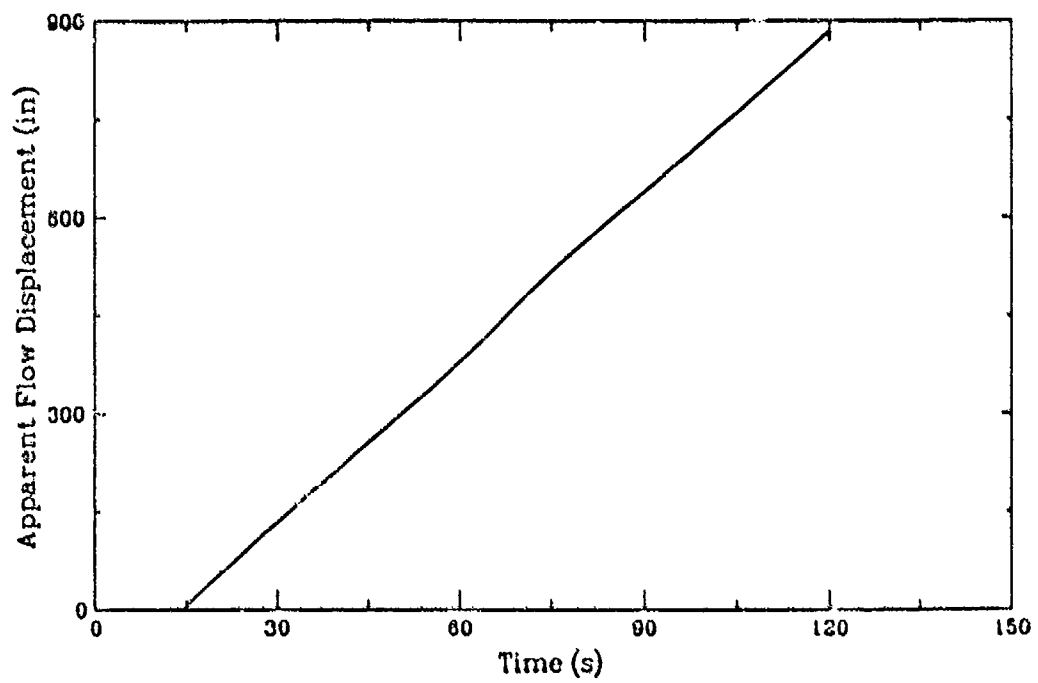
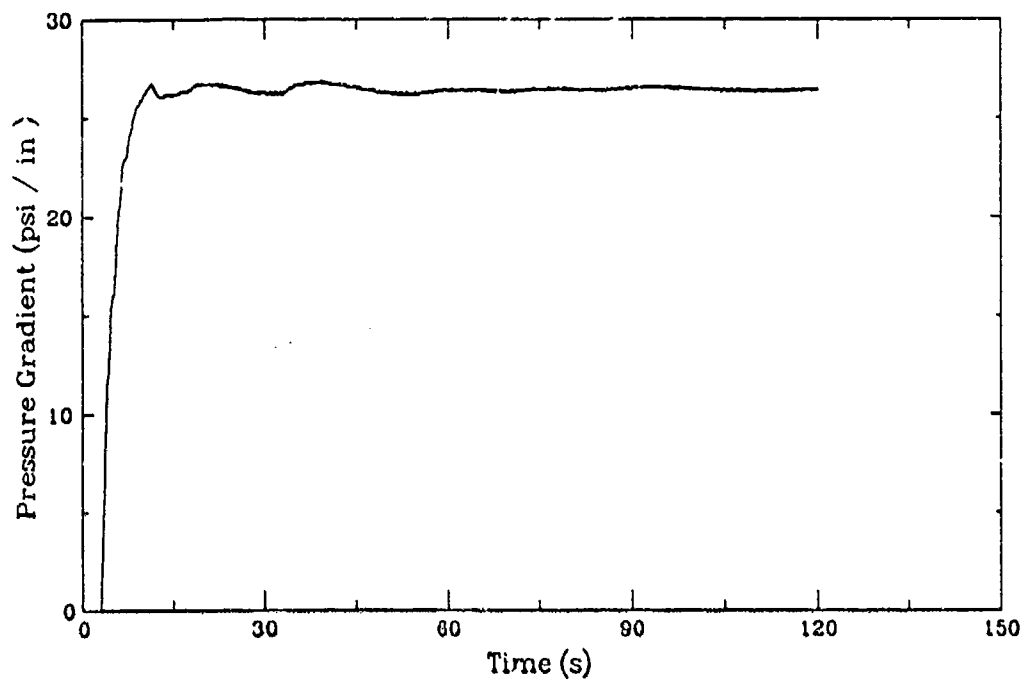
U27E8



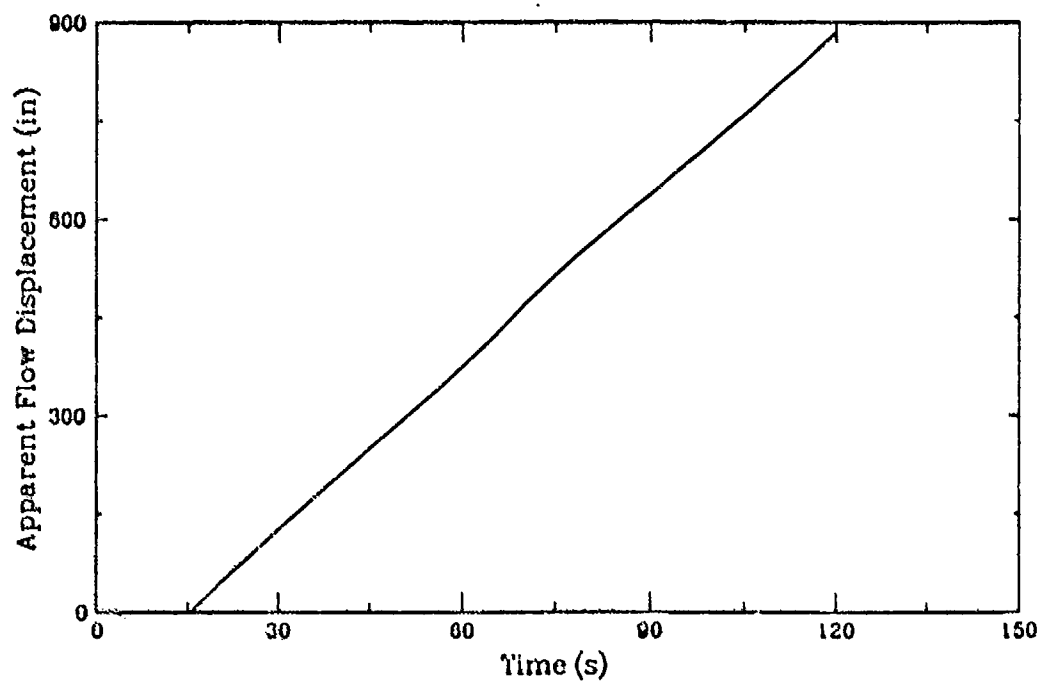
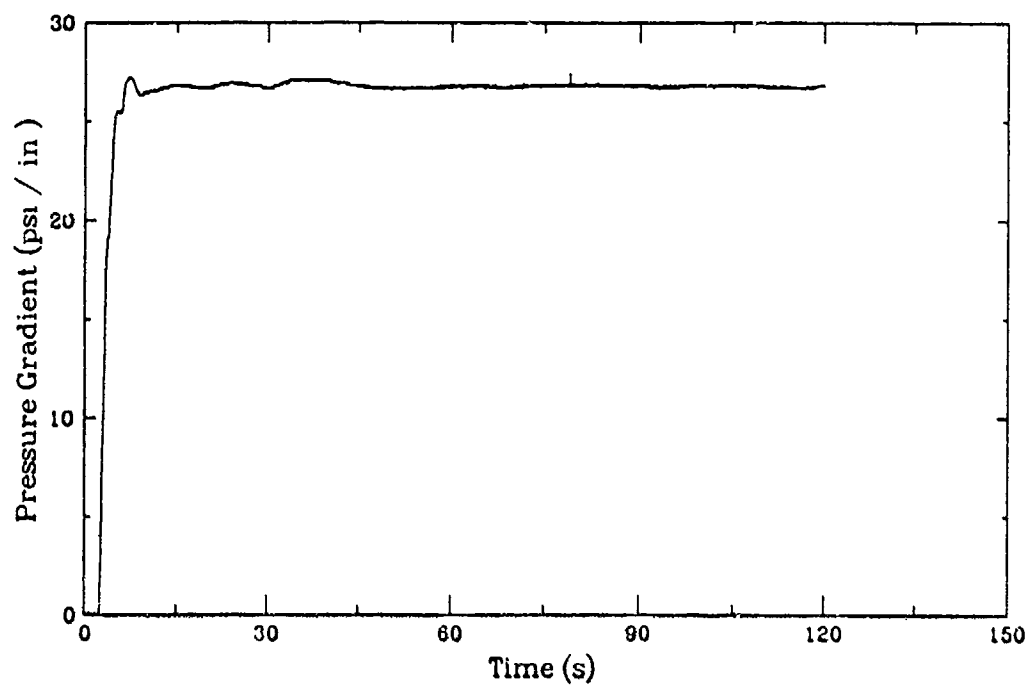
U27F8



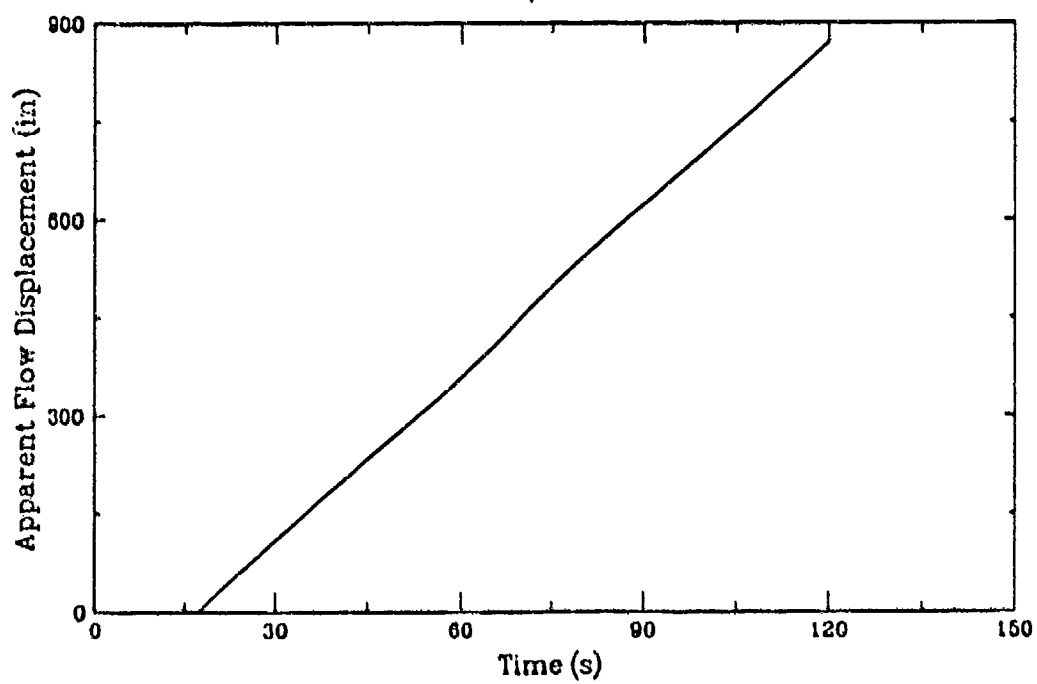
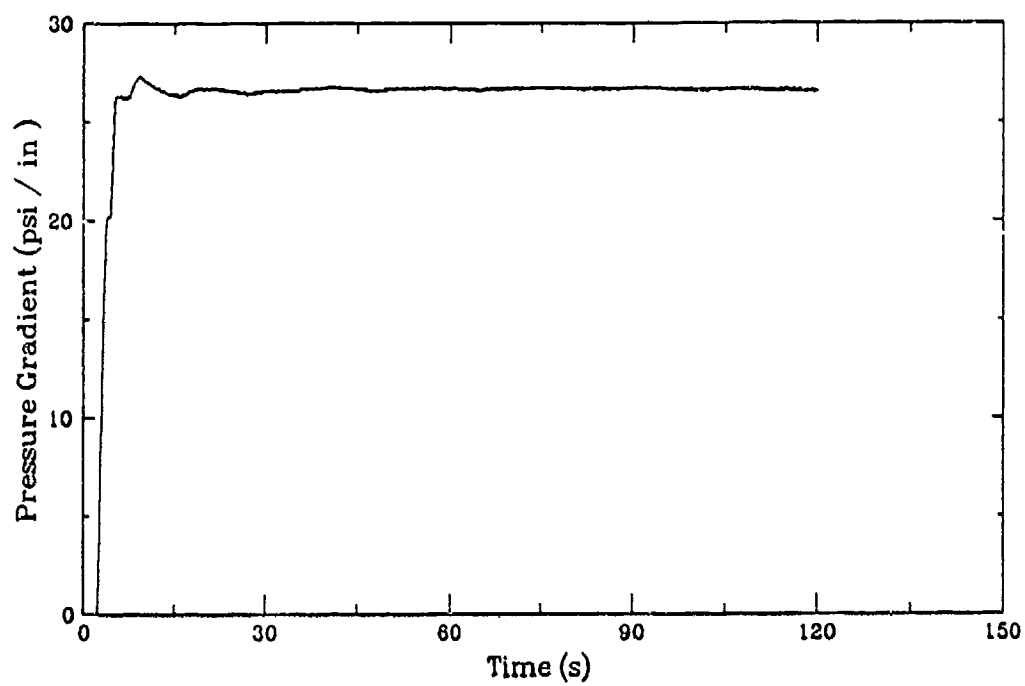
U27A8



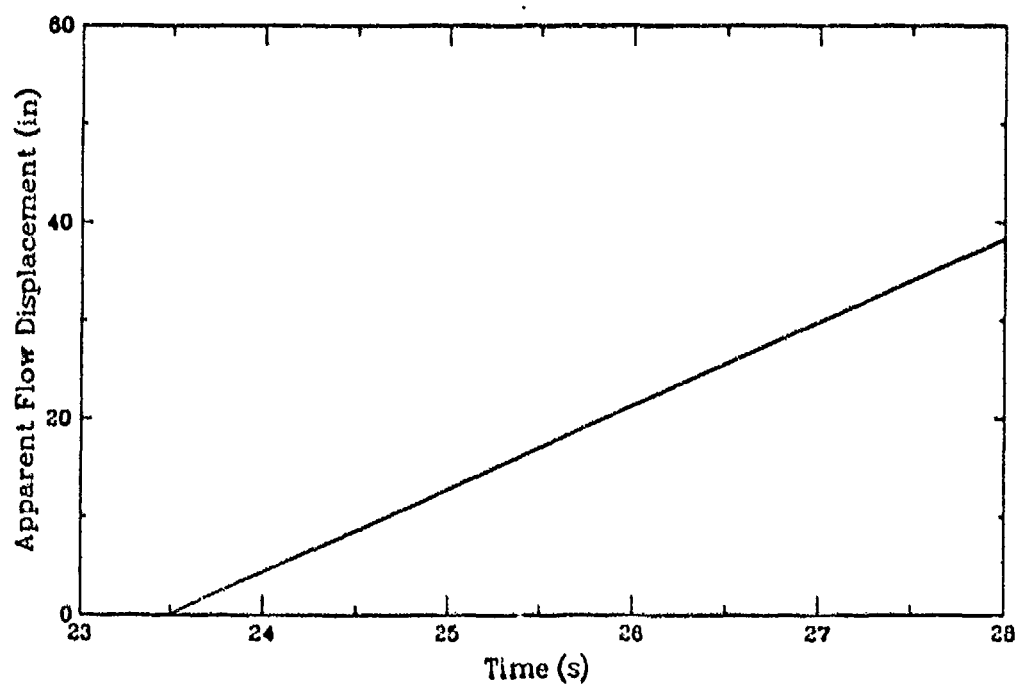
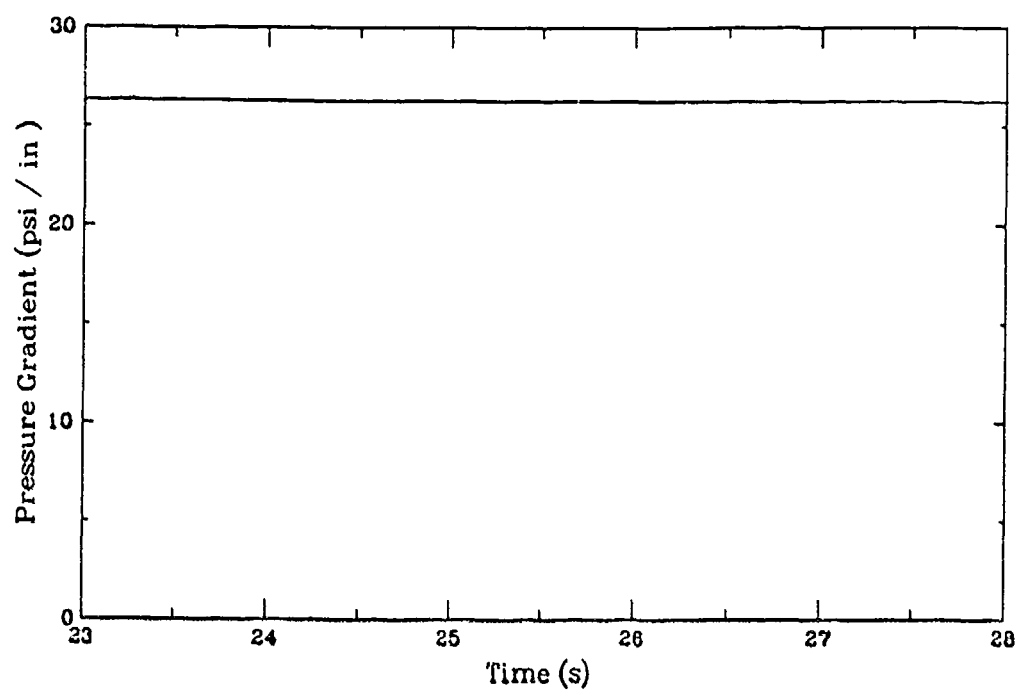
U27B8



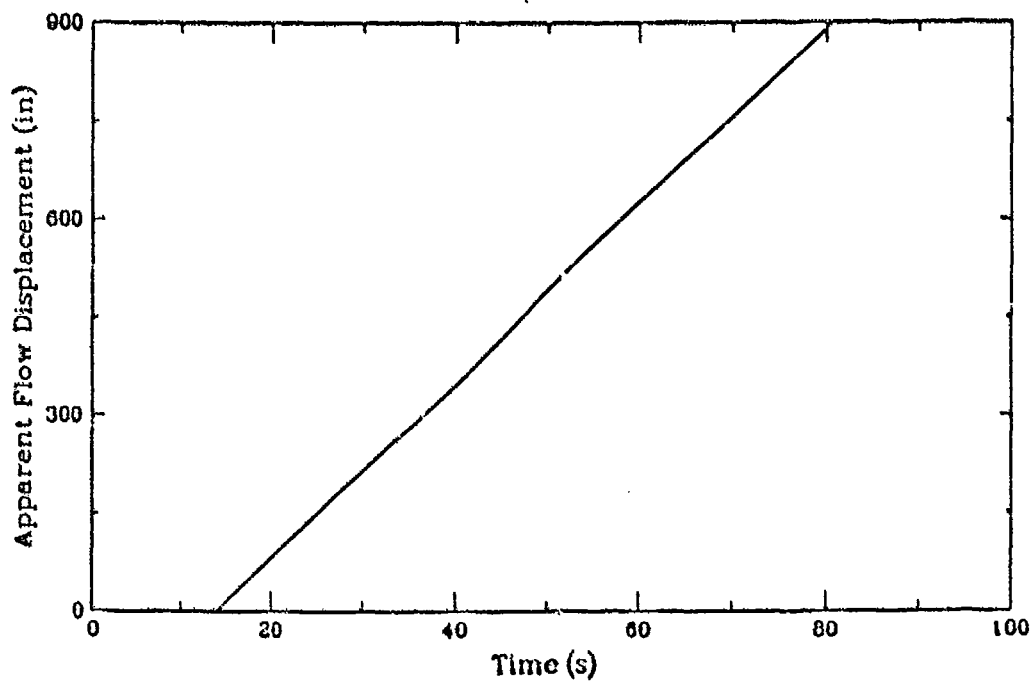
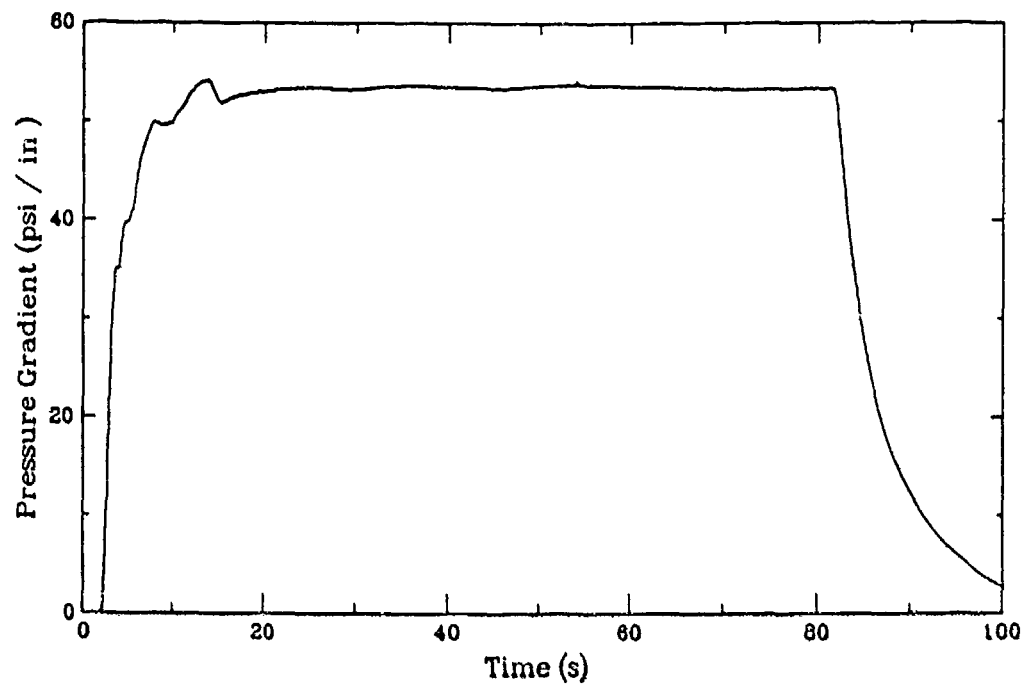
U27C8



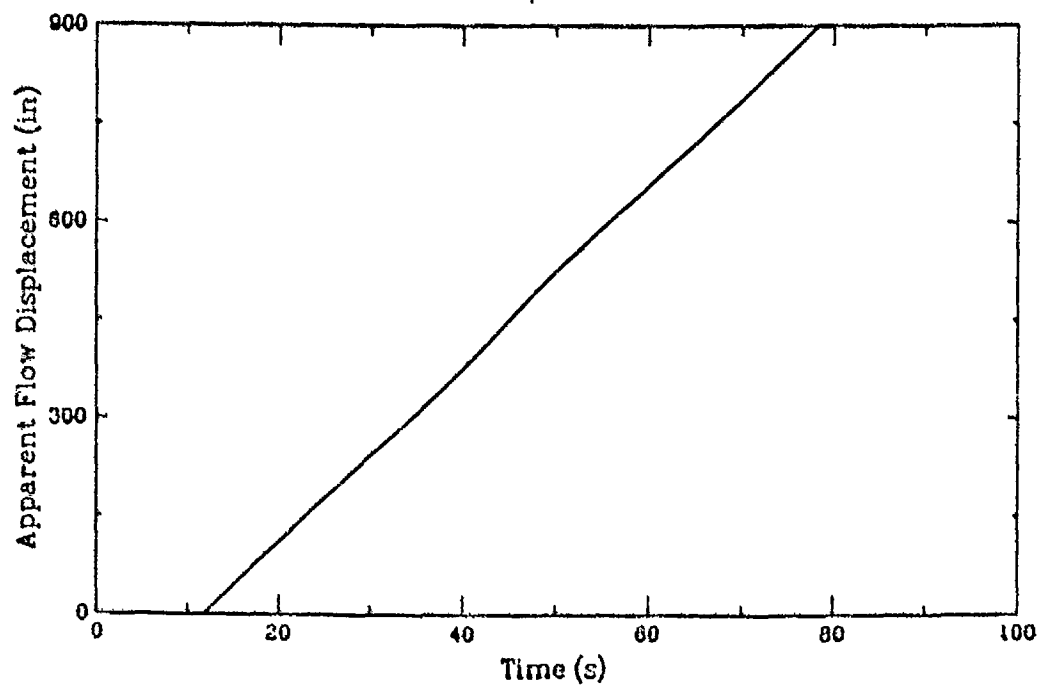
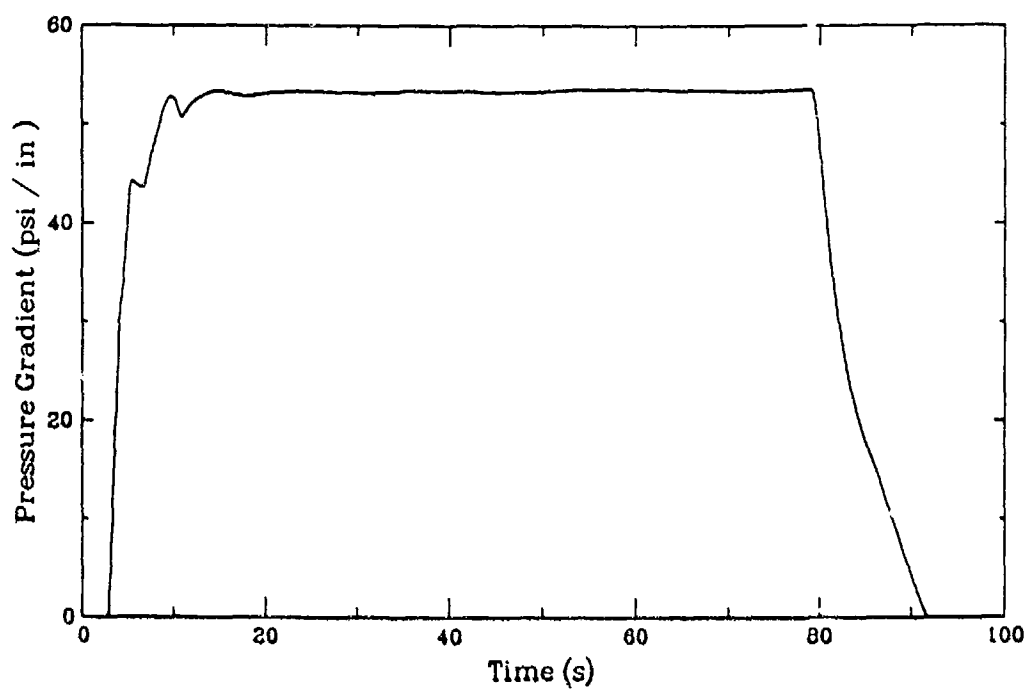
G9F8



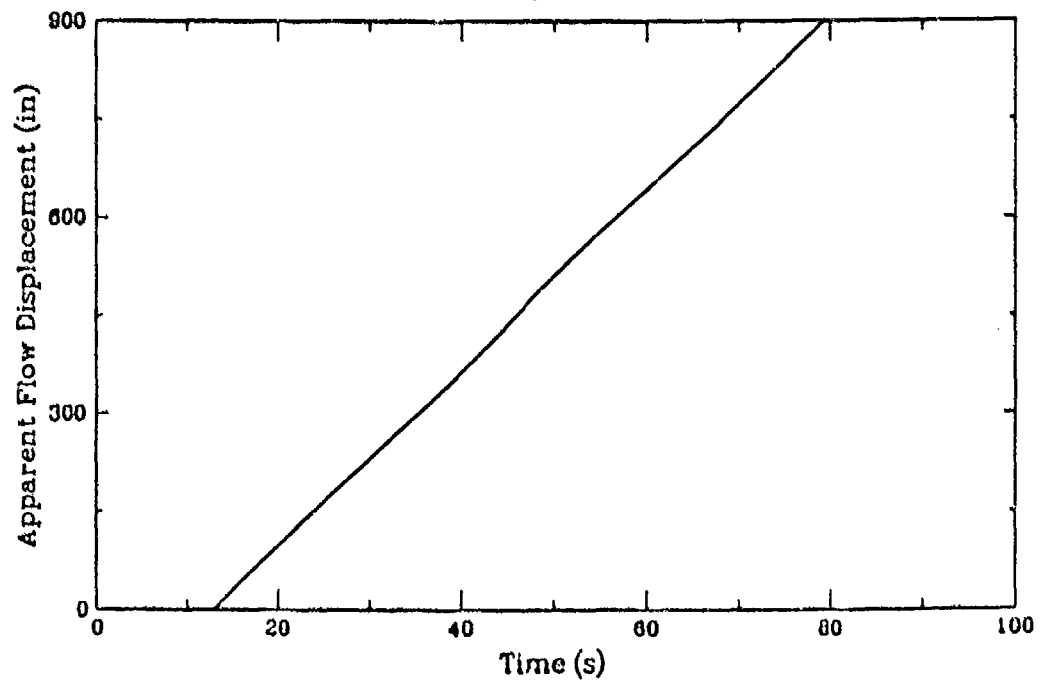
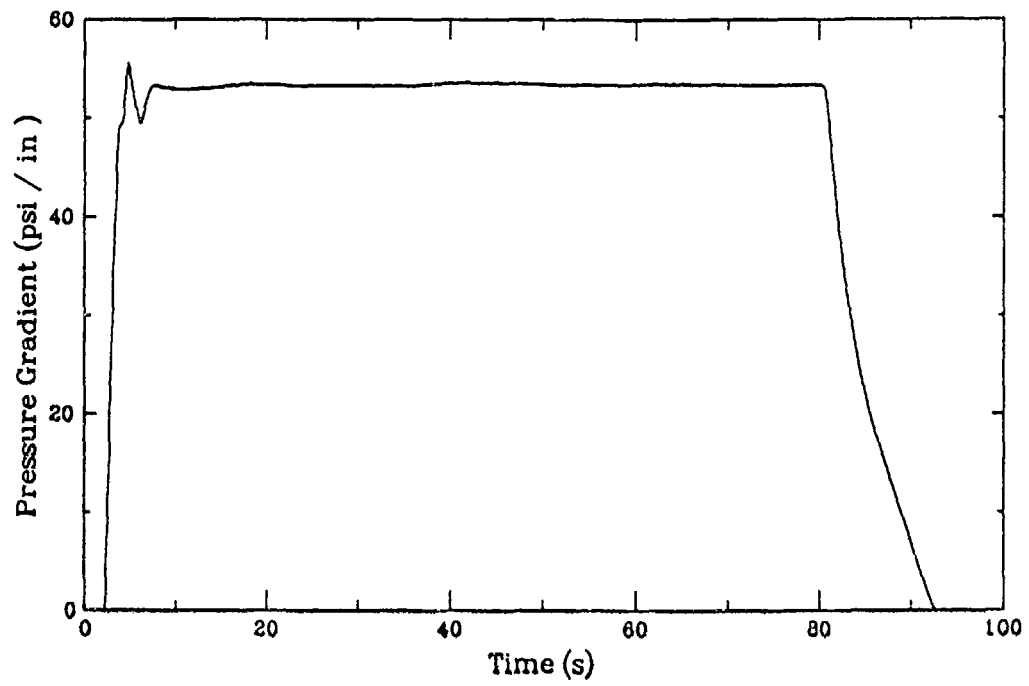
U27J8



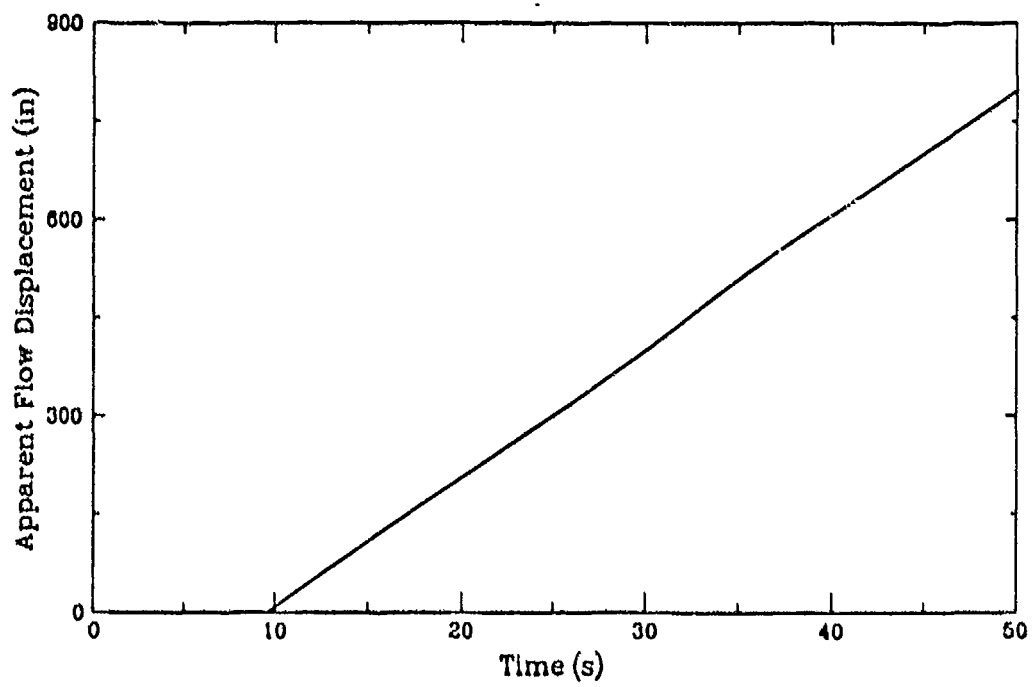
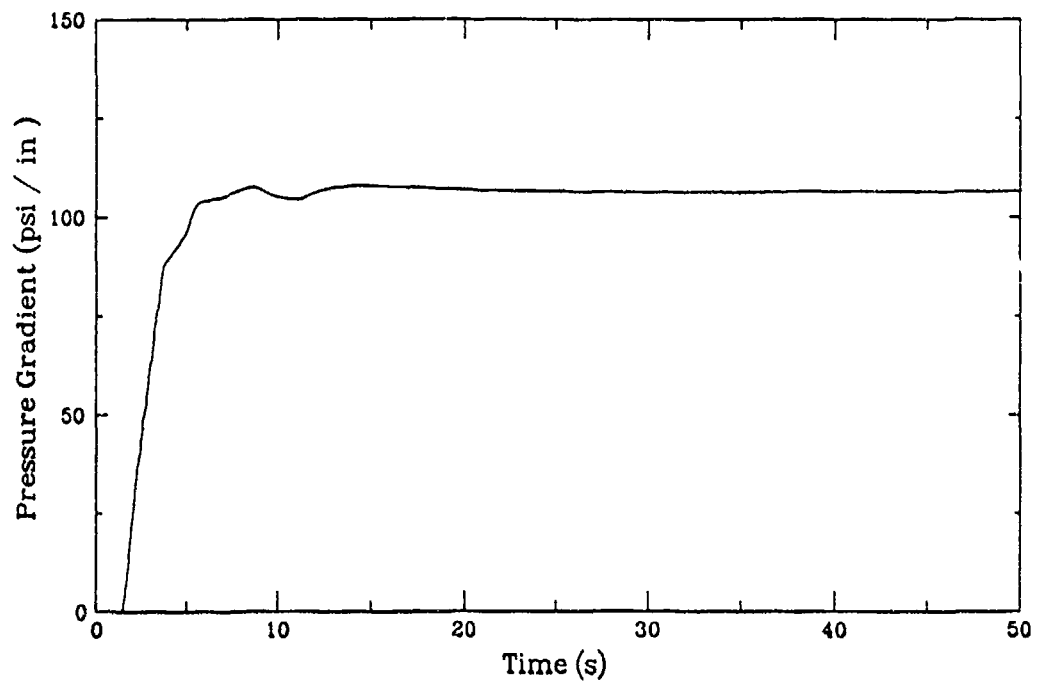
U27K8



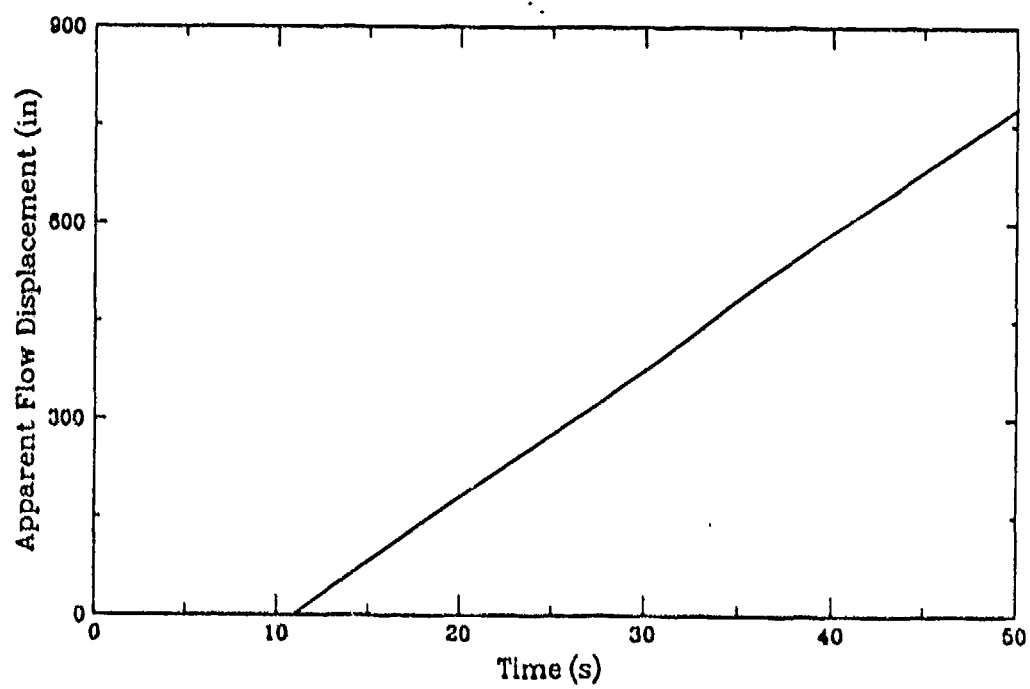
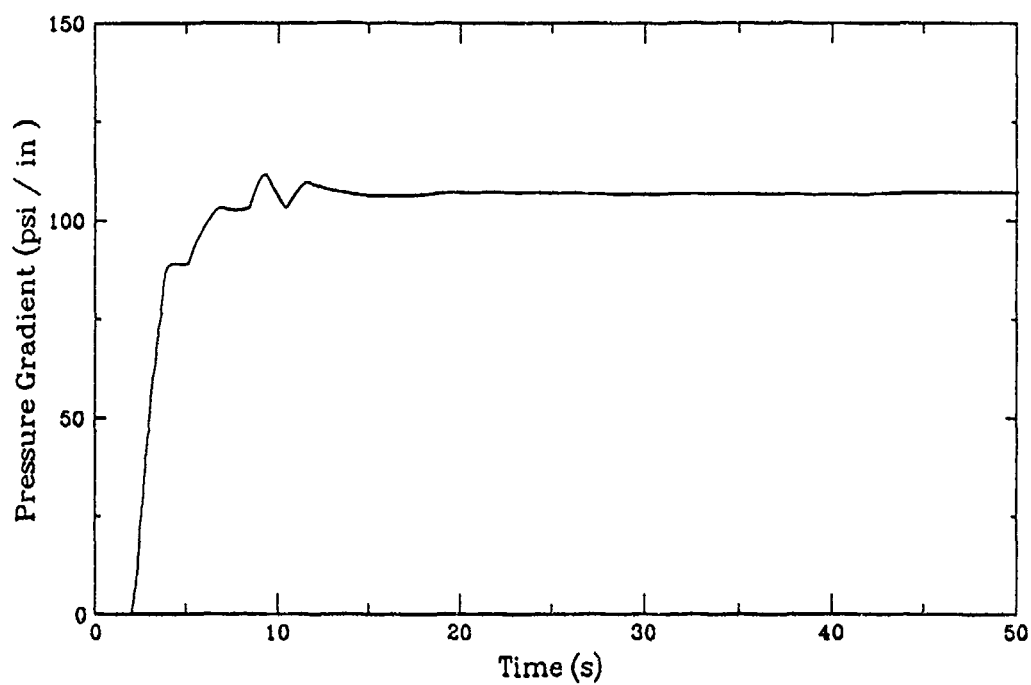
U27L8



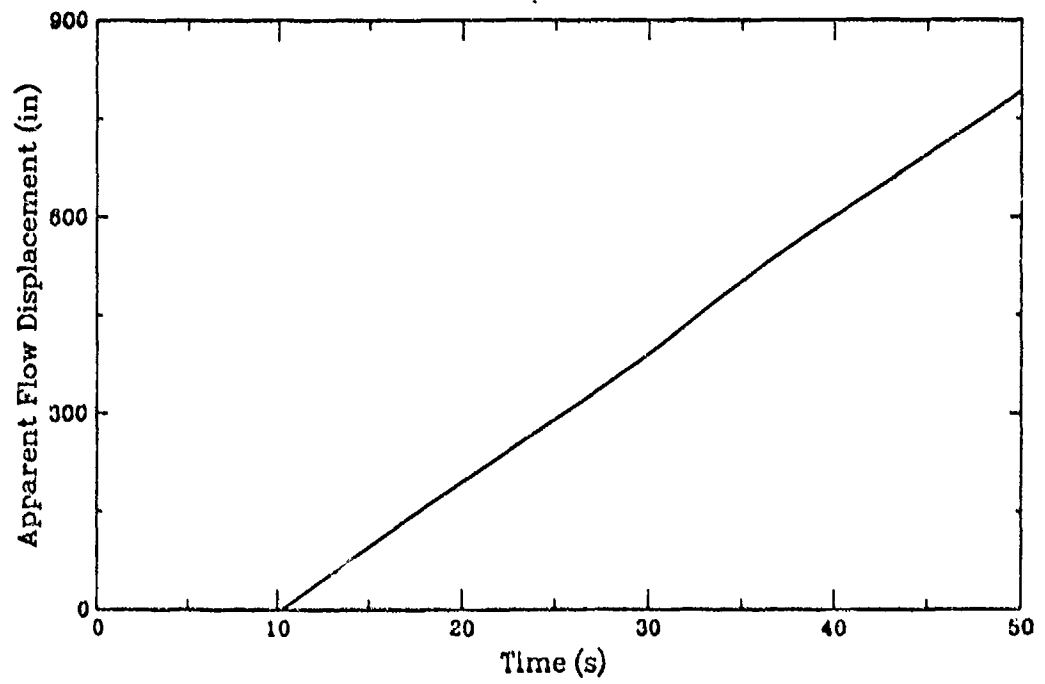
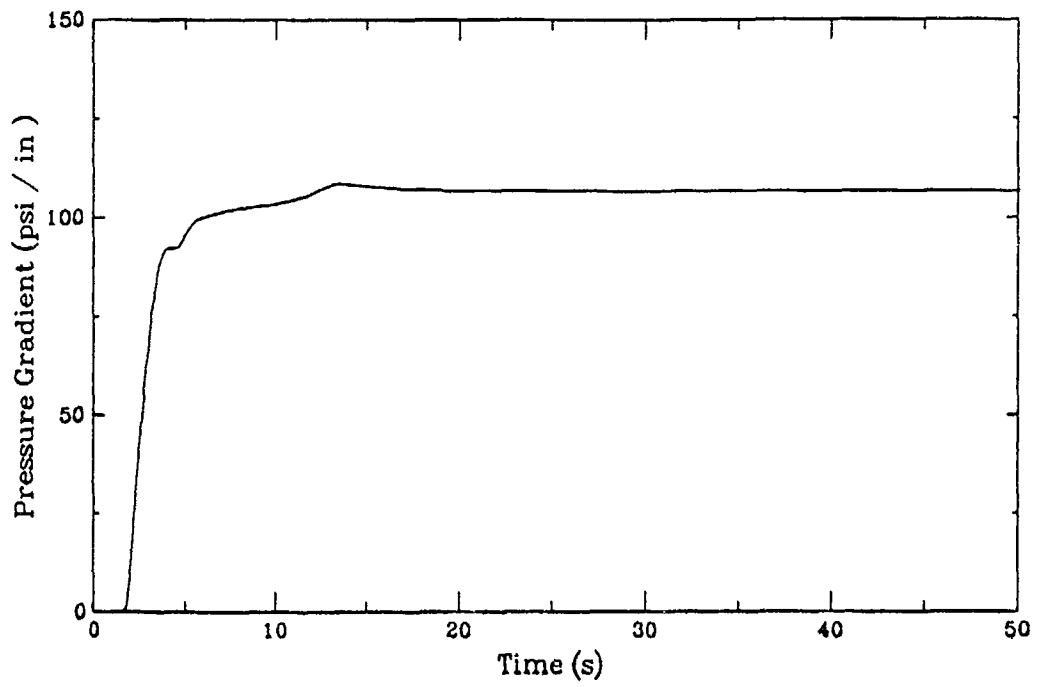
U20B8



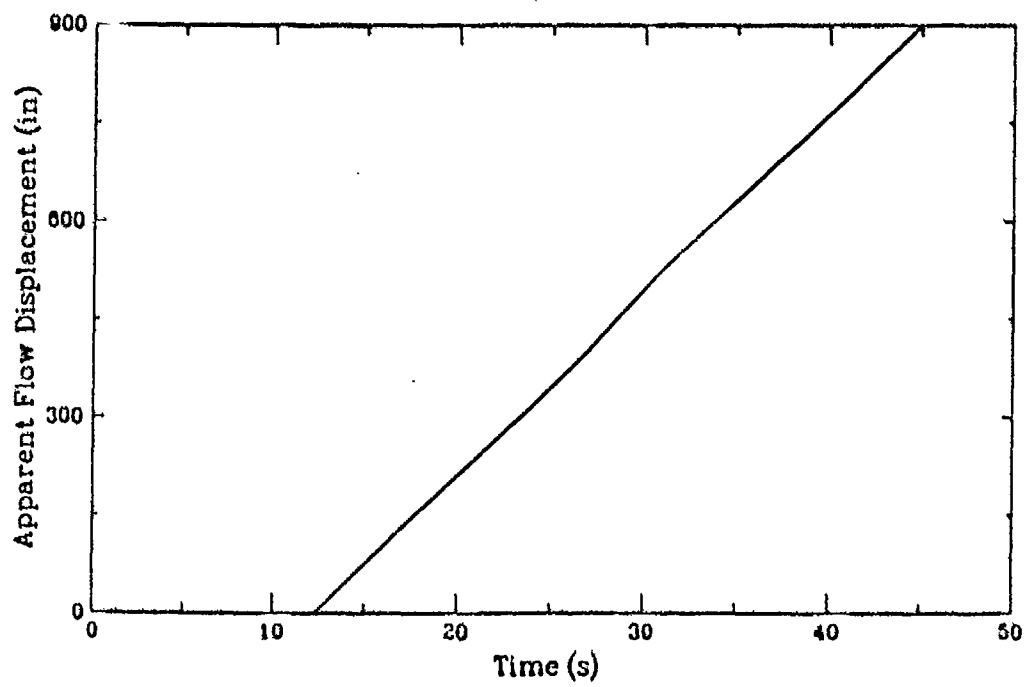
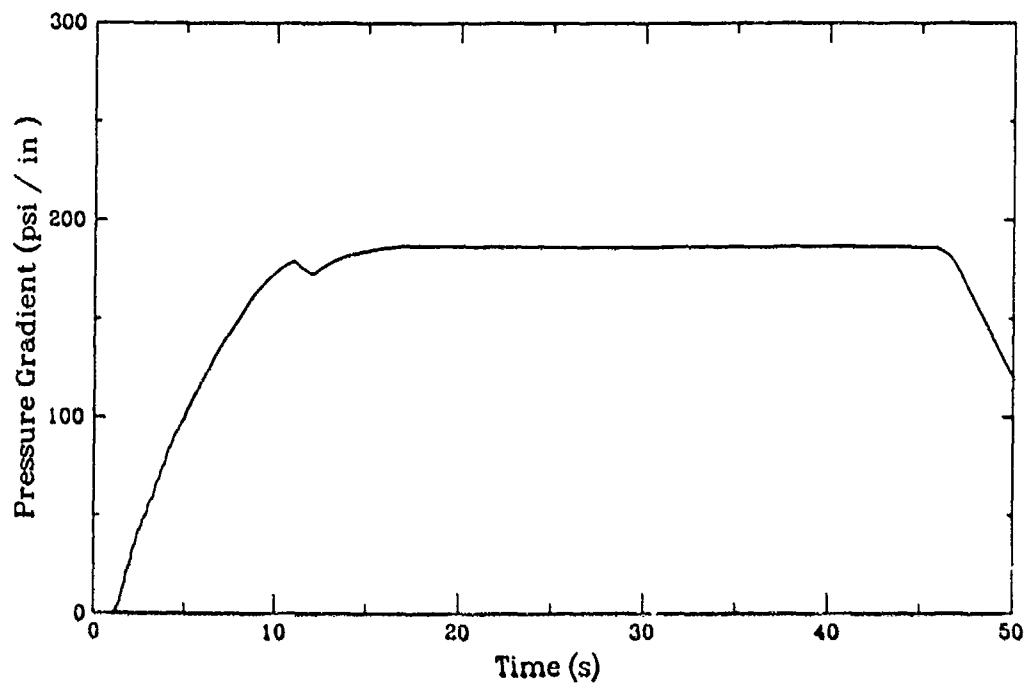
U20C8



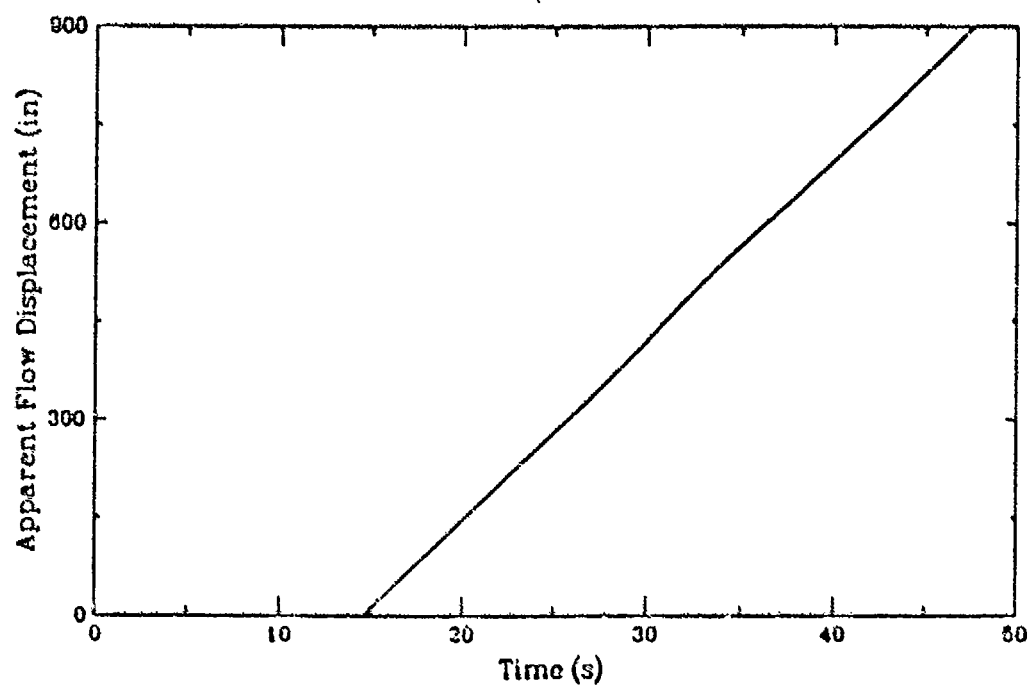
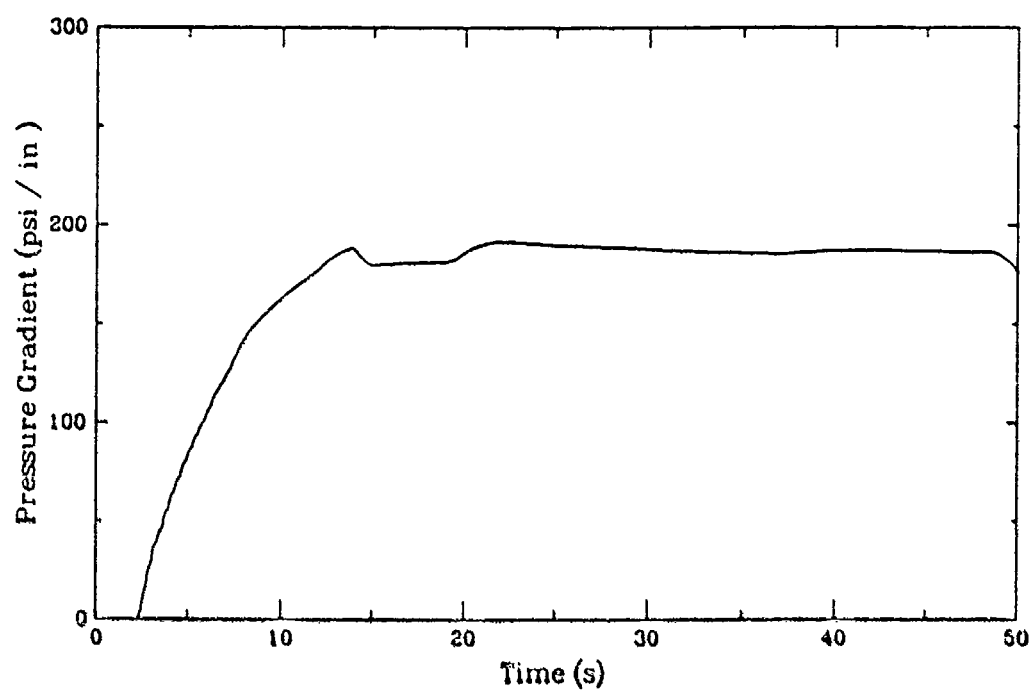
U20D8



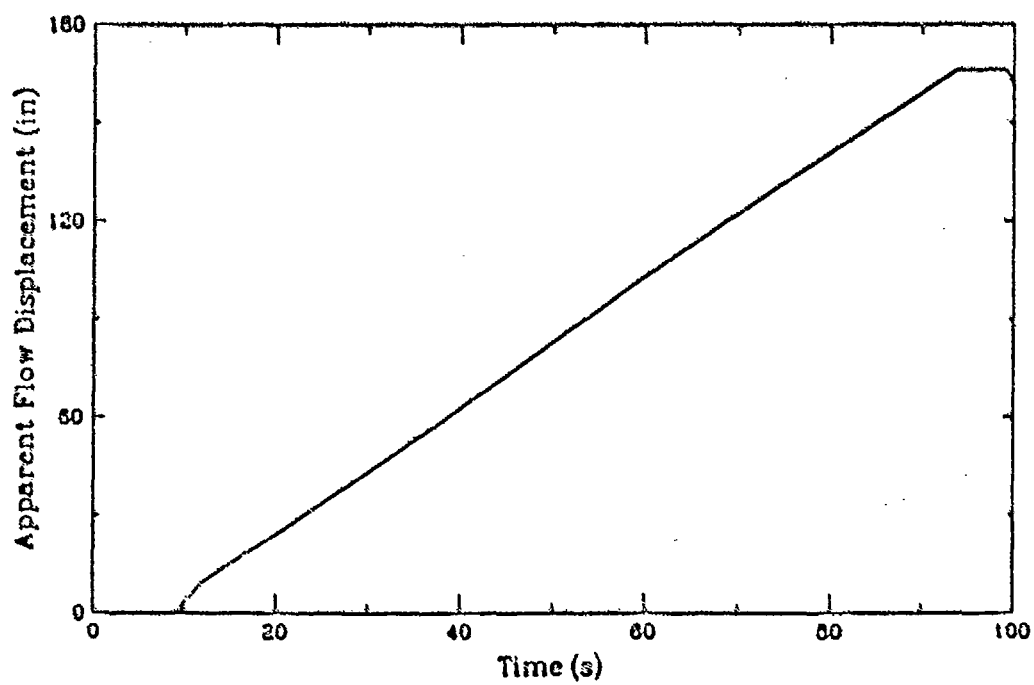
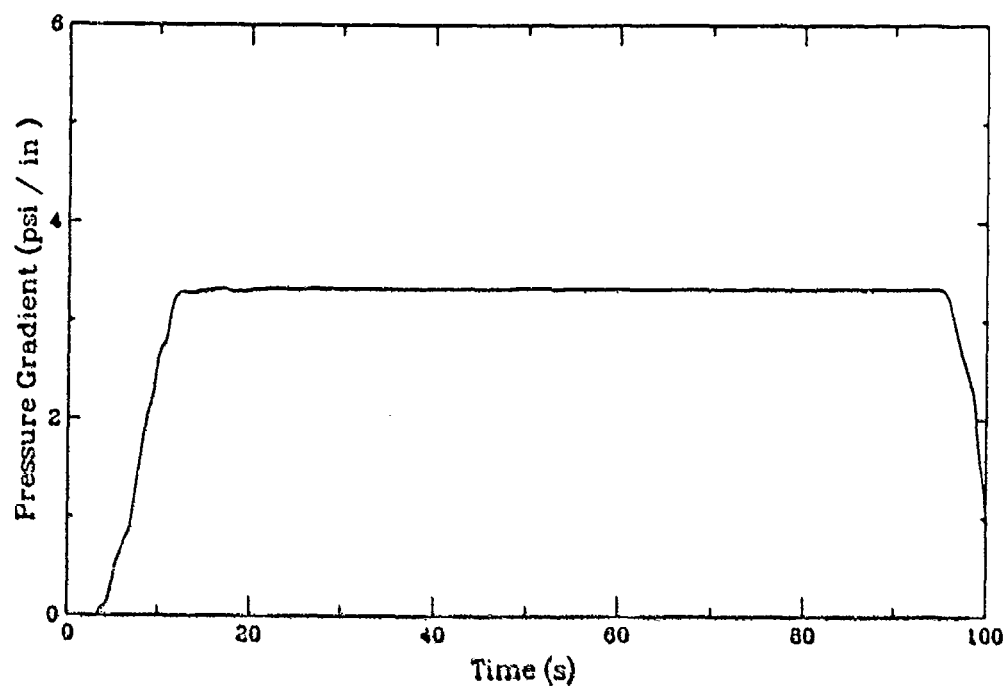
U21A8



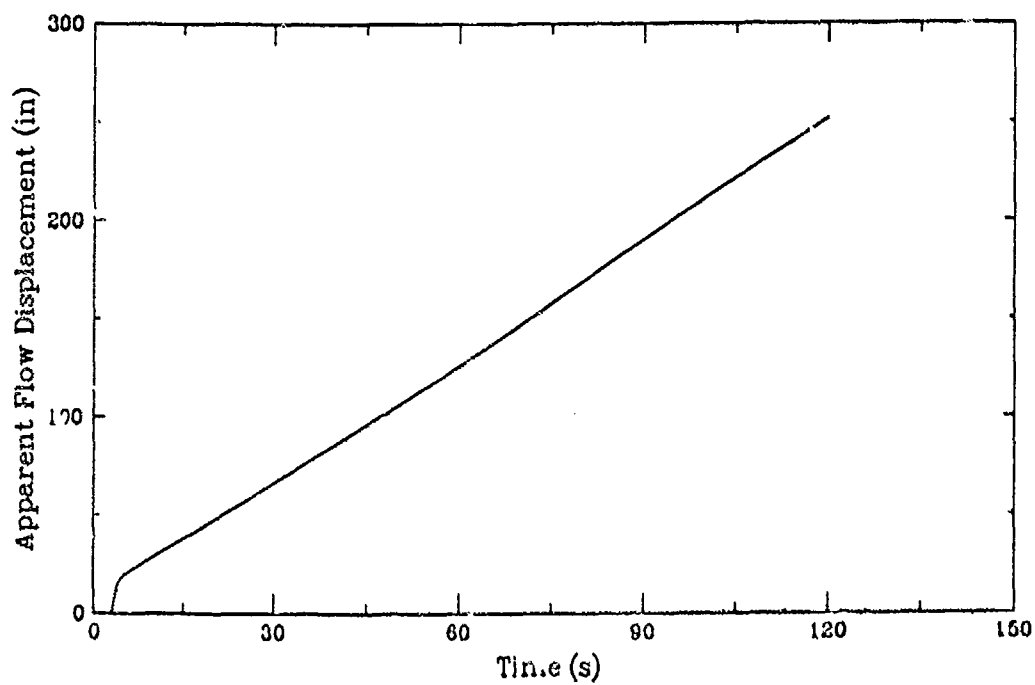
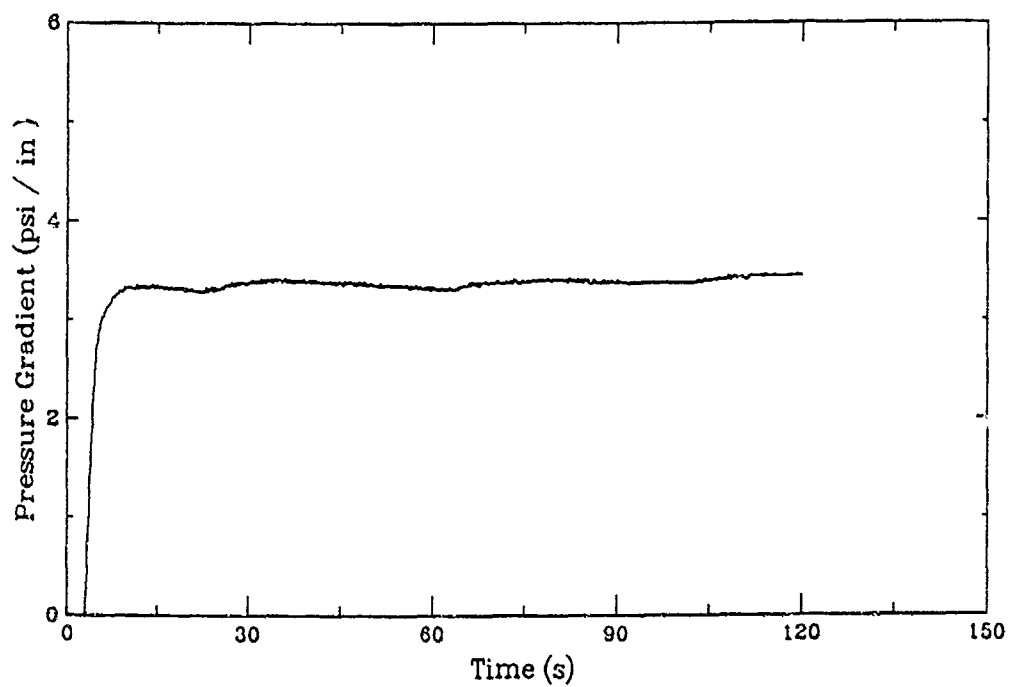
U21B8



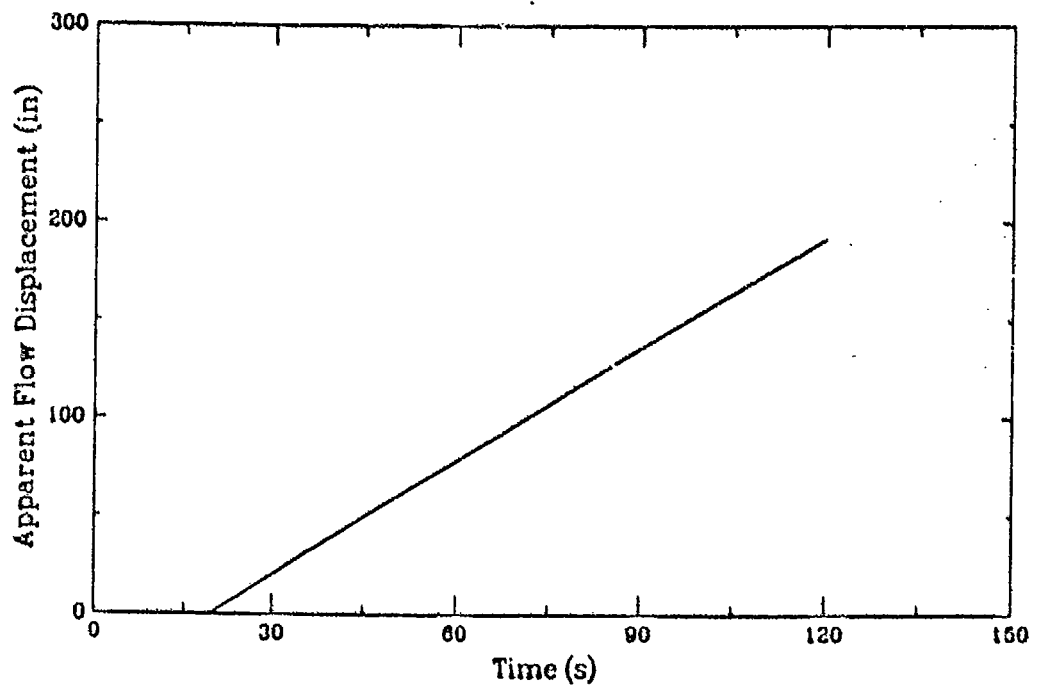
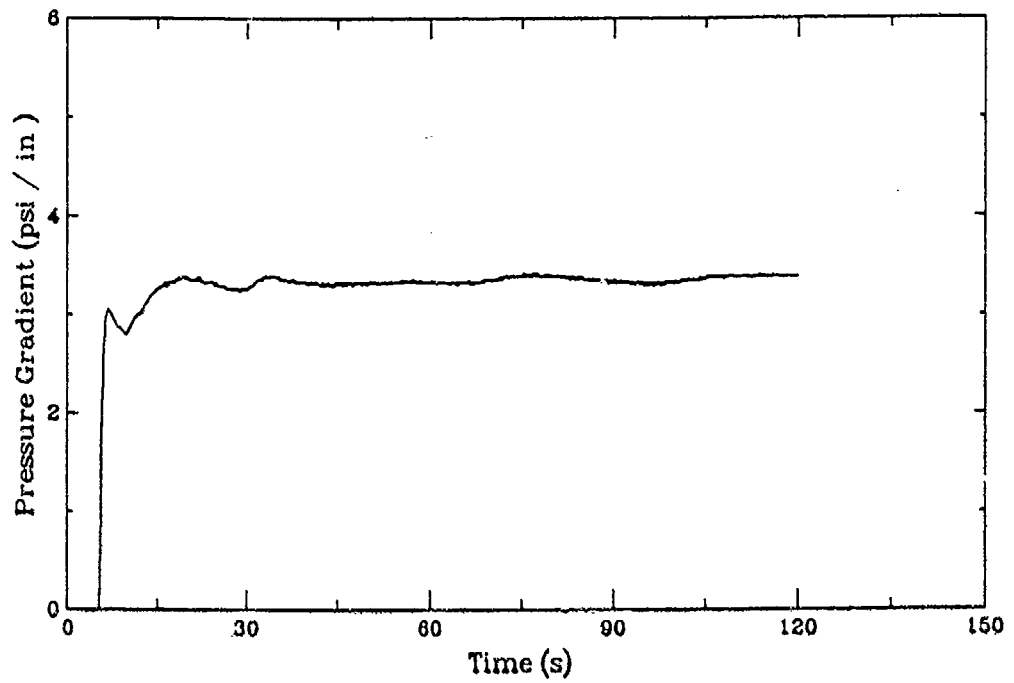
U30I8



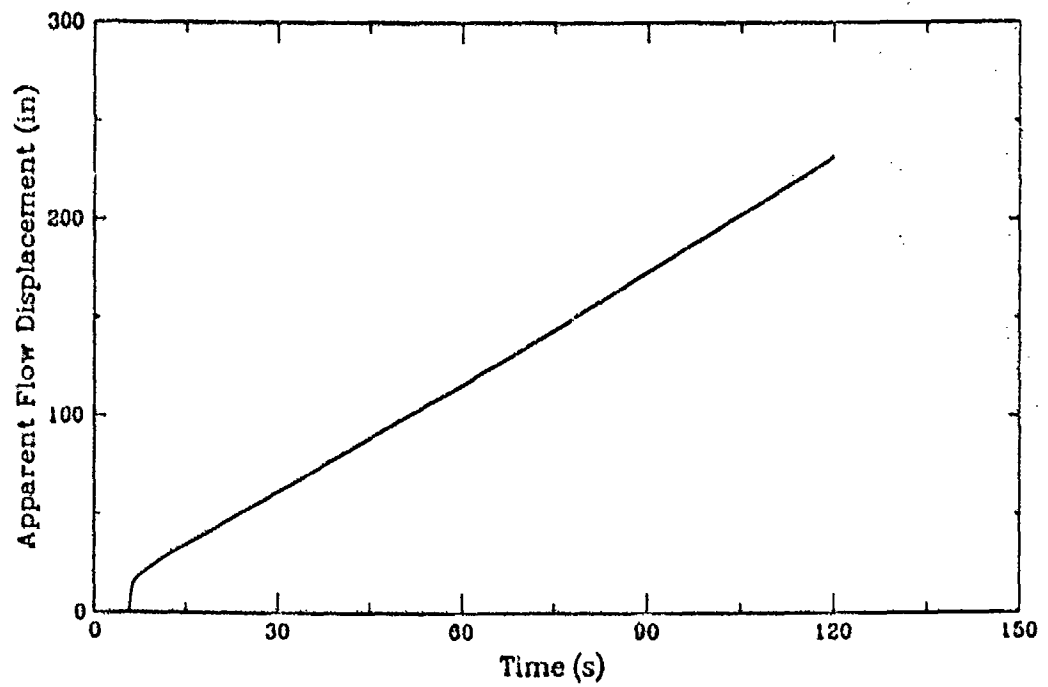
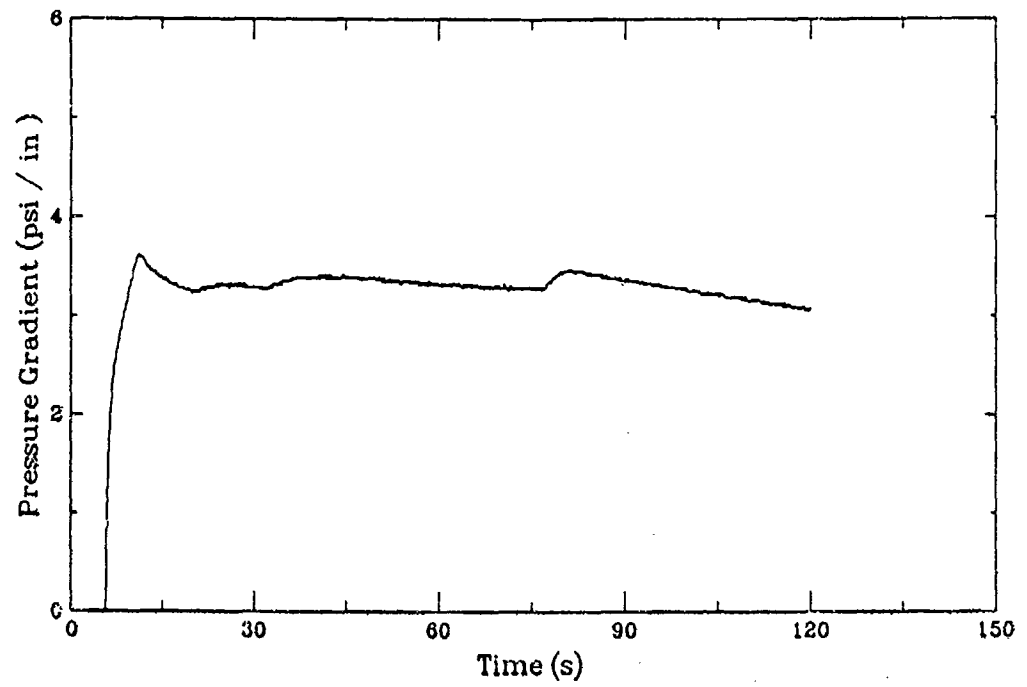
U23D8



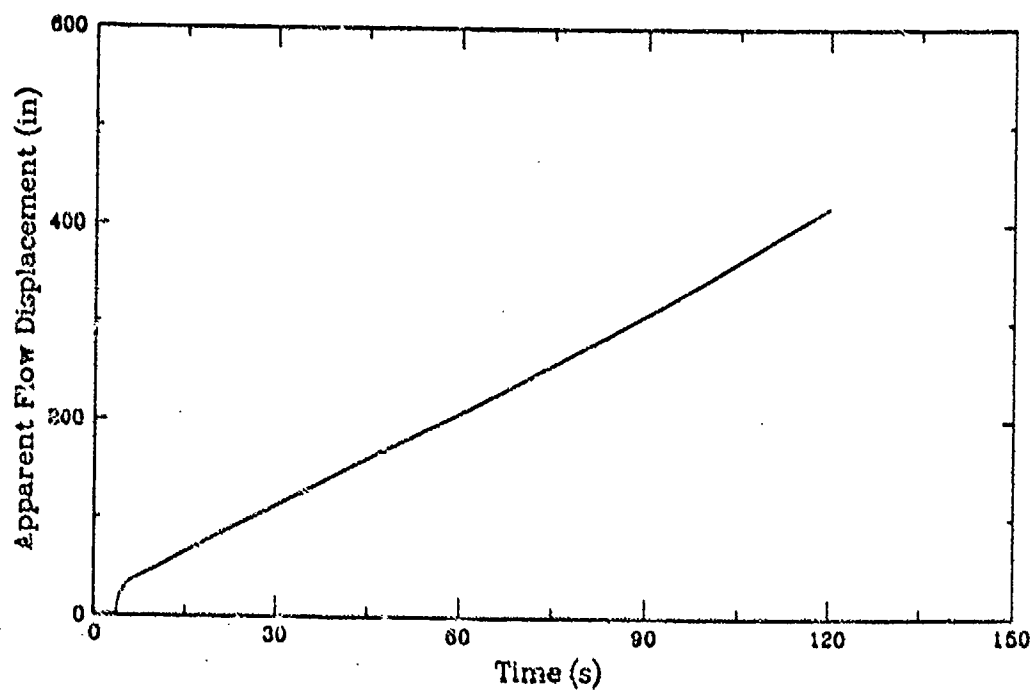
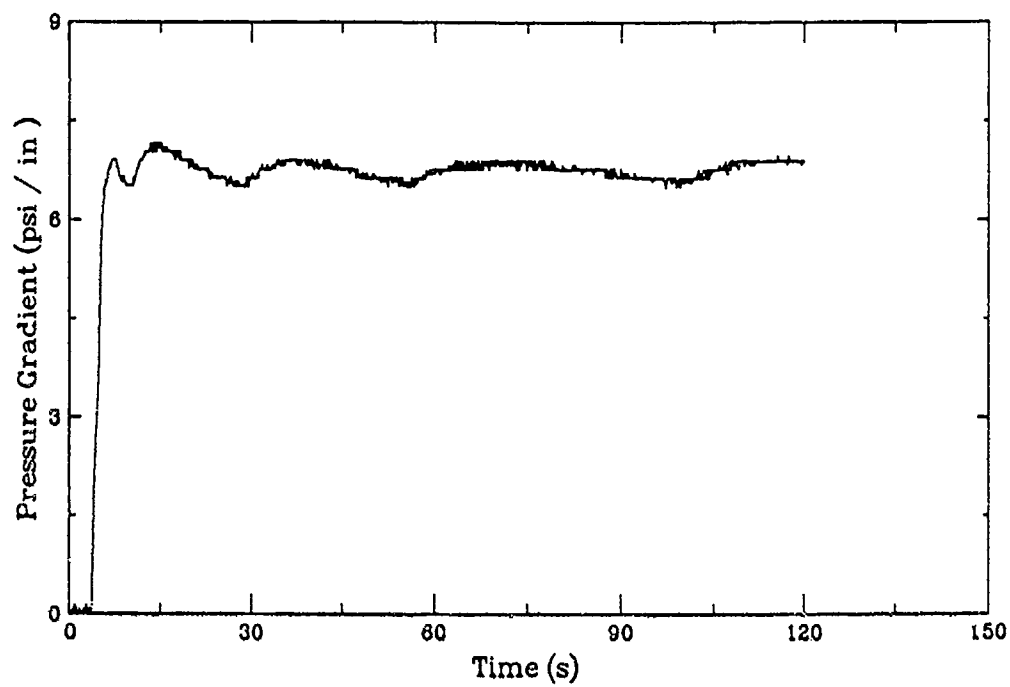
U23E8



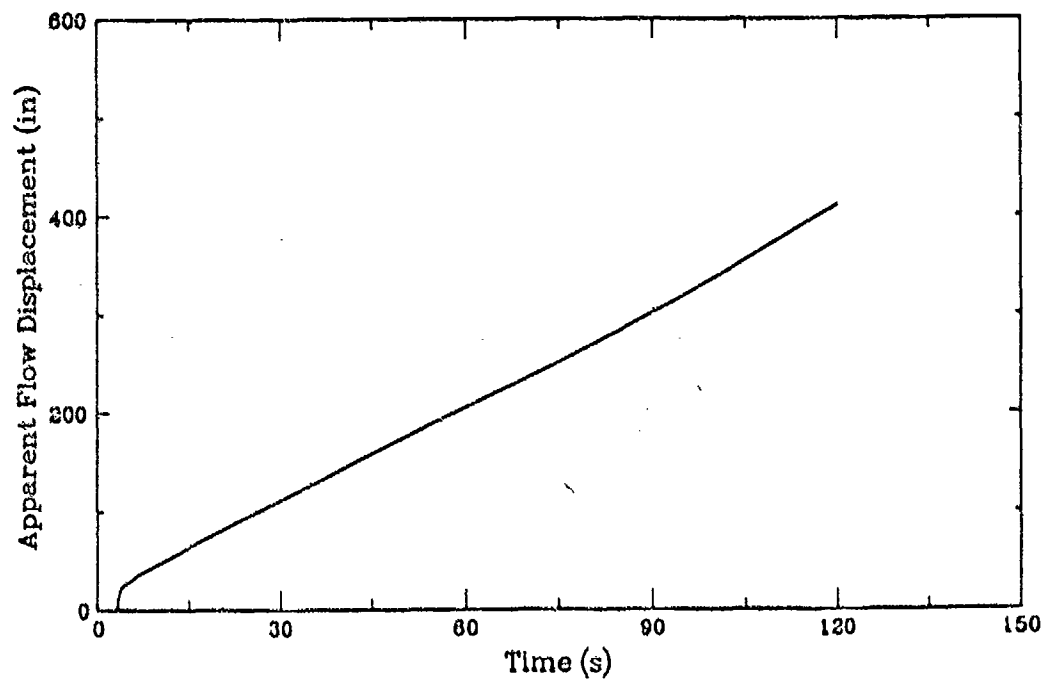
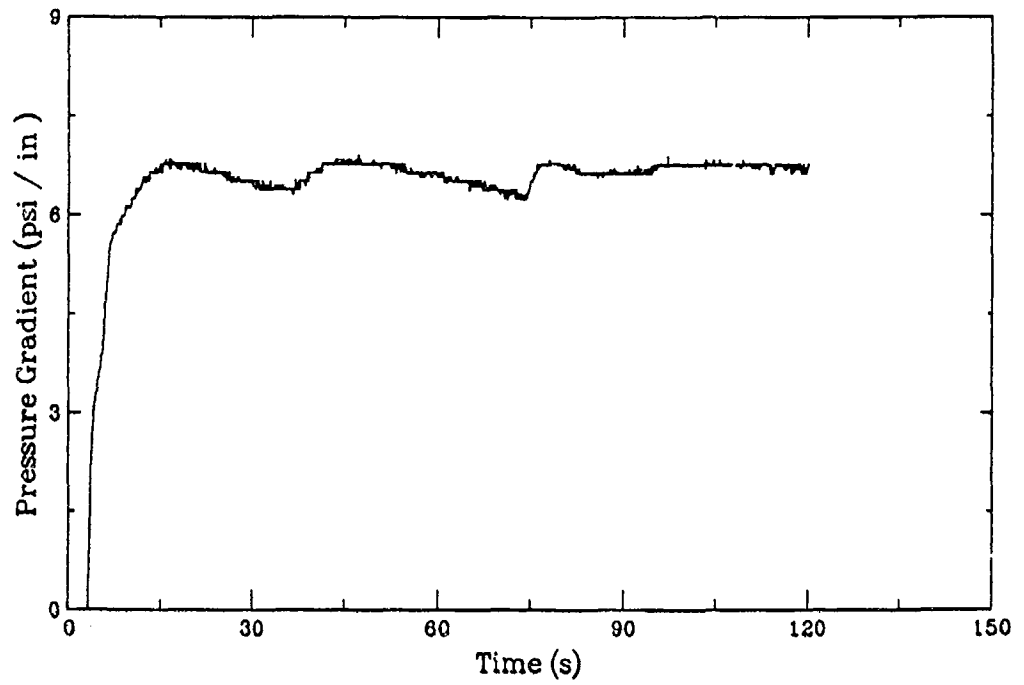
U23F8



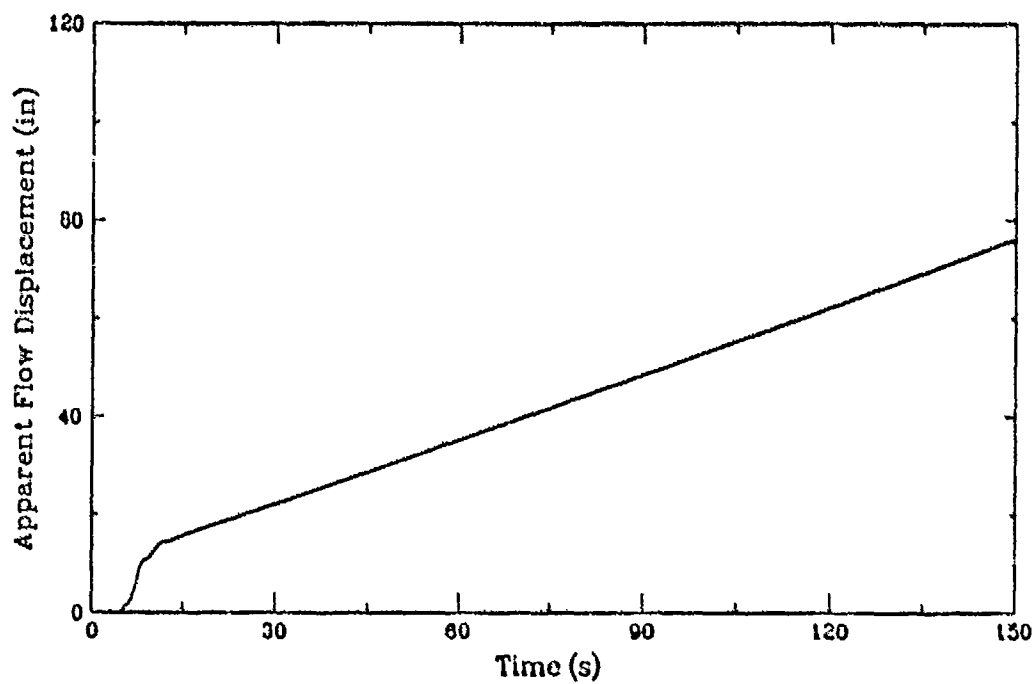
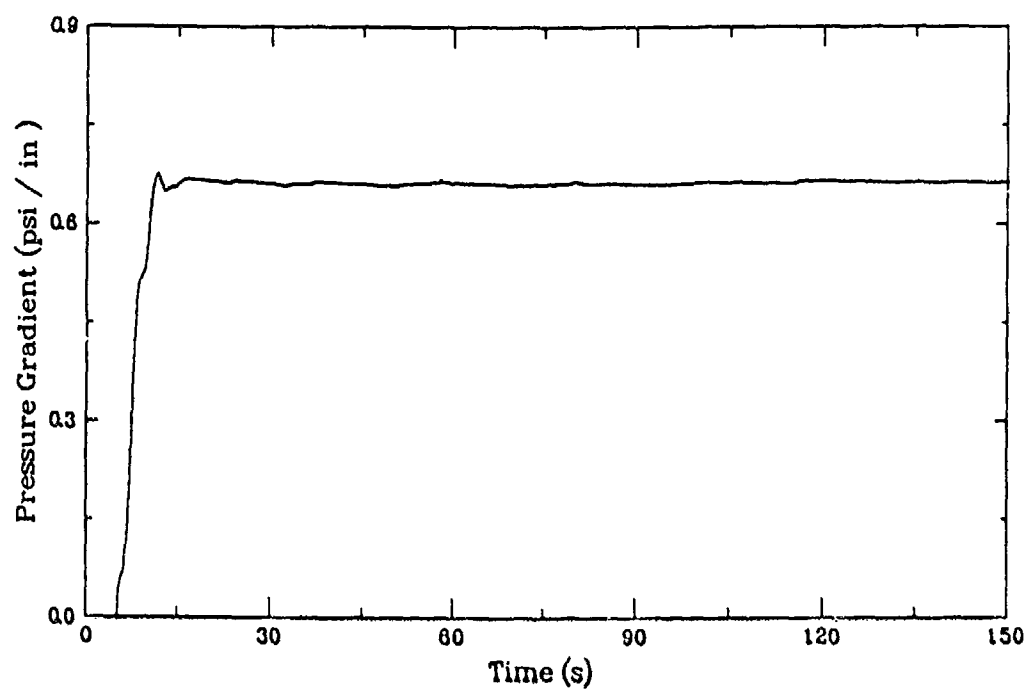
U27G8



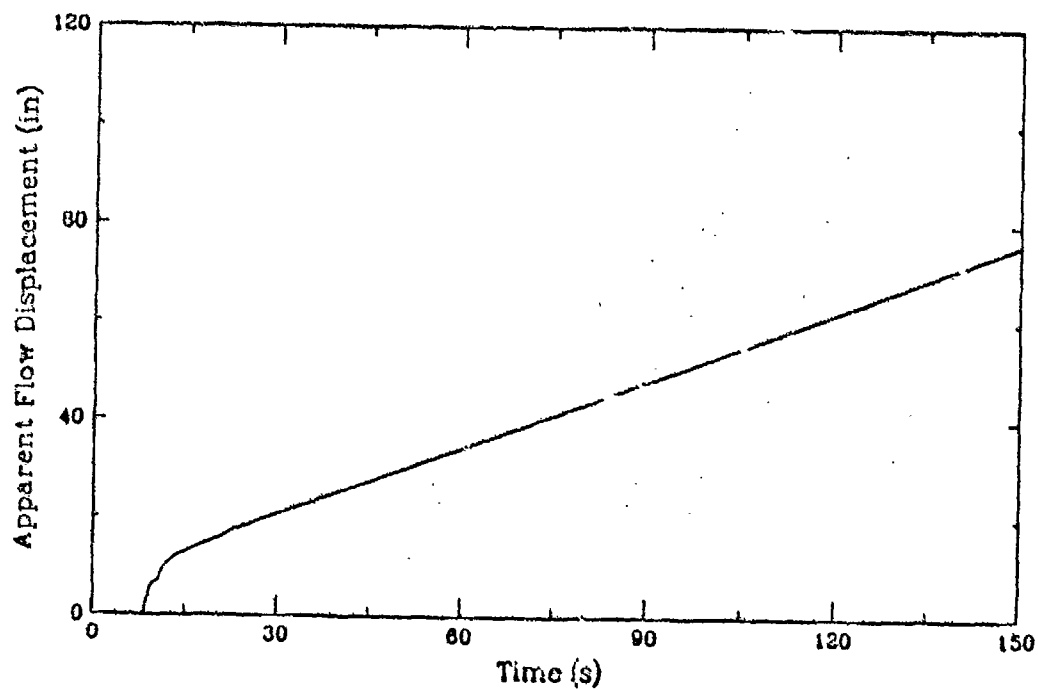
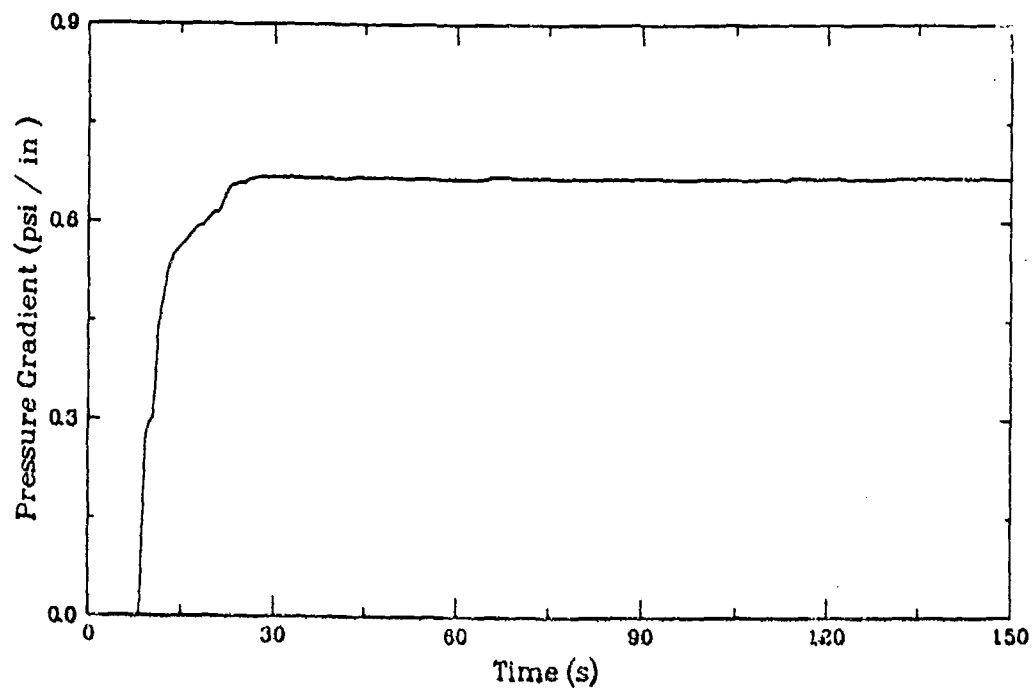
U27H8



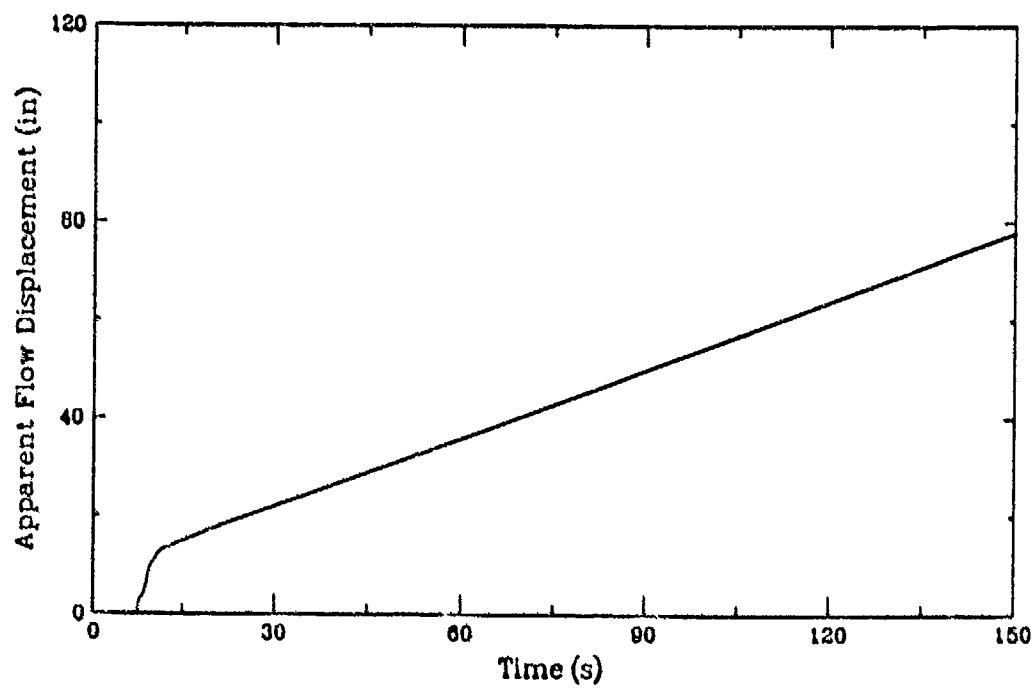
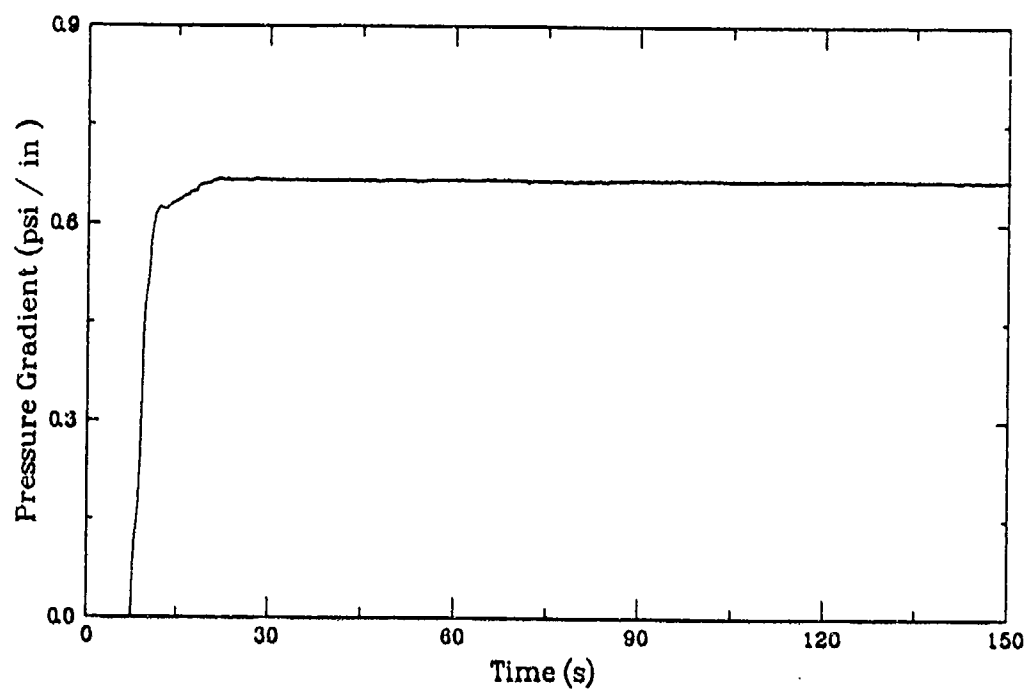
U30A8



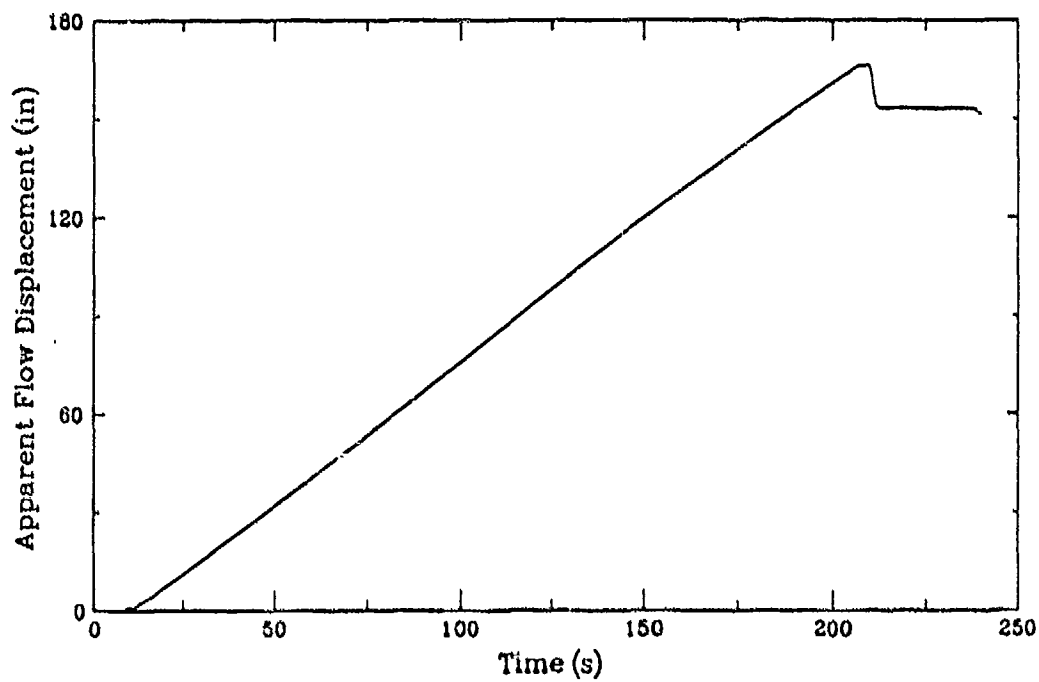
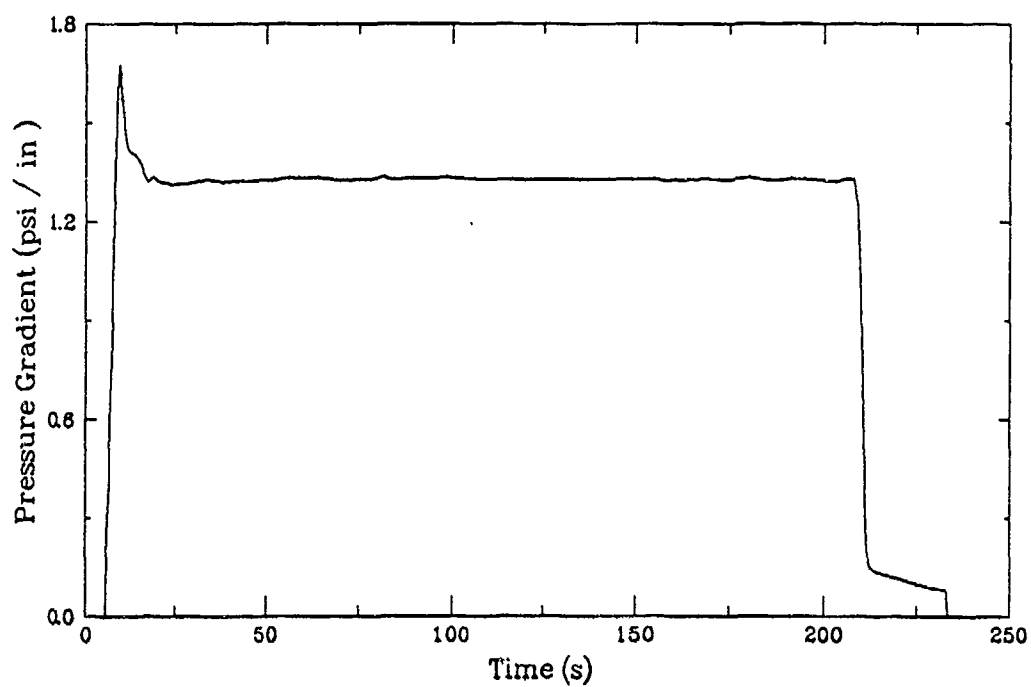
U30B8



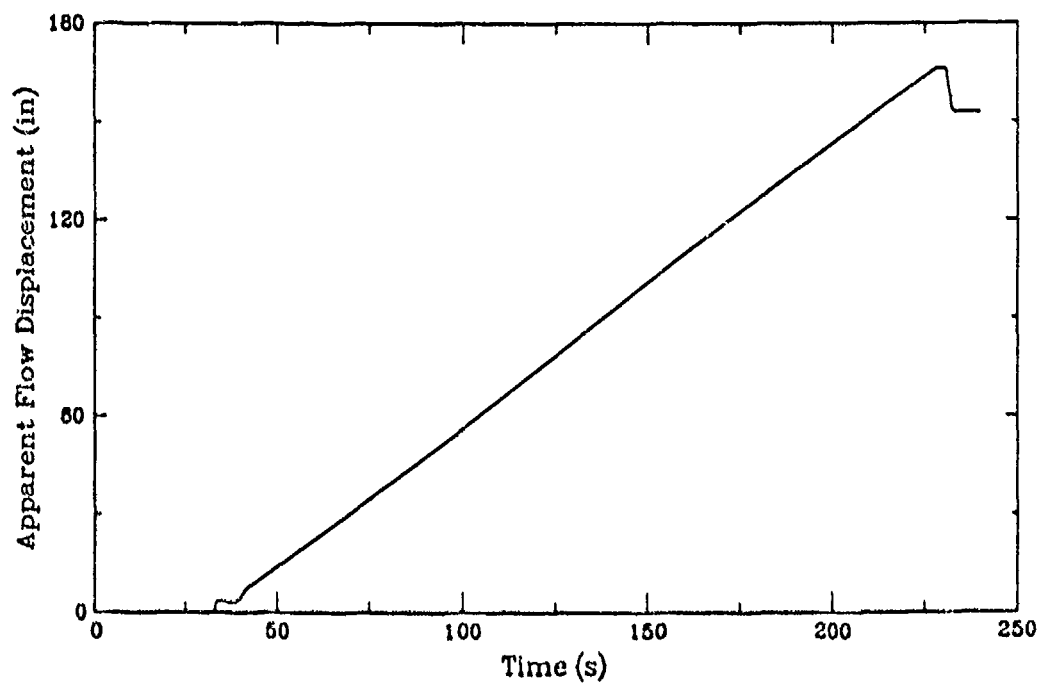
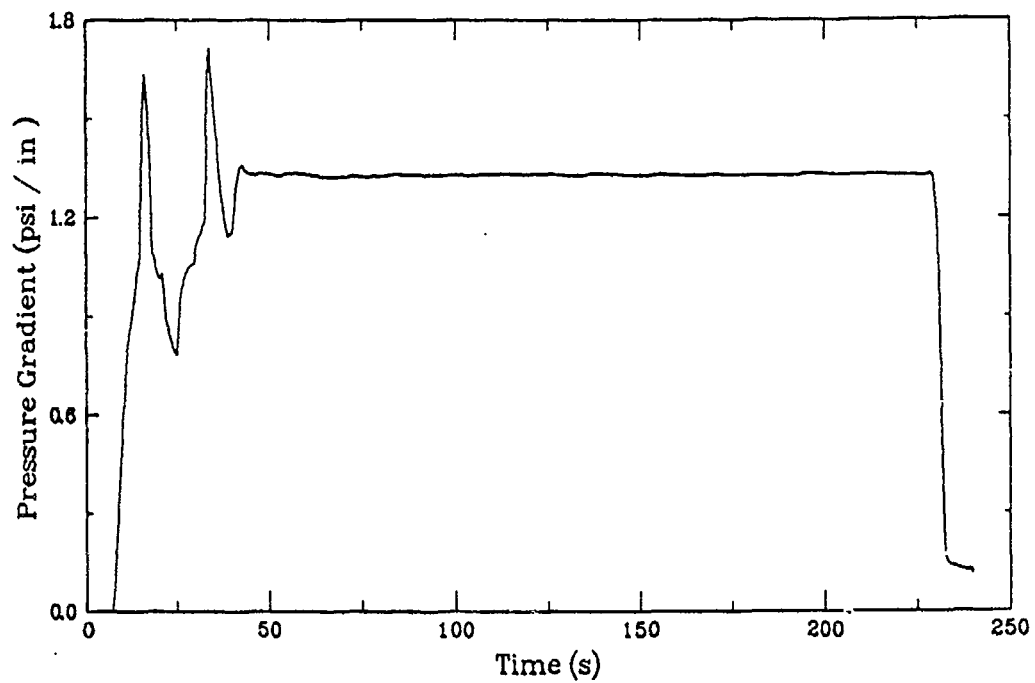
U30C8



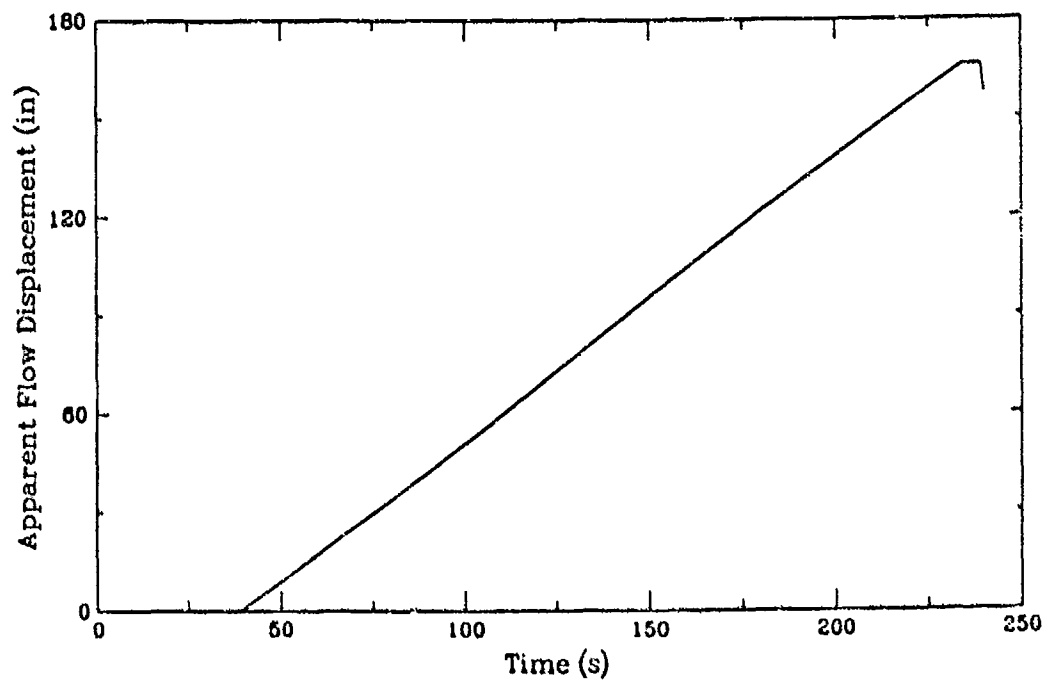
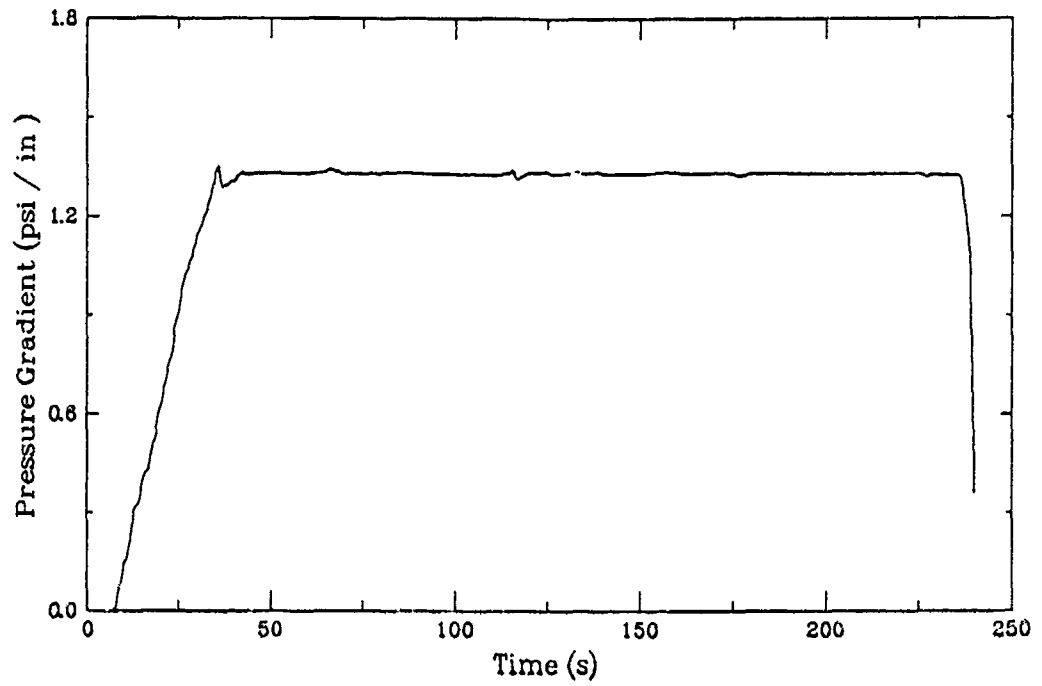
U30D8



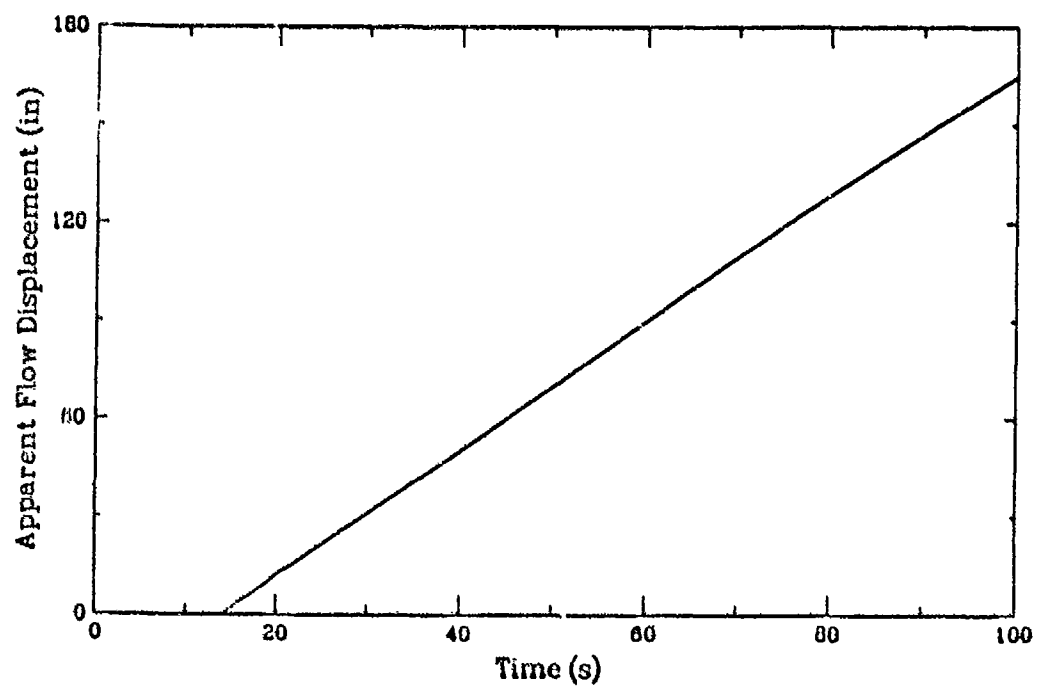
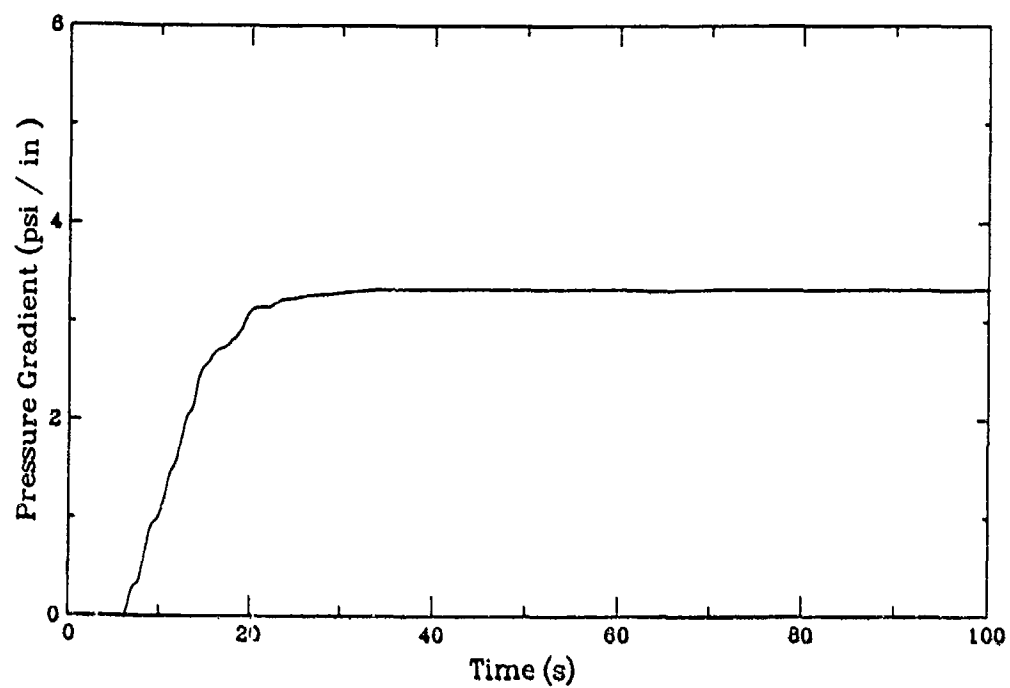
U30E8



U30F8



U30G8



U30H8

